RUHR-UNIVERSITÄT BOCHUM

RUB

Continuum modeling of ductile crystals with evolving microstructures

Christina Günther

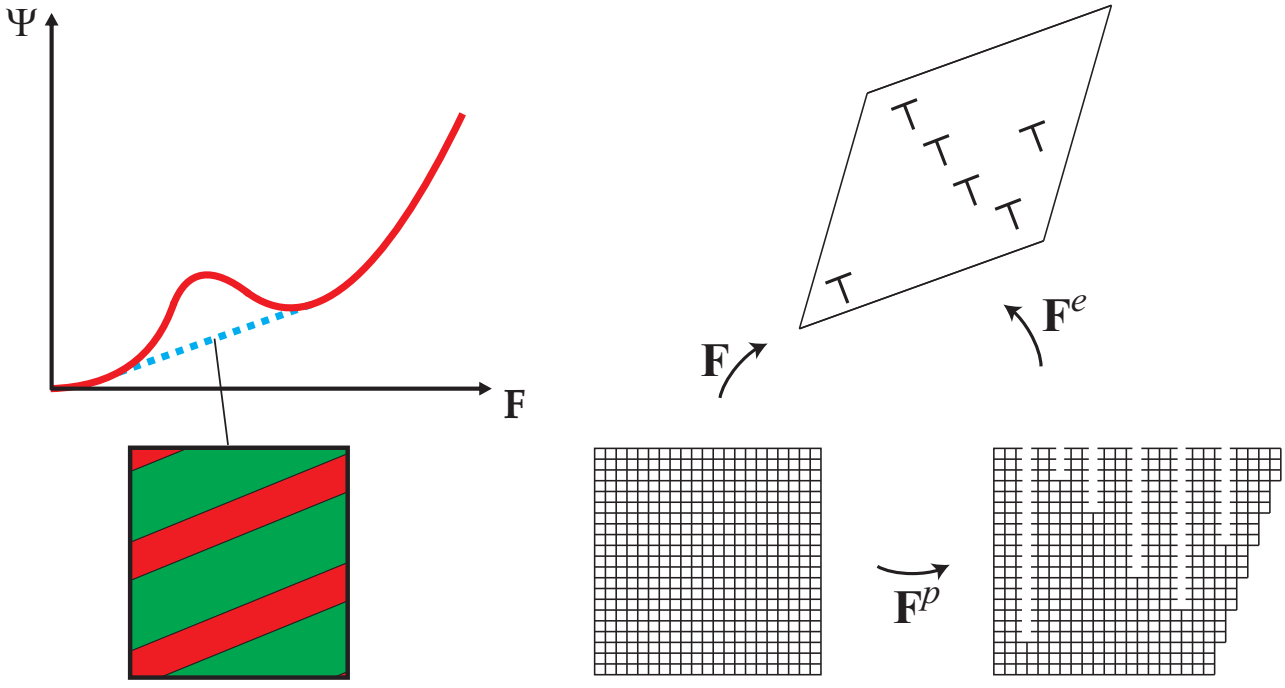

R U H R - U N I V E R S I T Ä T B O C H U M
I n s t i t u t f ü r M e c h a n i k

Christina Günther

Continuum modeling of ductile crystals with evolving microstructures

Mitteilungen aus dem Institut für Mechanik Nr. 165

Herausgeber:

Institut für Mechanik
— Schriftenreihe —
Ruhr-Universität Bochum
D-44780 Bochum

ISBN 978 3 935892 43 8

Mündliche Prüfung (thesis defense): 21.10.2015

1. Gutachter (first referee): Prof. Dr. rer. nat. Klaus Hackl
2. Gutachter (second referee): Prof. Dr. rer. nat. Khanh Chau Le
3. Gutachter (third referee): Prof. Dr.-Ing. Christian Miehe
Vorsitzender (committee chair): Prof. Dr.-Ing. Tom Schanz

Acknowledgments

This work was funded by the Forschergruppe Microplast, which is gratefully acknowledged. Not for only the financial support but especially the interaction and discussions with other researchers, made possible within this group, were a great inspiration.

I want to thank both of my supervisors, Prof. Klaus Hackl and Prof. Khanh Chau Le, without whose guidance, this thesis would not exist. Prof. Hackl gave me the opportunity to work at his chair and he introduced me into the field of modeling microstructures, especially by using the principle of the minimum of the dissipation potential. He always gave me the freedom to do things my own way. In this content, I express my thanks also to Dr. Philipp Junker, who took the time for discussions and advices. Prof. Le introduced me already as a student to the topic of dislocations, later to the concept of continuum dislocation theory. He was always a kind and patient teacher.

Further I want to thank Prof. Christian Miehe for being the third supervisor and the rest of the examination board, Prof. Rüdiger Höffer and Prof. Tom Schanz.

A huge thank you goes to my colleagues, Dr. Ulrich Hoppe, my roommates (former and actual) Pramio and Nicola and also Stephan, Johanna, Khiem and Barbara for being not only colleagues but friends. My thanks also go to the rest of the chair for the nice atmosphere and the friendship.

Last but not least I thank Dominik, Katharina and Theresa for being there and supporting me.

Kurzfassung

Das makroskopische Verhalten eines Materials das sich elastisch-plastisch verformt hängt stark von seinem mikrostrukturellen Aufbau ab. Verändert sich dieser Aufbau unter externer Belastung, wie z.B. bei Rekristallisation, Martensittransformation oder der Bildung von Mikrobändern, beeinflusst dies auch das Materialverhalten. Somit ist, um elastisch-plastisches Verhalten zu verstehen und zu simulieren, die Untersuchung von diesen Mikrostrukturen sinnvoll.

In dieser Arbeit werden zwei Modelle präsentiert, bei denen die jeweiligen Mikrostrukturen als Minimierer nichtkonvexer Energien beschrieben werden. Beide Modelle haben einen variationellen Charakter und untersuchen zunächst die Mikrostrukturen an einem Einkristall, d. h. an einem homogenen Kristallgitter, unter Annahme großer Deformationen.

In dem ersten Modell entsteht eine Laminatstruktur, deren Energie einer relaxierten Energiehülle des Einkristalls entspricht. Um den Zustand dieses Einkristalls und die zeitliche Entwicklung der Mikrostruktur zu beschreiben, wird das Prinzip der minimalen Energie und des minimalen Dissipationspotentials verwendet. Dafür müssen lediglich die freie Energie und das Dissipationspotential definiert werden. Für die freie Energie wird ein inkompressibles Neo-Hooke Material mit einem Gleitsystem verwendet. Das Dissipationspotential besteht aus einem ratenunabhängigen und einem ratenabhängigen Anteil. Dieses Dissipationspotential modelliert visko-plastisches Materialverhalten. Dieser ratenabhängige Anteil des Dissipationspotentials regularisiert das Modell, so dass die numerische Implementierung einfach umsetzbar und stabil ist. Es werden erste numerische Ergebnisse gezeigt.

Das zweite Modell bezieht die Versetzungsdichte in die freie Energie ein, indem die nichtlineare Kontinuumsversetzungstheorie verwendet wird. Dieses Modell enthält eine räumliche Regularisierung der Kristallplastizität, da die Versetzungsdichte in Abhängigkeit des Gradienten der plastischen Gleitung eingeführt wird. In der Literatur wurde die physikalisch sinnvolle Kinematik der nichtlinearen Kontinuumsversetzungstheorie noch nicht vollständig untersucht, daher wird in dieser Arbeit eine begründete Kinematik vorgestellt. Davon abhängig werden die freie Energie und Dissipation beschrieben. Mithilfe der Variationsrechnungen können dann Probleme gelöst werden. Um diese Theorie zu bestätigen, wird sie an dem Beispiel ”finite anti-plane constrained shear”verifiziert.Danach wird die Martensittransformation mit involvierten Versetzungen an dem Beispiel ”finite plane-strain constrained shear”ßimuliert, wobei eine Martensitphase als Minimierer einer nichtkonvexen Energie entsteht.

Beide Modelle simulieren die Entstehung von Mikrostrukturen in Einkristallen mit einem Gleitsystem. Trotz dieser starken Vereinfachungen sind die Ergebnisse physikalisch sinnvoll und zeigen die Anwendbarkeit beider Modelle.

Inhaltsverzeichnis

Nomenclature

Latin notations

a	width of a crystal
$\mathbf{b}_r$	resultant Burgers vector
c	dimensionless parameter
$\mathbf{C}$	right Cauchy Green tensor
D	dissipation
E	energy
$\mathscr{E}$	dimensionless energy functional
$\mathbf{E}$	Green-St. Venant strain tensor
$\mathbf{F}$	deformation gradient
h	height of a crystal
I_i	invariants of a tensor
J	determinant of deformation gradient
$\mathscr{I}$	energy functional
$\mathbf{I}$	unit matrix
k	material constant
K	kinetic energy
l	dimensionless length
L	length of a crystal
$\mathscr{L}$	Lagrangian
m	mass
$\mathbf{m}$	normal vector of slip direction
$\mathbf{n}$	normal vector
p	hardening parameter
$\mathbf{P}$	first Piola-Kirchhoff stress tensor
Q	heat flow
r	critical resolved shear stress
s	viscous parameter
$\mathbf{s}$	slip direction
$\mathbf{S}$	second Piola-Kirchhoff stress tensor
$\mathbf{T}$	dislocation density tensor
$\mathbf{t}$	traction vector
dt	time step
$\mathbf{u}$	displacement field
$\mathbf{v}$	velocity
w	strain, control parameter
W	work
x_i	coordinate
$\mathbf{z}$	internal variables

Greek notation

$\boldsymbol{\alpha}$	dislocation density tensor for small deformations
α	angle of slip system
$\boldsymbol{\beta}$	plastic slip
δ_{ij}	Kronecker delta
δ	thickness of viscous zone
∂	partial derivative
∇	gradient
Δ	dissipation potential
$\boldsymbol{\epsilon}$	strains for small deformations
$\boldsymbol{\varepsilon}$	permutation tensor
γ	plastic slip
η	dimensionless material constant
κ	hardening modulus
λ	volume fraction
μ	shear modulus
ν	Poisson's ratio
ϕ	angle of laminate
$\boldsymbol{\phi}$	mapping
φ	energy density
Ψ	free energy
ϑ	factor for pseudo-velocity
ρ	density
$\boldsymbol{\sigma}$	stress tensor
τ	shear stress
ξ	dimensionless variable
Ω	volume of a material body in the actual configuration
Ω_0	volume of a material body in the reference configuration

1. Abstract

From experiments it is well observed that homogeneous materials may build a microstructure under certain loading conditions, [20]. This microstructure strongly influences the macroscopic material behavior and therefore it can be applied for example for the strengthening of materials. One already investigated mechanism is the Hall Petch strengthening, where grains are refined in order to obtain a higher yield stress. Thus, the investigation of the origin and evolution of microstructures has a great importance. One typical example for microstructual patterns is provided by the martensitic phase transition in carbon steels (see for example [3] or [71]). Another interesting example, where the macroscopic material behavior depends on the microstructure, is the martensitic phase transition of shape memory alloys [43]. These formations of patterns in homogeneous crystals often occur for plastic material behavior. Ewing and Rosenhain observed already in 1899 [22] in experiments that slip steps on the surface of a crystal arise at plastic deformations of metals. In order to model the plastic behavior of crystals, crystal plasticity was introduced. The basic mechanism of crystal plasticity is dislocation movement within the material. During loading, dislocations travel through the crystal lattice along certain crystal planes and slip bands may be developed as microstructure. As most of the metals and alloys have a periodic atomic structure, they can be interpreted as crystals. Hence, the plastic deformation and the evolving microstructure of these materials may be examined at single crystal level.

As the basic mechanism for plastic material behavior has already been well known for a long time, there is a variety of models which try to simulate this material behavior. In this thesis, two different approaches are presented, however, both have a variational character.

The first approach models microbands in a single crystal. For this modeling technique, two quantities have to be defined: the Helmholtz free energy and the dissipation potential within the range of large deformations. Kochmann and Hackl [48] already developed a model which simulates the evolution of a first order laminate in a crystal due to loading. For modeling plastic material behavior, they have chosen a rate independent dissipation potential. In order to improve the stability of this algorithm, the dissipation potential is extended by including a rate dependent contribution which can be regarded as a regularization in time. The simulated microbands are considered as a first order laminate. By employing the principle of minimum of the dissipation potential, the evolving microstructure is obtained as a minimizer of a non-convex energy potential. The deformations are obtained by the principle of minimum of total energy. The application of the first order laminate leads to a rank-one-convex approximation of the non-convex energy. Due to the chosen dissipation potential, explicit evolution equations are derived which display the evolution of the first order laminate.

The second approach in this thesis can model the martensitic phase transition, accommodated by dislocation arrays. As the plastic deformation of the crystal is introduced by the movement of a large number of dislocations, the energy contribution of the dislocation network is taken into account. Therefore, before determining the energy and the dissipation potential, the kinematically independent quantities, which characterize the deformed state

of the crystal and the change of the dislocation network, have to be defined. Then, analogously to the first approach, the free energy and the dissipation potential are determined. Afterwards the variational calculus is applied and analytical solutions can be obtained which display the evolution of the corresponding variables (here chosen: plastic slip) in space. In this modeling approach, not a regularization in time but in space is introduced by the gradient of the plastic slip. Also this approach leads to a phase transition for minimizing the energy if a non-convex energy density is considered.

This thesis starts with the Chapter 2, where the fundamental laws of continuum mechanics are shown, as the conservation laws and thermodynamic principles. From this macroscopic scale, we zoom in Chapter 3 onto the micro level. There, dislocations, which cause plastic deformation on the macro level, are introduced and the basic mechanisms of microstructures are presented.

In Chapter 4 an approach, which models the time continuous rate dependent evolution of inelastic microbands in finite plasticity, is presented. This approach is based on the model of Kochmann and Hackl [47]. The dissipation potential is adapted by a viscous contribution. After the derivation of the explicit evolution equations, a shear test and a tension-compression test are performed. Due to the rate dependent behavior of this model the material behavior at a longer relaxation time, here referred to as pseudo-velocity, has to be examined. Afterwards a comparison to the results of the previous model by Kochmann and Hackl [48] is shown and cycling tests are performed. This chapter closes with a discussion.

In Chapter 5 crystal plasticity is modeled by taking the huge number of dislocations in the crystal into account therefore, this ansatz is based on the nonlinear dislocation theory. The first and important step is to clarify the kinematically independent quantities which describe the energy of the crystal containing dislocations. Then similar to the previous chapter, the energy and the dissipation have to be defined and a variational method is used. Applying this approach, the behavior of dislocations due to load can be analyzed. The first examined example is a single crystal loaded in finite anti-plane constrained shear under the assumption of a convex energy. In this case, the distribution of dislocations and the dislocation pile up can be found. As a second example a crystal is loaded by plane-strain constrained shear. In this example a non-convex energy is considered. In this case, a microstructure appears as a minimizer, since this is energetically favorable. We will see that dislocations are involved in the phase transition process and this leads to the incoherent phase interfaces. We find also the material response to the load during this phase transition process involving dislocations.

This thesis concludes with Chapter 6, where a conclusion and an outlook are given.

A short overview of the essential mathematics, which are used, is given in the Appendix A.

2. Continuum mechanics

In continuum mechanics a body can be interpreted as a continuum in which the molecular lattice or any other discrete composition of the material is ignored. For that continuum, the laws of physics have to be fulfilled:

1. Kinematics (relation between strain and displacement)
2. Conservation of mass
3. Balance of linear momentum
4. Balance of angular momentum
5. Balance of energy (first law of thermodynamics)
6. Second law of thermodynamics

In addition to these laws, constitutive equations (e. g. stress-strain relation) have to be defined. Then the mechanical behavior and deformations of a body due to external loads can be fully described. In the following sections, these laws are shortly provided. For further details of the derivations, we refer to [18], [39], [78] or [33].

2.1. Description of motion and kinematics

In order to describe the motion of every material point in the space, a time-invariant Cartesian coordinate system, with the basis defined by the unit vectors $\mathbf{e}_i$ and the fixed origin O is introduced. As shown in Figure 2.1, in this coordinate system the undeformed body occupies the volume Ω_0. After a deformation, the body occupies the volume Ω. In the undeformed state, also called reference configuration, every material point is described by a position vector $\mathbf{x}$. In the deformed configuration, the position vector is denoted by $\mathbf{y}$. The deformation from the reference to the deformed configuration can be realized as a one-to-one mapping $\boldsymbol{\phi}$. Then the deformed configuration is expressed through the undeformed by

$$\mathbf{y} = \boldsymbol{\phi}(\mathbf{x}). \tag{2.1}$$

We also introduce the displacement field $\mathbf{u}$ (illustrated in Figure 2.1), dependent either on the reference configuration

$$\mathbf{u}(\mathbf{y}) = \mathbf{y} - \mathbf{x}(\mathbf{y}), \tag{2.2}$$

or on the deformed configuration

$$\mathbf{u}(\mathbf{x}) = \mathbf{y}(\mathbf{x}) - \mathbf{x}. \tag{2.3}$$

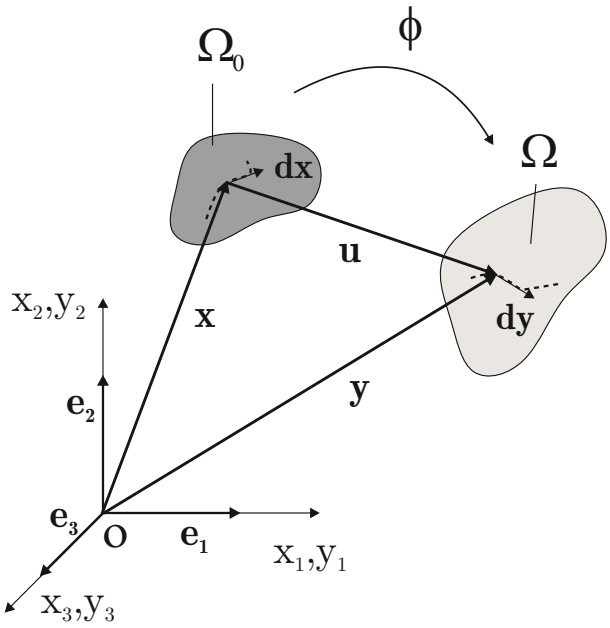

Figure 2.1.: Deformation of a body in space

An infinitesimal line segment **dx** on the undeformed body Ω_0 becomes **dy** in the deformed configuration by

$$\mathbf{dy} = \frac{\partial \mathbf{y}}{\partial \mathbf{x}} \cdot \mathbf{dx} = \mathbf{F} \cdot \mathbf{dx}, \tag{2.4}$$

with **F** denoting the deformation gradient. It is a tensor and defined by Equation (2.4) as

$$\mathbf{F} = \nabla \boldsymbol{\phi} \tag{2.5}$$

thereby,

$$F_{ij} = \delta_{ij} + u_{i,j} = \phi_{i,j}. \tag{2.6}$$

The deformation gradient relates every material line element (like **dx**) to the corresponding line element in the deformed configuration. When we assume that the deformation from one configuration to another is invertible,

$$\mathbf{dx} = \mathbf{F}^{-1} \cdot \mathbf{dy} \tag{2.7}$$

holds true. When the deformation is invertible, it is also nonsingular and therefore the determinant of this deformation gradient cannot be equal to zero. Since the determinant describes the ratio between the deformed and undeformed volume elements, it must be positive,

$$J = \det(\mathbf{F}) > 0. \tag{2.8}$$

An arbitrary deformation consists of three independent parts: rigid body translation (then: $\mathbf{F} = \mathbf{I}$), rotation and pure stretching.

The so called right Cauchy Green tensor **C** can be introduced in terms of **F**

$$\mathbf{C} = \mathbf{F}^{\mathrm{T}}\mathbf{F}. \tag{2.9}$$

Accordingly also the left Cauchy Green tensor $\mathbf{B}$ is introduced,

$$\mathbf{B} = \mathbf{F}\mathbf{F}^{\mathrm{T}}. \tag{2.10}$$

Both tensors are symmetric and positive-definite.

Another definition for the strains is given by the Green-Lagrange strain tensor

$$\mathbf{E} = \frac{1}{2}(\mathbf{C} - \mathbf{I}) = \frac{1}{2}\left(\mathbf{F}^{\mathrm{T}}\mathbf{F} - \mathbf{I}\right) \tag{2.11}$$

or in terms of the displacements

$$E_{ij} = \frac{1}{2}\left(u_{i,j} + u_{j,i} + u_{k,i}u_{k,j}\right). \tag{2.12}$$

This tensor is quite useful for applications, since it is referred to as an objective strain measure. Note that this strain tensor is zero when the body undergoes a translation or a pure rotation from the initial state [4].

In continuum mechanics, infinitesimal deformations are often assumed, which is valid if small elastic deformations are assumed. Since $\left|u_{i,j}\right| << 1$ in this case the Green-St. Venant strain tensor $\mathbf{E}$ reduces to

$$\epsilon_{ij} = \frac{1}{2}\left(u_{i,j} + u_{j,i}\right), \tag{2.13}$$

which is called the infinitesimal strain tensor $\boldsymbol{\epsilon}$.

When the body Ω deforms in space, each particle of the body has a velocity vector $\mathbf{v}$ which is a function of time and space

$$\mathbf{v}(\mathbf{x}, \mathrm{t}) = \lim_{\Delta \mathrm{t} \to 0} \frac{\mathbf{u}(\mathbf{x}, \mathrm{t} + \Delta \mathrm{t}) - \mathbf{u}(\mathbf{x}, \mathrm{t})}{\Delta \mathrm{t}} = \left.\frac{\partial \mathbf{u}}{\partial \mathrm{t}}\right|_{\mathbf{x}}. \tag{2.14}$$

2.2. Stresses

In the previous section the kinematic aspects of a deformation have been discussed. Now we focus on the forces, which may cause these deformations. An arbitrary body Ω can be loaded by external forces. These are classified as body (denoted by $\mathbf{g}$ in Figure 2.2) and surface forces. A typical example for a body force is the gravity of the earth. Surface forces are distributed forces (denoted by $\mathbf{q}\left[\frac{\mathrm{N}}{\mathrm{m}^2}\right]$ in Figure 2.2) acting on a surface area. Idealizations of these distributed forces are:

- Line forces (denoted by $\mathbf{p}\left[\frac{\mathrm{N}}{\mathrm{m}}\right]$ in Figure 2.2) acting on a line element
- Point forces (denoted by $\mathbf{f}$ [N] in Figure 2.2) acting either on the surface or in the body

Surface forces are contact forces. The part of the surface where the surface forces are acting is denoted with $\partial\Omega_{\mathrm{t}}$. The part where the displacements are prescribed is denoted by $\partial\Omega_{\mathrm{u}}$.

External forces have to cause a reaction inside the body. After cutting the deformed body, an internal stress vector $\mathbf{t}$, also referred as traction vector, becomes visible at the surface.

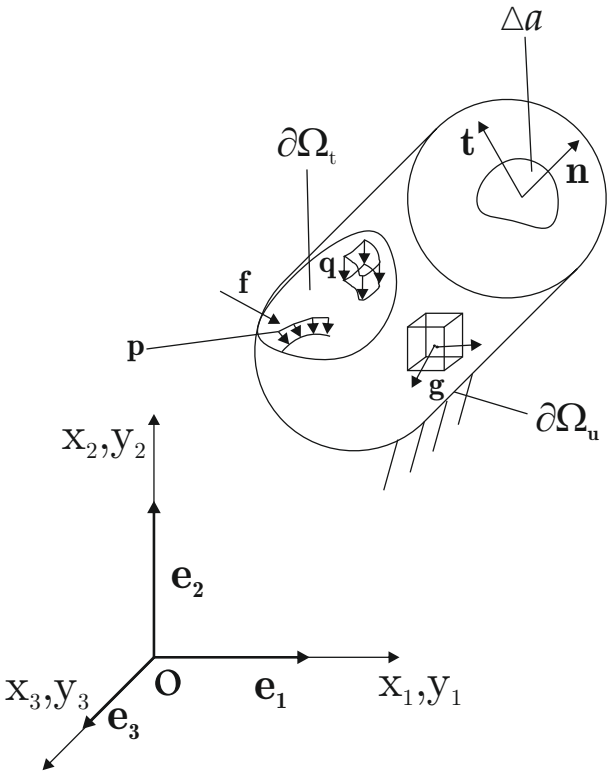

Figure 2.2.: Stresses as response to external loads

This traction vector **t**, illustrated in Figure 2.2, acting on an infinitesimal area element Δa is defined as

$$\mathbf{t} = \lim_{\Delta a \to 0} \frac{\Delta \mathbf{F}}{\Delta a}. \tag{2.15}$$

The traction vector **t** represents the stress on the cut area with the normal vector **n**. By cutting a cube out of the deformed body, six cut areas are obtained, all having a traction vector $\mathbf{t}_i$. Assembling the stresses of all directions at all surfaces leads to a tensor, called the Cauchy stress tensor $\boldsymbol{\sigma}$, see Figure 2.3. Due to the symmetry of the stress tensor, which

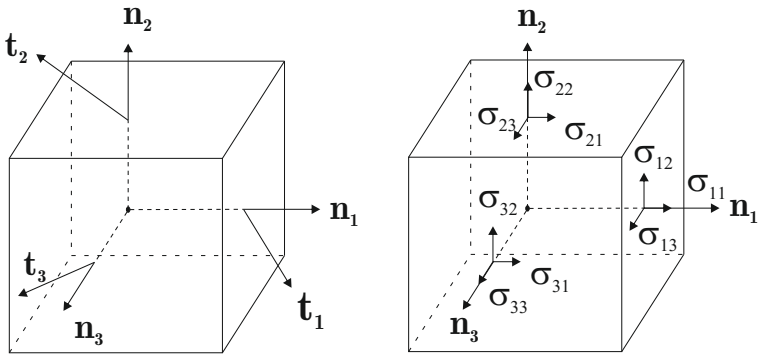

Figure 2.3.: Link between traction vector and stress tensor

will be proven later by the balance of angular moment, only three traction vectors need to be assembled. Hence the relation for the traction vector **t** at a surface and the Cauchy stress tensor reads

$$\mathbf{t} = \boldsymbol{\sigma} \cdot \mathbf{n}, \tag{2.16}$$

where **n** denotes the respective normal vector. This formula is also called the Cauchy stress formula.

Considering large deformations (using the deformation gradient **F**), the stress tensor can be described in three different ways. The Cauchy stress tensor $\boldsymbol{\sigma}$ represents the actual forces acting on the deformed (also actual) area, sketched on the left side of Figure 2.4. The first

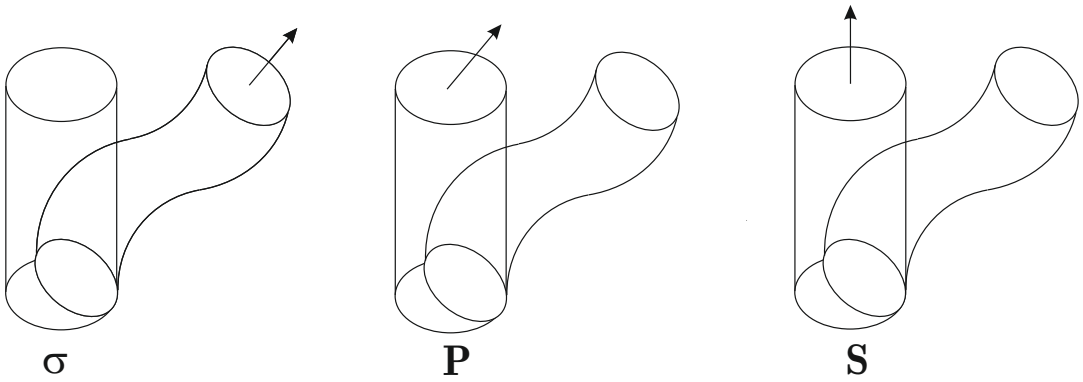

Figure 2.4.: Comparison of the configurations of the stress tensors: $\boldsymbol{\sigma}$: Cauchy stress, **P**: first Piola Kirchhoff stress tensor, **S**: second Piola Kirchhoff stress tensor

Piola-Kirchhoff stress tensor **P** represents the actual force, which is acting on the deformed configuration, but referred to the area in the undeformed configuration, illustrated in the middle of Figure 2.4. The first Piola-Kirchhoff stress tensor is linked to the Cauchy stress tensor by

$$\boldsymbol{\sigma} = \mathbf{P} \cdot \mathbf{F}^{\mathrm{T}} J^{-1}. \tag{2.17}$$

As already mentioned, $\boldsymbol{\sigma}$ is symmetric but **F** is in general arbitrary. Therefore, the first Piola-Kirchhoff stress tensor is not symmetric and the symmetric second Piola-Kirchhoff stress tensor **S** is introduced. This stress tensor maps the traction vector to the undeformed configuration and undeformed area (sketched on the right side of Figure 2.4). The link to the Cauchy stress tensor is given by

$$\boldsymbol{\sigma} = \mathbf{F} \cdot \mathbf{S} \cdot \mathbf{F}^{\mathrm{T}} J^{-1}. \tag{2.18}$$

From Equations (2.17) and (2.18), we obtain the relation

$$\mathbf{P} = \mathbf{F} \cdot \mathbf{S}. \tag{2.19}$$

2.3. Balance principles

2.3.1. Conservation of mass

Consider a body Ω with a constant mass m. This mass is always a positive scalar quantity and if there is no mass source or sink, the mass has to be constant during a motion, hence

$$\dot{m} = 0. \tag{2.20}$$

The mass of a body is defined as

$$m = \int_{\Omega} \rho(\mathbf{y}, t)\, dV, \tag{2.21}$$

with $\rho(\mathbf{y}, t)$ denoting the mass density in the actual configuration. Equation (2.20) infers that the mass in the reference configuration has to be equal to the mass in the actual configuration, hence

$$\int_{\Omega_0} \tilde{\rho}(\mathbf{x}, t)\, dv = \int_{\Omega} \rho(\mathbf{y}, t)\, dV, \tag{2.22}$$

with $\tilde{\rho}$ denoting the mass density in the reference configuration. The volume element dv of the reference configuration can be expressed by the actual configuration as

$$dv = dV\, J^{-1} \tag{2.23}$$

and Equation (2.22) becomes

$$\int_{\Omega} \left(\rho(\mathbf{y}, t) - \tilde{\rho}(\mathbf{x}, t)\, J^{-1}\right) dV = 0. \tag{2.24}$$

Since this relation has to hold in every domain of the body,

$$\tilde{\rho} = \rho J \tag{2.25}$$

has to be fulfilled as well. As the mass density in the reference configuration is a fixed function of the space for the reference time, independent of the time, the law of mass conservation can be expressed also by

$$\dot{\rho} + \rho \operatorname{div} \dot{\mathbf{x}} = 0. \tag{2.26}$$

2.3.2. Balance of linear momentum

The principle of conservation of linear momentum is equivalent to Newton's second law of motion which implies

$$\mathbf{F} = m\mathbf{a}, \tag{2.27}$$

with the mass m being constant, $\mathbf{a}$ denotes the acceleration and $\mathbf{F}$ is the resulting force. Considering an infinitesimal volume dV of the total volume V of the body, the body force of this infinitesimal volume is determined by the body force per unit mass (denoted by $\mathbf{f}$) times the density and the volume element. Hence the total body force can be obtained by integrating over the whole volume

$$\mathbf{F} = \int_{\Omega} \rho \mathbf{f}\, dV. \tag{2.28}$$

In addition to these body forces, there is also the resultant surface force stemming from the traction vector $\mathbf{t}$ acting on the surface. In order to get these forces over the whole body, the surface integral needs to be computed,

$$\mathbf{F} = \int_{\partial\Omega} \mathbf{t}\, dS. \tag{2.29}$$

By plugging these forces into the conservation of linear momentum, the formula finally reads

$$\int_{\partial\Omega} \mathbf{t}\,\mathrm{d}S + \int_{\Omega} \rho\mathbf{f}\,\mathrm{d}V = \int_{\Omega} \rho\frac{\partial^2\mathbf{u}}{\partial \mathrm{t}^2}\,\mathrm{d}V, \tag{2.30}$$

with $\mathbf{u}$ being the displacement vector defined in (2.2) or (2.3). The traction vector $\mathbf{t}$ can be replaced by employing the Cauchy stress formula. The divergence theorem (A.35) converts the surface integral into a volume integral. Then the principle can be written as

$$\nabla\cdot\boldsymbol{\sigma} + \rho\mathbf{f} = \rho\frac{\partial^2\mathbf{u}}{\partial \mathrm{t}^2} \tag{2.31}$$

or in Cartesian coordinates

$$\frac{\partial\sigma_{i,j}}{\partial y_j} + \rho f_i = \rho\frac{\partial^2 u_i}{\partial \mathrm{t}^2} \quad i = 1,2,3. \tag{2.32}$$

For static equilibrium, hence no acceleration terms, it reduces to

$$\frac{\partial\sigma_{i,j}}{\partial y_j} + \rho f_i = 0 \quad \text{with } i = 1,2,3. \tag{2.33}$$

These equations are also referred to as the equilibrium conditions. This balance law can also be described for the reference configuration, the Lagrangean equation of motion reads

$$\nabla\cdot\mathbf{P} + \tilde{\rho}\tilde{\mathbf{f}} = \tilde{\rho}\ddot{x}, \tag{2.34}$$

with $\tilde{\mathbf{f}} = \mathbf{f}(\boldsymbol{\phi}(\mathbf{y},\mathrm{t}))$.

2.3.3. Balance of angular momentum

If a body in a deformed configuration is subjected to a velocity field, the total momentum of the momentum of this body with respect to the origin is defined as

$$\int_{\Omega} \mathbf{y}\times\rho\dot{\mathbf{y}}\,\mathrm{d}V \tag{2.35}$$

and the moment resulting by external forces reads

$$\int_{\partial\Omega} \mathbf{y}\times\mathbf{t}\,\mathrm{d}S + \int_{\Omega} \mathbf{y}\times\rho\mathbf{f}\,\mathrm{d}V. \tag{2.36}$$

The balance law implies that the vectorial sum of moments acting on a body has to be equal to the rate of change of the moment of momentum of the body, hence

$$\int_{\Omega} \mathbf{y}\times\rho\mathbf{f}\,\mathrm{d}V + \int_{\partial\Omega} \mathbf{y}\times\mathbf{t}\,\mathrm{d}S = \frac{\mathrm{d}}{\mathrm{d}t}\int_{\Omega} \mathbf{y}\times(\rho\dot{\mathbf{y}})\,\mathrm{d}V. \tag{2.37}$$

The traction vector $\mathbf{t}$ may be replaced again by introducing $\boldsymbol{\sigma}$ into the equation by applying the Cauchy formula and the surface integral can be transformed to a volume integral by employing the divergence theorem (A.35). As the balance of linear momentum has to be fulfilled as well, this law implies the symmetry of the stress tensor, hence

$$\sigma_{ij} = \sigma_{ji}. \tag{2.38}$$

Due to Equations (2.17) and (2.18),

$$\mathbf{P}\mathbf{F}^{\mathrm{T}} = \mathbf{F}\mathbf{P}^{\mathrm{T}} \tag{2.39}$$

and

$$\mathbf{S} = \mathbf{S}^{\mathrm{T}} \tag{2.40}$$

have to hold as well.

2.3.4. Balance of energy

If a material particle is moved from one point to another one due to a force $\mathbf{F}$, the force has performed a work. The work dW represents the work which is performed by the force $\mathbf{F}$ by moving a particle an infinitesimal displacement $\mathbf{du}$,

$$\mathrm{d}W = \mathbf{F} \cdot \mathbf{du}. \tag{2.41}$$

Then the total work for moving a particle from point A to B is defined by

$$W = \int_A^B \mathbf{F} \cdot \mathbf{du}. \tag{2.42}$$

For a body, where an external work is performed, the rate of this mechanical external work is called external mechanical power and is defined as the power input on a region at time t done by forces, i. e.

$$W(\mathrm{t}) = \int_{\partial\Omega} \mathbf{t} \cdot \mathbf{v}\,\mathrm{d}S + \int_{\Omega} \rho\mathbf{f} \cdot \mathbf{v}\,\mathrm{d}V, \tag{2.43}$$

with $\mathbf{v}$ denoting the velocity. Considering a body Ω as a closed system and neglecting first any heat supply, the balance of energy implies that the power due to external forces has to be equal to the change of total energy of the body Ω,

$$\dot{E}_{\mathrm{total}} = W. \tag{2.44}$$

The total energy of the body E_{total} is the sum of kinetic energy K and potential or also called internal energy E,

$$E_{\mathrm{total}} = K + E. \tag{2.45}$$

K is defined by

$$K = \int_{\Omega} \frac{1}{2}\rho |\mathbf{v}|^2 \,\mathrm{d}V, \tag{2.46}$$

with the velocity $\mathbf{v}$ and the density ρ of the body. The internal energy is defined by

$$E = \int_{\Omega} \rho e \,\mathrm{d}V, \tag{2.47}$$

with e denoting the internal energy density.

2.4. Thermodynamic principles

In the conservation of energy, presented in the previous section, the heat supplies are neglected. If also the heat supply is taken into account, the conservation of energy leads to the first law of thermodynamics,

$$\dot{E} + \dot{K} = W + Q. \tag{2.48}$$

The new introduced quantity Q is the heat flow and represents the rate of energy, which is transferred into the body in form of heat. The definition for this heat flow reads

$$Q = \int_\Omega h \,\mathrm{d}V - \int_{\partial\Omega} \mathbf{q} \cdot \mathbf{n} \,\mathrm{d}A = \int_\Omega (h - \nabla \cdot \mathbf{q}) \,\mathrm{d}V, \tag{2.49}$$

with h as internal heat source per unit time and unit current volume due to nuclear fission or fusion etc. The time-dependent scalar function $\mathbf{q} \cdot \mathbf{n}$ represents the heat flux, respectively describes the heat per unit time and unit current volume.

The definitions for the internal energy E and the kinetic energy K are given in Equations (2.47) and (2.46). The internal energy may be also expressed in terms of the specific Helmholtz free energy Ψ. Then the internal energy is defined as

$$E = \int_\Omega \Psi \,\mathrm{d}V + \int_\Omega \theta s \,\mathrm{d}V. \tag{2.50}$$

Therefore the specific Helmholtz free energy is the total internal energy E minus the amount of thermal energy due to atomistic vibrations. The absolute temperature is denoted by θ, s describes the entropy density per unit volume.

The W in the energy balance (Equation (2.48)) represents the mechanical power, also called conventional external power, due to external forces $\mathbf{f}$ and externally acting traction forces $\mathbf{t}$. This power is already defined in Equation (2.43). Applying the Cauchy hypothesis, the divergence theorem and the balance of linear momentum, the mechanical power is expressed by

$$W = \int_\Omega \left(\frac{\mathrm{d}}{\mathrm{d}t} \frac{1}{2} \rho |\mathbf{v}|^2 + \boldsymbol{\sigma} : \dot{\boldsymbol{\epsilon}} \right) \mathrm{d}V. \tag{2.51}$$

Plugging in all derived expressions for the energies into the energy balance and assuming no acceleration, Equation 2.48 reads

$$\dot{\Psi} + \frac{\mathrm{d}}{\mathrm{d}t} (\theta s) = \boldsymbol{\sigma} : \dot{\boldsymbol{\epsilon}} + h - \nabla \cdot \mathbf{q}. \tag{2.52}$$

This equation is also defined as the first law of thermodynamics and governs the energy transfer.

The second law of thermodynamics is responsible for the direction of the energy transfer. Therefore, the concept of entropy needs to be introduced. In nature heat flows from warmer regions into colder regions of a body, not vice versa. In order to describe this behavior, the entropy s has a great importance. There are different explanations for the entropy, but it

can be interpreted as a quantitative measure of microscopic randomness and disorder. Then the rate of heat supply Q can be seen as a rate of entropy input. The difference between the rate of entropy input and rate of change of entropy $\dot{s}$ in a body Ω determines the total production of entropy per unit time. This total production of entropy can never be negative, in the reduced form the second law of thermodynamics becomes

$$\theta\dot{s} = \boldsymbol{\sigma} : \dot{\boldsymbol{\epsilon}} - \dot{\Psi} - s\dot{\theta} - \frac{1}{\theta}\mathbf{q} \cdot \nabla\theta \geq 0. \tag{2.53}$$

This relation defines the direction of the energy transfer and postulates the irreversibility of most thermodynamic processes. This relation is not a balance principle since it is an inequality. If there is no entropy production, the thermodynamic process is called reversible and for each loading cycle the material returns to the initial state. Reversible processes are usually an idealization of a real irreversible process. In this second law of thermodynamics, the Helmholtz free energy in general is a function of strains (or for large deformations the deformation gradient), internal variables (assembled in a vector λ) and sometimes of temperature. Applying the chain rule, the rate of Helmholtz free energy reads

$$\dot{\Psi} = \frac{\partial\Psi}{\partial\boldsymbol{\epsilon}} : \dot{\boldsymbol{\epsilon}} + \frac{\partial\Psi}{\partial\theta} : \dot{\theta} + \frac{\partial\Psi}{\partial\boldsymbol{\lambda}} : \dot{\boldsymbol{\lambda}}. \tag{2.54}$$

In order to fulfill the second law of thermodynamics, constitutive equations for the stress and entropy are obtained,

$$\boldsymbol{\sigma} = \frac{\partial\Psi}{\partial\boldsymbol{\epsilon}} \quad \text{and} \quad s = -\frac{\partial\Psi}{\partial\theta}. \tag{2.55}$$

2.5. Examples for constitutive equations

2.5.1. Elasticity

We already introduced the description of deformations in terms of the deformation gradient $\mathbf{F}$ or for small deformations by the strain tensor $\boldsymbol{\epsilon}$. Internal stresses as responses of a body due to external forces are obtained by equilibrium conditions or the balance of linear and angular momenta. The constitutive laws have to link these stresses and strains and should mimic the material behavior observed in experiments.

Figure 2.5 shows a typical stress strain curve for steel a uniaxial tension test. With increasing strain ϵ the normal stress σ increases linear to the yield stress σ_y. This yield stress is a material parameter obtained from experiments. Up to this yield stress, the stress-strain curve is linear, with the proportional factor E, the Youngs modulus. This linear curve represents an elastic material behavior. When the body is unloaded, all the strains will vanish. If the strain is increased further when $\sigma = \sigma_y$ is reached, the material begins to yield and the material does not behave elastic anymore. The stress remains constant and a plastic deformation takes place. This behavior will be described in the next section.

The rheological model for elasticity (linear stress-strain dependence) is a spring, like sketched in Figure 2.6. When the spring is loaded with an increasing load, the strain increases as well. If the device is unloaded, the strain vanishes completely.

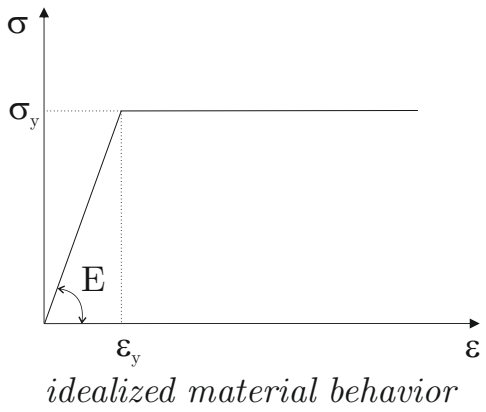

Figure 2.5.: Uniaxial stress strain curve

Figure 2.6.: One dimensional friction devise for elasticity

For the elastic material behavior, the constitutive relation for an elastic material is given for example from Hooke's law for linear elasticity

$$\boldsymbol{\sigma} = \mathbf{C} : \boldsymbol{\epsilon}. \tag{2.56}$$

The $\mathbf{C}$ represents the elasticity tensor and is in general a fourth order tensor with 81 components

$$\mathbf{C} = C_{ijkl}\mathbf{e}_i \otimes \mathbf{e}_j \otimes \mathbf{e}_k \otimes \mathbf{e}_l. \tag{2.57}$$

Due to the symmetry of stress and strain tensor and under the assumption of isotropic material behavior, the elasticity tensor can be described in terms of two independent material parameter, e. g. the Lamé elastic moduli μ and λ. Then the elasticity tensor reads

$$C_{ijkl} = \lambda\delta_{ij}\delta_{kl} + \mu\left(\delta_{ik}\delta_{jl} + \delta_{il}\delta_{jk}\right) \tag{2.58}$$

and the constitutive law for linear elasticity reduces to

$$\boldsymbol{\sigma} = \lambda(\mathrm{tr}(\boldsymbol{\epsilon}))\mathbf{I} + 2\mu\boldsymbol{\epsilon}. \tag{2.59}$$

Other material parameters for the elastic properties are the Youngs modulus E and the Poisson's ration ν. In the section of thermodynamic basics the relation

$$\boldsymbol{\sigma} = \frac{\partial \Psi}{\partial \boldsymbol{\epsilon}} \tag{2.60}$$

is derived with Ψ being the Helmholtz free energy (or also energy potential that stores the elastic energy). By finding Ψ via experiments, simulations or phenomenological approaches, we get implicitly the constitutive law from Equation (2.60). For the linear elasticity, the elastic energy potential reads

$$\Psi(\boldsymbol{\epsilon}) = \frac{1}{2}\boldsymbol{\epsilon}^{\mathrm{T}} : \mathbf{C} : \boldsymbol{\epsilon}. \tag{2.61}$$

For finite deformations other constitutive laws exist and therefore also other elastic energy potentials. An important energy potential, because widely used for material models, is the compressible neo-Hookean material model with the Helmholtz free energy

$$\Psi_{\mathrm{NH}}(\mathbf{C}) = \frac{\mu}{2}(\mathrm{tr}(\mathbf{C}) - 3) + \frac{K}{4}\left[\det(\mathbf{C}) - \frac{K+2\mu}{K}\ln(\det(\mathbf{C})) - 1\right] \tag{2.62}$$

with K being the bulk modulus. Important for this model is the logarithmic term which penalizes the reduction of the body-volume to zero. As in the case of linear elasticity, the constitutive law can be obtained by differentiation. In the regime of large deformations, the three different stress tensors are obtained from the Helmholtz free energy, the first Piola-stress tensor

$$\mathbf{P} = \frac{\partial \Psi}{\partial \mathbf{F}}, \tag{2.63}$$

the second Piola stress tensor

$$\mathbf{S} = \frac{\partial \Psi}{\partial \mathbf{E}}, \tag{2.64}$$

and the Cauchy stress tensor as

$$\boldsymbol{\sigma} = \mathbf{F} \cdot \mathbf{S} \cdot \mathbf{F}^{\mathrm{T}} (\det(\mathbf{F}))^{-1}. \tag{2.65}$$

So far we get constitutive laws that link elastic strains with elastic stresses for homogeneous materials.

2.5.2. Plasticity

As explained in the previous section, materials, for example metals, often behave elastic until the yield stress is reached. Then the material starts to behave plastic. This plastic behavior is time independent but irreversible, since energy is dissipated. The rheological model for pure plasticity is a friction device [1], like illustrated in Figure 2.7. When the

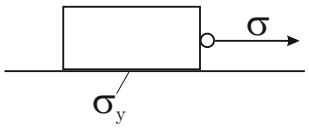

Figure 2.7.: One dimensional friction devise for plasticity

body is loaded, there will not be any displacement or strains until the load reaches σ_{y}. Then displacements and strains occur even the load remains constant from there on.

Often materials behave elasto-plastic. In Figure 2.8, a typical idealization for the stress strain curve for a uniaxial tension test with one load cycle is shown. After reaching the yield stress, with further increasing strain, the stress also increases, but with a lower slope. This section is called hardening line. At unloading, the stress follows an elastic curve but some part of the strain remains at zero stress in the material, this strain is called plastic strain.

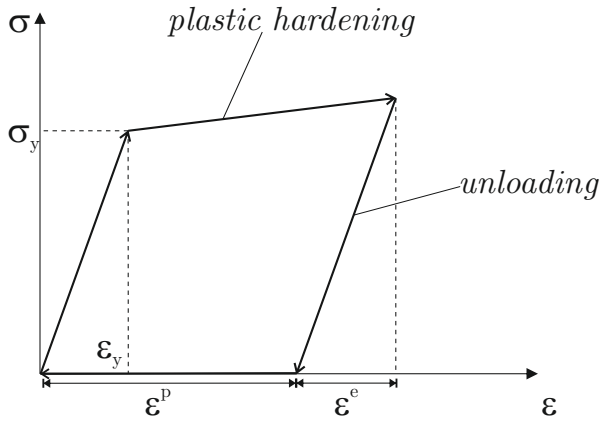

Figure 2.8.: Stress strain cycle

The part which vanishes at unloading is referred to the elastic strain. Considering small deformations, the strain can be decomposed additively

$$\boldsymbol{\epsilon} = \boldsymbol{\epsilon}^{\mathrm{p}} + \boldsymbol{\epsilon}^{\mathrm{e}}. \tag{2.66}$$

For large deformations, a multiplicative decomposition is introduced in [61]

$$\mathbf{F} = \mathbf{F}^{\mathrm{e}} \cdot \mathbf{F}^{\mathrm{p}}. \tag{2.67}$$

For any plastic deformation

$$\det(\mathbf{F}^{\mathrm{p}}) = 1 \tag{2.68}$$

is fulfilled.

The plastic material response depends strongly on the loading and the loading history. In addition to the hardening effect, the Bauschinger effect takes place. This effect influences the yield stress, hence the elastic region is changed. If a material is loaded for example by tension up to the plastic region, under pressure the yield stress is then decreased since dislocations block each other or even sum up by the loading in opposite direction.

The rheological model for elasto-plasticity is the friction device coupled with a spring, illustrated in Figure 2.9 While the load is smaller than σ_{y}, strains only occur in the spring,

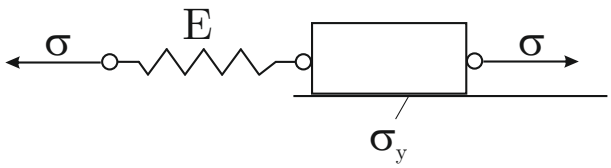

Figure 2.9.: One dimensional friction devise for elastic plastic material behavior

which models the elastic material behavior. After the yield stress σ_{y} is reached, the body starts to move, hence plastic deformations occur.

2.5.3. Viscosity

Viscosity is a time dependent material behavior, which is often used to model fluids. The viscous material behavior is dissipative, but independent from loading history. The rheological model (shown in Figure 2.10) for viscosity is a damper [1] with the damping coefficient equal to the viscosity, which is a material constant. Therefore the response of the material is dependent on the loading velocity.

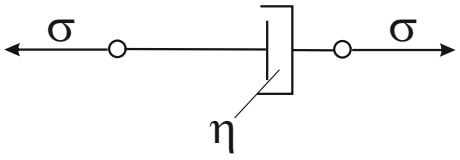

Figure 2.10.: Rheological model for viscosity

This material model can also be coupled with other material models. An elasto viscoplastic material behavior is dissipative, time and load dependent. When the load is applied, until σ_y is reached, the material behaves purely elastic. Afterwards, the material behavior is viscoplastic. The plastic response occurs directly while the viscous responds needs a relaxation time. The rheological model for this material model is a coupling of damper, spring and friction device (taken from [83]) and shown in Figure 2.11.

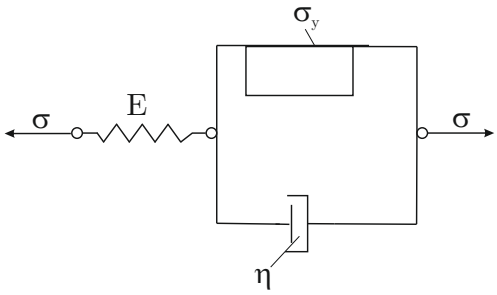

Figure 2.11.: Rheological model for viscoplasticity

2.6. Energy minimization

2.6.1. Principle of minimum of total energy

The principle of minimum of total energy (details are revealed for example in [86]) states, that a body will always deform such that the total energy achieves its minimum therefore

$$\delta \mathcal{I} = 0 \tag{2.69}$$

has to be fulfilled, which is the necessary condition for a minimum. The sufficient condition also needs to be fulfilled for a minimum. In the previous section 2.4 the Helmholtz free

energy Ψ is already introduced. Then the total stored energy in a material is called internal potential and defined as

$$\mathcal{I}_{\text{int}} = \int_{\Omega} \Psi(\nabla \mathbf{u}) \, \mathrm{d}V. \tag{2.70}$$

Analogously to this definition, the potential of all external forces may be defined as

$$\mathcal{I}_{\text{ext}} = -\int_{\Omega} \mathbf{f} \cdot \mathbf{u} \, \mathrm{d}V - \int_{\partial\Omega} \mathbf{t} \cdot \mathbf{u} \, \mathrm{d}A, \tag{2.71}$$

where $\mathbf{t}$ is the prescribed traction vector acting on the surface. Then the sum of both potentials gives the total energy potential of the body,

$$\mathcal{I} = \mathcal{I}_{\text{int}} + \mathcal{I}_{\text{ext}}. \tag{2.72}$$

The minimization of this total energy potential results to the equilibrium condition (Equation (2.31)) and to the Cauchy formula (2.16) on the surface of the body. On the other hand, this principle may be used for determining unknown deformations $\mathbf{u}$,

$$\mathbf{u} = \operatorname{argmin}\{\mathcal{I} \,|\, \mathbf{u} = \mathbf{u}^* \text{ on } \partial\Omega_{\mathbf{u}}\}, \tag{2.73}$$

where $\mathbf{u}^*$ is the prescribed deformation of the boundary.

2.6.2. Energy minimizer

As already described by the principle of minimum of total energy, the deformation of a material can be found by energy minimization. If the energy landscape is quasiconvex, the energy landscape has a global minimum.

If the energy landscape is not quasiconvex, there is no global minimum in a certain range of loading. Then a microstructure may be built in order to reduce the energy of the body. Then the energy of these microstructures correspond to an energy minimizing hull. Mathematically, this method is obtained by the relaxation theory, [49]. The relaxation is a quasiconvexication of the energy, therefore a quasiconvex hull should be determined. Then the minimization may be rewritten as

$$\mathbf{u} = \arg\min\left\{\mathcal{I}_{\text{Q}} \middle| \mathbf{u} = \mathbf{u}_0 \text{ on } \partial\Omega_{\mathbf{u}}\right\}. \tag{2.74}$$

$\mathcal{I}_{\text{Q}}$ is the relaxed energy functional and according to Dacorogna [19] defined as

$$\mathcal{I}_{\text{Q}} = \int_{\Omega} \text{Q}\Psi \, \mathrm{d}V - \ell \tag{2.75}$$

with $\text{Q}\Psi$ being the quasiconvex hull (definition is given by Equation (A.38)) of the energy density Ψ. This quasiconvex hull is based on a small-scale fluctuation field which describes the observed microstructure [48].

In reality, the microstructure which may appear exhibit a great variety. Therefore, the computation of the quasiconvex hull is often too complex and this hull may be replaced by a rank-one-convex hull. Then the minimizing problem reads

$$\mathbf{u} = \arg\min\left\{\mathcal{I}_{\text{R}_1} \middle| \mathbf{u} = \mathbf{u}_0 \text{ on } \partial\Omega_{\mathbf{u}}\right\} \tag{2.76}$$

with

$$\mathcal{I}_{\mathrm{R}_1} = \int_\Omega \mathrm{R}_1\Psi \,\mathrm{d}V - \ell. \tag{2.77}$$

The rank-one-convex hull $\mathrm{R}_1\Psi$ corresponds to the energy of a first order laminate microstructure and the definition can be taken from [19]. In Chapter 4 the energy of a first order laminate with two domains will be applied, which can be determined as [47]

$$\mathrm{R}_1\Psi = \inf_{\lambda_i,\mathbf{F}_i} \left\{ \sum_{i=1}^{2} \lambda_i \Psi(\mathbf{F}_i) \,|\, \text{constr.} \right\} \tag{2.78}$$

under the constraints

$$0 \le \lambda_i \le 1, \quad \sum_{i=1}^{2} \lambda_i = 1, \quad \sum_{i=1}^{2} \lambda_i \mathbf{F}_i = \mathbf{F}, \quad \mathrm{rank}\,(\mathbf{F}_1 - \mathbf{F}_2) \le 1. \tag{2.79}$$

The split of the homogenous material into a mixture of domains with different deformation states is schematically shown in Figure 2.12 for a one dimensional problem. This evolving

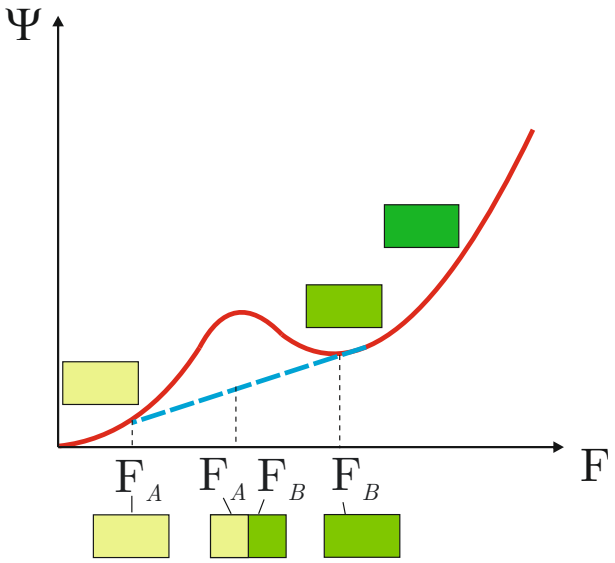

Figure 2.12.: Energy minimization

microstructure has to fulfill the given boundary conditions. In finite plasticity commonly a laminar structure arises in order to minimize the energy, like a first order laminate sketched in Figure 2.13 with two domains. The minimizing deformation gradient is the sum of the deformation gradients of the domains (in Figure 2.13 $\mathbf{F}_A$, $\mathbf{F}_B$), weighted with their respective volume fractions (in Figure 2.13 λ_A, λ_B). For the example shown in Fig.2.13, the deformation gradient reads

$$\mathbf{F} = \mathbf{F}_A\lambda_A + \mathbf{F}_B\lambda_B. \tag{2.80}$$

A second order laminate is shown in Figure 2.14. Analogously to the deformation gradient of a first order laminate with two domains, the deformation gradient for a second order laminate with two domains is found as

$$\mathbf{F} = \mathbf{F}_A\lambda_A + \mathbf{F}_B\lambda_B. \tag{2.81}$$

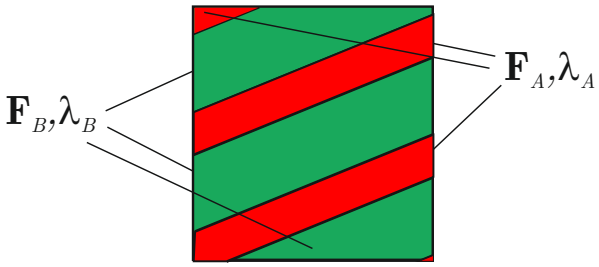

Figure 2.13.: First order laminate with two phases

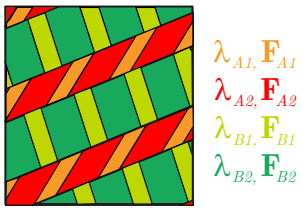

Figure 2.14.: Second order laminate with two domains

For a second order laminate $\mathbf{F}_A$ and $\mathbf{F}_B$ are obtained by

$$\mathbf{F}_A = \mathbf{F}_{A1}\lambda_{A1} + \mathbf{F}_{A2}\lambda_{A2} \tag{2.82}$$

and

$$\mathbf{F}_B = \mathbf{F}_{B1}\lambda_{B1} + \mathbf{F}_{B2}\lambda_{B2}. \tag{2.83}$$

The interfaces between two domains have to be planar. When the deformation is assumed to be continuous, the deformation gradient has to suffer a jump. However if the domains are compatible, the compatibility condition

$$[\![F_{ia}]\!] = \chi_i n_a, \tag{2.84}$$

with χ being a vector and $\mathbf{n}$ the unit normal on the interface between the domains, has to be fulfilled for a first order laminate [58]. The jump is the difference between the deformation gradients of both domains, which can be denoted by $\mathbf{F}^-$ and $\mathbf{F}^+$ (see Fig.2.15) and has to be equal to a rank one tensor. Using relation (2.4), the deformation gradient can be replaced by an actual infinitesimal line segment in the actual configuration and the kinematic compatibility or also referred as Hadamard condition reads

$$\mathbf{dx}^+ - \mathbf{dx}^- = \chi(\mathbf{n}\cdot\mathbf{dx}) \tag{2.85}$$

with $-$ and $+$ denoting the two domains. Since the normal vector is perpendicular to the interface boundary, the right hand side of this equation vanished thus the kinematic compatibility yields

$$\mathbf{dx}^+ - \mathbf{dx}^- = 0, \tag{2.86}$$

ensuring simply the compatible domains.

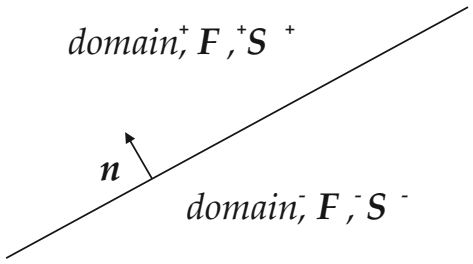

Figure 2.15.: Interface boundary between two domains.

For a higher order laminate, kinematic compatibility has to be fulfilled in the average. At the interface, also the equilibrium condition has to be fulfilled, which may be written as

$$\left(\mathbf{S}^{+} - \mathbf{S}^{-}\right)\mathbf{n} = 0. \tag{2.87}$$

3. From macro to microscale

3.1. Crystal plasticity

In the previous section, we introduced plastic deformation and phenomenological models at the macroscale in order to describe the observed material behavior. If a material behaves plastically, non homogenous deformations may occur. One typical example is a tension test. By loading a sample by tension, at plastic deformation slip bands occur on the surface of the metal [22] and plastic slip takes place along certain planes. For understanding that behavior, the crystal effects on microlevel have to be studied. By zooming into the material, the homogeneous material consists of many grains with different crystal orientations. These grains form a polycrystal. In the following we restrict our model to a single crystal, that means one grain. This grain consists of a crystal lattice where the smallest unit is the elementary cell. There are different kinds of structures for this unit cell, the most popular ones are called face-centered cubic (fcc), body-centered cubic (bcc) or hexagonal closed packed (hcp).

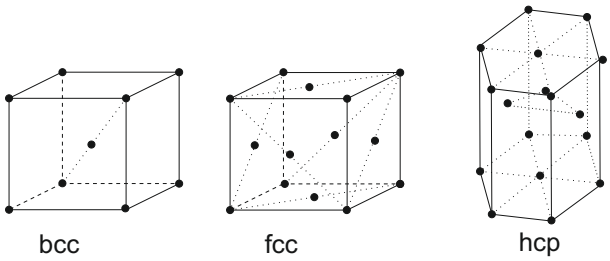

Figure 3.1.: Examples for atom arrangement in a unit cell

Experiments on a single crystal under tension test exhibit a similar stress strain behavior as observed at the macroscale. A schematical sketch in Fig.3.2 illustrates a typical stress strain relation: up to a yield stress σ_y, the stress strain curve is linear, thus the material deforms elastically. Then the crystal behaves plastic, with increasing strain, the stress remains unchanged. Afterwards the stress slightly increases again as a hardening process takes place. In these experiments the formation of slip bands is observed starting at plastic material behavior [42]. These observed slip bands produce a plastic deformation. This deformation is irreversible, parts of a crystal glide along a glide plane (normal vector $\mathbf{m}$) into a slip direction (vector $\mathbf{s}$). Glide plane and slip direction represent a slip system. Ewing and Rosenheim ([22] and [23]) were the first who discovered that the slip occurs at the closed packed planes of the atoms. The distance between these slip bands lies between several microns. From the tensile stress σ which is applied, the shear component in the slip plane is obtained from

$$\tau = \mathbf{m} \cdot \sigma \cdot \mathbf{s} = \sigma \cos\varphi \cos\lambda. \tag{3.1}$$

The definition for the angles λ and φ are shown in Figure 3.3. The gliding process, therefore also the plastic deformation, only takes place if the shear stress reaches a critical value.

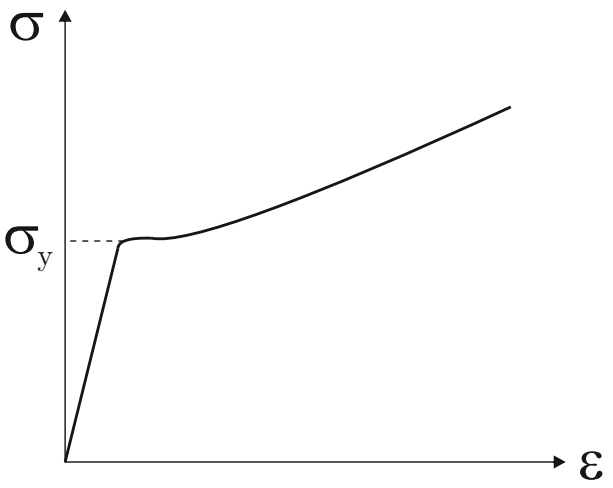

Figure 3.2.: Stress strain relation for a tension test

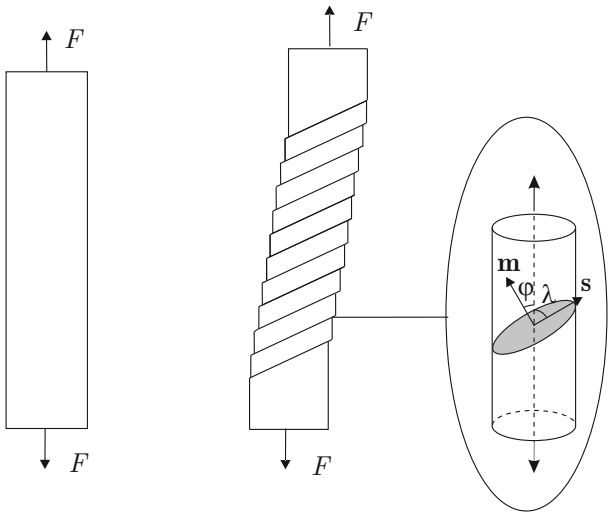

Figure 3.3.: Plastic deformation for a tension test

The critical stress is dependent on the material and also called critical resolved shear stress. This dependence is known as Schmid's law. Assuming a perfect crystal lattice, the critical resolved shear stress represents the theoretical stress, which is needed to move the crystal block. Then it can be approximated by

$$\tau_{\text{crit}} = \frac{b}{a}\frac{\mu}{2\pi} \approx \frac{\mu}{2\pi}. \tag{3.2}$$

The denotation for b and a can be taken from Figure 3.4 and represent the atomistic distances, μ the shear modulus. More details about the derivation are given in [51]. According to the calculation of Mackenzie, the critical resolved shear stress for the gliding in the basal plane of hexagonal lattice is $\tau_{\text{crit}} = \frac{\mu}{30}$. Both ways for calculating the critical resolved shear stress lead to values which are much larger than that observed in experiments. As an example, zinc, has at 0 Kelvin a critical resolved shear stress $\tau_{\text{crit}} = 0.784\frac{N}{mm^2}$, verified by experiments (taken from [51]). Therefore the theoretical value $\tau_{\text{crit}} = \frac{\mu}{30} = 620.9\frac{N}{mm^2}$ differs strongly from the one observed in experiments. Since the crystalline structure of metals is already well investigated, the error of this approximation can only lie in the assumption of a

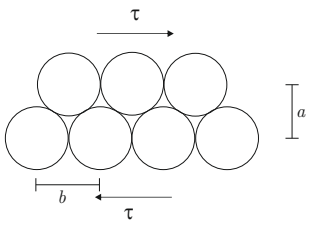

Figure 3.4.: Shear applied on atoms

perfect crystal lattice.

3.2. Defects

Experiments show that every crystal includes a huge number of defects. Zero-dimensional or point defects are

1. Displaced atoms

2. Interstitially solute foreign atoms or vacancies

3. Schottky defects (a lattice atom wandered to the surface and leaving a vacancy) and Frenkel defects (a lattice atom leaves its position and becomes a intestitial atom nearby) [46]

These defects occur due to thermal fluctuations. An atom leaves its position (leaving a vacancy) and moves to the surface or may settle down as an intersitial atom. This movement of atoms may explain some diffusion processes. Some of these defects are illustrated in Figure 3.5.

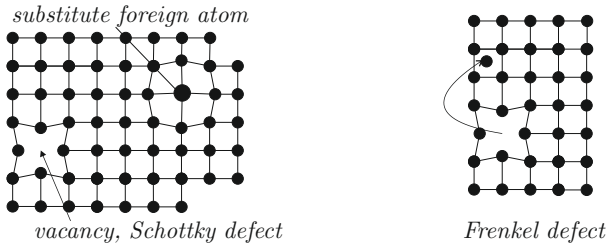

Figure 3.5.: Zerodimensional effects

3.3. Dislocations

One-dimensional or linear defects are irregularities in the crystal lattice, for example extra half planes in the lattice or missing half planes, see 3.6.

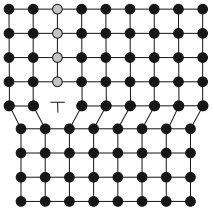

Figure 3.6.: Edge dislocation

Having one dimensional defects, the atoms are dislocated from their equilibrium position, therefore these defects are also called dislocations. The concept of dislocations was first introduced by Orowan [73], Polanyi [76] and Taylor [85] in 1934. These dislocations are responsible for the lower strength of crystals than that obtained by assuming a perfect crystal lattice. The plastic deformation of the slip can be explained by the movement of a dislocation, schematically shown in Figure 3.7. A dislocation is introduced in a perfect crystal

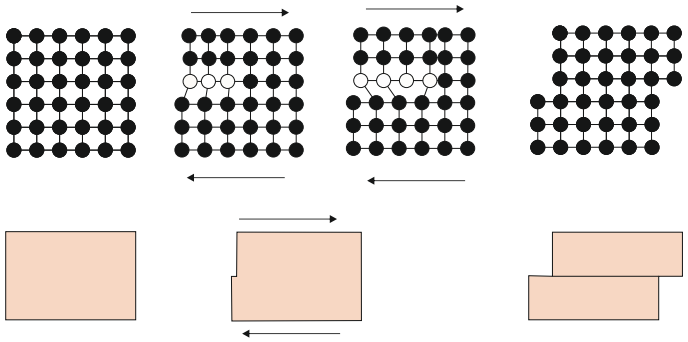

Figure 3.7.: Movement of dislocation causes plastic slip

lattice by a small shear stress. As the dislocation moves, the atoms above have to slip. When the dislocation travels along the whole plane, all the atoms above have slipped. The stress, which causes this movement is much smaller than the stress which is required to move the whole block without any dislocation. Therefore the strength of the crystal depends strongly on these dislocations. Dislocations can be basically distinguished between edge and screw dislocations, both are shortly defined in the following sections.

3.3.1. Edge dislocation

A schematic image of an edge dislocation is shown in Figure 3.6. The atoms are arranged regulary except the gray marked atoms, which symbolize an extra half plane. The dislocation line is the edge of this half plane.

Burgers vector

In order to describe the dislocation, the so called Burgers vector **b** is introduced. This vector denotes the slip direction of the dislocation. This Burgers vector is found by building the

Burger circuit, a closed path surrounding the dislocation line and involving two lattice directions. Then the Burgers vector closes the circuit path. Figure 3.8 illustrates the definition

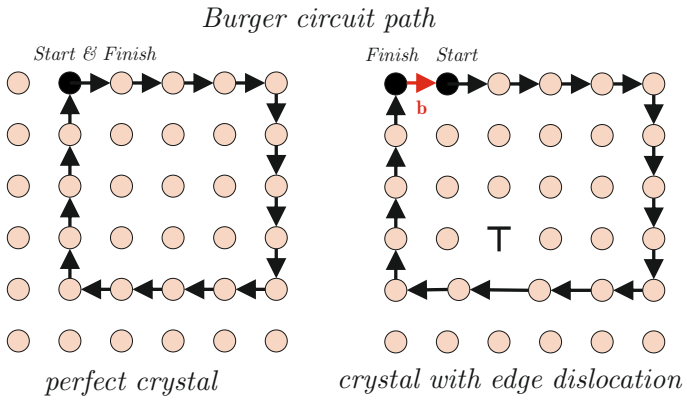

Figure 3.8.: Burgers vector for an edge dislocation

of the Burgers vector. The Burger circuit starts, going four atoms to the right, afterward four atoms down and then four atoms left and up. In the case of a perfect crystal, this circuit is closed. In the case of crystal including a dislocation, this path is not closed. The Burgers vector **b** is required to close the path. The slip plane of a dislocation has to contain the Burgers vector and dislocation line. This definition of the Burgers vector is valid for one dislocation, it does not give informations, how a resultant Burgers vector of a dislocation network, occuring at macroscopic deformations, can be determined.

Stress field

A dislocation is a defect which disturbs the crystal lattice, due to that disturbance a stress and a displacement field occur. In order to determine the stress field, the crystal including an edge dislocation, which is defined by the Burgers vector **b**, is assumed as an isotropic cylindrical ring with the inner radius r_i and an outer radius r_a. Instead of the dislocation, the endings of the cylindrical ring are deformed like illustrated in Figure 3.9.

Due to the complexity, the calculations are omitted and the results are simply presented,

$$\sigma_{xx} = -Dy\frac{3x^2+y^2}{(x^2+y^2)^2} \tag{3.3}$$

$$\sigma_{yy} = Dy\frac{x^2-y^2}{(x^2+y^2)^2} \tag{3.4}$$

$$\sigma_{zz} = \nu\left(\sigma_{xx}+\sigma_{yy}\right) \tag{3.5}$$

$$\tau_{xy} = \tau_{yx} = Dx\frac{x^2-y^2}{(x^2+y^2)^2} \tag{3.6}$$

and $\tau_{yz} = \tau_{zy} = \tau_{xz} = \tau_{zx} = 0$ with ν being the Poisson's ratio and

$$D = \frac{\mu b}{2\pi(1-\nu)} \tag{3.7}$$

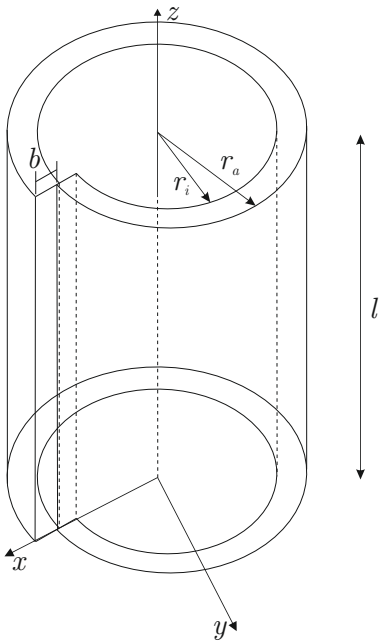

Figure 3.9.: Elasticity model for edge dislocation

with μ being the shear modulus. In cylindrical coordinates, these results read

$$\sigma_{rr} = \sigma_{\varphi\varphi} = -D\frac{\sin\varphi}{r}, \tag{3.8}$$

$$\sigma_{zz} = -2D\nu\frac{\sin\varphi}{r} \tag{3.9}$$

and

$$\sigma_{r\varphi} = D\frac{\cos\varphi}{r}. \tag{3.10}$$

Obviously, these stresses have a singularity at $r = 0$. However, they are only valid for $r >$ the radius of the dislocation core, afterwards the continuum model is not suitable anymore and the situation becomes more complex. [88] determined that the radius of the dislocation core is equal to $5b$. For $r > 5b$, the stresses decrease drastically, but still this stress field is long-ranged and may interact with other stress fields. The displacements can be found as

$$u = -\frac{b}{8\pi}\left[\tan^{-1}\frac{x}{y} + \frac{1}{2(1-\nu)}\frac{xy}{x^2+y^2}\right], \tag{3.11}$$

$$v = \frac{b}{2\pi(1-\nu)}\left[(1-2\nu)\ln\left(x^2+y^2\right) + \frac{x^2-y^2}{x^2+y^2}\right] \tag{3.12}$$

and $w = 0$. If a circuit around the z axis is made, the displacement u changes by the amount of $-b$ [88]. This jump is the closure failure introduced by an inverse plastic distortion. Therefore the plastic contribution contributes only locally near the dislocation, while the elastic deformation (second part of (3.11)) is long-ranged. Since deformation v contains a logarithmic term, which converges to infinity close to the dislocation core, the displacement cannot be determined elastically for coordinates smaller than the dislocation core.

Elastic stored energy

The elastic energy which is stored in the cylindrical region can be found by using the stress field of the dislocation. We get the elastic energy per unit length by calculating the work which is needed to introduce this dislocation into the perfect lattice. More details can be found in [84]. The result reads

$$E_{\mathrm{el}} = \frac{\mu b^2}{4\pi(1-\nu)} \ln\left(\frac{r_a}{r_i}\right). \tag{3.13}$$

3.3.2. Screw dislocation

The second type of dislocation is the screw dislocation, schematically shown in Figure 3.10. The upper part of the crystal is shifted with respect to the lower part. Correspondingly to the edge dislocation, the Burgers vector is found by the Burger circuit, presented in Figure 3.10. The dislocation line points into the same direction as the Burgers vector. For screw

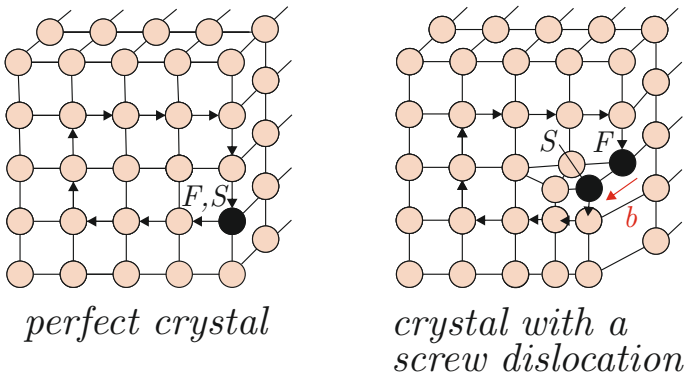

Figure 3.10.: Screw dislocation

dislocations, the Burgers vector is parallel to the dislocation line (as already mentioned), for edge dislocations, the Burgers vector and the dislocation line are perpendicular to each other.

Stress field

Analogously to the edge dislocations, the stress field of a screw dislocation is found by using a distorted cylindrical ring of isotropic material (see Figure 3.11) instead of the crystal including the dislocation. The derivation for the stress field is omitted, for details see [45]. The results are

$$\sigma_{yz} = \sigma_{zy} = \frac{\mu b}{2\pi} \frac{x}{x^2+y^2} \tag{3.14}$$

$$\sigma_{xz} = \sigma_{zx} = -\frac{\mu b}{2\pi} \frac{y}{x^2+y^2} \tag{3.15}$$

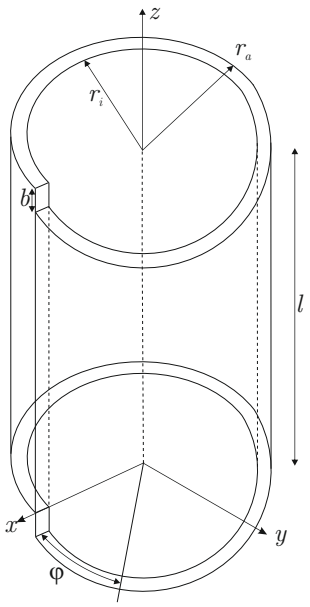

Figure 3.11.: Elasticity model for screw dislocation

and

$$\sigma_{xx} = \sigma_{yy} = \sigma_{zz} = \sigma_{xy} = \sigma_{yx} = 0. \tag{3.16}$$

These stresses can also be expressed in cylindrical coordinates by

$$\sigma_{r\varphi} = \frac{\mu b}{2\pi r} \tag{3.17}$$

and the other components are zero. Analogously to the stress field of an edge dislocation, these results are only valid for $r > 5b$, hence if the radius is bigger than the dislocation core. For smaller radii, the continuum approach is not valid anymore and the discrete nature of the crystal becomes important [88]. The stress field behaves in the same manner as for the edge dislocation: it is long-ranged but the stress decreases strongly with increasing radius. The displacements due to the distortion can be found as

$$u = v = 0 \tag{3.18}$$

and

$$w = \frac{b}{2\pi}\tan^{-1}\frac{x}{y}. \tag{3.19}$$

If a circuit is made around the dislocation line, the displacement from the beginning and the ending have to differ [88] by the amount of b. Thus the displacement maintains the closure failure due to the inverse plastic distorsion. Similar to the displacements of edge dislocations, the plastic deformation only contributes locally near the dislocation.

Stored energy of a screw dislocation

From this known stress field, the elastic stored energy per unit length is calculated as

$$E_{el} = \frac{1}{2}\int_{r_i}^{r_a} \frac{\mu b^2}{2\pi r}\,\mathrm{d}r = \frac{\mu b^2}{4\pi}\ln\frac{r_a}{r_i}. \tag{3.20}$$

3.3.3. Force on a dislocation

The movement of dislocations produces the plastic slip of the crystal. In order to move these dislocations, a material force has to act on it. This force, also referred as Peach-Koehler force, acting on the dislocation line results from the applied stress on the crystal. Mott and Nabarro [70] introduced in 1948 the following definition: The force per unit length is defined as

$$F = \tau b. \tag{3.21}$$

The derivation of this formula can be taken for example from [45]. Another definition for the force is obtained from the work which is done when the unit length of dislocation moves a unit distance. This idea leads to the same result as Equation (3.21).

3.3.4. Dislocation loops

Screw dislocations and edge dislocation may appear in a real crystal combined in a form of a loop or a ring, see Figure 3.12. The slip plane contains of two regions, outside the

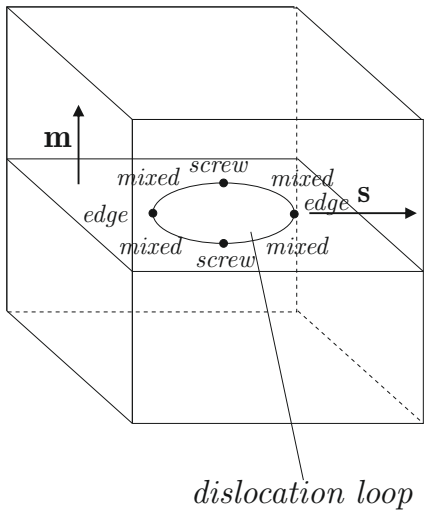

Figure 3.12.: Dislocation loop

loop, the atoms have not slipped from the lower atoms. Inside the loop, the atoms glide along the plane into the slip direction. If the Burgers vector is parallel to the slip direction, the dislocation loop is an edge dislocation. If it is perpendicular to the slip direction, the dislocation is a screw dislocation. If the Burgers vector is neither parallel nor perpendicular to the dislocation line, this dislocation is a mixed dislocation. Then, the Burgers vector is the sum of two Burgers vectors, parallel and perpendicular to the dislocation line, see Figure 3.13,

$$\mathbf{b} = \mathbf{b}_1 + \mathbf{b}_2, \tag{3.22}$$

with $|\mathbf{b}_1| = |\mathbf{b}|\,\mathrm{Sin}\varphi$ and $|\mathbf{b}_2| = |\mathbf{b}|\,\mathrm{Cos}\varphi$.

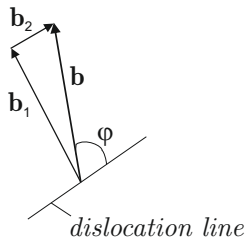

Figure 3.13.: Mixed Burgers vector

3.3.5. Dislocation multiplication and pile ups

As determined by experiments, the dislocation density in annealed metals is not high enough to produce the observed slip bands. Therefore, during loading dislocations need to be nucleated. Various sources in a crystal may generate new dislocations and hence increase the dislocation density. One of the most common sources is the Frank-Read source (see [25]), which was observed in experiments by Dash in 1956. A Frank-Read source is a dislocation, which is locked at both ends. The shear stress, which is applied to the glide plane causes a force on the straight dislocation line. If the endings are locked, the line forms a half-circle. The dislocation moves further and rotates around the locked endings when the shear stress increases further. Then the dislocation line completely rotates round the endings and eventually returns to its original position. A new dislocation loop is the result. During loading, dislocations can also be nucleated from dipoles (two dislocations with different sign). These dipoles are introduced in the crystal by thermal stresses and may remain there, until shear stresses seperate them. Then these disloactions are pulled to other directions and are called geometrically necessary dislocations. If dislocations remain at their arbitrary positions, they are called statistically stored dislocations.

There are different kinds of obstacles for the dislocation movement in the crystal. One obstacle is the grain boundary. The dislocations which meet the obstacle cannot move any further, hence they pile up. These piled up dislocations exhibit a force to the obstacle. This results in an internal stress, characterized as τ_p and can be calculated via

$$\tau_p = n\tau \tag{3.23}$$

with n being the number of dislocations. This number is obtained by

$$n = \frac{\pi l_0 \tau}{\mu b} \tag{3.24}$$

for edge dislocations and

$$n = \frac{\pi l_0 \tau (1-\nu)}{\mu b} \tag{3.25}$$

for screw dislocations. G represents the shear modulus, b the magnitude of the Burgers vector, τ the applied shear stress and l_0 is the length on the slip plane where the dislocations are piling up. The internal stress at the grain boundary τ_p causes a hardening effect of the crystal. Therefore, this pile-up is also responsible for the Bauschinger effect.

3.4. Continuum theory of dislocations

In the previous section, dislocations and their nucleation are introduced. A real crystal consists of a huge number of dislocations (range from 10^8 to 10^{15} dislocations per square meter), therefore in order to describe the behavior of so many dislocations, the continuum dislocation theory was developed. Kondo [50], Bilby [12] and Kröner ([54] and [53]) were the first who introduced that concept. Kinematic quantities which characterize the deformed state of the crystal and the rate of change of the dislocation network are be chosen. Then the energy and the dissipation have to be described in terms of these quantities. When these are determined, the continuum theory of dislocations follows the thermodynamic laws.
As an introduction to the theory, small deformations are considered, hence the linear theory is presented. These basics and further informations are revealed in [82] and [58].

3.4.1. Linear continuum theory of dislocations

Elastic and Plastic Distortion

In order to define the elastic and plastic distortions of a crystal, we first assume a crystal which is stress free. Kröner [53] described the geometrical changes of a crystal in terms of a relative plastic displacement $\delta\mathbf{g}$. As an example, a former homogeneous element can be split up into infinitesimal small volume elements with the width δx_2. Then the relative plastic displacement displaces each volume element to the other, see Figure 3.14, and the volume element is deformed plastically. By using the relative plastic displacement, the

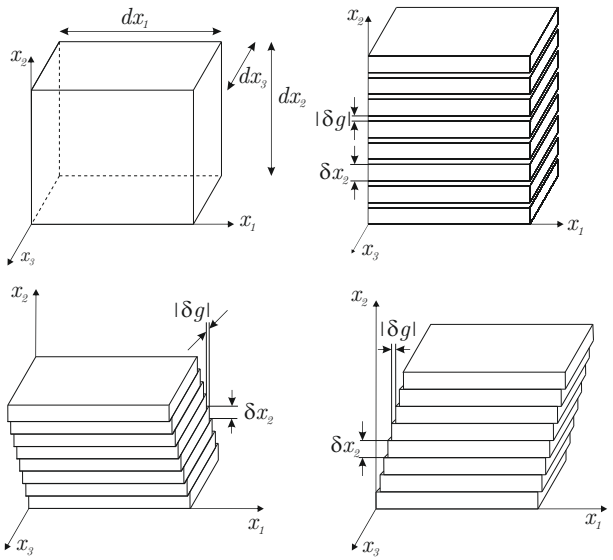

Figure 3.14.: Plastic distortion

plastic distortion $\beta_{i,j}$ is introduced by

$$\delta g_j = \beta_{ij}\delta x_i. \tag{3.26}$$

The entries of the diagonal of the plastic distortion tensor can be interpreted as the plastic strains, the other entries are the plastic shear. The first index of the tensor denotes the glide

plane and the second the slip direction. The plastic distortion can be split up into plastic strains and plastic rotations,

$$\beta_{ij} = \epsilon^{\mathrm{p}}_{ij} + \omega^{\mathrm{p}}_{ij}. \tag{3.27}$$

In other terms, the plastic strains are the symmetric part of the plastic distortion,

$$\epsilon^{\mathrm{p}}_{ij} = \frac{1}{2}\left(\beta_{ij} + \beta_{ji}\right). \tag{3.28}$$

The orientation of the volume elements are not changed due to the plastic distortion, while the elastic distortion rotates and distorts the orientation of the volume element, see Figure 3.15. For small strains, the total strain is the sum of the elastic strain and the plastic strain, hence

$$\epsilon = \epsilon^{\mathrm{e}} + \epsilon^{\mathrm{p}}. \tag{3.29}$$

The plastic strain tensor, which is the symmetric part of the plastic distortion, brings the un-

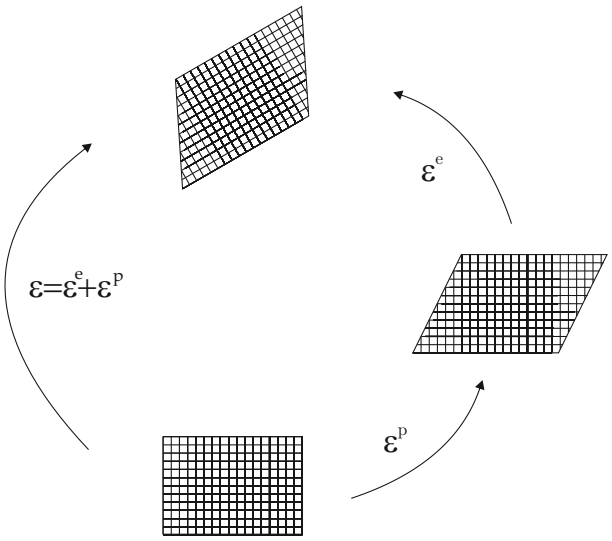

Figure 3.15.: Additive decomposition of the strain

deformed crystal to the reference stress free crystal, thus without deforming the lattice. The elastic strain tensor deforms the crystal according to Hooke's law [58] and may introduce a shape and a lattice change. However, during any elastic deformation, the neighboring atoms remain always neighbors. In contrast to the classical plasticity theory, also the plastic rotation needs to be considered. This may be explained by an Gedankenexperiment, visualized in Fig. 3.16. First a crystal is deformed by a homogeneous plastic deformation caused by edge dislocations with the Burgers vector along x_1 axis, afterward by a second homogeneous plastic deformation by similar edge dislocations, but this time with Burgers vector along x_2 axis. For an isotropic material, even if two plastic deformations have taken place, the final result is only a plastic rotation by the angle ϕ. In classical plasticity theory, this rotation is neglected. However, the energy has to change from the initial to the rotated state due to the two dislocation movements [6].

Concerning a crystal which undergoes a single slip, the plastic distortion is found by

$$\beta_{ij} = \beta s_i m_j, \tag{3.30}$$

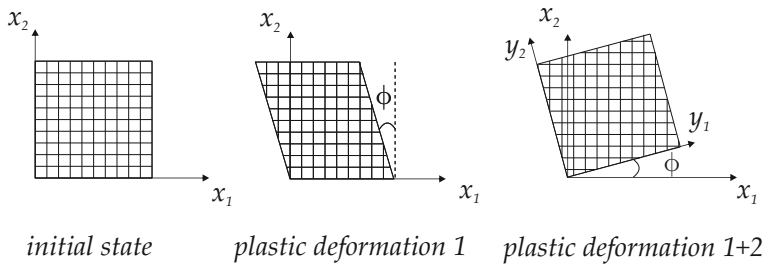

Figure 3.16.: Gedankenexperiment

with **m** and **s** describing the slip system as already described before, see [58]. In general, the plastic distotion does not cause any volumetric changes, therefore $\beta_{ii} = 0$. If a crystal contains n- number of slip systems, the plastic distortion can be calculated by

$$\beta_{ij} = \sum_{k=1}^{n} \beta s_i^k m_j^k. \tag{3.31}$$

Dislocation density

The relative displacement of two neighboring points with the distance **dx** may be introduced by

$$\mathrm{d}u_j^{\mathrm{T}} = \beta_{ij}^{\mathrm{T}} \mathrm{d}x_i, \tag{3.32}$$

$$\mathrm{d}u_j^{\mathrm{e}} = \beta_{ij}^{\mathrm{e}} \mathrm{d}x_i \tag{3.33}$$

and

$$\mathrm{d}u_j^{\mathrm{p}} = \beta_{ij} \mathrm{d}x_i, \tag{3.34}$$

where $\mathbf{du}^{\mathrm{T}}$ denotes the total, $\mathbf{du}^{\mathrm{e}}$ the elastic and $\mathbf{du}^{\mathrm{p}}$ the plastic relative displacement. The total distortion $\boldsymbol{\beta}^{\mathrm{T}}$ is obtained by the sum of the elastic and plastic distortion, thus

$$\boldsymbol{\beta}^{\mathrm{T}} = \boldsymbol{\beta}^{\mathrm{e}} + \boldsymbol{\beta}. \tag{3.35}$$

Under the assumption, that the elements of a plastic deformed body remain connected, the total relative displacement has to be compatible, so that

$$\oint_C \mathrm{d}u_j^{\mathrm{T}} = \oint_c \mathrm{d}u_j^{\mathrm{e}} + \oint_C \mathrm{d}u_j^{\mathrm{p}} = 0 \tag{3.36}$$

has to be fulfilled for every circuit C. Replacing the relative deformation by their definitions (3.32), (3.33) and (3.34) and employing Stoke's theorem (A.35) on an arbitrary infinitesimal area with the normal vector **n**, Equation (3.36) leads to

$$\mathrm{curl}\boldsymbol{\beta}^{\mathrm{T}} = 0, \tag{3.37}$$

which simply is the compatibility condition, and

$$\mathrm{curl}\boldsymbol{\beta}^{\mathrm{e}} = -\mathrm{curl}\boldsymbol{\beta}, \tag{3.38}$$

which shows the incompatibility of the elastic distortion. Burger [14] defined the resultant Burgers vector as

$$\mathbf{b} = \oint_C \mathbf{du}^{\mathrm{e}}. \tag{3.39}$$

With the use of the incompatibility of the elastic distortion (3.38) and Eq. (3.34), the resultant Burgers vector can expressed as

$$b_j = \oint_C \beta_{ij}\,\mathrm{d}x_i. \tag{3.40}$$

For one dislocation, the Burgers vector characterizes the jump of the deformations on the slip surface. The resultant Burgers vector characterizes analogously the total closure failure of all dislocations in the crystal at the slip surface. The application of Stoke's theorem yields

$$b_j = \int_A (\mathrm{curl}\beta)_{ij}\, n_i\,\mathrm{d}A. \tag{3.41}$$

Consequently Nye [72] introduced 1953 the dislocation density tensor α_{ij} as

$$\boldsymbol{\alpha} = \mathrm{curl}\boldsymbol{\beta} \tag{3.42}$$

or

$$\alpha_{ij} = \varepsilon_{jkl}\beta_{il,k}. \tag{3.43}$$

with β being the plastic distortion and ε_{jkl} the permutation, defined in (A.11). With this quantity, the resultant Burgers vector of all dislocations whose dislocations lines cross the area A can be calculated by

$$b_j = \int_A \alpha_{ij} n_i\,\mathrm{d}A \tag{3.44}$$

with n_i being the normal vector of the area A. For a crystal with one active slip system, the number of dislocations per unit area is given by the scalar dislocation density,

$$\rho = \frac{1}{b}\left|\varepsilon_{jkl}\beta_{,k} m_i n_j\right|. \tag{3.45}$$

In this equation, b denotes the magnitude of the Burgers vector.

Energy of dislocation network

Kröner [55] introduced the dislocation density tensor and the elastic strain as state variables. Taking these state variables, the state of the body can be calculated uniquely without any knowledge of the history (e. g. loading).

For isothermal processes, the free energy per unit volume of a crystal including dislocations consists of two terms,

$$\varphi(\boldsymbol{\epsilon}^{\mathrm{e}}, \boldsymbol{\alpha}) = \varphi^{\mathrm{e}}(\boldsymbol{\epsilon}^{\mathrm{e}}) + \varphi^{\mathrm{m}}(\boldsymbol{\alpha}). \tag{3.46}$$

The first term, $\varphi^{\mathrm{e}}(\boldsymbol{\epsilon}^{\mathrm{e}})$ is contributed from the elastic deformation of the crystal. Applying the equations (3.29), (3.28) and (2.13), the state variable $\boldsymbol{\epsilon}^{\mathrm{e}}$ for infinite small deformations can be calculated by

$$\epsilon^{\mathrm{e}}_{ij} = u_{(i,j)} + \beta_{(ij)}, \tag{3.47}$$

the bracket in the indices denotes the symmetrization [82]. The second part of the energy density, $\varphi^{\mathrm{m}}(\boldsymbol{\alpha})$ is contributed by the dislocation network. This energy has to be chosen in the form that the thermodynamic principles are fulfilled. Gurtin [31] proposed 1972 the energy density as the quadratic form

$$\varphi^{\mathrm{m}} = \frac{1}{2}\boldsymbol{\alpha} : \mathbf{E} : \boldsymbol{\alpha} \tag{3.48}$$

with $\mathbf{E}$ being a material tensor which has to be chosen. Berdichevsky [5] introduced 2006 a new ansatz for the energy density in the form

$$\varphi^{\mathrm{m}} = \mu k \left(\ln \frac{1}{1 - \sqrt{\frac{\rho}{\rho_{\mathrm{s}}}}} - \sqrt{\frac{\rho}{\rho_{\mathrm{s}}}} \right) \tag{3.49}$$

with k being a material constant. Instead of the dislocation density tensor, the scalar dislocation density is the state variable. The saturated dislocation density ρ_{s} is a material parameter which describes the closest packing of dislocations in a certain domain. If the scalar dislocation density ρ reaches ρ_{s}, the energy density gets very large, if ρ is small the energy is nearly linear. As an approximation,

$$\varphi^{m} = \mu k \ln \frac{1}{1 - \frac{\rho}{\rho_{\mathrm{s}}}} \tag{3.50}$$

can be taken.

System of equations

The free energy of the crystal in the undeformed region Ω_0 is obtained by

$$\Psi = \int_{\Omega_0} \varphi(\boldsymbol{\epsilon}^{\mathrm{e}}, \boldsymbol{\alpha}, \boldsymbol{\beta}) \, \mathrm{d}v, \tag{3.51}$$

assuming a constant temperature. Following the laws of thermodynamic, the difference between the rate of this free energy and the power has to bigger than zero, thus

$$\frac{\mathrm{d}}{\mathrm{d}t} \int_{\Omega_0} \Psi(\boldsymbol{\epsilon}^{\mathrm{e}}, \boldsymbol{\alpha}, \boldsymbol{\beta}) \, \mathrm{d}v - W \geq 0, \tag{3.52}$$

with W being the power. When the crystal is adiabatically isolated and heat conductivity is neglectible, the first law of thermodynamics states that the power is equal to the time derivative of the free energy [5], thus

$$W = \dot{\Psi}. \tag{3.53}$$

Due to the chosen form of the energy it reads[81]

$$W = \int_{\partial\Omega_0} \left(\sigma_{ij} n_j \dot{u}_i + \sigma_{ijk} n_k \dot{\beta}_{ij}\right) \mathrm{d}a, \tag{3.54}$$

where $\mathbf{n}$ is the normal vector on $\partial\Omega_0$. The power contains higher order stresses, since the energy density is dependent on the gradient of the plastic distorsion. Mathematical treatments (see for example [58]) lead to the inequality

$$\tau_{ij}\dot{u}_{i,j} + \kappa_{ij}\dot{\beta}_{ij} + \tau_{ijk}\dot{\beta}_{ij,k} + \sigma_{ij,j}\dot{u}_i \geq 0, \tag{3.55}$$

with $\tau_{ij} = \sigma_{ij} - \frac{\partial\varphi}{\partial\epsilon_{ij}}$, $\tau_{ijk} = \sigma_{ijk} - \frac{\partial\varphi}{\partial\alpha_{im}}\varepsilon_{mkj}$ and $\kappa_{ij} = -\frac{\partial\varphi}{\partial\beta_{ij}} + \sigma_{ijk,k}$. For any rigid body rotation where $\dot{u}_{i,j}$, β_{ij} and $\dot{\beta}_{ij,k}$ are zero, the energy has to be also zero, therefore $\sigma_{ij,j} = 0$ has to hold as well and this inequality can only be fulfilled if $\sigma_{ij} = \sigma_{ji}$. From the laws of thermodynamic, the dissipation may be introduced as

$$D\left(\dot{u}_{i,j}, \dot{\beta}_{ij}, \dot{\beta}_{ij,k}\right) = \tau_{ij}\dot{u}_{i,j} + \kappa_{ij}\dot{\beta}_{ij} + \tau_{ijk}\dot{\beta}_{ij,k}. \tag{3.56}$$

By assuming a rate-independent process, the dissipation function is a homogeneous first order function of the internal variable rates and we can identify $\tau_{ij} = \frac{\partial D}{\partial \dot{u}_{i,j}}$, $\kappa_{ij} = \frac{\partial D}{\partial \dot{\beta}_{ij}}$ and $\tau_{ijk} = \frac{\partial D}{\partial \dot{\beta}_{ij,k}}$. Related to this dissipation, a dissipation potential Δ can be introduced. This dissipation potential has to be a homogeneous function, thus the Euler's homogeneous function theorem,

$$\frac{\partial\Delta}{\partial\dot{u}_{i,j}}\dot{u}_{i,j} + \frac{\partial\Delta}{\partial\dot{\beta}_{ij}}\dot{\beta}_{ij} + \frac{\partial\Delta}{\partial\dot{\beta}_{ij,k}}\dot{\beta}_{ij,k} = m\Delta\left(\dot{u}_{i,j}, \dot{\beta}_{ij}, \dot{\beta}_{ij,k}\right) \tag{3.57}$$

has to be fulfilled. Then, by assuming a rate-independent process (thus $m = 1$) [82] we obtain

$$\Delta = D. \tag{3.58}$$

With these derived equations, the system is closed for solving the unknowns u_i and β_{ij}, if the energy density φ (see previous section) and the dissipation potential Δ are chosen.

3.4.2. Nonlinear continuum dislocation theory

In the nonlinear continuum dislocation theory, large deformations are assumed, hence the additive decomposition of the strain tensor is not valid anymore. The treatment, however, remains the same: the kinematic quantities which characterize the deformed state of the crystal and the rate of change of the dislocation network are defined. These quantities should be independent from loading history. The energy and the dissipation have to be considered, depending only on these quantities. Then the thermodynamic laws are applied.

Kinematics

Similar to the macroscopic deformation gradient, Bilby [12] decomposed the deformation gradient for large deformation multiplicatively, see Eq. (2.67). In general, $\mathbf{F}^{\mathrm{e}}$ and $\mathbf{F}^{\mathrm{p}}$ are incompatible but volume preserving and their corresponding inverse deformation exist,

$$\det\mathbf{F}^{\mathrm{e}} > 0 \ , \ \det\mathbf{F}^{\mathrm{p}} > 0. \tag{3.59}$$

In [12], the deformation gradient $\mathbf{F}$ is referred as a shape deformation, $\mathbf{F}^{\mathrm{e}}$ a lattice deformation and $\mathbf{F}^{\mathrm{p}}$ as a dislocation deformation. Kröner [53] started a Gedankenexperiment and defined the inverse elastic deformation gradient $\mathbf{F}^{e-1}$ as a deformation which releases all dislocations in the current state to the surface, so that a stress and dislocation free crystal is obtained. Therefore he introduced an intermediate configuration of the crystal. Applying Eq. (2.67), the plastic deformation gradient is then found as

$$\mathbf{F}^{\mathrm{p}} = \mathbf{F}^{\mathrm{e}-1} \cdot \mathbf{F}. \tag{3.60}$$

This definition does not agree with the idea of Bilby [12], where the elastic deformation does only change the lattice but no dislocation movement occurs. Therefore the physical interpretation of the plastic deformation gradient is still questionable. The introduction of an intermediate configuration should be investigated further. The vectors which describe a material can be distinguished between shape and lattice vectors. A shape vector is connected to the material and changes whenever the material deforms plastically. The lattice vectors are only linked to the crystal lattice, which does not change due to a pure plastic deformation. Therefore the introduction of the intermediate configuration is not necessary, the plastic deformation gradient $\mathbf{F}^{\mathrm{p}}$ can be seen as a map in the reference configuration, transforming the shape vectors but not the lattice vectors. However, due to the variety of definitions for the plastic deformation gradient, before applying the nonlinear continuum dislocation theory, the definition should be clarified.

Similar to the linear continuum dislocation theory, a commonly used kinematic quantity is the dislocation density. It can be found by determining the resultant Burgers vector, which is dependent on the plastic deformation gradient. The resultant Burgers vector has to change when the material behaves plastic, since plastic deformation is accomodated by creating dislocations. But the resultant Burgers vector should not depend on the loading history. Kondo [50] and Bilby [11] introduced the definition for the resultant Burgers vector as

$$\mathbf{b}_{\mathrm{r}} = \mathbf{F}^{\mathrm{e}} \oint \mathbf{F}^{\mathrm{e}-1} \, \mathrm{d}\mathbf{y}. \tag{3.61}$$

However, Ortiz and Repetto [74] defined the resultant Burgers vector in a different way

$$\mathbf{b}_{\mathrm{r}} = \oint \mathbf{F}^{\mathrm{p}} \, \mathrm{d}\mathbf{y}. \tag{3.62}$$

For one active slip system, this formula is valid. However, it can be shown that this resultant Burgers vector is not invariant with respect to arbitrary superimposed plastic deformations. Berdichevsky [5] defined the resultant closure failure, leading to the dislocation density tensor

$$\mathbf{T} = -\mathbf{F}^{\mathrm{p}-1} \cdot (\mathbf{F}^{\mathrm{p}} \times \nabla). \tag{3.63}$$

Cermelli and Gurtin [17] required that the true resultant Burgers vector has to measure the local failure per unit area in an intermediate configuration. However, this requirement is questenable, as the suggestions of [53], including the intermediate configuration, have been already critically discussed above. Hence, there exist different definitions of the key quantity which characterizes the state of the dislocation network and the kinematics have to be examined before applying this framework.

3.5. Microstructures

Microstructures can be understood as material instabilities, hence lattice defects which are not in thermodynamic equilibrium form a microstructure. There are also structures which are produced as deformation mechanisms at plastic material behavior. Usually, these mechanisms are caused by dislocation networks, which are already introduced in the previous section. In the following section, these deformation mechanisms at plastic material behavior are presented. The outlined information are based on [34] and [41].

3.5.1. Grains and phases

In reality, a bulk material consists not of one perfect crystal lattice, but of different crystal grains. This means that the crystal lattices may be rotated to have different directions, hence one crystal lattice forms one grain, a lattice with a different orientation another grain. The boundary between two grains, referred as grain boundary, can be described by five orientation parameters (also referred as Euler angles). If the grains are tilted by a small angle, the boundary is a low-angle grain boundary and formed by parallel edge dislocations (presented in Fig.3.17 with $\alpha << 1$). Then the relation between the tilt angle α, the amount of

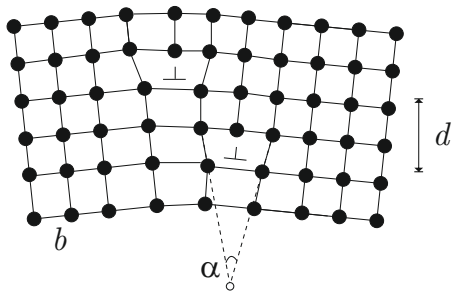

Figure 3.17.: Low-angle grain boundary

the Burgers vector (b) and the distance of dislocations (d) reads

$$\tan\alpha \approx \alpha \approx \frac{b}{d}, \tag{3.64}$$

if $\alpha << 1$. For larger tilt angles, it is not possible forming a boundary by a network of edge dislocations. However, there is the possibility to find a coincidence lattice, hence this lattice is shared by both grains. A special case is a coherent twin boundary (illustrated in Fig. 3.18), where the two grains are simply mirrored and share the complete lattice at the boundary. The formation of twins will be described later.

If two grains not only differ in orientation but also in structure and/or composition, these two grains are referred as different phases. The interface boundary (between two phases) can be coherent, semi-coherent or incoherent, like shown in Fig 3.19.

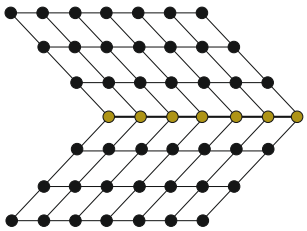

Figure 3.18.: Coherent twin boundary

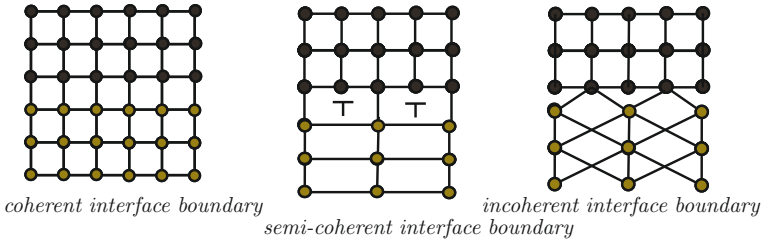

Figure 3.19.: interface boundaries

3.5.2. Deformation twinning

Deformation twinning, similar to the formation of slip bands, may occur during a plastic deformation. This mechanism can only take place in appropriate structures (for example in fcc crystals) at low temperature but fast loading velocity. Otherwise the formation of slip bands is favorable. For deformation twinning, instead of a sliding of planes, a part of the lattice tilts and a new grain with a different orientation is formed. The boundary between the twins can be coherent (see Fig 3.18) or incoherent. If the boundary is incoherent, the boundary consists of Shockley partial dislocations. These Shockley partial dislocations are dissociated perfect dislocations and cause the twinning shear. One by one the partial dislocations climb up a screw dislocation and convert one plane after another into the twin orientation. This procedure is also referred as pole mechanism.

3.5.3. Martensitic transformation

Another deformation mechanism at plastic material behavior is the martensitic transformation. Commonly the cubic lattice of austenite is transformed to a tetragonal lattice of martensite (other transformation possibilities are orthorombic or monoclinic lattices). This effect can be generated externally by a decrease of temperature or shear stresses and is often used for tempering steel. The transformation process is reversible, hence by an increase of temperature or unloading, the initial state can be obtained again. The martensitic transformation is a diffusion free phase transformation and a coordinated movement of atoms takes place in a crystalline solid. There are different choices at the lattice scale how the cubic austenite can transform to the martensite. For tetragonal martensite, three states can occur, which are called martensite variants and are rotated to each other around the axis (see Fig.3.20).

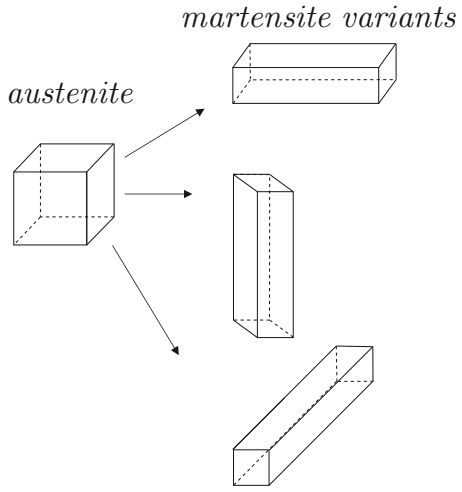

Figure 3.20.: Tetragonal martensite variants.

The martensitic transformation has certain crystallographic features, as the habitus plane, which is invariant for both phases, or the orientation relationship between the martensitic and the matrix phase (the closed packed planes and directions have to be parallel for both lattices). The martensitic deformation is a lattice deformation, thus a coherent change of structure and results in a volume and shape change of this phase. Therefore this phase is associated with a high strain energy. In order to decrease this energy, a accommodation process, either slip bands or twinning, occurs. Both processes are illustrated in Fig. 3.21. This figure corresponds to the theory presented for example in [41] or [10]. In this figure,

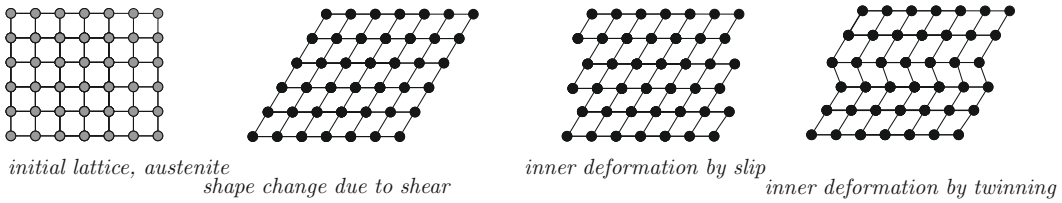

Figure 3.21.: Martensitic transformation

after the accommodation processes, the martensite is still not stress free and contains an elastic deformation, thus there is still an essential amount of bulk energy. In this thesis, we will present a model for the martensitic phase transformation, where the martensite is afterwards stress free, thus the energy is reduced further.

Commonly the martensitic phase occurs at grain boundaries and forms a sharp needle or plate.

The martensitic transformation forms on the material surface a structure as sketched in Fig. 3.23. A scratch on the surface may show the unevenness due to the martensitic phase, [21].

Fig.3.23 reveals, that the habitus plane is also the interface boundary. Since the lattice has changed, it is semi-coherent. Therefore in order to fit this boundary, it has to contain either an array of dislocations or the martensitic phase has to consist of different variants. Energetically both mechanism are possible. If dislocations are involved in this transformation process, they have to be considered in a model as well, since their movement to the

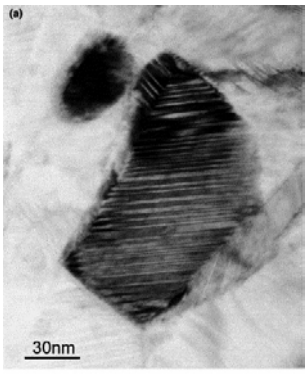

Figure 3.22.: TEM bright field image of a martensitic grain. The twin lamellae show bright and dark contrast. Reprinted by permission from [87]

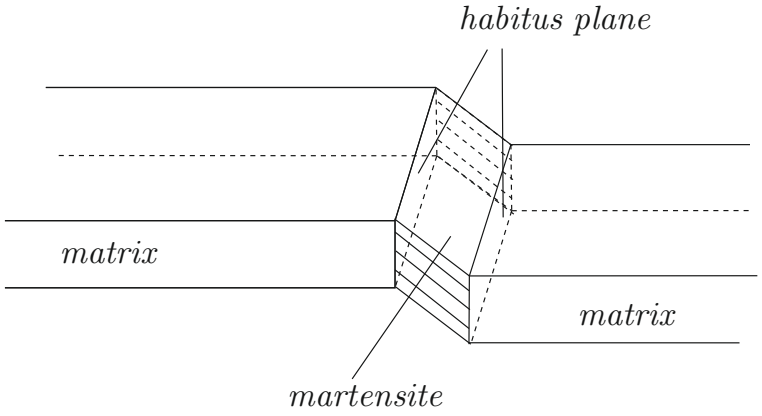

Figure 3.23.: Matrix and martensitic phase

boundaries and formation of legs cause definitly an amount of dissipation. Due to the high number of involved dislocations, the continuum disloaction theory seems to be favorable. Even several models are already established (for example [75]), until now, no model, using the nonlinear continuum dislocation theory, combines the reversible transformation strain and the plastic deformation, caused by the dislocations.

3.5.4. Recrystallization

The previous presented mechanisms are processes which are introduced by dislocations and its network. Recrystallization removes defects by forming new grains or by growing existing grains. Even if the recrystallization removes defects, this structure is not in thermodynamic equilibrium as grains remain in the material and form a recrystallization texture. There exist two kinds of recrystallization, the first one is called primary recrystallization. This process is temperature and deformation dependent and driven by the stored dislocation energy. A critical deformation has to be overcome so that the process can initiate. At higher deformations, less temperature is needed for the recrystallization. An important aspect are the kinetics as the number of recrystallization nuclei per unit volume increases with time. The recrystallization starts in most deformed regions, since the dislocation density is high there.

The secondary recrystallization, or also referred as grain growth, is driven by the grain boundary energy. The growth rate of grains depend on the orientation difference, the position, the degree of deformation and temperature. At grain growth, some grains grow at the expense of others, so that finally the material consists of less but bigger grains than before.

3.5.5. Modeling microbands

Horiuchi et al. [40] showed 1975 that drawn copper reveals linear lines under the microscope. First a twinning process was assumed, but X-Rays detected that no twin orientation was produced. An electron microscope showed finally that these lines were microbands, starting already at small deformations. Microbands are areas or domains of the crystal which have a different dislocation density, or are even dislocation free. The density of these microbands increased with a higher degree of deformation, and in the experiments of [40], some bands even join at 90% deformation. In their investigations, the orientation of the crystal is changed due to the microbands. From their results, they could exclude that microbands occur due to an elongation of the previous cells. However, they were still not able to determine the mechanism of microband formation. 2009 Dmitrieva et al [20] examined the formation of microbands in a single crystal of copper under a shear test at plastic deformation. Fig 3.24 shows a result of this shear test, an EBSD map, where the microbands are present and a laminar structure is visible. They assumed that a lack of convexity in

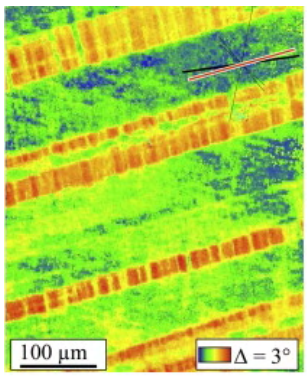

Figure 3.24.: EBSD map of the part of the deformed area with several microbands. The map shows the relative crystallographic orientation changes within 3° according to the color scale. Reprinted by permission from [20]

the energy is the basic mechanism for the formation of the microstructure, comparable like already others identified for similar microstructures ([74], [57], [16]).

Generally, a microband arises in order to reduce the energy, therefore it is dictated by the free energy of the material and the dissipation, which is caused for example by the dislocation movement. The resulting microband can be computed by employing the relaxation theory [3]. In the relaxation theory, microstructures build the quasiconvex hull of the free energy [2]. As this quasiconvex hull is rather complex to determine, this hull is often replaced by a rank one convex envelope [37], [15], which models a first order laminate. First order laminates are able to display microbands, since a material including microbands also consists of two domains and hence has a laminar structure.

In order to model these microbands, two aspects have to be treated: the initiation of the microstructure (commonly nowadays starting from the loss of convexity) and the evolution of this microband (as experiments showed that the state of the microband is deformation dependent [40], [20]). Several authors already outlined models to simulate the formation of such or similar microstructures ([74], [57], [65], [68]). They have chosen suitable potentials in a time-incremental setting and used a condensed energy functional (minimization of the sum of the Helmholz free energy and dissipation distance with respect to the internal variables) for this formation. Unfortunately this approach is based on the assumption, that at the beginning of each time step no microstructure is present. Therefore, these models can only display the initiation of the microstructure correctly. For the subsequent evolution, also the dissipation, which is caused by microstructural changes have to be taken into account [47].

In order to simulate a time-continuous evolution of a microband properly, Kochmann and Hackl [48] outlined a model which also captures the effect of an existing microstructure at the beginning of a time step. Instead of using the condensed energy, this model uses a partially relaxed energy and a relaxed dissipation potential, which captures the dissipation due to changes in the microstructure. They have chosen a first order laminate as a microstructure in order to model microbands. By employing the principle of dissipation potential, evolution equations are obtained. The dissipation potential is considered as a rate independent ansatz, therefore the derived evolution equations are given implicitly. This model is capable to display all microstructural characteristics in every time step for a first order laminate. However, due to the kind of derived evolution equations, this model involves a global minimization in every time step. This makes the numerical simulation rather evolved and sometimes unstable. In order to improve the numerical effort and stability, we modify this model. This modification will be presented in the next chapter.

4. Modeling the viscous evolution of laminate microstructures in finite crystal plasticity

As introduced in the previous section, under certain load conditions, homogenous single crystals may develop microbands in order to reduce its energy. This microstructure influences the plastic behavior on the macroscale, therefore an appropriate simulation of the evolving microstructure is needed. In this chapter, a variational ansatz is used to model crystal plasticity with a first order laminate as the microstructure. For this concept, two quantities have to be defined: the Helmholtz free energy and the dissipation potential. Then the microstructure arises as a minimizer for the non convex energy potential without further assumptions. The basic idea of this method was first introduced by Ortiz and Repetto, [74], Carstensen et al. [16] and Mielke [67]. The here outlined model and parts of the examples are also presented in [30], [28] and [29].

4.1. Variational framework

The developed material model is based on the idea that homogeneous deformations cannot be found as minimizers for non convex energy densities [20]. Then the former homogenous material may form a microstructure which reduces the energy of the crystal instead (see 2.6.2). In this case, the non convex energy density is replaced by a quasi convex hull and the admissible microstructures are pre-accounted. These microstructures minimize the energy instead [2], [3]. As the computation of the quasiconvex hull is in general not feasible, this hull is replaced here by a rank-one-convex hull. The rank-one-convex hull corresponds to the energy of first order laminates [66].

The total free energy of a body is described by

$$\mathcal{I}(\mathrm{t}, \mathbf{u}, \nabla\mathbf{u}, \mathbf{z}) = \int_\Omega \Psi(\nabla\mathbf{u}, \mathbf{z})\, \mathrm{d}V - \mathcal{I}_{\mathrm{ext}}(\mathrm{t}, \mathbf{u}), \tag{4.1}$$

where $\mathbf{z}$ is a tensorial generalized internal variable which has to describe totally the current state of the microstructure and $\mathbf{u}$ the displacement field. The actual displacements are obtained by the principle of minimum of total energy, introduced in section 2.6.1,

$$\mathbf{u} = \operatorname{argmin}\{\mathcal{I}(\mathrm{t}, \mathbf{u}, \nabla\mathbf{u}, \mathbf{z}) \,|\, \mathbf{u} = \mathbf{u}_0 \text{ on } \Omega_u\}. \tag{4.2}$$

In order to describe the current state of a body, the internal variables have to be determined as well. For their determination, the principle of the minimum of the dissipation potential is applied. This principle is introduced in the following section.

4.2. Principle of the minimum of dissipation potential

In order to derive evolution equations for the internal variables, which characterize the current state of the microstructure, the principle of the minimum of dissipation potential is introduced. For further details and explanations, we refer to [63], [62], [64] and [35]. In [44] a derivation for non- isothermal processes is presented.

We consider a mechanical system, described by the derivative of the displacements $\nabla\mathbf{u}$ and internal variables $\mathbf{z}$. Thus their material time derivatives can be determined and denoted by $\nabla\dot{\mathbf{u}}$ and $\dot{\mathbf{z}}$. The specific Helmholtz free energy is described in terms of both variables, hence $\Psi = \Psi(\nabla\mathbf{u}, \mathbf{z})$. This energy is differentiable and the thermodynamic forces may be calculated as $-\frac{\partial\Psi}{\partial z_j}$. Since the formation of microstructure is accommodated by dissipation, $\Delta(\mathbf{z}, \dot{\mathbf{z}})$ is introduced as the dissipation potential. Then the true internal variables $\mathbf{z}$ have to fulfill the variational equation [80]

$$\delta\mathcal{I}(\mathrm{t}, \mathbf{u}, \nabla\mathbf{u}, \mathbf{z}) + \int_\Omega \frac{\partial\Delta}{\partial\dot{\mathbf{z}}} : \delta\mathbf{z}\,\mathrm{d}V = 0. \tag{4.3}$$

Since the energy of the body is independent from the rate of the internal variables, by applying the chain rule, the variation of the energy reads

$$\delta\mathcal{I} = \int_\Omega \frac{\partial\Psi(\nabla\mathbf{u}, \mathbf{z})}{\partial\mathbf{u}} : \delta\mathbf{u}\,\mathrm{d}V - \frac{\partial\mathcal{I}_{\mathrm{ext}}(\mathrm{t}, \mathbf{u})}{\partial\mathbf{u}} : \delta\mathbf{u} + \int_\Omega \frac{\partial\Psi(\nabla\mathbf{u}, \mathbf{z})}{\partial\nabla\mathbf{u}} : \delta\nabla\mathbf{u}\,\mathrm{d}V + \int_\Omega \frac{\partial\Psi}{\partial\mathbf{z}} : \delta\mathbf{z}\,\mathrm{d}V. \tag{4.4}$$

Due to the principle of minimum of total energy only the last contribution in not equal to zero. Therefore, the variational equation 4.3 becomes

$$\int_\Omega \left[\frac{\partial\Psi}{\partial\mathbf{z}} + \frac{\partial\Delta}{\partial\dot{\mathbf{z}}}\right] : \delta\mathbf{z}\,\mathrm{d}V = 0 \tag{4.5}$$

for all arbitrary $\delta\mathbf{z}$. If all thermodynamic forces are assembled in a vector denoted by $\mathbf{q}$,

$$\mathbf{q} = \frac{\partial\Delta}{\partial\dot{\mathbf{z}}} \tag{4.6}$$

has to hold as well.

Another derivation of the principle of the minimum of the dissipation potential is the introduction of the Lagrangean,

$$\mathscr{L} = \dot{\Psi} + \Delta, \tag{4.7}$$

with

$$\dot{\Psi} = \left.\frac{\partial\Psi}{\partial\nabla\mathbf{u}}\right|_{\mathbf{z}=\mathrm{const.}} : \nabla\dot{\mathbf{u}} + \left.\frac{\partial\Psi}{\partial\mathbf{z}}\right|_{\nabla\mathbf{u}=\mathrm{const.}} : \dot{\mathbf{z}}. \tag{4.8}$$

Then the principle of minimum of dissipation potential can be written in the form

$$\mathscr{L} = \dot{\Psi} + \Delta \rightarrow \min_{\dot{\mathbf{z}}}. \tag{4.9}$$

The minimization of the Lagrangean leads to

$$\frac{\partial\Psi}{\partial\mathbf{z}} + \frac{\partial\Delta}{\partial\dot{\mathbf{z}}} = 0, \tag{4.10}$$

thus again

$$\frac{\partial \Delta}{\partial \dot{\mathbf{z}}} = \mathbf{q}. \tag{4.11}$$

Employing on Equation (4.11) a Legendre transformation, the Legendre conjugate dissipation potential

$$J(\mathbf{z}, \mathbf{q}) = \max\{\mathbf{q} : \dot{\mathbf{z}} - \Delta(\mathbf{z}, \dot{\mathbf{z}}) | \mathbf{q}\} \tag{4.12}$$

leads to the evolution equations of the internal variables,

$$\dot{\mathbf{z}} = \frac{\partial J}{\partial \mathbf{q}}. \tag{4.13}$$

The principle of the minimum of the dissipation potential is valid for any arbitrary time step and only the energy density and the dissipation have to be chosen. By employing an integration scheme, the updated internal variables $\mathbf{z}$ can be obtained from $\dot{\mathbf{z}}$ and the internal variable from the previous time step.

K. Hackl and D. Kochmann [49] established a model for the evolution of microstructure based on a rate independent dissipation potential

$$\Delta_1 = r_1 |\dot{\mathbf{z}}|. \tag{4.14}$$

The Lagrangean then reads

$$\mathscr{L} = \dot{\Psi} + \Delta_1 \tag{4.15}$$

and the principle of minimum of dissipation potential takes the form

$$\mathscr{L} = \dot{\Psi} + \Delta_1 \rightarrow \min_{\dot{\mathbf{z}}}. \tag{4.16}$$

For the rate independent dissipation potential Δ_1 considered in the model from Kochmann and Hackl [49], the minimization leads to the stationary conditions of the Lagrangean. Replacing $\frac{\dot{\mathbf{z}}}{|\dot{\mathbf{z}}|}$ by $\mathrm{Sign}(\dot{\mathbf{z}})$ the evolution equations read

$$\mathrm{Sign}(\dot{\mathbf{z}}) \ni -\frac{1}{r_1} \frac{\partial \Psi}{\partial \mathbf{z}}. \tag{4.17}$$

This kind of evolution equation is rather complicated to solve because the update of the internal variable is not given explicitly. Therefore establishing a numerical procedure with these kind of evolution equations is very demanding as a global minimization is involved in every time step.

4.2.1. Visco-plastic dissipation potential

The dissipation potential is an assumption, therefore a different kind of a possible dissipation potential can be considered in the form

$$\Delta_2 = \frac{r_2}{2} (\dot{\mathbf{z}})^2. \tag{4.18}$$

Inserting this dissipation potential into the Lagrangean and employing the principle of minimum of dissipation potential (Equation (4.16)),

$$\mathscr{L} = \dot{\Psi} + \Delta_2 \rightarrow \min_{\dot{\mathbf{z}}},$$

the resulting stationary conditions of this Lagrangean read

$$\frac{\partial \Psi}{\partial \mathbf{z}} + r_2 \dot{\mathbf{z}} = 0. \tag{4.19}$$

From these conditions the derivation of the evolution equations of the internal variables leads to

$$\dot{\mathbf{z}} = -\frac{1}{r_2}\frac{\partial \Psi}{\partial \mathbf{z}}. \tag{4.20}$$

Thus, obviously from the dissipation potential (4.18) explicit evolution equations can be derived. With this kind of evolution equations, the updating procedure is rather easy, but these evolution equations lead to a time dependent material behavior. Therefore this material behavior cannot interpreted as plastic anymore but as viscous.

In our ansatz for modeling finite plasticity, the sum of both dissipation potentials Δ_1 and Δ_2 is chosen. Dissipation potential Δ_1 represents the plastic behavior and by employing dissipation potential Δ_2 the evolution equations get an rate dependent explicit character and therefore the viscous dissipation potential also regularizes the minimization problem in time. For modeling plasticity, the contribution of this viscous dissipation potential to the dissipation potential should be negligible small in comparison to the rate independent part, so that the dominant material behavior is plasticity and a viscosity limit is reached. The principle of minimum of dissipation potential with both dissipation potentials finally reads

$$\mathscr{L} = \dot{\Psi} + \Delta_1 + \Delta_2 \rightarrow \min_{\dot{\mathbf{z}}} \tag{4.21}$$

The minimization leads to the stationary conditions of the Lagrangean,

$$\frac{\partial \Psi}{\partial \mathbf{z}} + r_1 \frac{\dot{\mathbf{z}}}{|\dot{\mathbf{z}}|} + r_2 \dot{\mathbf{z}} \ni 0. \tag{4.22}$$

Due to mathematical treatments [35], the stationary conditions become

$$\frac{\partial \Psi}{\partial \mathbf{z}} + r_1 \mathrm{Sign}\left(-\frac{\partial \Psi}{\partial \mathbf{z}}\right) + r_2 \dot{\mathbf{z}} \ni 0. \tag{4.23}$$

In order to obtain the evolution of the internal variables we follow the procedure of [49] and impose a Legendre transformation,

$$J = \sup_{\mathbf{q}} \left\{ \dot{\mathbf{z}} : \mathbf{q} - r_1 |\dot{\mathbf{z}}| - \frac{r_2}{2}\dot{\mathbf{z}}^2 \right\}, \tag{4.24}$$

with the thermodynamic forces denoted by $\mathbf{q}$. Using Equation (4.22), $\frac{\dot{\mathbf{z}}}{|\dot{\mathbf{z}}|}$ can be expressed by

$$r_1 \frac{\dot{\mathbf{z}}}{|\dot{\mathbf{z}}|} = \mathbf{q} - r_2 \dot{\mathbf{z}}. \tag{4.25}$$

Inserting this relation, the Legendre transformation may be written as

$$J = \sup_{\mathbf{q}} \left\{ \frac{|\dot{\mathbf{z}}|}{r_1} \left(\mathbf{q} : \mathbf{q} - r_1^2 \right) - \frac{|\dot{\mathbf{z}}|}{r_1} r_2 \dot{\mathbf{z}} : \mathbf{q} - \frac{r_2}{2} (\dot{\mathbf{z}})^2 \right\}. \tag{4.26}$$

The supremum of this transform only exists if all summands of the Legendre transformation are negative. Otherwise this function may be tending to infinity and no supremum exists. Therefore $\left(\mathbf{q} : \mathbf{q} - r_1^2 \right) \leq 0$ has to be fulfilled since the two remaining parts of this supremum are always negative. Hence this term can be identified as the yield function $\boldsymbol{\phi}$ and reads

$$\boldsymbol{\phi} = \mathbf{q} : \mathbf{q} - r_1^2. \tag{4.27}$$

This yield function has to be always smaller than or equal to zero and can be reformulated to

$$\boldsymbol{\phi} = |\mathbf{q}| - r_1 \leq 0. \tag{4.28}$$

If the yield function $\boldsymbol{\phi}$ is bigger than zero, the evolution of the internal variables takes place. Thus the updates of the internal variables are determined by the evolution equations, which take the form

$$\dot{\mathbf{z}} = \frac{1}{r_2} (|\mathbf{q}| - r_1)_+ \operatorname{Sign}(\mathbf{q}). \tag{4.29}$$

Here $()_+$ infers $(|\mathbf{q}| - r_1)$ if the expression is bigger than zero or zero is taken instead. These evolution equations may be also expressed in terms of the yield function

$$\dot{\mathbf{z}} = \frac{1}{r_2} \boldsymbol{\phi}_+ \operatorname{Sign}(\mathbf{q}). \tag{4.30}$$

4.3. Lamination

The microbands are modeled as first order laminates, illustrated in Figure 4.1. The domains of the laminate are described by chosen internal variables. In this model, each domain i is characterized by a volume fraction λ_i, a plastic slip γ_i and a hardening p_i. Since the microbands are not oriented along the slip system, the laminate may be rotated by an angle ϕ. The normal vector $\mathbf{b}$ of the laminate can be expressed in terms of the angle ϕ.

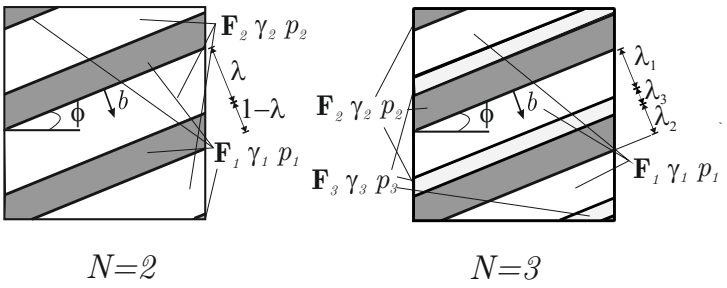

Figure 4.1.: Sketch of a first order laminate, different number of domains

In every domain of the laminate we have a constant deformation gradient $\mathbf{F}_i$ which can be defined by

$$\mathbf{F}_i = \mathbf{F} (\mathbf{I} + \mathbf{a}_i \otimes \mathbf{b}), \tag{4.31}$$

with $\mathbf{a}_i$ representing some deformation amplitude vector. At the laminate interfaces, the compatibility of the deformation gradient has to be fulfilled, so that a corresponding deformation field exists. Therefore the volume average of the deformation gradient has to be imposed [47],

$$\sum_{i=1}^{N} \lambda_i \mathbf{F}_i = \mathbf{F}, \tag{4.32}$$

or alternatively

$$\sum_{i=1}^{N} \lambda_i \mathbf{a}_i = 0. \tag{4.33}$$

On the other hand, each domain has to be incompressible [49],

$$\det \mathbf{F}_i = 1. \tag{4.34}$$

Since the whole material is incompressible, $\det \mathbf{F} = 1$ has to be fulfilled as well and Equation (4.34) leads to

$$\mathbf{a}_i \cdot \mathbf{b} = 0. \tag{4.35}$$

According to [49], the normal vector $\mathbf{b}$ is considered as ingrained into the material, otherwise any rotation changes the state of the internal variables and dissipation would be produced. The amplitude vector $\mathbf{a}$ may be changed elastically. Then the partially relaxed energy of a material consisting of a first order laminate is defined as

$$\Psi^{\mathrm{rel}}(\mathbf{F}, \boldsymbol{\lambda}, \boldsymbol{\gamma}, \mathbf{p}, \mathbf{b}) = \inf \left\{ \sum_{i=1}^{N} \lambda_i \Psi(\mathbf{F}_i, \gamma_i, p_i) \middle| \mathbf{a}_i; \sum_{i=1}^{N} \lambda_i \mathbf{a}_i \right\}. \tag{4.36}$$

A microstructure exhibits dissipation, therefore the relaxed dissipation potential for a first order laminate has to be found as well. For a fixed normal vector, hence the laminate cannot rotate, the relaxed dissipation is given by

$$\begin{aligned} \Delta^* \left(\boldsymbol{\lambda}, \dot{\boldsymbol{\lambda}}, \boldsymbol{\gamma}, \mathbf{p}, \mathbf{b}, \dot{\boldsymbol{\gamma}}, \dot{\mathbf{p}} \right) &= \sum_{i=1}^{N} \lambda_i \Delta(\gamma_i, p_i, \dot{\gamma}_i, \dot{p}_i) \\ &+ \inf \left\{ \sum_{i,j=1}^{N} \Delta\lambda_{ij} D\left(\gamma_i, p_i, \dot{\gamma}_i, \dot{p}_i, \gamma_j, p_j, \dot{\gamma}_j, \dot{p}_j\right) | \Delta\lambda_{ij}; \right. \\ &\left. \sum_{i=1}^{N} \Delta\lambda_{ij} = \dot{\lambda}_j, \sum_{j=1}^{N} \Delta\lambda_{ij} = \dot{\lambda}_i, \Delta\lambda_{ij} = 0 \text{ for } |(i-j) \bmod N| \neq 1 \right\} \end{aligned} \tag{4.37}$$

[47]. D is the dissipation distance, defined in [67] and applied to the outlined problem in [47]. This dissipation potential does not include a rotation of the laminate. However, a rotation of the laminate may take place. This rotation causes a change in the regions of the domains, therefore also the amount of plastic slip change in these regions, which results in a dissipation. This amount is determined by

$$D_{\mathbf{b}}(\boldsymbol{\lambda}, \boldsymbol{\gamma}, \mathbf{p}, \mathbf{b}) = \sum_{i=1}^{N} \sum_{j=1}^{N} \lambda_i \lambda_j D\left(\gamma_i, p_i, \mathbf{b}, \gamma_j, p_j, \right). \tag{4.38}$$

4.3.1. Constitutive framework for neo-Hookean material with one active slip system

For modeling finite plasticity, large deformations are assumed, hence the deformation gradient $\mathbf{F}$ has to be decomposed multiplicatively into its elastic and plastic part according to the definition given by Equation (2.67).

As introduced in Section 3.1, the plastic deformation occurs due to a gliding process of dislocations along an active slip system. A slip system, like sketched in Figure 3.3, is defined by the unit vectors $\mathbf{s}$ and $\mathbf{m}$ which denote the slip direction and the normal vector of the glide plane, respectively. For n slip planes, the plastic flow rule can be given by

$$\dot{\mathbf{F}}^{\mathrm{p}}\mathbf{F}^{\mathrm{p}\text{-}1} = \sum_{i}^{n} \dot{\bar{\gamma}}_i \mathbf{s}_i \otimes \mathbf{m}_i, \tag{4.39}$$

see [16].

If we assume that all slip directions lie within one plane, thus $\mathbf{m}_i = \mathbf{m}$, it can be shown that $\mathbf{m} \cdot \dot{\mathbf{F}}^{\mathrm{p}} = 0$ (note $\mathbf{s} \cdot \mathbf{m} = 0$). With the initial condition $\mathbf{F}^{\mathrm{p}} = \mathbf{I}$, integration of this expression leads to $\mathbf{m} \cdot \mathbf{F}^{\mathrm{p}} = \mathbf{m}$. Then Eq.(4.39) leads to

$$\dot{\mathbf{F}}^{\mathrm{p}} = \sum_{i}^{n} \dot{\bar{\gamma}}_i \mathbf{s}_i \otimes \mathbf{m} \cdot \mathbf{F}^{\mathrm{p}} = \sum_{i}^{n} \dot{\bar{\gamma}}_i \mathbf{s}_i \otimes \mathbf{m}. \tag{4.40}$$

Employing a time integration with the initial condition $\gamma_i(0) = 0$, the plastic deformation gradient reads

$$\mathbf{F}^{\mathrm{p}} = \mathbf{I} + \sum_{i}^{n} \bar{\gamma}_i \mathbf{s}_i \otimes \mathbf{m}. \tag{4.41}$$

From the condition $\mathbf{F}^{\mathrm{p}}\mathbf{F}^{\mathrm{p}\text{-}1} = \mathbf{I}$ the inverse plastic deformation gradient is obtained as

$$\mathbf{F}^{\mathrm{p}\text{-}1} = \mathbf{I} - \sum_{i}^{n} \bar{\gamma}_i \mathbf{s}_i \otimes \mathbf{m}. \tag{4.42}$$

Due to the restriction to single slip plasticity, which is also referred as infinite latent hardening, this flow rule can be simplified to

$$\mathbf{F}^{\mathrm{p}\text{-}1} = \mathbf{I} - \bar{\gamma}\mathbf{s} \otimes \mathbf{m}, \tag{4.43}$$

where $\bar{\gamma}$ is the total amount of plastic slip caused by this slip system and reads for N domains

$$\bar{\gamma} = \sum_{i}^{N} \lambda_i \gamma_i. \tag{4.44}$$

An additional flow rule for isotropic hardening reads

$$\dot{p} = |\dot{\gamma}| \tag{4.45}$$

with the initial condition $p(0) = 0$. The hardening parameter p is responsible for the plastic contribution to the energy.

In this model, neo-Hookean material, with the elastic free energy density defined in Equation (2.62), is considered. Assuming incompressibility the energy density reads

$$\Psi(\mathbf{F}^{\mathrm{e}}, \mathbf{p}) = \frac{1}{2}\mu\left[\mathrm{tr}\mathbf{F}^{\mathrm{e}\,\mathrm{T}}\mathbf{F}^{\mathrm{e}} - 3\right] + \kappa p^{\alpha} \tag{4.46}$$

with μ being the shear modulus and κ the hardening modulus. $\mathbf{F}^{\mathrm{e}}$ denotes the elastic deformation gradient. The factor α describes the influence of the hardening. Commonly α is set to 2, which represents linear hardening or $\alpha = 4$ is considered. Equation (4.46) describes the elastic energy for a homogeneous material. If a first order laminate is initiated, the partially relaxed energy of a material consisting of several domains has to be determined according to Eq. (4.36).

A detailed derivation of the relaxed energy of a first order laminate is given in [47]. In order to find the relaxed energy density, the energy density of the laminates Ψ^{lam} has to be found by summing up the energy of all domains, taking the incompressibility condition (4.35) and the compatibility condition (4.32) into account. These constraints are introduced to the elastic energy by employing Lagrangian multipliers, here denoted as ρ_i and $\mathbf{\Lambda}$. Then the energy density of the laminate reads

$$\Psi^{\mathrm{lam}}(\mathbf{F}, \lambda, \gamma, p, \mathbf{b}) = \frac{\mu}{2}\sum_{i=1}^{N}\left[\lambda_i \mathrm{tr}\mathbf{C}_i^{\mathrm{e}} - 2\lambda_i \mathbf{\Lambda}\cdot\mathbf{a}_i - 2\lambda_i\rho_i\mathbf{a}_i\cdot\mathbf{b}\right] - \frac{3}{2}\mu + \kappa\sum_{i=1}^{N}\lambda_i p_i^{\alpha}, \tag{4.47}$$

where i denotes the actual domain over which is summed up. The elastic right Cauchy Green tensor of domain i may be written as

$$\mathbf{C}_i^{\mathrm{e}} = \mathbf{F}_i^{\mathrm{e}\,\mathrm{T}}\mathbf{F}_i^{\mathrm{e}}. \tag{4.48}$$

The elastic deformation gradient of each domain can be obtained by $\mathbf{F}_i^{\mathrm{e}} = \mathbf{F}_i\mathbf{F}_i^{\mathrm{p\text{-}1}}$, hence

$$\mathbf{F}_i^{\mathrm{e}} = \mathbf{F}(\mathbf{I} + \mathbf{a}_i\otimes\mathbf{b})(\mathbf{I} - \bar{\gamma}_i\mathbf{s}\otimes\mathbf{m}). \tag{4.49}$$

The unknown amplitude vector $\mathbf{a}_i$ and the Lagrange parameters ρ_i and $\mathbf{\Lambda}$ are determined by a minimization of the energy density of the laminates (4.47) with respect all unknowns. The result reads

$$\rho_i = \frac{\mathbf{b}_i\cdot\mathbf{b}}{\mathbf{b}\cdot\mathbf{C}^{-1}\mathbf{b}}, \tag{4.50}$$

$$\mathbf{\Lambda} = \frac{\mathbf{C}}{\sum_{i=1}^{N}\frac{\lambda_i}{\mathbf{b}_i\cdot\mathbf{b}}}\left(\sum_{i=1}^{N}\frac{\lambda_i}{\mathbf{b}_i\cdot\mathbf{b}}\mathbf{b}_i\right) - \frac{1}{\mathbf{b}\cdot\mathbf{C}^{-1}\mathbf{b}}\mathbf{C}^{-1}\mathbf{b} \tag{4.51}$$

and

$$\mathbf{a}_i = \frac{1}{\mathbf{b}_i\cdot\mathbf{b}}\mathbf{C}^{-1}\mathbf{\Lambda} + \frac{1}{\mathbf{b}\cdot\mathbf{C}^{-1}\mathbf{b}}\mathbf{C}^{-1}\mathbf{b} - \frac{1}{\mathbf{b}_i\cdot\mathbf{b}}\mathbf{b}_i \tag{4.52}$$

where $\mathbf{b}_i$ is defined as

$$\mathbf{b}_i = \mathbf{b} - \gamma_i(\mathbf{b}\cdot\mathbf{m}\,\mathbf{s} + \mathbf{b}\cdot\mathbf{s}\,\mathbf{m}) + \gamma_i^2\mathbf{b}\cdot\mathbf{s}\,\mathbf{s}. \tag{4.53}$$

Finally these expressions may be reinserted into the energy of the laminates. Then the partially relaxed energy density reads

$$\Psi^{\mathrm{rel}}(\mathbf{F},\lambda,\gamma,p,\mathbf{b}) = \inf\left\{\Psi^{\mathrm{lam}} \,|\, \mathbf{a}_i\right\} = \kappa\sum_i^N \lambda_i p_i^\alpha$$
$$+\frac{\mu}{2}\left[\frac{1}{\sum_i^N \frac{\lambda_i}{\mathbf{b}_i\mathbf{b}}} + \left(\sum_j^N\sum_k^N \frac{\lambda_j\lambda_k \mathbf{b}_j\cdot\mathbf{C}\mathbf{b}_k}{\mathbf{b}_j\cdot\mathbf{b}\mathbf{b}_k\cdot\mathbf{b}} - \frac{1}{\mathbf{b}\cdot\mathbf{C}^{-1}\mathbf{b}}\right) + \sum_i^N \lambda_i\left(\frac{\mathbf{b}_i\cdot\mathbf{b}}{\mathbf{b}\cdot\mathbf{C}^{-1}\mathbf{b}} - \frac{\mathbf{b}_i\cdot\mathbf{C}\mathbf{b}_i}{\mathbf{b}_i\mathbf{b}}\right)\right. \tag{4.54}$$
$$\left. +\mathrm{tr}(\mathbf{C}) + \sum_i^N \lambda_i\left(\gamma_i^2\mathbf{s}\cdot\mathbf{C}\mathbf{s} - 2\gamma_i\mathbf{s}\cdot\mathbf{C}\mathbf{m}\right) - 3\right]$$

with N denoting the number of domains.

Analogously to the determination of the relaxed energy for a first order laminate, the relaxed dissipation potential, which is caused by changes in the microstructure, has to be defined. As mentioned before, the dissipation potential consists of a rate independent contribution, which is already examined by D. Kochmann and K. Hackl [48] and a quadratic term in the rate of plastic slip which captures viscous effects. The complete dissipation potential takes the form

$$\Delta(\dot\gamma) = r|\dot\gamma| + \frac{s}{2}\dot\gamma^2, \tag{4.55}$$

with s being a viscous parameter and r the critical resolved shear stress. As already derived in Section 4.2, this ansatz for the dissipation potential leads to explicit evolution equations for the internal variables.

For simplicity the number of domains in the material is set to two in the following, hence $N = 2$. The resulting laminate is shown schematically on the right hand side of Figure 4.1. Due to the restriction of two domains, the volume fraction in domain 1 can be expressed as $\lambda - 1$, consequently the volume fraction in domain 2 reads λ.

If any microstructural change appears, dissipation is produced. The dissipation potential caused by the changes of the plastic slips can be found easily by weighting the dissipation potential (4.55) for each domain with its respective volume fraction, hence for two domains

$$\Delta_1^*(\lambda,\dot\gamma_i) = (1-\lambda)\left[r|\dot\gamma_1| + \frac{s}{2}\dot\gamma_1^2\right] + \lambda\left[r|\dot\gamma_2| + \frac{s}{2}\dot\gamma_2^2\right]. \tag{4.56}$$

Any change of volume fraction is also a dissipative process, as the change of region also changes the amount of plastic slip in this region, illustrated in Figure 4.2.

Therefore also the change of volume fraction contributes a dissipation to the relaxed dissipation potential. D. Kochmann and K.Hackl [36] already derived the rate independent dissipation potential as

$$\Delta_{2a}^*\left(\gamma_i,\dot\lambda\right) = r|\gamma_2-\gamma_1|\left|\dot\lambda\right|. \tag{4.57}$$

For the determination of the viscous contribution, the viscous part of the dissipation potential may interpreted as an introduced viscous zone between the laminate domains instead of a sharp interface. If a change of the volume fraction occurs, this zone moves with the velocity

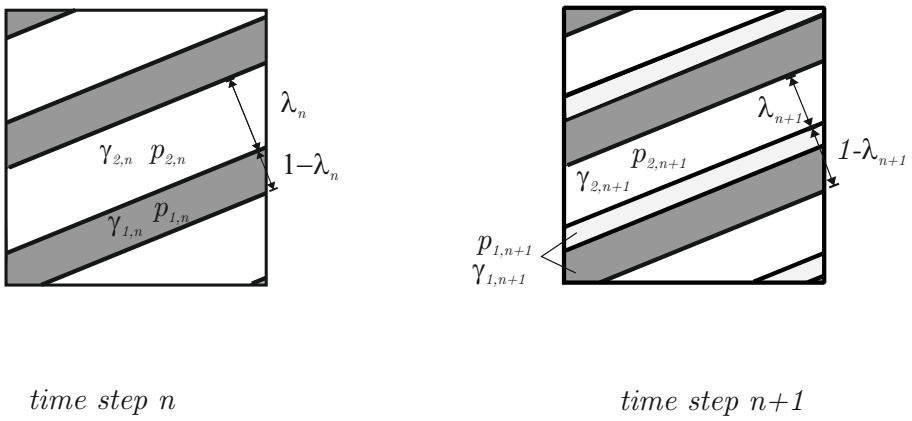

Figure 4.2.: From time step n to $n+1$ the volume fraction of the first domain, $1-\lambda$ changes (the light grey highlighted area is added), respectively in this area the plastic slip is transformed from γ_2 to γ_1.

v, illustrated in Figure 4.3. Since two viscous transition zones exist, the link between the velocity of this zone and the rate of volume fraction can be determined as

$$v = \frac{\dot{\lambda}}{2}. \tag{4.58}$$

Furthermore, the smooth transition zone is described by its width δ (volume ratio) and the viscous parameter s.

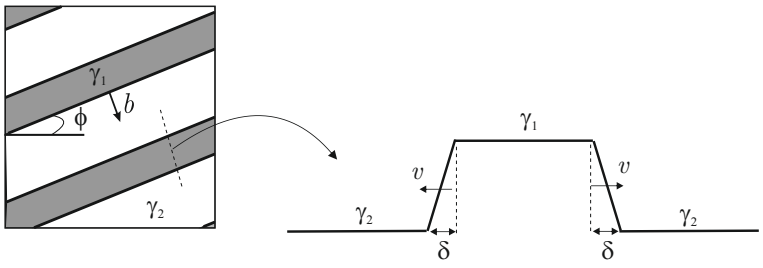

Figure 4.3.: Newly added viscous zone between the laminate domains, reprinted from [29]

For the viscous part of the dissipation potential, the intercept theorem which states

$$\dot{\gamma} = \frac{|\gamma_2 - \gamma_1|}{2\delta}\dot{\lambda} \tag{4.59}$$

can be employed for the triangle of the transition zone. This equation allows to calculate the dissipation of the viscous zone due to the change of volume fraction as $\frac{s}{2}\frac{(\gamma_2-\gamma_1)^2}{2\delta}\dot{\lambda}^2$, hence the dissipation potential due to a change of volume fraction reads

$$\Delta_2^*\left(\gamma_i, \dot{\lambda}\right) = r|\gamma_2 - \gamma_1|\left|\dot{\lambda}\right| + \frac{s}{2}\frac{(\gamma_2-\gamma_1)^2}{2\delta}\dot{\lambda}^2. \tag{4.60}$$

Then the total relaxed dissipation potential due to microstructual changes is the sum of both dissipation potentials $\Delta_1^* + \Delta_2^*$,

$$\Delta^*\left(\lambda, \gamma_i, \dot{\lambda}, \dot{\gamma}_i\right) = r|\gamma_2 - \gamma_1|\left|\dot{\lambda}\right| + \frac{s}{2}\frac{(\gamma_2-\gamma_1)^2}{2\delta}\dot{\lambda}^2 + (1-\lambda)\left[r|\dot{\gamma}_1| + \frac{s}{2}\dot{\gamma}_1^2\right] + \lambda\left[r|\dot{\gamma}_2| + \frac{s}{2}\dot{\gamma}_2^2\right]. \tag{4.61}$$

Inserting the relaxed dissipation potential (4.61) and the relaxed neo-Hookean energy (4.54) into the Lagrangian, introduced in (4.7), we get

$$\mathscr{L}\left(\mathbf{F},\lambda,\gamma_i,p_i,\dot{\lambda},\dot{\gamma}_i,\mathbf{b}\right)=\frac{\mathrm{d}}{\mathrm{dt}}\Psi^{\mathrm{rel}}\left(\mathbf{F},\lambda,\gamma_i,p_i,\mathbf{b}\right)+\Delta^*\left(\lambda,\gamma_i,\dot{\lambda},\dot{\gamma}_i\right). \tag{4.62}$$

4.4. Numerical treatment of the time-continuous evolution of finite crystal plasticity

By employing the principle of minimum of dissipation potential the stationary conditions of the Lagrangian are obtained in the form

$$0\in\frac{\partial\Psi^{\mathrm{rel}}}{\partial\lambda}+r|\gamma_2-\gamma_1|\mathrm{Sign}\dot{\lambda}+\frac{s}{2\delta}\left(\gamma_2-\gamma_1\right)^2\dot{\lambda} \tag{4.63}$$

$$0\in\frac{\partial\Psi^{\mathrm{rel}}}{\partial\gamma_i}+r\lambda_i\mathrm{Sign}\dot{\gamma}_i+\lambda_i s\dot{\gamma}_i \tag{4.64}$$

We follow the derivation from the section (4.2) and by imposing the Legendre transformation the yield function is obtained. The resulting evolution equations can be written as

$$\dot{\lambda}=-\frac{2\delta}{s\left(\gamma_1-\gamma_2\right)^2}\left(\left|\frac{\partial\Psi^{\mathrm{rel}}}{\partial\lambda}\right|-r|\gamma_1-\gamma_2|\right)_+\mathrm{sign}\frac{\partial\Psi^{\mathrm{rel}}}{\partial\lambda} \tag{4.65}$$

and

$$\dot{\gamma}_i=-\frac{1}{s\lambda_i}\left(\left|\frac{\partial\Psi^{\mathrm{rel}}}{\partial\gamma_i}\right|-r\lambda_i\right)_+\mathrm{sign}\frac{\partial\Psi^{\mathrm{rel}}}{\partial\gamma_i}. \tag{4.66}$$

The direction of the evolution of the microstructure is given by the sign of the respective driving force. The magnitude is indicated by the yield function. For the rate of plastic slip this function reads

$$\left(\left|\frac{\partial\Psi^{\mathrm{rel}}}{\partial\gamma_i}\right|-r\lambda_i\right), \tag{4.67}$$

for the rate of volume fraction, the yield function is expressed as

$$\left(\left|\frac{\partial\Psi^{\mathrm{rel}}}{\partial\lambda}\right|-r|\gamma_1-\gamma_2|\right). \tag{4.68}$$

As mentioned before, the evolution only takes place if the yield function is positive. Otherwise this expression is zero and therefore the update is also zero and the microstructure remains frozen. According to [49], the driving forces in these evolution equations may be calculated analytically. The driving force for the volume fraction reads

$$-\frac{\partial\Psi^{\mathrm{rel}}}{\partial\lambda}=-\frac{\mu}{2}\left[\mathrm{tr}\left(\mathbf{C}_2^{\mathrm{e}}\right)-\mathrm{tr}\left(\mathbf{C}_1^{\mathrm{e}}\right)-2\boldsymbol{\Lambda}\cdot\left(\mathbf{a}_2-\mathbf{a}_1\right)-2\left(\rho_2\mathbf{a}_2-\rho_1\mathbf{a}_1\right)\cdot\mathbf{b}\right]-\kappa\left(p_2^{\alpha}-p_1^{\alpha}\right) \tag{4.69}$$

with the elastic right Cauchy Green tensor of each domain $\mathbf{C}_i^{\mathrm{e}}$ defined in (4.48) and the Lagrange multipliers ρ_i and $\boldsymbol{\Lambda}$ defined in Eqs (4.50) and (4.51). The driving forces for the plastic slip are determined as

$$-\frac{\partial\Psi^{\mathrm{rel}}}{\partial\gamma_i}=\mu\lambda_i\mathrm{tr}\left(\mathbf{m}\otimes\mathbf{s}\left(\mathbf{I}+\mathbf{b}\otimes\mathbf{a}_i\right)\mathbf{C}\left(\mathbf{I}+\mathbf{a}_i\otimes\mathbf{b}\right)\left(\mathbf{I}-\gamma_i\mathbf{s}\otimes\mathbf{m}\right)\right). \tag{4.70}$$

For the two domain laminate, $\lambda_1 = 1 - \lambda$ and $\lambda_2 = \lambda$ may be inserted.

Once a laminate exists, a change of orientation of the laminate is possible. A higher order laminate is built and is vanished directly, this may relocate the laminate and thus leads to a rotation. When the laminate rotates, the domains with their corresponding plastic slip change and dissipation is produced. This domain-changing due to the rotation is illustrated in Figure 4.4.

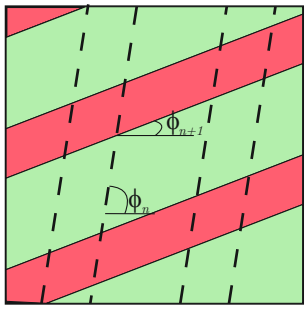

Figure 4.4.: Rotation of the original laminate to the rotated system

The dashed lines correspond to the former location of the rotated domain. The produced dissipation is proportional to the changed areas of the domains and to the dissipation distances which are required for the change of the domains. For a single slip system with two domains, this dissipation reads

$$D_\phi = 4r\lambda(1-\lambda)|\gamma_1 - \gamma_2| \tag{4.71}$$

[48]. Therefore the rotation only takes place when energetically favorable, hence if

$$\inf\left\{\Psi^{\text{rel}}[\mathbf{F}, \mathbf{z}, \phi_{n+1}] - \Psi^{\text{rel}}[\mathbf{F}, \mathbf{z}, \phi_n]\right\} + D_\phi \leq 0. \tag{4.72}$$

is fulfilled.

The dissipation potential caused by rotation should be consistent to the previous dissipation potentials. Therefore it is considered in the form

$$\Delta_\phi^{\text{rel}} = a\left|\dot{\phi}\right| + b\dot{\phi}^2, \tag{4.73}$$

with a and b may depending on λ_i and γ_i. Up to now, no canonical way determines a and b, however the limit behavior should be fulfilled, thus if $\lambda \to 0$, $1 - \lambda \to 0$ or $\gamma_1 - \gamma_2 \to 0$, the dissipation potential has to tend to zero as well. According to this condition, a and b are chosen as

$$a = 4r\lambda(1-\lambda)|\gamma_1 - \gamma_2| \tag{4.74}$$

and

$$b = \frac{s}{\delta}\lambda(1-\lambda)(\gamma_1 - \gamma_2)^2. \tag{4.75}$$

Then the dissipation potential reads

$$\Delta_\phi^{\text{rel}} = 4r\lambda(1-\lambda)|\gamma_1 - \gamma_2|\left|\dot{\phi}\right| + \frac{s}{\delta}\lambda(1-\lambda)(\gamma_1 - \gamma_2)^2\dot{\phi}^2. \tag{4.76}$$

The first part of this dissipation (a) is similar to the dissipation potential considered by Kochmann and Hackl [48], determining the changed plastic slip due to the rotation. The second contribution of this dissipation potential is chosen for regularization and considered analogously to the dissipation potential which is exhibited by the change of volume fraction.

As the change of the angle is considered to be small, the global minimization of the free energy for determining the angle is replaced by a local minimization, hence by taking the tangent, shown in Figure 4.5. Then the evolution of the angle is similar to the updates of the

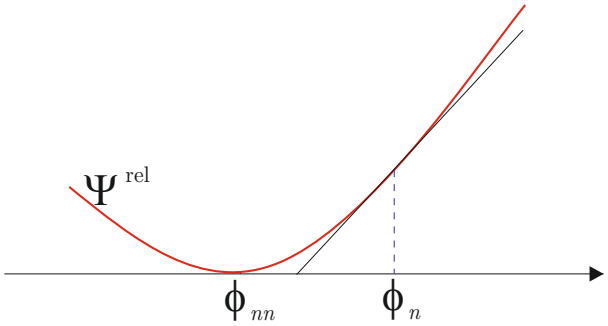

Figure 4.5.: Local minimization of the angle

volume fraction and plastic slip (Equations (4.66) and (4.65)) and reads

$$\dot{\phi} = -\frac{\delta}{2s\lambda(1-\lambda)(\gamma_1-\gamma_2)^2}\left(\left|\frac{\partial \Psi^{\text{rel}}}{\partial \phi}\right| - 4r\lambda(1-\lambda)|\gamma_1-\gamma_2|\right)_+ \text{Sign}\frac{\partial \Psi^{\text{rel}}}{\partial \phi} \tag{4.77}$$

The remaining internal variable, which has to be updated, is the hardening parameter p_i. According to [47], it has to be updated twice. The first update is caused by the change of the volume fraction. When the volume fraction of one domain changes, the region, associated previously with the other hardening parameter has to change as well (illustrated in Figure 4.2). The updated values are obtained by an energetic averaging,

$$(\lambda_n + \Delta\lambda)\, p^{\alpha}_{2,n+1} = \lambda_n p^{\alpha}_{2,n} + \Delta\lambda p^{\alpha}_{1,n} \quad p_{1,n+1} = p_{1,n} \tag{4.78}$$

for $\Delta\lambda > 0$ with $\lambda_{n+1} = \lambda_n + \Delta\lambda$. For $\Delta\lambda < 0$, the updating procedure

$$(1-\lambda_n-\Delta\lambda)\, p^{\alpha}_{1,n+1} = (1-\lambda_n)\, p^{\alpha}_{1,n} - \Delta\lambda p^{\alpha}_{2,n} \quad p_{2,n+1} = p2_{1,n} \tag{4.79}$$

holds true where $\Delta\lambda$ is the update for the volume fraction for each time step dt, hence

$$\Delta\lambda = \dot{\lambda}\text{dt}. \tag{4.80}$$

The second updating follows according to the flow rule given by Equation (4.45),

$$\Delta p_1 = |\Delta\gamma_1| \tag{4.81}$$

and

$$\Delta p_2 = |\Delta\gamma_2| \tag{4.82}$$

with $\Delta\gamma_i = \dot{\gamma}_i\text{dt}$.

Our aim is to model the time-continuous evolution of a microstructure. If the initial data $\mathbf{F}_n, \gamma_{i,n}, p_{i,n}, \lambda_n, \phi_n$ at the beginning of a time step is known, for a given small time step dt

with a known deformation gradient at the end of the time step $\mathbf{F}_{n+1}$, the update of the internal variables may be found as

$$\Delta\lambda = \dot{\lambda}\mathrm{d}t, \tag{4.83}$$

$$\Delta\gamma_i = \dot{\gamma}_i\mathrm{d}t, \tag{4.84}$$

and

$$\Delta\phi = \dot{\phi}\mathrm{d}t. \tag{4.85}$$

The rates of the internal variables are determined by the evolution equations which are derived above. Since all evolution equations for the internal variables which describe the microstructure are already obtained, the microstructural changes in every time step with given initial data can be computed.

Another crucial aspect of this modeling technique is the initiation of the evolution from the former homogenous material. Microstructures only appear if it is energetically favorable that the homogenous crystal splits up. Therefore a test function λ_{test} is defined,

$$\lambda_{\text{test}} = \lambda_n + \frac{\frac{\partial\Psi}{\partial\lambda}}{\left|\frac{\partial\Psi}{\partial\lambda}\right|}. \tag{4.86}$$

This test function indicates whether the evolution of the volume fraction tends to the "right" direction. As an example: If $\lambda_n = 0$, the test function should be positive and therefore the evolving volume fraction as well. Otherwise a lamination does not reduce the energy and the crystal stays homogenous. If the test function indicates that a laminate should be established, the volume fraction and the plastic slip of the domain, which should arise, are set to an infinitely small value. Then the remaining internal variables are updated according to their evolution equations.

In the model of Kochmann and Hackl [47], the laminate arises directly when it is energetically favorable, illustrated in Figure 4.6.

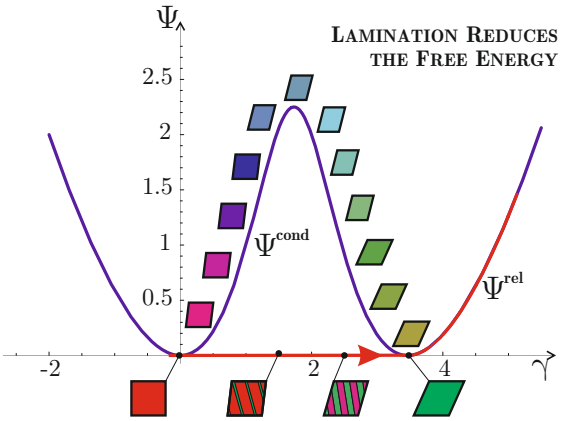

Figure 4.6.: Initiation in the model from Kochmann and Hackl, [47].

In the new approach, the dissipation of the material contains also a viscous contribution. Therefore a delay due to the viscosity occurs before the microstructure can minimize the

energy (Figure 4.7) and the energy follows the non convex path until the the microstructure is built. Then the energy shakes down to the rank-one-convex hull. Due to viscous effects, also the vanishing of the microstructure is delayed.

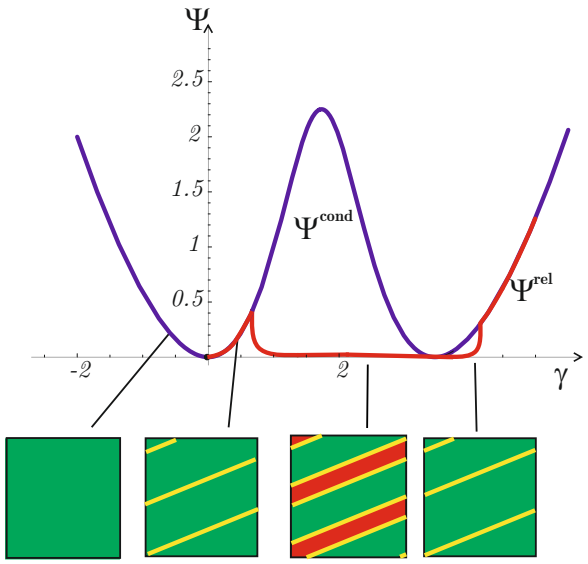

Figure 4.7.: Initiation of the modified approach including a viscous contribution.

This model can be implemented and testings performed, algorithm 1 illustrated the procedure. Until now, this model is performed on a material point. For a continuum with several material points and boundary conditions, this scheme has to be implemented in a finite element code.

Algorithm 1 Numerical scheme for the incremental evolution for single slip plasticity

for incremental load update: $\mathbf{F}_{n+1} = \mathbf{F}_n + \Delta\mathbf{F}$ **do**

if $\lambda = 0$ or $\lambda = 1$ **then**

→ Homogenous material

Calculate testfunction: $\lambda_{\text{test}} = \lambda_n + \frac{\frac{\partial\Psi}{\partial\lambda}}{\left|\frac{\partial\Psi}{\partial\lambda}\right|}$

if $0 < \lambda_{\text{test}}$ and $\lambda_n = 0$ **then**

$\lambda_{n+1} = \epsilon$ and $\gamma_{2,n+1} = \epsilon$ with $\epsilon \longrightarrow 0$

$$\gamma_{1,n+1} = \gamma_{1,n} - \frac{1}{s(1-\lambda_n)}\left(\left|\frac{\partial\Psi}{\partial\gamma_{1,n}}\right| - r(1-\lambda_n)\right)_+ \operatorname{sign}\frac{\partial\Psi}{\partial\gamma_{1,n}}\mathrm{dt}$$

$$\phi_{n+1} = \phi_n - \frac{\delta}{2s\lambda_n(1-\lambda_n)(\gamma_{1,n}-\gamma_{2,n})^2}\left(\left|\frac{\partial\Psi}{\partial\phi_n}\right| - 4r\lambda_n(1-\lambda_n)\left|\gamma_{1,n}-\gamma_{2,n}\right|\right)_+ \operatorname{sign}\frac{\partial\Psi}{\partial\phi_n}\mathrm{dt}$$

if $\lambda_{\text{test}} < 1$ and $\lambda_n = 1$ **then**

$1 - \lambda_{n+1} = \epsilon$ and $\gamma_{1,n+1} = \epsilon$ with $\epsilon \longrightarrow 0$

$$\gamma_{2,n+1} = \gamma_{2,n} - \frac{1}{s\lambda_n}\left(\left|\frac{\partial\Psi}{\partial\gamma_{2,n}}\right| - r\lambda_n\right)_+ \operatorname{sign}\frac{\partial\Psi}{\partial\gamma_{2,n}}\mathrm{dt}$$

$$\phi_{n+1} = \phi_n - \frac{\delta}{2s\lambda_n(1-\lambda_n)(\gamma_{1,n}-\gamma_{2,n})^2}\left(\left|\frac{\partial\Psi}{\partial\phi_n}\right| - 4r\lambda_n(1-\lambda_n)\left|\gamma_{1,n}-\gamma_{2,n}\right|\right)_+ \operatorname{sign}\frac{\partial\Psi}{\partial\phi_n}\mathrm{dt}$$

if $0 < \lambda < 1$ **then**

→ Existing microstructure

$$\lambda_{n+1} = \lambda_n - \frac{2\delta}{s(\gamma_{1,n}-\gamma_{2,n})^2}\left(\left|\frac{\partial\Psi}{\partial\lambda_n}\right| - r\left|\gamma_{1,n}-\gamma_{2,n}\right|\right)_+ \operatorname{sign}\frac{\partial\Psi}{\partial\lambda_n}\mathrm{dt}$$

$$\gamma_{1,n+1} = \gamma_{1,n} - \frac{1}{s(1-\lambda_n)}\left(\left|\frac{\partial\Psi}{\partial\gamma_{1,n}}\right| - r(1-\lambda_n)\right)_+ \operatorname{sign}\frac{\partial\Psi}{\partial\gamma_{1,n}}\mathrm{dt}$$

if $\lambda_{n+1} - \lambda_n > 0$ **then**

Update of p_i according to $(\lambda_n + \Delta\lambda)\, p^\alpha_{2,n+1} = \lambda_n p^\alpha_{2,n} + \Delta\lambda p^\alpha_{1,n} \qquad p_{1,n+1} = p_{1,n}$

if $\lambda_{n+1} - \lambda_n < 0$ **then**

Update of p_i according to $(1-\lambda_n-\Delta\lambda)\, p^\alpha_{1,n+1} = (1-\lambda_n)\, p^\alpha_{1,n} + \Delta\lambda p^\alpha_{2,n} \qquad p_{2,n+1} = p_{2,n}$

$$\gamma_{2,n+1} = \gamma_{2,n} - \frac{1}{s\lambda_n}\left(\left|\frac{\partial\Psi}{\partial\gamma_{2,n}}\right| - r\lambda_n\right)_+ \operatorname{sign}\frac{\partial\Psi}{\partial\gamma_{2,n}}\mathrm{dt}$$

$$p_{1,n+1} = p_{1,n+1} + \left|\gamma_{1,n+1} - \gamma_{1,n}\right|$$

$$p_{2,n+1} = p_{2,n+1} + \left|\gamma_{2,n+1} - \gamma_{2,n}\right|$$

$$\phi_{n+1} = \phi_n - \frac{\delta}{2s\lambda_n(1-\lambda_n)(\gamma_{1,n}-\gamma_{2,n})^2}\left(\left|\frac{\partial\Psi}{\partial\phi_n}\right| - 4r\lambda_n(1-\lambda_n)\left|\gamma_{1,n}-\gamma_{2,n}\right|\right)_+ \operatorname{sign}\frac{\partial\Psi}{\partial\phi_n}\mathrm{dt}$$

4.5. Results

The in the previous section presented numerical scheme can be applied to any arbitrary deformation. As the relaxed energy density is derived under the assumption of incompressibility, the here tested deformation should be volume-preserving. In this chapter, a shear test and a tension-compression test are performed on the material point level. For solving the evolution equations, if not otherwise indicated, a forward Euler integration is used. The resulting stresses which are shown in the results are the Cauchy stresses and calculated by

$$\sigma = \mu\left(\mathbf{F}^{\mathrm{e}} \cdot \mathbf{F}^{\mathrm{eT}} - \mathbf{I}\right). \tag{4.87}$$

4.5.1. Shear test

The first test is a shear test, the loading and the loading path are schematically sketched in Figure 4.8.

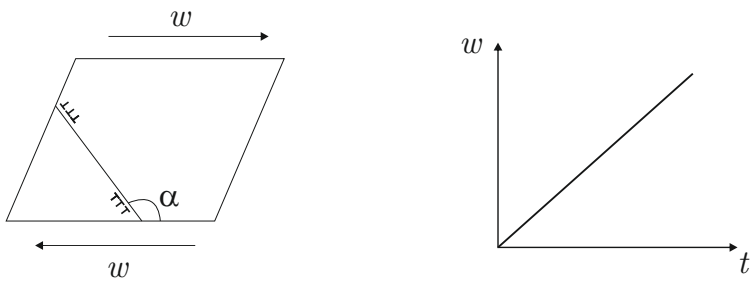

Figure 4.8.: Shear test, partly reprinted from [29].

The angle α in Figure 4.8 describes the angle of the slip system, such that the slip direction can be obtained by $\mathbf{s} = \{\cos\alpha, \sin\alpha, 0\}^T$ and the normal vector is given by $\mathbf{m} = \{-\sin\alpha, \cos\alpha, 0\}^T$. In this test, the angle is chosen as $\alpha = 150°$. For this simple shear test the given deformation gradient reads

$$\boldsymbol{F} = \begin{pmatrix} 1 & w & 0 \\ 0 & 1 & 0 \\ 0 & 0 & 1 \end{pmatrix}. \tag{4.88}$$

The calculations are evaluated with the material parameters $\mu = 1$ [GPa] (shear modulus), the hardening modulus $\kappa = 0.001$ [GPa] and the critical resolved shear stress is chosen as $r = 0.1$ [GPa]. The viscous parameters are considered as $s = r * t^{\star}$ ($t^{\star} = 0.01$ [s]) and $\delta = r * j$ [mm] ($j = 0.1$ [mm^3/N]). This shear test is driven with an incremental load update $dw = 0.001$ and with an time increment dt = 0.0001 [s]. Fig. 4.9 shows the unrelaxed energy density, hence the energy if the material remains homogeneous. Obviously, when no microstructure occurs, the energy is non convex and thus a microstructure is energetically favorable.

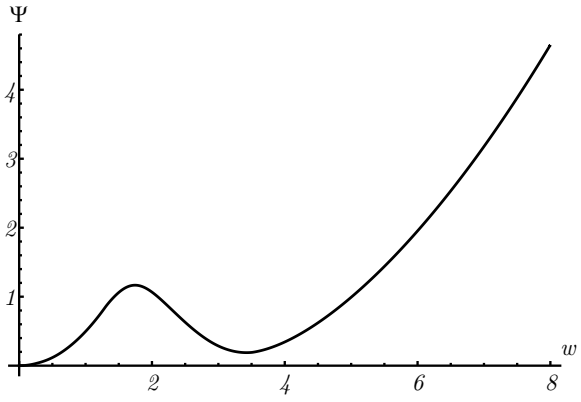

Figure 4.9.: Unrelaxed energy for a shear test.

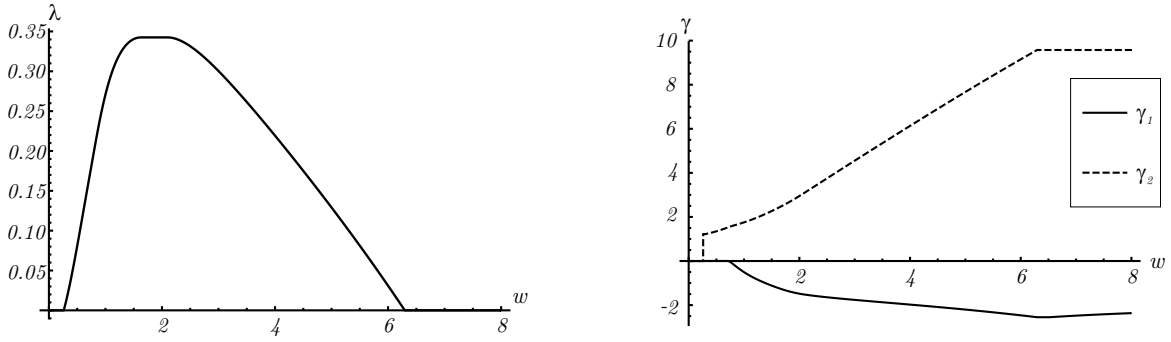

Figure 4.10.: Volume fraction of the second domain and plastic slip in both domains for a shear test.

On the left-hand side of Figure 4.10, the volume fraction of the second domain of the laminate during the loading is presented (λ). When the material is loaded with shear, at first no microstructure evolves and the crystal stays homogenous. This can be expected: lamination will set in only when a critical external load has been applied to the material (an explanation for this behavior can be found in Section 3.1). In this example, the critical load is reached at approximately $w = 0.25$ and the volume fraction of domain two starts to evolve. With increasing the shear approximately 34% of the material will "transform" to domain two at maximum before this value stays constant over a short loading period. Increasing the external load in terms of prescribed deformation gradient over $w > 2.50$ forces the volume fraction to shrink again and the domain vanishes completely at $w = 6.50$.

The evolution of the volume fraction of domain two of the laminate indicates that a microstructure is built. Therefore also the other internal variables which describe the current state of the microstructure may evolve as well. The plastic slip γ_i occurs in both domains, presented on the right hand side of Figure 4.10. The plastic slip in domain two is positive and jumps from zero to $\gamma_2 = 1.4$. During further loading, it increases slowly. First the bigger domain one behaves elastically after initiation, thus the plastic slip is zero. At $w = 0.80$ the plastic slip in domain one occurs and decreases.

The huge increase of γ_2 after the initiation may seem surprising at first glance. However, as the initiation of the microstructure takes place, we consider a very small volume fraction of domain two. This volume fraction may be too small to minimize the energy completely.

Therefore a drastic evolution of plastic deformation is first observed when the associate laminate structure λ establishes. Although the plastic slip is very huge within that domain, the total amount of plastic deformation, that is $(1-\lambda)\gamma_1 + \lambda\gamma_2$, presented in Figure 4.11, remains very limited (and smooth). Due to the high external deformation that is necessary to initialize evolution of a laminate, a huge plastic deformation within the newly establish laminate is physically sound.

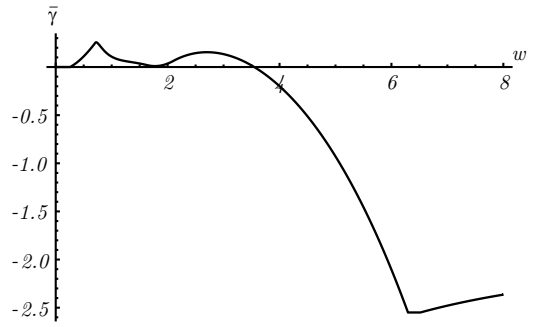

Figure 4.11.: Total amount of plastic slip for a shear test.

The microstructure may also rotate, which is described by the angle of the laminate, presented on the left hand side of Figure 4.12. At the beginning of loading, the angle of the laminate is zero, which is not surprising because the entire material is homogenous. At the onset of lamination (at $w = 0.25$), the angle starts to evolve. The laminate rotates until the total amount of plastic slip (figure 4.11) reaches its maximum and the plastic slip in domain one starts to increase. Then, the laminate does not need to rotate further and the angle of the laminate remains constant at 0.071 rad.

The right-hand side of Figure 4.12 shows the hardening parameters of both domains. Because the plastic slip in domain two evolves from the beginning of the lamination, there is also an increasing hardening due to the coupled evolution of hardening to the evolution of plastic slip. The hardening increases monotonously, similar to the slope of the plastic slip. Domain one behaves elastically first, therefore the hardening is zero until it onsets when the corresponding plastic slip starts to evolve. When domain two no longer exists, no further evolution of plastic slip nor hardening takes place in that domain. Therefore, p_1 remains constant from here on while p_2 slightly increases further.

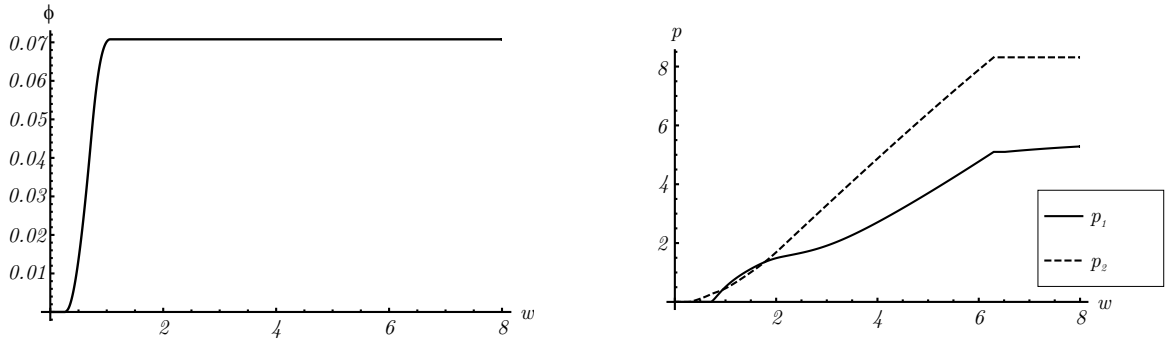

Figure 4.12.: Angle of laminate and hardening parameter in both domains for a shear test.

The important evolution steps of the laminate are schematically sketched in Fig. 4.13.

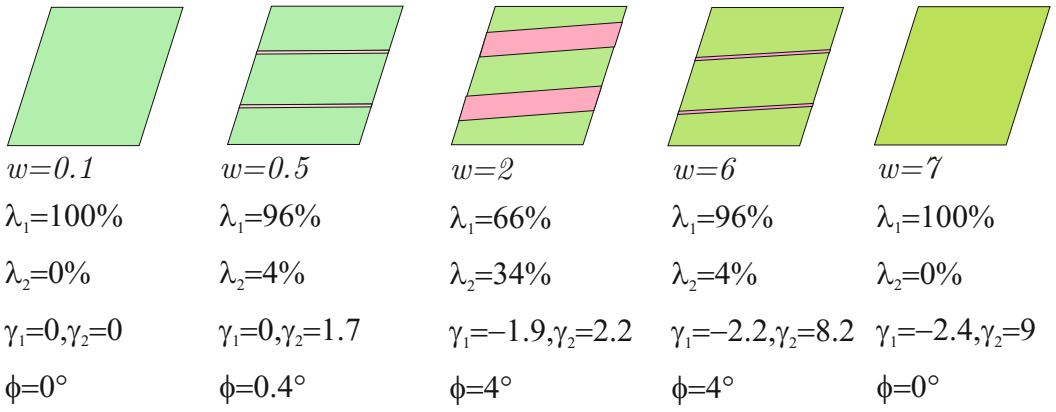

Figure 4.13.: Evolution of the microstructure.

First the material deforms elastically and is homogeneous, then a small second domain is build with an angle nearly zero. This second domain behaves plastic, while the larger domain remains elastic. With increasing strain up to $w = 3$, the laminate domains rotate around 4° and the area of the second domain increases up to 34% of the whole material and the first domain behaves plastically as well. Increasing the shear strain further, the second domain decreases and finally vanishes at $w = 6.3$.

The resulting Cauchy shear stress (calculated according to Equation (4.87)) and the energy (according to Equation (4.54)) of this shear test are presented in Figure 4.14.

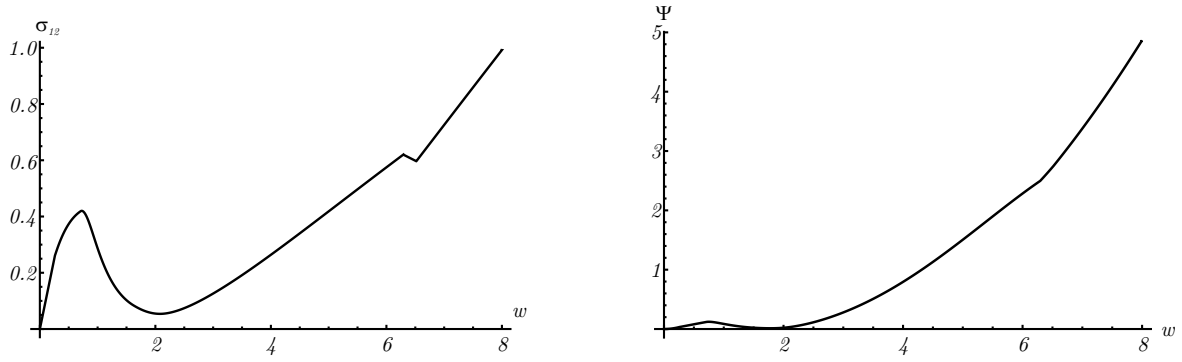

Figure 4.14.: Cauchy shear stress and energy of a shear test.

The left-hand side of Figure 4.14 shows the shear component of the Cauchy stress. During the first part of the shearing, the stress increases non-linearly (which is not over pronounced). This follows from the non-linear neo-Hookean energy that we choose and the delay of the microstructure. The slope of the stress decreases when the second domain of the laminate starts to evolve (in which plastic slip is present). However, the total amount of plastic deformation during this period remains too small to influence stresses to a very large degree. When the plastic slip in domain one (that is $1 - \lambda$, which is here much larger than λ) also evolves, this indeed has a strong impact on the stresses: they drop quite drastically. In total, this stress strain curve does not display plastic material behavior. Therefore further investigations are needed.

At a loading larger than $w > 2$, it is energetically more favorable to reduce the amount of domain two in the laminate (see also Figure 4.10). The total amount of plastic deformation

then reduces again (which is intensified by the fact that that the plastic slip in domain one remains more or less constant). This, in turn, yields that the stress increases again. When the microstructure vanishes, at $w = 6.5$, a viscous delay occurs before the crystal is homogenous again. Therefore, we see a kink in the shear stress.

The viscous regularization also influences the energy of this material. The minimization of the energy by the microstructure is delayed. This is visible in the energy plot in the right-hand side of Figure 4.14. Until the laminate evolves, the energy increases. While the microstructure adapts to the external loading in an energy-minimizing way, the energy decreases. So the energy has still a non-convexity but less distinct. When domain two has reached its maximum volume fraction, the energy increases again as does the shear stress.

In Fig.4.15 the unrelaxed energy (dashed) and the relaxed energy are presented. When

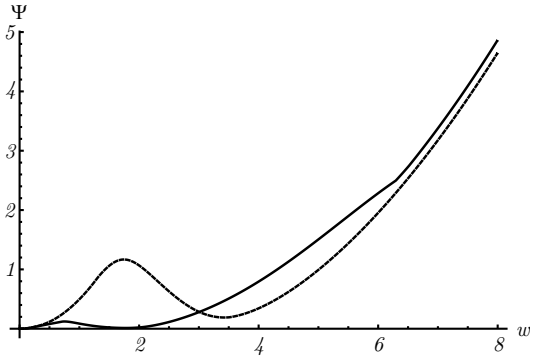

Figure 4.15.: Comparison of relaxed and unrelaxed energy.

the unrelaxed energy is non convex, the relaxed energy is smaller and the non convexity is drastically reduced. Afterward, the unrelaxed energy has lower values, which is rather surprising. When the microstructure is vanished (at $w > 6$) the unrelaxed energy is still a little bit smaller. The reason for that behavior are probably viscous effects.

4.5.2. Tension-compression test

As a second testing a tension-compression test is performed. The loading and the loading path of this test are depicted in Figure 4.16.

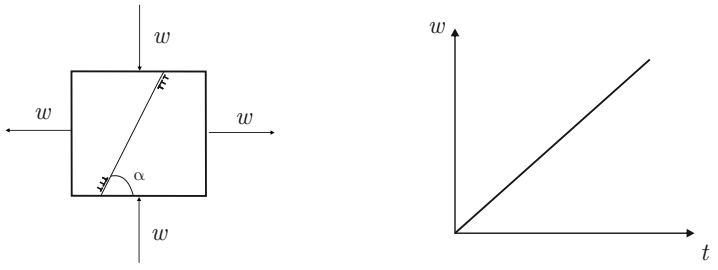

Figure 4.16.: Tension-compression test, partly reprinted from [29]

The deformation gradient for this test is expressed as

$$\mathbf{F} = \begin{pmatrix} 1+w & 0 & 0 \\ 0 & \frac{1}{1+w} & 0 \\ 0 & 0 & 1 \end{pmatrix} \tag{4.89}$$

The slip system is chosen under an angle of $\alpha = 80°$. Furthermore, the same material constants are taken as in the shear test. As incremental load update $dw = 0.01$ and as time increment $\mathrm{dt} = 0.0001\,[s]$ are taken. Under these loading conditions, the homogeneous material splits up and forms a microstructure since the unrelaxed energy is non convex (see Fig. 4.17).

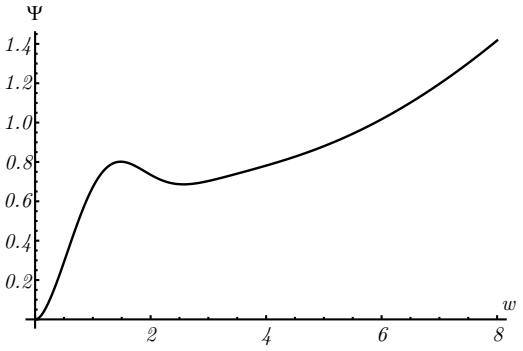

Figure 4.17.: Unrelaxed energy of a tension-compression test.

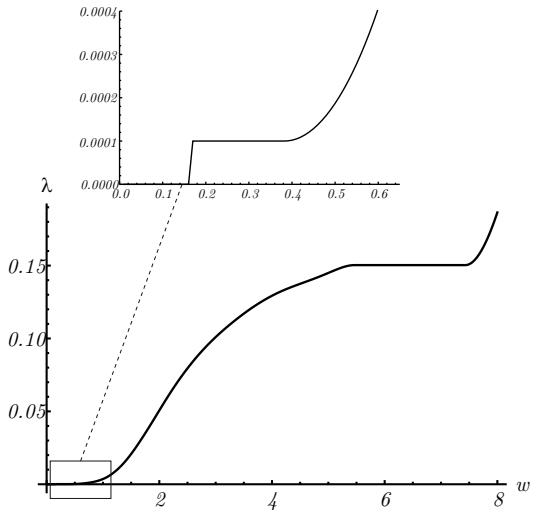

Figure 4.18.: Volume fraction of the second domain for a tension-compression test

In this test, the initiation of microstructure begins at $w = 0.16$ (see Figure 4.18), before the material remains homogeneous. At the beginning of the evolution of the microstructure (up to $w = 0.8$), the volume fraction (presented in Figure 4.18) of domain two is approximately zero even the plastic slip of this domain is evolving. Magnification of this small area reveals that there is a small constant volume fraction in this region. Subsequently, the volume fraction increases rapidly up to a value of 16% and remains constant until the load reaches $w = 7.5$. From here on, the laminate increases again. Thus, domain one is dominant together with a slight amount of domain two (with volume fraction λ). The maximum volume fraction of domain 2 is 16%.

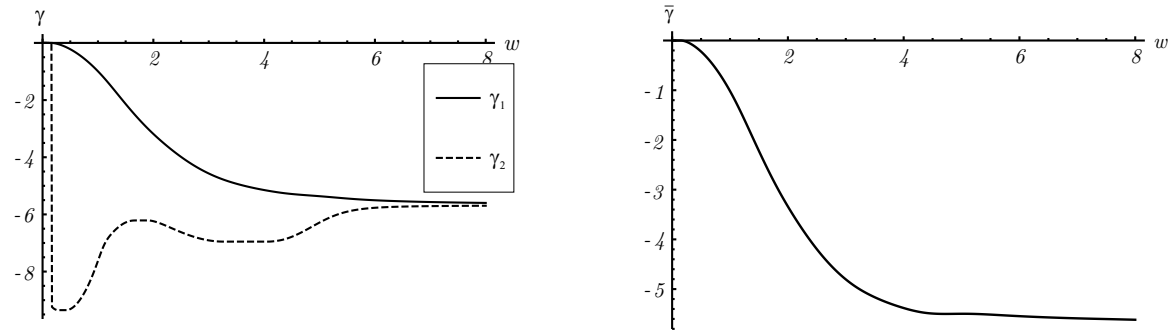

Figure 4.19.: Plastic slip in both domains and total amount of plastic slip for a tension-compression test.

The plastic slip of domain two seems to jump from zero to -9 (left-hand side in Figure 4.19). The plastic slip then increases up to -6 and afterward slightly de- and increases. The huge amount of plastic slip in the beginning of the plastic slip in domain two is induced, in analogy to the shear test, by having a very small volume fraction at the initiation. Even there is the huge amount of the plastic slip in domain two, the total amount of plastic slip (right-hand side of Figure 4.19) decreases slowly and smoothly from zero to -5.6, since the volume fraction of domain two is quite small.

The plastic slip in domain one evolves in this example directly at the onset of the microstructure, hence both domains behave plastic directly after their initiation. The plastic slip in domain one is negative and constantly decreasing. At a high external load it asymptotically approaches the amount of plastic slip in domain two.

The last internal variables that describe the laminate are the hardening parameters and the angle of the laminate, presented in Figure 4.20.

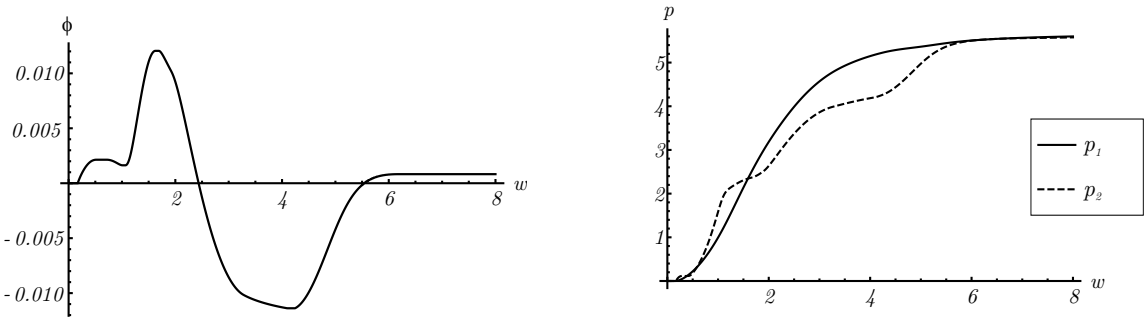

Figure 4.20.: Angle of the laminate and hardening parameter in both domains for a tension-compression test.

The angle is shown at the left-hand side of Figure 4.20. In this example, the laminate rotates quite often. However, the absolute values still remain small. A comparison with the slope of the plastic slip in domain two reveals that both slopes behave similarly since both internal variables are coupled.

The hardening parameters are plotted on the right-hand side of Figure 4.20. Hardening is caused by the change of plastic slip and a small amount is contributed by the change of

volume fraction. Since the influence due to the changes of plastic slips is much larger than due to changes of the volume fractions, the hardening parameters are similar to the absolute values of the plastic slip, except the jump of the plastic slip in domain two. When the plastic slip and the hardening parameters (Figure 4.20) of both domains coincide, the material is homogeneous, since these parameters are the differences between the two domains. This case occurs at $w = 8$, therefore the material becomes homogeneous again.

Taking this microstructure into account, the Cauchy stresses and the energy can be determined. Figure 4.21 shows the normal stresses σ_{11} and σ_{22}.

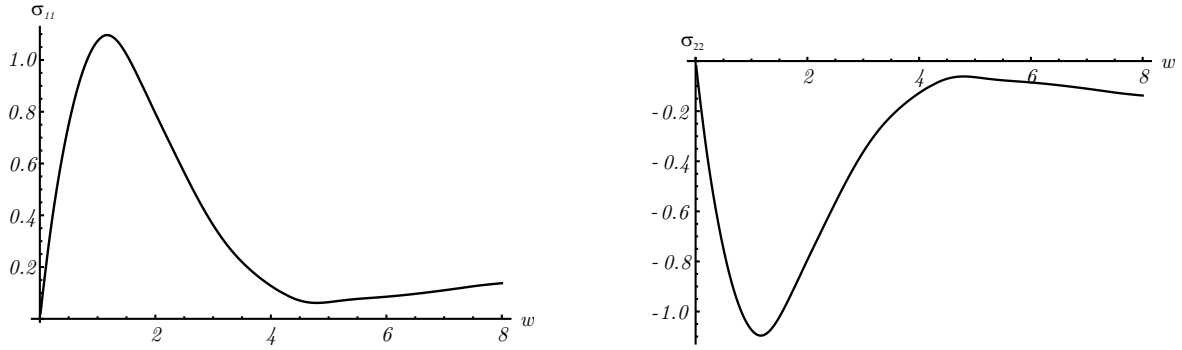

Figure 4.21.: Cauchy normal stresses for a tension-compression test.

The normal stress σ_{11} is presented on the left-hand side of Figure 4.21. During the first loading steps, the stress strongly increases up to a maximum value of 1.4 [GPa]. Before the microstructure is established, the material behaves purely elastic. Then the initiation of lamination takes place and these patterns reduce the energy. In the beginning, the volume fraction of domain two is negligible due to the viscous effect: even there is a large amount of plastic slip in domain one, the total amount of plastic slip is too small to decrease the stress. Therefore the stress still increases. With the increase of volume fraction and the plastic slip in domain one, the stress drops drastically to 0.1 [GPa] and slightly increases due to the hardening effect.

The evolution of σ_{22} coincides with the evolution of σ_{22}, it is simply mirrored at the horizontal axis. Figure 4.22 shows the energy of this tension-compression test and the unrelaxed energy (dashed line). The behavior of the relaxed energy is similar to the energy of the shear test. Before the microstructure can evolve, the viscous contribution delays th minimization of the energy. While the laminate evolves, it is still not adapted to the external loading, hence the energy is not minimized and increases. Thereafter, the energy is minimized by the microstructure and decreases. Thus, the energy is still non-convex. However, the comparison between the relaxed and unrelaxed reveals that the non convexity of the laminate is smaller compared to the non convexity of a homogeneous material.

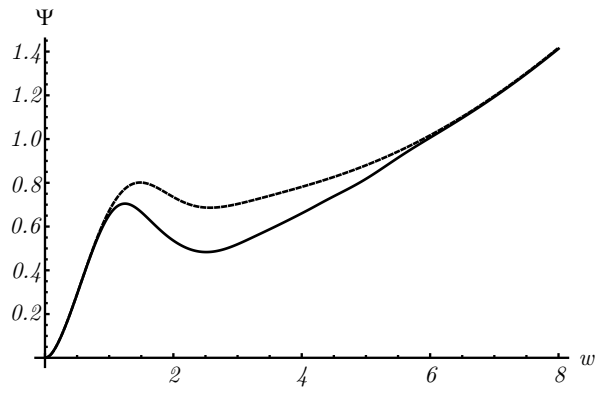

Figure 4.22.: Comparison of relaxed and unrelaxed energy

4.5.3. Viscous effects

In the previous section, the stress-strain curves do not exhibit a typical plastic material behavior and the energies still reveal non-convexities, thus the introduced viscosity should be reduced. Due to the chosen viscous dissipation potential contribution, the evolution of the microstructure is time dependent. This viscous influence may be decreased by increasing the relaxation time for the material. Therefore the loading velocity $\Delta w/(\Delta \mathrm{t})$ influences the material behavior. In order to compare the behavior resulting from different loading velocities, a factor ϑ is introduced. This quantity is an integer that controls the number of updates that are performed for a fixed external load w. Then a pseudo-velocity can be defined as $\Delta w/(\vartheta \Delta \mathrm{t})$. For larger values of ϑ, the pseudo-velocity decreases and the material has more "time" to relax. Consequently, this factor is supposed to influence the material behavior to a remarkable extent. All results in the previous section to this point were calculated with $\vartheta = 1$. This means, with every time step, the load is also updated. In the following, we provide more time for the material to adapt to the external load by increasing ϑ. Figure 4.23 visualizes this pseudo- velocity in the updating procedure.

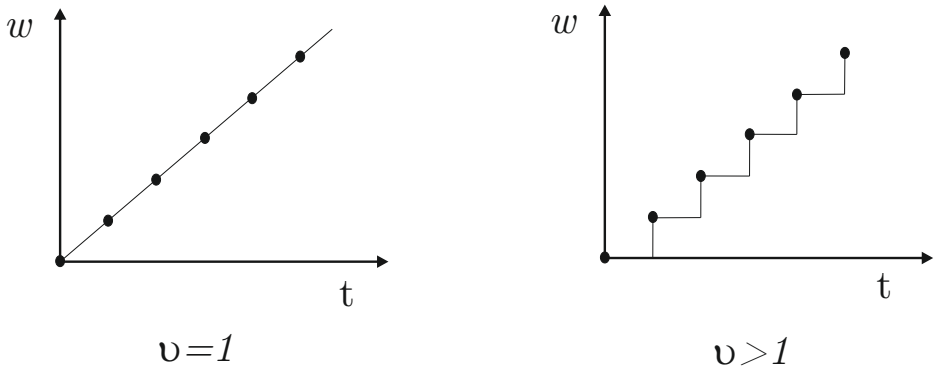

Figure 4.23.: Update with different pseudo-velocities.

Shear test with decreased pseudo-velocity

For a first examination of the influence of the relaxation time, the pseudo-velocity factor is increased from $\vartheta = 1$ to $\vartheta = 20$. In order to make a comparison, all constants are taken from

the previous shear test.

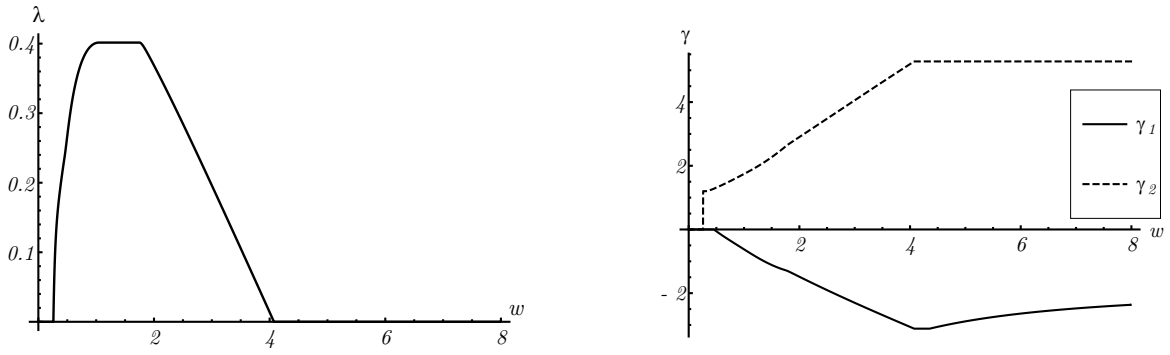

Figure 4.24.: Volume fraction of the second domain and plastic slip for both domains for a shear test, $\vartheta = 20$.

The slope of the evolution of the volume fraction of domain two (left-hand side of Fig 4.24) is bigger, therefore the volume increases much faster but also decreases faster. Understandably, the maximum value is reached earlier and a higher maximum value is achieved compared to the previous one with $\vartheta = 1$ (see Figure 4.10 left-hand side). The slope of the plastic slip instead remains nearly the same (right-hand side). It is remarkable, that the onset of the plastic slip in domain one starts earlier and develops with a higher slope. Obviously, the delay of the plastic slip in the previous test is caused by viscous effects and is decreased by a longer relaxation time.

The two remaining internal variables, the angle of the laminate and the hardening, are presented in Figure 4.25.

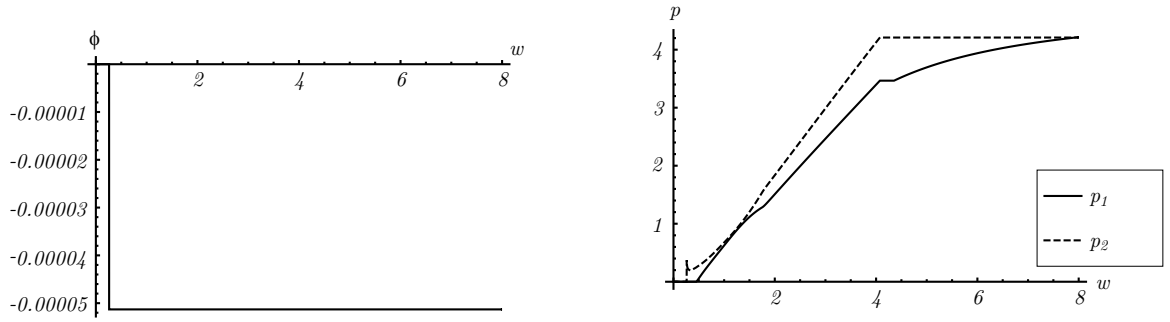

Figure 4.25.: Angle of laminate and hardening in both domains for a shear test, $\vartheta = 20$.

When the microstructure is initiated, the angle is found as $\phi = -0.00005$ [rad] and then the laminate does not need to rotate further (note: the variables are only plotted at the beginning of each new load step, thus when w changes). The hardening parameters in both domains are nearly equal the positive amount of plastic slip in both domains. Therefore compared to the hardening with pseudo- velocity $\vartheta = 1$, the hardening of domain one starts earlier, thus also in this evolution the viscous effect is decreased.

These slightly changed internal variables influence strongly the behavior of the Cauchy stress and the energy, which are presented in Figure 4.26.

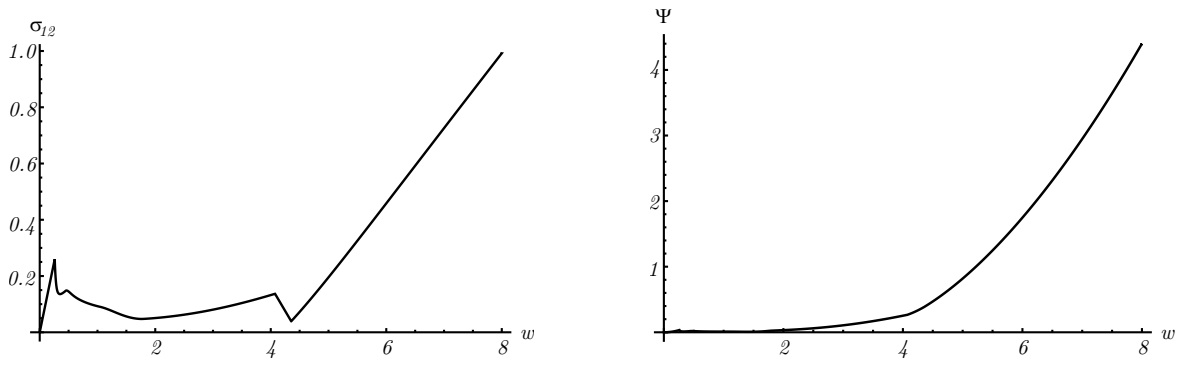

Figure 4.26.: Cauchy shear stress and energy for a shear test, $\vartheta = 20$.

The increased time for the material to relax, which results in an "intensified" microstructure, is visible in the results for stress and energy: the viscous peak in the stress and the non convexity in the energy are not as high and are less distinct (Figure 4.26). The peak in the stress for the initial pseudo-velocity has reached up to 0.4 [GPa], whereas for a reduced pseudo-velocity the stress peak is only 0.25 [GPa]. This indicates that a viscous treatment, which allows the material to relax , leads to a proper solution in which the energy tends to be convex, Figure 4.26. In Fig.4.27 the comparison of the unrelaxed (dashed) and relaxed energy is shown.

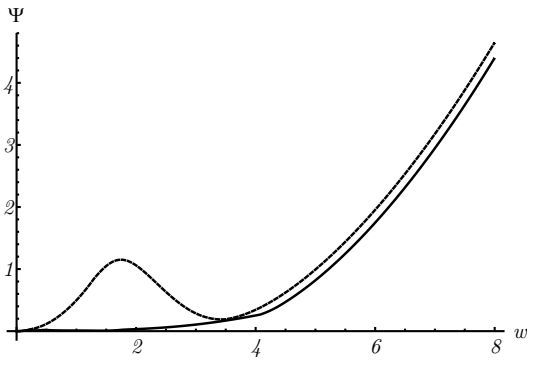

Figure 4.27.: Comparison of relaxed and unrelaxed energy for a shear test, $\vartheta = 20$.

When the material has more time to relax, viscous effects decrease and the energy is convex. The comparison reveals, that with this relaxation time, the relaxed energy curve lies always under the unrelaxed energy. This hints that the surprising behavior for $\vartheta = 1$ appears due to viscous effects. Since the microstructure influences strongly the plastic slip, the relaxed energy does not correspond completely to the unrelaxed energy, even when the material is homogeneous again.

Varying pseudo- velocities in a shear test

In the previous example, the changes in the microstructure due to a certain decrease of loading-velocity is studied. Now the evolving microstructure is compared under several loading-velocities in order to gain insight how this velocity influences the microstructure

and if a viscosity limit can be reached. For this comparison we take again the parameters from the previous shear tests.

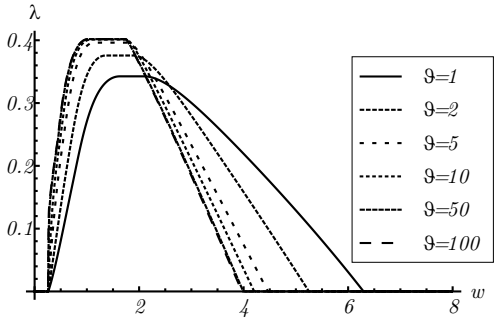

Figure 4.28.: Volume fraction of the second domain for a shear test under several pseudo-velocities.

Figure 4.28 shows the evolution of the volume fraction of the laminate for different pseudo-velocities: $\vartheta = 1$, $\vartheta = 2$, $\vartheta = 5$, $\vartheta = 10$, $\vartheta = 50$ and $\vartheta = 100$. Independent from the pseudo-velocity, the initiation of the microstructure takes place at $w = 0.3$, hence the initiation is not affected by the relaxation time. This is reasonable as the material is homogeneous up to this point. As already explained, for $\vartheta = 1$ the volume fraction of domain two increases up to 0.34, stays constant from $w = 1.6$ up to $w = 2.4$ and then decreases. The laminate vanishes at $w = 6.3$. With an increasing factor ϑ, the volume fraction increases stronger and reaches higher maximum values. The highest maximum value is achieved with $\vartheta = 100$ with $\lambda = 0.4$. The decreasing slope is also increasing with an increasing factor ϑ and therefore the laminate vanishes earlier. It is remarkable that the increase from $\vartheta = 1$ to $\vartheta = 2$ leads to a rather big change in the evolution: the maximum value for the volume fraction raises from 0.34 up to 0.37 and the microstructure finishes at $w = 5.3$ instead of $w = 6.3$. Therefore, the evolution of the volume fraction is changed quite drastically. On the other hand, the increase from $\vartheta = 50$ up to $\vartheta = 100$ only slightly influences the evolution: the maximum value $\lambda = 0.4$ and the ending point of the microstructure $w = 4$ remain nearly unchanged. This indicates that the evolution of volume fraction converges to this solution.

The evolution of plastic slip is presented in Figure 4.29.

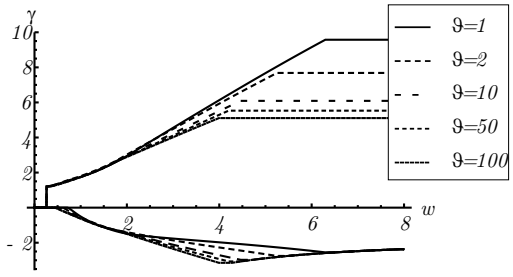

Figure 4.29.: Plastic slip in both domains for a shear test under several pseudo-velocities.

The plastic slip in domain two is just slightly affected by the factor ϑ. For every pseudo-velocity the plastic slip starts to evolve at $w = 0.3$ where the initiation of the microstructure takes place. The plastic slip of the second domain increases drastically from zero to $\gamma_2 = 1.4$

and then increases further. Starting from load $w = 2$, the slope of the plastic slip slightly depends on the factor ϑ: a smaller factor ϑ leads to a higher slope of the plastic slip of domain two. When the microstructure vanishes, the plastic slip remains constant. Since this point strongly depends on the factor ϑ (see the evolution of volume fraction in Figure 4.28), from there on the values of the plastic slip strongly depend on the factor ϑ as well. However, since from this point the corresponding volume fraction is vanished, the plastic slip of domain two is not important anymore. The onset of the plastic slip in domain one is influenced by the factor ϑ: An increasing factor leads to an earlier onset of the plastic slip, hence the delay due to the viscous contribution is reduced. Then the plastic slip decreases: the smaller the factor ϑ, the smaller the slope of the plastic slip. Once the microstructure vanishes, the evolutions of the plastic slips with different factors follow the same path. This behavior is comprehensible since the pseudo-velocity only influences the material if a microstructure is present.

The total amount of plastic slip is shown in Figure 4.30. On the left hand side of Figure 4.30 a close up of the evolution at the onset of microstructure is presented.

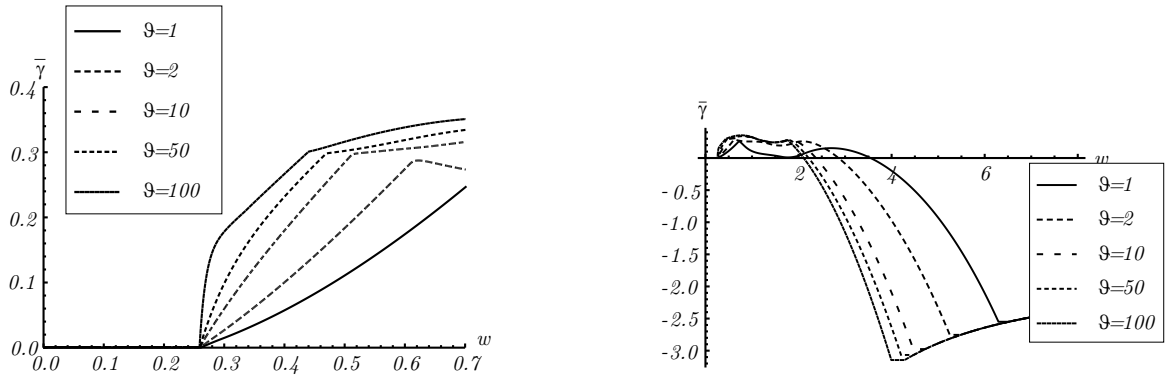

Figure 4.30.: Zoom in and total view of total amount of plastic slip for a shear test under several pseudo-velocities.

The total amount of plastic slip is calculated by $\bar{\gamma} = (1-\lambda)\gamma_1 + \lambda\gamma_2$. Since both internal variables λ and γ are affected by ϑ, the total amount of plastic slip strongly depends on the factor ϑ. Once the microstrucure is initiated, the total amount of plastic slip increases. The factor ϑ influences the slope of the total amount of plastic slip. For $\vartheta = 1$, the slope is nearly linear while for $\vartheta = 100$ the slope seems to be nearly quadratic. As already mentioned for the evolution of the volume fraction, the total amount of plastic slip converges with an increasing factor ϑ. Up to $w = 2$, a small factor leads to a smaller total amount of plastic slip. Afterward, the total amount is bigger for smaller factors. When material is homogeneous again, the total amount of plastic slip is independent from the factor ϑ which is physically consistent.

The angle of the laminate is presented in Figure 4.31.

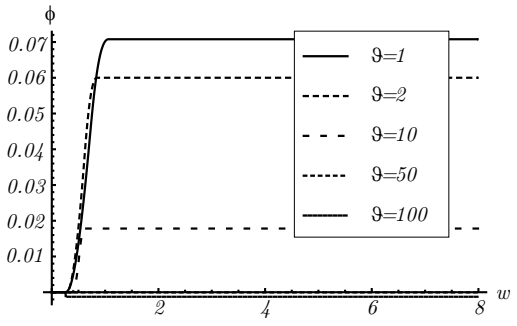

Figure 4.31.: Angle of laminate for a shear test under several pseudo- velocities.

At the onset of the lamination, the laminate rotates. For $\vartheta = 1$, the laminate rotates under the load $w = 0.3$ up to $w = 0.8$. Then the angle remains constant at $\phi = 0.072$[rad] for an increasing shear. For higher factors ϑ, the constant angle is found faster. For $\vartheta = 100$, the constant angle is directly found as $\phi = 0.0009$[rad], which is nearly zero hence no remarkable rotation takes place anymore. By reducing the pseudo-velocity, also the constant angle of the laminate decreases (from $\phi = 0.007$ [rad] at $\vartheta = 1$ to $\phi = 0.0009$ [rad] at $\vartheta = 100$).

Figure 4.32 shows the evolution of the hardening parameters p_1 and p_2 under several pseudo-velocity factors ϑ.

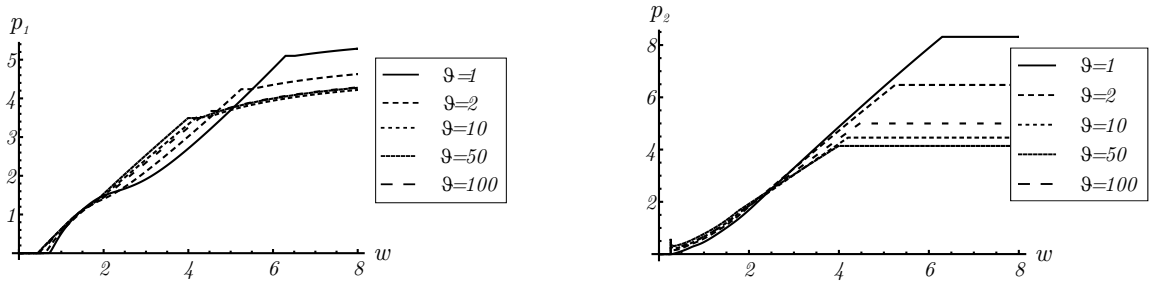

Figure 4.32.: Hardening parameters of both domains for a shear test under several pseudo-velocities.

On the left hand side of Figure 4.32, the hardening of domain one is presented and on the right hand side the hardening of domain two. The hardening in domain two is similar to the absolute values of the evolution of the plastic slip in domain two. The hardening of the first domain is also similar to the absolute amount of plastic slip in its domain up to the loading step where the microstructure is vanished again. This loading step is dependent on the pseudo- velocity, for $\vartheta = 1$ it is reached at $w = 6.3$, while employing $\vartheta = 100$ the material is homogenous again at $w = 4$. Then the hardening increases with a smaller slope linearly. The slope is independent from the pseudo velocity. Therefore, $\vartheta = 1$ leads to the biggest amount of hardening.

These microstructural changes due to the increasing pseudo-velocity influence the Cauchy stresses and the energy. In Figure 4.33 the Cauchy shear stress is presented.

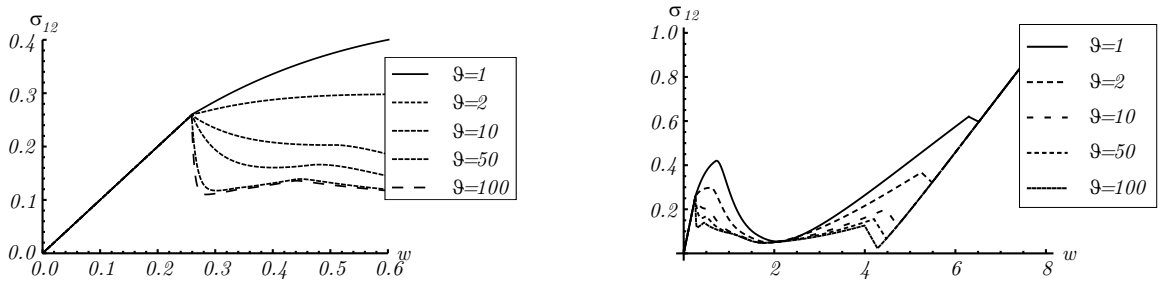

Figure 4.33.: Zoom in and total view of Cauchy shear stress for a shear test under several pseudo-velocities.

On the left hand side of Figure 4.33, a close up of the shear stress at the initiation of the microstructure is shown. First the stress behaves purely elastic, hence it is independent of the pseudo-velocity. At $w = 0.3$ the laminate is built and therefore the internal variables influence the material behavior. For $\vartheta = 1$, the stress still increases but with a lower slope. With an increasing factor, the slope is reduced and for factors bigger than 10 the stress decreases. For $\vartheta = 50$ and $\vartheta = 100$, the stress drops down from $\sigma_{12} = 0.26\,[\text{GPa}]$ to $\sigma_{12} = 0.12\,[\text{GPa}]$. Since the stress with $\vartheta = 1$ still increases after the initiation of the microstructure, the stress has a huge viscous peak in the beginning, which is already discussed in the previous section. With more relaxation time, this peak shrinks from $\sigma_{12} = 0.45\,[\text{GPa}]$ to $\sigma_{12} = 0.26\,[\text{GPa}]$. This is a reduction of 57.7 % and hints that a reduced pseudo-velocity reduces the viscous effects. The evolution of the shear stress with $\vartheta = 50$ and $\vartheta = 100$ are quite similar, therefore the evolution converges and the viscous effects cannot be reduced further. As the microstructure evolves, the stress behaves nearly constant for long relaxation times. As the laminate vanishes, viscous effects occur again, independent from the relaxation time. Afterward the material is homogeneous again, hence the evolution of the stress is again independent from the pseudo-velocity.

In Figure 4.34 the energy is presented.

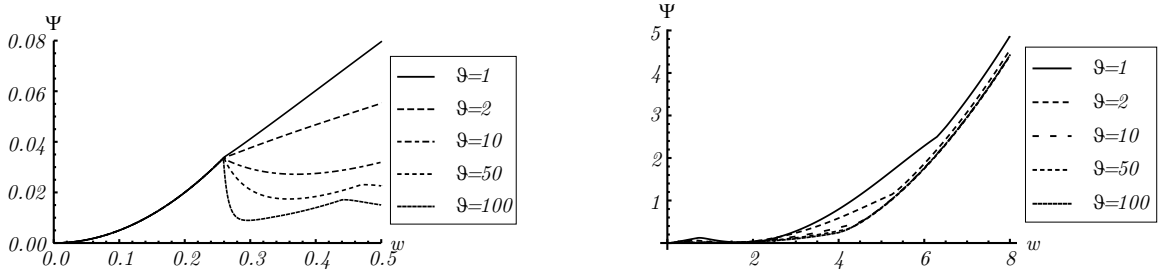

Figure 4.34.: Zoom in and total view of energy for a shear test under several pseudo-velocities.

Analogously to the behavior of the Cauchy stress, the non-convexity of the energy at the beginning of the microstructure is reduced for higher relaxation times. For high factors ϑ, the solutions converge. Aside from the non-convexity in the beginning, the energy is convex for all factors. Since the hardening parameter are influenced by the relaxation time, the amount of energy in the material is as well influenced.

Tension-Compression test with decreased pseudo-velocity

Similar to the results of the shear test, also the results of the tension-compression test are influenced by the relaxation time. Hence, analogously to the shear test, the factor of the pseudo-velocity is set from $\vartheta = 1$ to $\vartheta = 20$. Therefore, by increasing the factor, the material gets more time to relax and the viscous effects may decrease. The material parameters, the loading and the time increment are taken from the previous tension-compression test.

Figure 4.35 shows the corresponding evolution of the volume fraction with the increased factor $\vartheta = 20$.

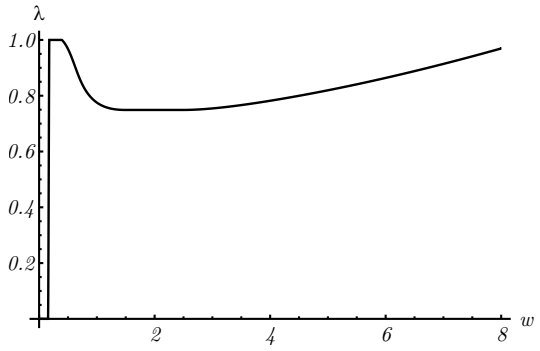

Figure 4.35.: Volume fraction of the second domain for a tension-compression test, $\vartheta = 20$.

As the pseudo-velocity does not affect the starting point of initiation, the onset of the lamination takes place again at $w = 0.16$, which is also the starting point of the microstructure with $\vartheta = 1$. However, the region where the volume fraction remains rather small is drastically reduced from $w = 0.4$ to $w = 0.28$. As explained before, in every load step, the material has more time to relax. Therefore, the viscous effects decrease and the volume fraction of the domain two λ can increase faster. Here, the volume fraction increases until $\lambda = 1$ is reached at load $w = 6$. Then the microstructure is vanished again and the material consists homogeneously of domain λ.

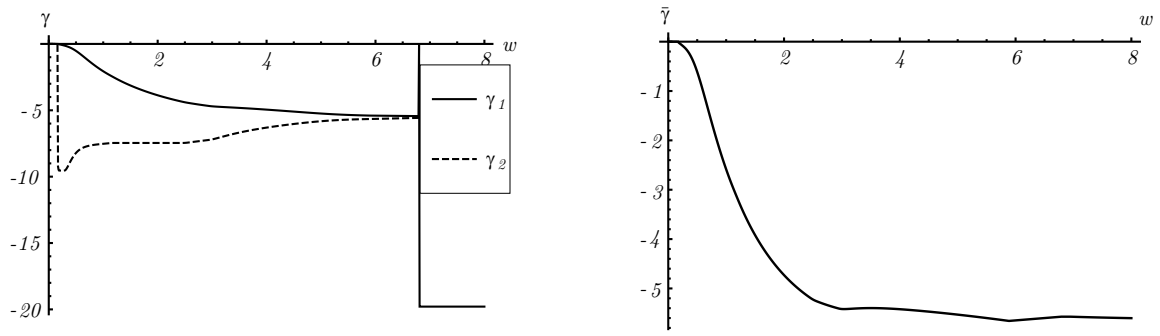

Figure 4.36.: Plastic slip in both domains and total amount of plastic slip for a tension-compression test, $\vartheta = 20$.

In Figure 4.36 the plastic slip in both domains and the total amount of plastic slip is visualized. The slope of the plastic slip in domain one (left hand side of Figure 4.36) remains nearly unchanged compared to the slope with $\vartheta = 1$, whereas the slope of the plastic slip in

domain two is smoother than before. At first glance, the drop in the plastic slip of domain one at $w = 8$ seems questionable. However, at that load, the material consists only of λ, thus domain one does not exist anymore so this jump is rather a numerical artifact. This can be also verified by the plot of the total amount of plastic slip (right-hand side) which proves that the total amount of plastic slip is smooth and limited at any load step.

Figure 4.37 presents the angle and the hardening parameters of the laminate.

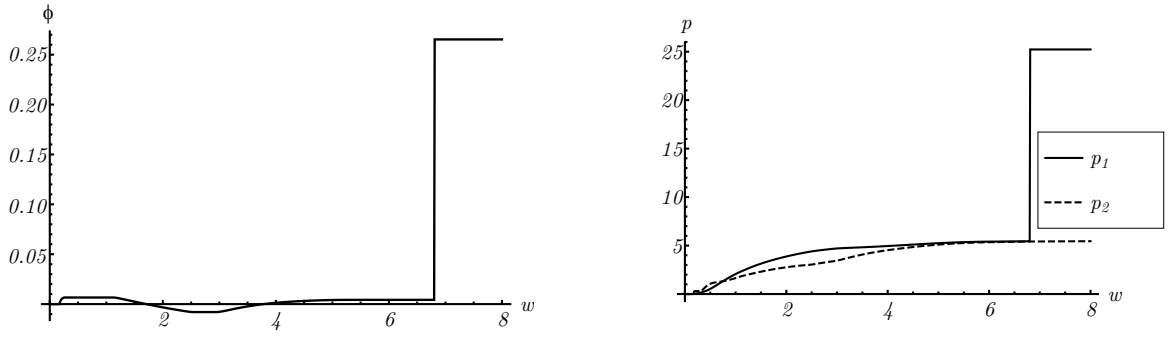

Figure 4.37.: Angle of the laminate and hardening in both domains for a tension-compression test, $\vartheta = 20$.

After the initiation, the angle of the laminate reaches a constant value $\phi = 0.007$ [rad] for loads between $w = 0.15$ and $w = 1.8$. Subsequently, the laminate rotates again to $\phi = -0.008$ [rad]. From $w = 2.2$ up to $w = 2.5$ the laminate stays constant under this angle. Then it rotates to a constant angle of $\phi = 0.005$ [rad]. Altogether, the angle remains again rather small and the rotation is reduced. At $w = 7$, the angle jumps to a relatively large value. However, because the laminate has already vanished at this load step, this is again a numerical artifact. Comparable to the previous examples, the hardening parameters correspond to the absolute values of the plastic slip in the corresponding domains.

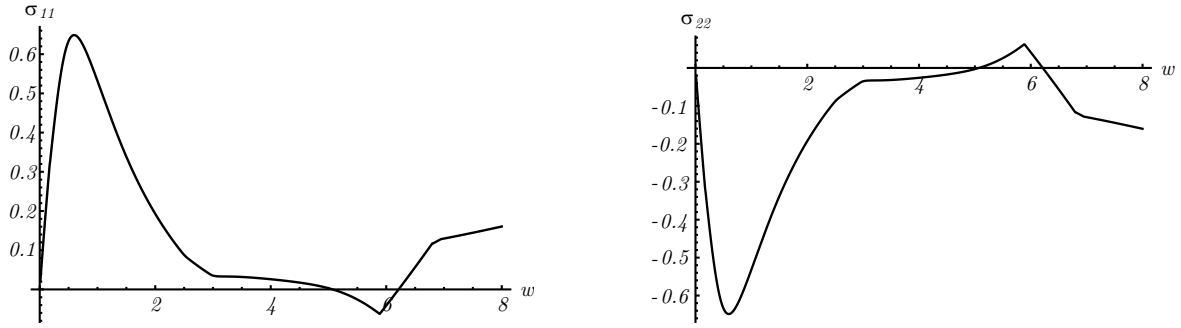

Figure 4.38.: Cauchy normal stresses for a tension-compression test, $\vartheta = 20$.

The Cauchy normal stresses are plotted in Figure 4.38. As a first impression, the viscous peaks at the onset of the microstructure still seem to be quite high, but in fact they are now drastically reduced. In the previous tension-compression test with the factor $\vartheta = 1$, the peak in σ_{11} is 1.4 [GPa], whereas for the slower loading velocity ($\vartheta = 20$) the peak ranges only up to 0.65 [GPa]. Hence, the peak is reduced by more than about 45% due to more relaxation time. The height of the peak is also reduced: it is present until $w = 4$ for fast loading, whereas it has already dropped at $w = 3$ for slow loading. In this example, the laminate vanishes at

the ending of the microstructure, which means that the viscous effects occur again before the material behaves homogeneous. Thus, a small stress drop occurs then.

The last result of this tension-compression test is the energy which is shown in Fig. 4.39, the dashed curve represents the unrelaxed solution.

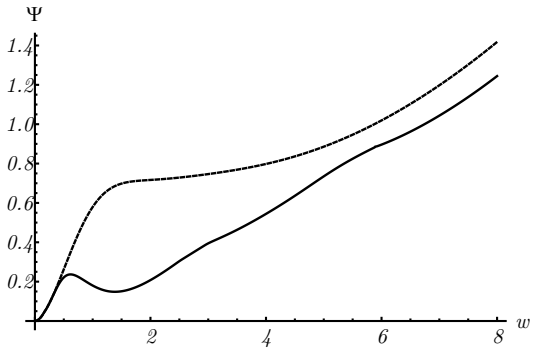

Figure 4.39.: Comparison of relaxed and unrelaxed energy for a tension-compression test, $\vartheta = 20$.

At the onset of lamination, a non-convexity in the relaxed energy curve still occurs due to viscous effects. However, similar to the behavior of the stresses, the height is reduced by about 45 % and the relaxed energy lies always under the unrelaxed one.

Varying pseudo-velocities for a tension-compression test

In this section, we investigate the influence of a decreasing the pseudo-velocity for the tension-compression test. For this comparison the material constants are taken again from the previous tension-compression test. The evolution of the microstructure for the pseudo-velocity factors $\vartheta = 1$, $\vartheta = 2$, $\vartheta = 10$, $\vartheta = 50$ and $\vartheta = 100$ is investigated.

In Figure 4.40 the evolution of the volume fraction of domain two for several pseudo-velocities is presented.

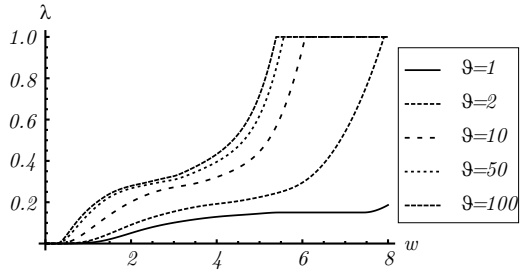

Figure 4.40.: Volume fraction of the second domain for a tension-compression test under several pseudo-velocities.

Similar to the shear test, the onset of the lamination is independent from the pseudo-velocity and takes place at $w = 0.2$. For $\vartheta = 1$, the evolution of the volume fraction is delayed: after

the onset the volume remains rather small, as presented in the previous section. Then the volume fraction increases with a small slope up to $\lambda = 0.2$ and then remains nearly constant. For the factor $\vartheta = 2$ the volume fraction also remains small in the beginning, but it starts to evolve earlier and with a stronger slope. From $w = 6.5$ the volume fraction increases drastically from $\lambda = 0.3$ up to $\lambda = 1$ at $w = 7.5$. Then the material only consists of domain 2, hence the material is homogenous again. With an increasing factor ϑ, the volume fraction evolves faster and $\lambda = 1$ is reached earlier. By decreasing the pseudo-velocity, the evolution of the volume fraction tends asymptotically to one solution. Since the evolution for $\vartheta = 50$ and $\vartheta = 100$ still differ, a higher factor may reduce the viscous effects further.

The evolution of the plastic slip in both domains under different pseudo-velocities is shown in Figure 4.41.

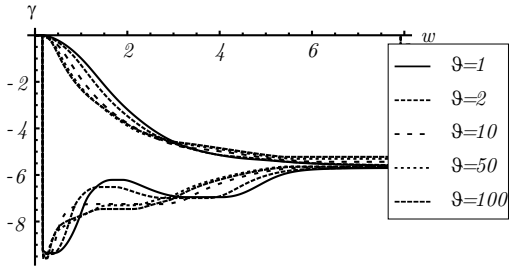

Figure 4.41.: Plastic slip in both domains for a tension-compression test under several pseudo- velocities.

At the onset of the lamination, independent from the pseudo-velocities, the plastic slip of domain two decreases rapidly to $\gamma_2 = -9.5$ and then increases with a rather small slope up to $\gamma_2 = -6$ at $w = 6$ and remains constant from there on. For loading steps $w < 6$, the evolution varies for different factors ϑ, afterwards the are no significant differences. The plastic slip of both domains asymptotically approach to each other. Hence, analogously to the results of the shear test, the evolution of plastic slip for a tension-compression test is not seriously affected by the pseudo-velocity compared to the evolution of the volume fraction.

The rotation of the laminate, represented by the angle, is presented in Figure 4.42.

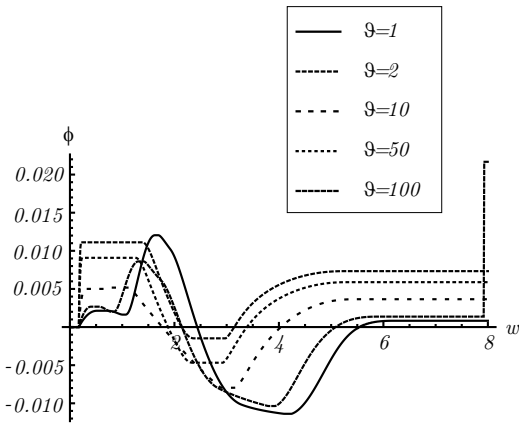

Figure 4.42.: Angle of laminate for a tension-compression test under several pseudo-velocities.

The laminate rotates in a very small range of 0.03 [rad], hence the angle is nearly zero for all relaxation times. For $\vartheta = 1$, the laminate rotates quite often, as already described in the previous section.With decreasing the pseudo-velocity, the laminate does not need to rotate such often, it seems to be stabilized. The constant angle for high loading depends on the pseudo-velocity: the higher the factor ϑ, the bigger the angle.

The remaining internal variable which characterizes the state of the microstructure is the hardening which is visualized in Figure 4.43.

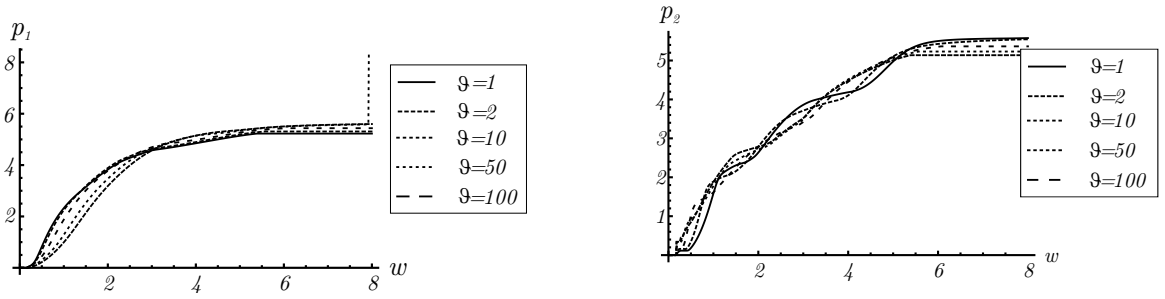

Figure 4.43.: Hardening parameters of both domains for a tension-compression test under several pseudo- velocities.

Similar to the results of the shear test, a decrease of the pseudo- velocity just slightly affects the evolution of the hardening in both domains. The hardening of both domains increases monotonously and nearly reaches 6.

In Figure 4.44 the Cauchy normal stress σ_{22} is presented. The evolution of the normal stress σ_{11} is correspondingly simply mirrored at the abscissa.

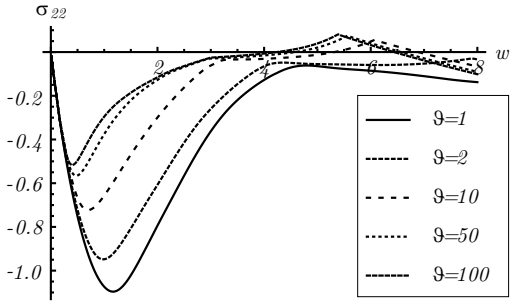

Figure 4.44.: Cauchy normal stress for a tension-compression test under several pseudo-velocities.

For factor $\vartheta = 1$, the normal stress decreases to -1.1 [GPa] at $w = 1.5$. Then the stress increases up to -0.1 [GPa] at $w = 5$. Therefore the stress has a big peak due to a viscous effect which is already discussed before. With an increasing pseudo-velocity factor this peak is reduced, for $\vartheta = 100$, the height of the peak is reduced to -0.5 [GPa] and the width to $w = 3$, hence the height of this peak is reduced more than 45 % and the width is reduced up to 60 %. As already explained in the previous examples, the viscous part in the dissipation is responsible for this big peak in the stress. With an increasing factor ϑ (and a decreasing pseudo-velocity) the material has time to relax and the viscous effects decrease. In this

example, a higher factor $\vartheta > 100$ may still change the evolution of the internal variables, hence the viscous peak may be reduced further.

The evolution of the energy, shown in Figure 4.45, is also strongly influenced by the state of the microstructure, hence of the relaxation time.

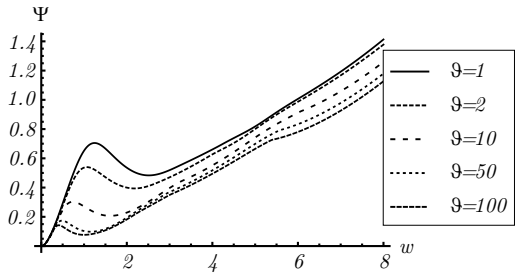

Figure 4.45.: Energy for a tension-compression test under several pseudo-velocities.

Similar to the evolution of the normal stress, the evolution of the energy is not convex due to viscous effects. However with an increasing factor ϑ, this peak is reduced. Comparing the peak with $\vartheta = 1$ and $\vartheta = 100$, the peak is reduced in its height up to 20 % (from 0.75 to 0.15) and in its width up to 40 % ($w = 2.5$ to $w = 1$). Aside this viscous peak, which is reduced by a decreased pseudo-velocity, the energy is lower with a decreased pseudo-velocity, because for higher relaxation times more energy is dissipated.

4.5.4. Comparison to the results of the rate independent model

This outlined numerical scheme is based on a modification of the model of D.Kochmann and K.Hackl by introducing a viscous contribution to the dissipation potential. Therefore, a comparison of the numerical results of both approaches is interesting. The fundamentals, the numerical scheme and the results of the rate independent model of D.Kochmann and K. Hackl are presented in [48] and [47]. In [48], the numerical scheme is applied to a shear and a tension-compression test. For the comparison, these tests are performed with the here outlined model taking the same material data and compared to the results in [48]. The results of the rate independent model are taken from [48] and reprinted with permission. The here presented model is also referred as the modified model in the following section. As integration scheme for obtaining the internal variables of the new time step, the second order Runge-Kutta method is used.

Comparison of a shear test

The applied load is given by Equation (4.88) and illustrated in Figure 4.8. The slip system is considered under an angle of 135°, as material data $\mu = 2\,[\text{GPa}]$, $r = 0.001\,[\text{GPa}]$ and $\kappa = 0.1\,[\text{GPa}]$ are taken according to [48]. For the modified model, the viscous parameters are chosen as $\delta = 0.1r$ and $s = 0.01r$, like in the previous examples. In order to reduce viscous effects, the relaxation time is increased, hence $\vartheta = 10$.

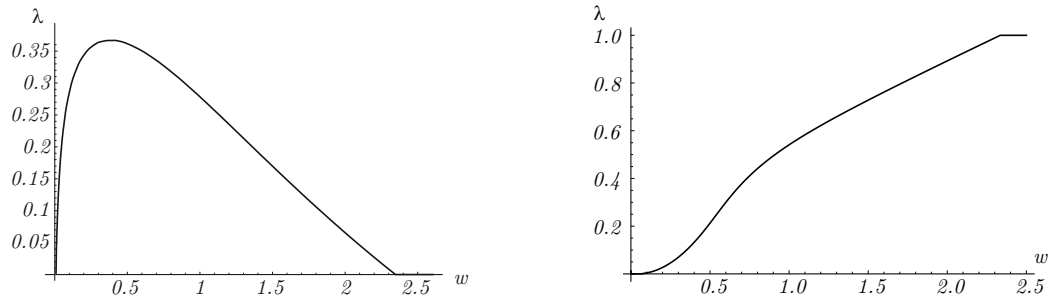

Figure 4.46.: Evolution of volume fraction of the second domain of a shear test, a with the rate independent model presented in [48], b with the modified approach, reprinted from [29].

In Figure 4.46, the evolution of the volume fraction of domain two is presented. On the left side, the result is obtained with the rate independent model of Kochmann and Hackl. The volume fraction of the second domain begins almost directly to evolve and reaches a maximum value of $\lambda = 0.36$ at $w = 0.4$. Then the volume fraction decreases again until $\lambda = 0$ at $w = 2.35$, from thereon the material is homogeneous again. On the right-hand side of Figure 4.46, the volume fraction of the arising second domain with the here presented modified model is shown. When the material is loaded, at first there is no evolving microstructure: lamination will set in only when the energy looses its ellipticity. Here, this is the case at approximately $w = 0.10$ when the volume fraction of domain two starts to evolve. Therefore in comparison to the rate independent model, the initiation is delayed. At approximately $w = 2.35$, a uniform microstructure has established that only consists of the second domain of the laminate. Thus, both models lead to a homogeneous material for higher loadings (at $w = 2.35$ for the rate independent model and $w = 2.45$ for the modified model).

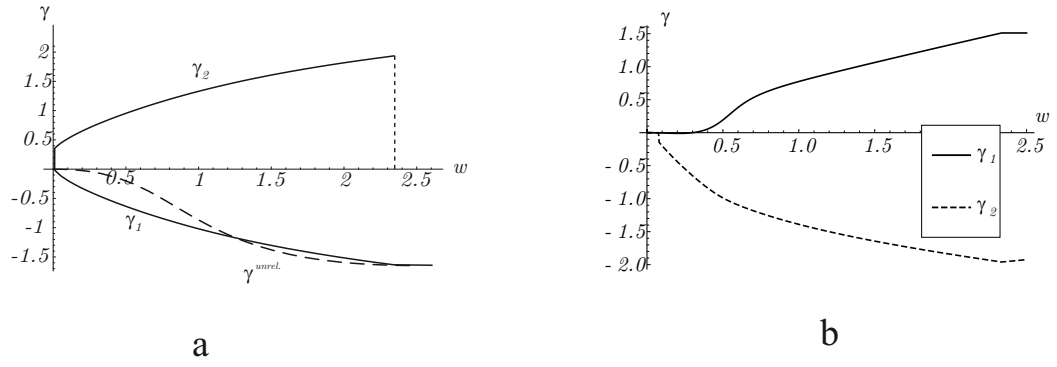

Figure 4.47.: Evolution of plastic slips in both domains of a shear test, a with the rate independent model presented in [48], b with the modified approach, reprinted from [29].

Simultaneously to the evolution of the volume fraction, plastic slip evolves in both domains of the laminate for the rate independent approach (both approaches are shown in 4.47). The plastic slip in domain one decreases from zero to $\gamma_1 = -1.6$. The plastic slip in domain two jumps to $\gamma_2 = 0.4$ and then increases further to $\gamma_2 = 2$. For the modified model, the evolution of the plastic slip in domain one is drastically delayed due to the viscous effects and starts at

$w = 0.35$. Thereafter the plastic slip increases to $\gamma_2 = 1.4$, then the material consists only of the first domain. Except the delay at the onset of the microstructure, the values of the plastic slip of the first domain correspond to the absolute values resulting for the rate independent model, only the sign differs. The plastic slip in domain two is negative and jumps from zero to $\gamma_2 = -0.15$. During further loading, its absolute value increases slowly to $|\gamma_2| = 1.9$, which is again similar to the absolute value of the results of the rate independent model.

Already slight differences in the microstructure influence the stress to a large extend. In Figure 4.48 the Cauchy shear stresses are presented, the results of the rate independent approach are again shown on the left hand and the result with the here derived modified model on the right hand side.

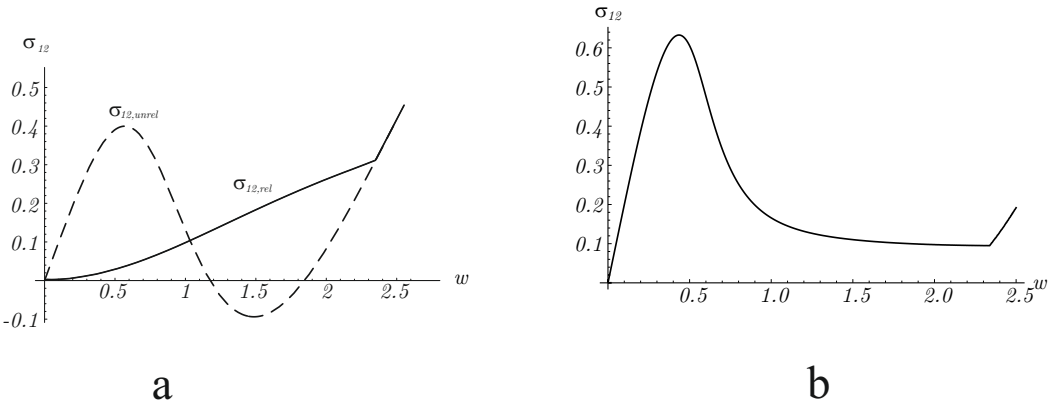

Figure 4.48.: Cauchy shear stress of a shear test, a with the rate independent model presented in [48], b with the modified approach, reprinted from [29].

For the rate independent model, while the microstructure evolves the resulting stress increases slowly due to the hardening. When the material is homogeneous again, the stress increases with a stronger slope. On the right hand side, the stresses of the here derived approach are presented: Due to the non-linear neo-Hookean energy, the stress increases non-linearly during the first part of the shearing, as already explained for the previous shear test. The slope of the stress is reduced even more when the first domain of the laminate is established (in which plastic slip is present). When the plastic slip also evolves in domain one (which has the larger contribution to the material), this has a strong impact on the stresses: they drop quite drastically. Afterwards, a Maxwell line can be easily identified. At a loading larger than $w > 2.35$, the material is homogeneous again, thus the Maxwell line is left and stresses start to increase again. Summarized, even the plastic slips in both models are similar to each other, the evolutions of the shear stresses for the two models are not comparable, as the precise values of the microstructure have a great impact.

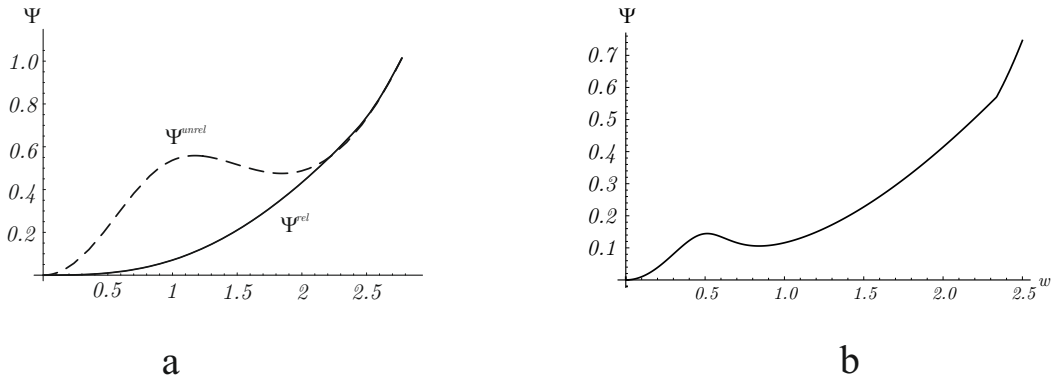

Figure 4.49.: Energy of a shear test, a with the rate independent model presented in [48], b with the modified approach, reprinted from [29].

The energies of the shear tests are presented in Figure 4.49. The energy for the rate independent model (left hand side of Fig. 4.49) is convex. Due to the viscous delay of the microstructure, the energy for the modified model (right hand side of Fig.4.49) still exhibits a non convexity at the onset and the ending of the microstructure. In addition, the energy obtained by the modified model is smaller than for the rate independent one, which is physically sound due to the viscous extension of the dissipation functional.

The next presented comparison is a tension-compression test, such as that depicted in Figure 4.16. We choose a slip system with an angle of $\alpha = 70°$ according to [48]. Furthermore, we use the same material constants as in the previous example, except of $\kappa = 0.01$ which is, again, chosen in analogy to [48]. For the here derived modified model, the relaxation time is increased again, hence $\vartheta = 10$.

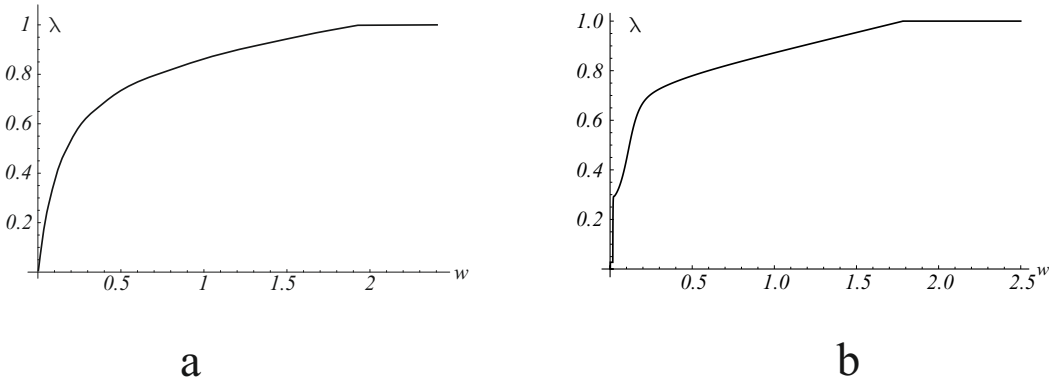

Figure 4.50.: Evolution of volume fraction of the second domain of a tension compression test, a with the rate independent model presented in [48], b with the modified approach, reprinted from [29].

Figure 4.50 shows on the left-hand side the evolution of the volume fraction of the second domain occurring due to the rate independent model from Kochmann and Hackl and on the right-hand side due to the here outlined model. Both evolutions have similar characteristics: directly at the onset of loading the material forms a microstructure. The second domain is formed and increases to one (rate independent model at $w = 1.9$ and modified model

at $w = 1.8$), then the material is completely transformed and consists homogeneously of domain two. Slight differences appear in the slope: the slope for the rate independent model is smooth while for the modified model the volume fraction increases rapidly up to a value of 30% before the slope is less pronounced.

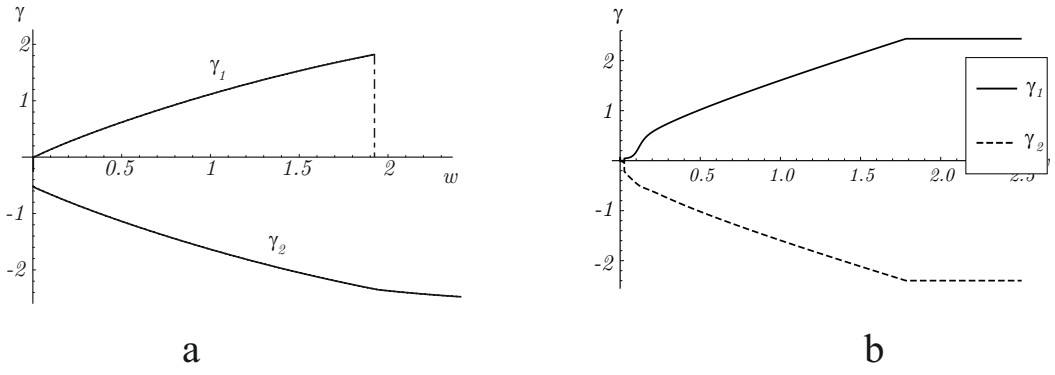

Figure 4.51.: Evolution of plastic slips in both domains of a stension compression test, a with the rate independent model presented in [48], b with the modified approach, reprinted from [29].

The evolutions of the plastic slips are presented in Figure 4.51, again on the left-hand side the results of the rate independent model and on the right side of the modified model. The plastic slip in domain one for to the rate independent model increases from zero to $\gamma_1 = 2$, then the material only consists of the second domain. Meanwhile the plastic slip in domain one of the modified model is delayed and then increases to $\gamma_1 = 2.5$, from thereon the plastic slip remains constant as the corresponding domain is vanished. For the rate independent model the plastic slip of domain two has a huge jump in the beginning: from zero to $\gamma_2 = -0.55$. Afterwards the plastic slip decreases further to $\gamma_2 = -2.4$. In the modified model the plastic slip of the second domain decreases from zero to -0.15. The plastic slip then decreases further to $\gamma_2 = -2.00$ until the microstructure vanishes. In the modified model, the plastic slips in both domains have similar absolute values, only their sign differs.

These microstructures strongly influence the resulting Cauchy normal stresses, which are shown for both approaches in Figure 4.52.

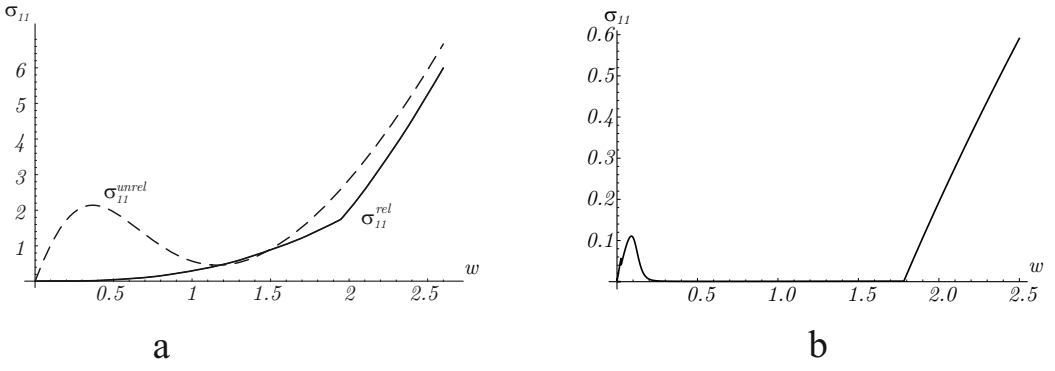

Figure 4.52.: Cauchy normal stress of a tension compression test, a with the rate independent model presented in [48], b with the modified approach, reprinted from [29].

For the rate independent approach, the normal stress σ_{11} increases slowly due to the hardening while the microstructure evolves. When the material is homogeneous again, the stress slope increases. During the first loading steps, the normal stress of the here presented model increases up to a maximum value of 0.12 [GPa]. Due to the viscous contribution, the volume fraction of domain two is negligible. Thus, even there is an amount of plastic slip in domain two, the total amount of plastic slip is too small to decrease the stress. With the increase of volume fraction and the plastic slip in domain one, the stress drops drastically to $\sigma_{11} = 0.0$ [GPa] and then remains constant. Therefore, in contrast to the rate independent model, no global hardening effect occurs. However, the hardening constitutes as an "inner" hardening in each laminate, since the plastic slip is identical in both domains, except of the sign. Therefore, a "global" hardening effect is removed (see also Equation (4.42)).

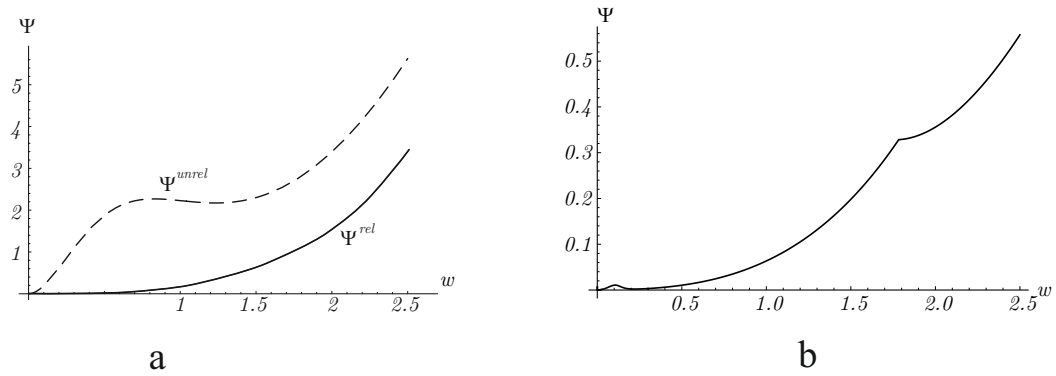

Figure 4.53.: Energy of a tension compression test, a with the rate independent model presented in [48], b with the modified approach, reprinted from [29].

Figure 4.53 presents the energy of this tension-compression test for the rate independent (left-hand side) and for the modified model (right hand side). While the energy of the rate independent model is again convex, the energy of the here outlined model exhibits still a small non convexity due to the delay of the microstructure. Before the microstructure can minimize the energy, the viscous effects occur again. First, while the laminate evolves, it is still not adapted to the external loading, hence the energy is not minimized and increases. Again, as the dissipation of the modified model is higher, the energy of the material is smaller compared to the rate independent model.

4.5.5. Cycling tests

Cycling of a shear test

The material behavior due to loading is already discussed in the previous section. Since the behavior at unloading is also interesting, one load cycle will be performed, hence loading and unloading is investigated in this section. Afterwards more than one load cycle is examined. In order to decrease the effect of hardening, we examine the model with linear hardening, hence $\alpha = 2$ and for the shear test, the hardening modulus reduced to $\kappa = 0.0001$ [GPa]. The other material constants are taken from the shear test of the previous example. The factor for the pseudo-velocity is set to $\vartheta = 100$, thus the viscous effects stay minimal.

On the left hand side of Figure 4.54 the loading path for one load cycle is illustrated. The material is loaded from zero to $w = 4$. Then the material is unloaded until w is zero again.

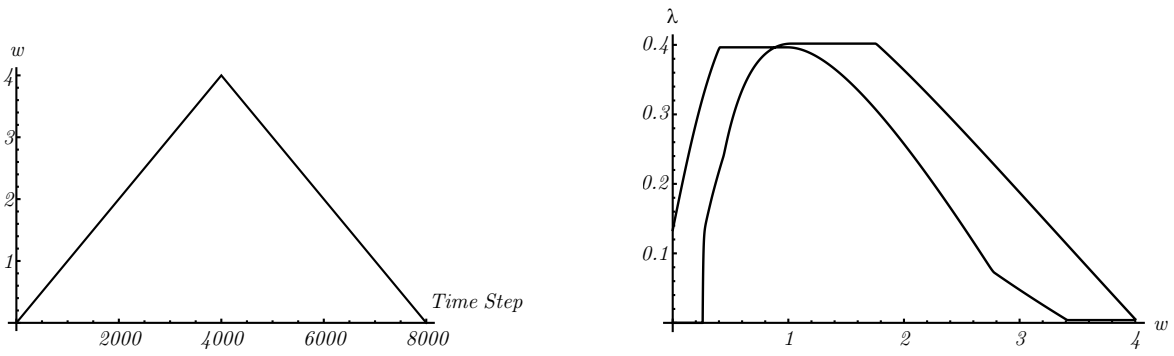

Figure 4.54.: Load cycle of a shear test and corresponding evolution of volume fraction of the second domain.

The right hand side of Figure 4.54 presents the resulting volume fraction of the laminate which evolves under this load cycle. The behavior of the material at loading is already discussed in the previous section: When energetically favorable, a second domain with the volume λ is built. The volume of the domain increases up to 40 % of the total volume. After remaining constant the volume of domain two decreases to zero. While the material is unloaded, from $w = 4$ up to $w = 3.5$ the material stays homogeneous. Afterwards the microstructure is established again and the volume fraction of domain two increases again. From $w = 2.8$, the slope of the volume fraction increases. The volume fraction increases until the maximum value 4 is achieved again, from thereon it remains constant up to $w = 0.4$ then it starts to shrink. At zero loading the microstructure is not vanished but remains in the material with a small volume fraction ($\lambda = 0.15$) of the second domain.

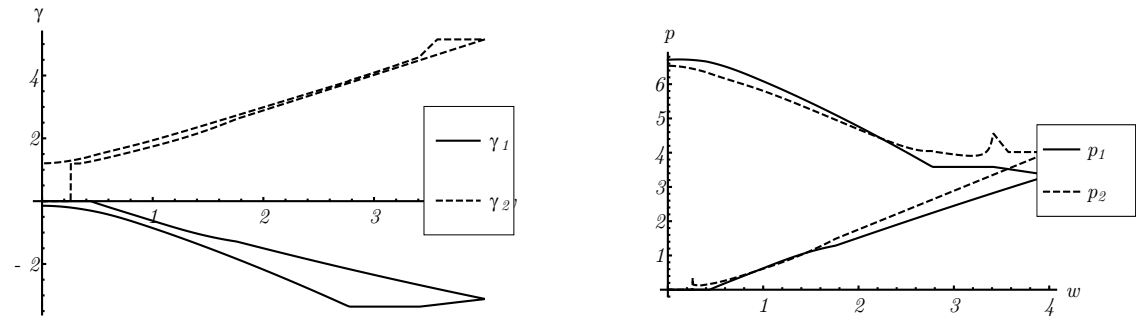

Figure 4.55.: Plastic slip and hardening in both domains for one shear load cycle.

The plastic slip in both domains for one load cycle is shown on the left hand side of Figure 4.55. The evolution of these variables under loading is already discussed. At the beginning of unloading, a kink in the plastic slip of domain two appears. This kink is negligible since from $w = 4$ to $w = 3.5$ the volume fraction λ of domain two is zero and the material only consists of domain one. Then the plastic slip of the second domain decreases with the same slope as for loading. For zero loading the remaining plastic slip is $\gamma_2 = 1.25$. This value equals the huge increase of plastic slip at the onset of the lamination at loading, for zero loading this value is more energetically favorable than zero. At unloading the plastic slip of domain one first slightly decreases (when the material is homogeneous) then it remains constant at $\gamma_1 = -2.4$ up to $w = 2.8$. Afterwards the plastic slip increases to nearly zero.

The hardening parameters are presented on the right hand side of Figure 4.55. The hardening

increases for both domains for loading and for unloading nearly linear with a similar slope as the absolute values of the corresponding plastic slip. The small kink in the hardening of domain 2 at the beginning of the unloading is a result of the kink in the corresponding plastic slip. Since the hardening increases also for unloading, a huge amount of hardening is introduced into the material after one load cycle.

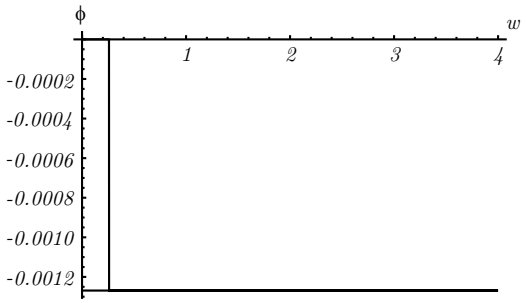

Figure 4.56.: Angle of the laminate for one shear load cycle.

In Figure 4.56 the angle of the laminate is presented. For this load cycle, the laminate does not need to rotate, neither for loading nor for unloading. Once after the initiation, the angle is found and stays constant as nearly zero.

This established microstructure strongly influences the behavior of the stress and the energy, which are both presented in Figure 4.57.

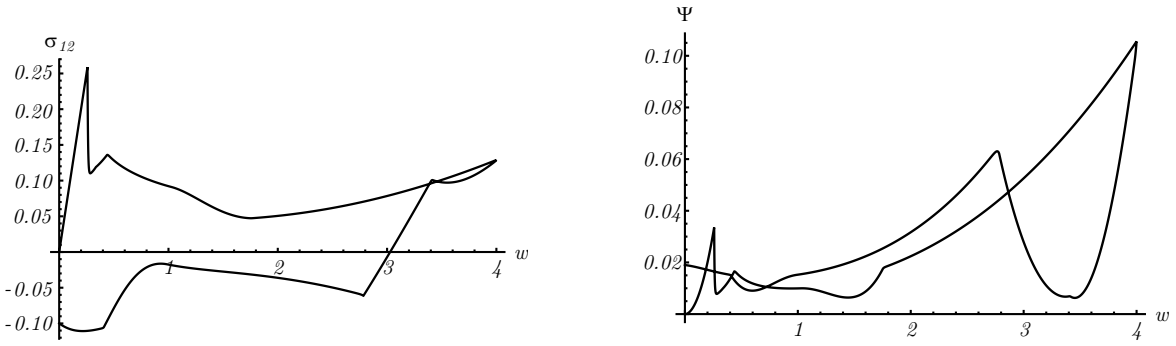

Figure 4.57.: Cauchy shear stress and energy for one shear load cycle.

Due to already discussed viscous effects, the shear stress (left side) has a huge peak at the onset of the microstructure for loading. Then the stress strain curve correlates to a plateau. At the beginning of unloading, while material remains homogeneous, the stress follows for a short loading period the same path as for loading. This effect is again caused by the viscous contribution: at loading the laminate is vanished, but the viscous effects have to be vanished as well. Afterwards the stress decreases linearly and the material is unloaded elastically. As the microstructure evolves, the stress remains nearly constant. At $w = 2.8$, the slope of the volume fraction changes, as a result, the slope of the stress is decreased. Altogether, for one load cycle the stress strain curve exhibits a hysteresis loop.

The energy (right side of Figure 4.57) has a peak due to the viscous effect at the onset of the lamination. Then it increases monotonously. At the beginning of unloading (from $w = 4$ to

$w = 3.5$), the energy decreases strongly. As the microstructure is established to minimize the energy, viscous effects occur again and result a peak in the energy. Afterwards the energy decreases monotonously. All in all, viscous effects occur at the onsets of the microstructure, hence at loading and unloading.

For two load cycles (left hand side of Figure 4.58), the corresponding evolution of the volume fraction is presented in Figure 4.58.

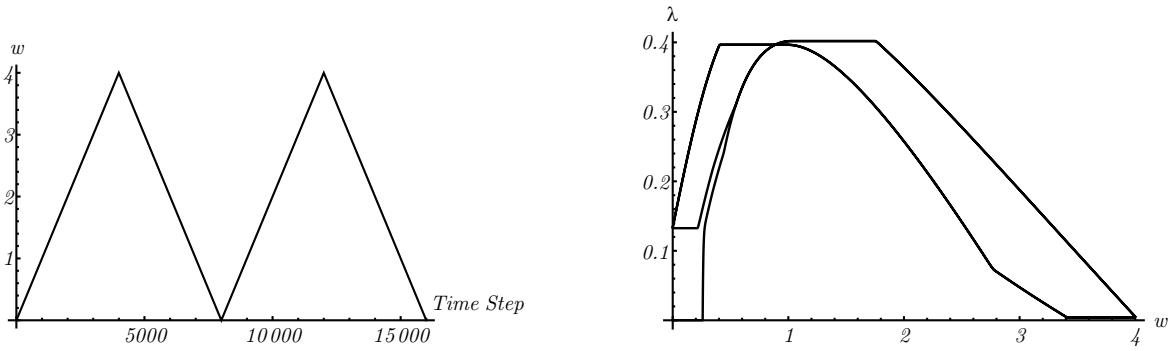

Figure 4.58.: Loading path for two load cycles of shear and corresponding evolution of volume fraction of domain two.

At the end of the first load cycle, a small second domain of the laminate still exists. At the second loading path the volume fraction first remains constant up to $w = 0.2$. As the load reaches the value where the initiation of the microstructure takes place in the first cycle, the volume fraction starts to increase again, following the same path as in the first cycle. Therefore the only difference between the evolution in both cycles is the remaining volume fraction at loading from zero loading up to the initiation of the microstructure in the first cycle.

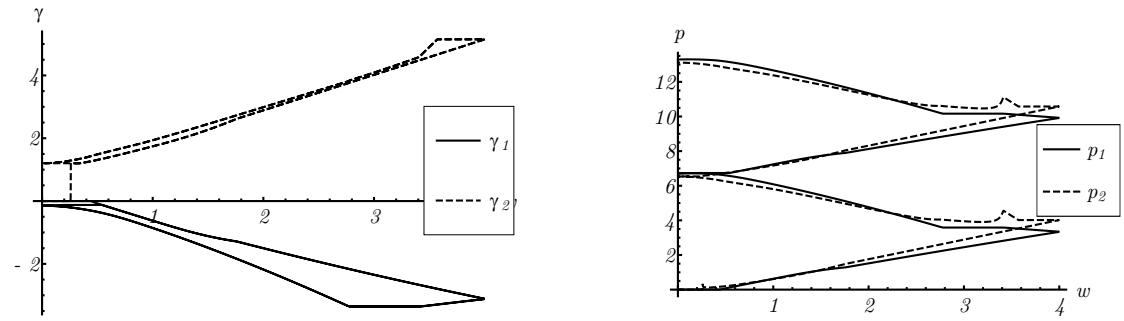

Figure 4.59.: Plastic slip and hardening in both domains two shear load cycles.

The plastic slip (left side of Figure 4.59) of both domains evolves for both cycles similar. The only difference appears, similar to the evolution of the volume fraction, in the evolution of the plastic slip in domain two in the range between zero loading and the loading when the microstructure is established in the first cycle: Instead of a huge increase (from zero to 1.3), like in the first cycle, the plastic slip in the second cycle starts from $\gamma_2 = 1.3$, which seems to be energetically favorable. The hardening parameters (right side of Figure 4.59) increase in the second cycle further in the same manner as in the first cycle. The values of the hardening

parameters reach already quite high values, therefore the influence of the hardening has to be reduced by choosing linear hardening and a decreased hardening modulus for this cycling test.

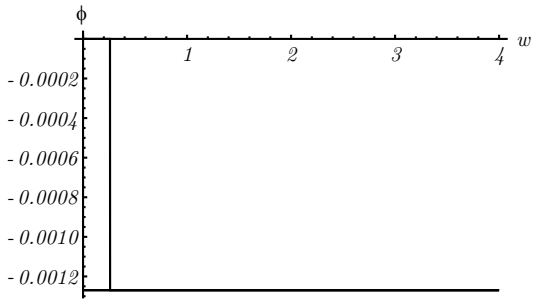

Figure 4.60.: Angle of laminate for two shear load cycles.

Again, also for the second load cycle, the laminate does not need to rotate: once the angle (Figure 4.60) is found, it remains constant, also for the second cycle.

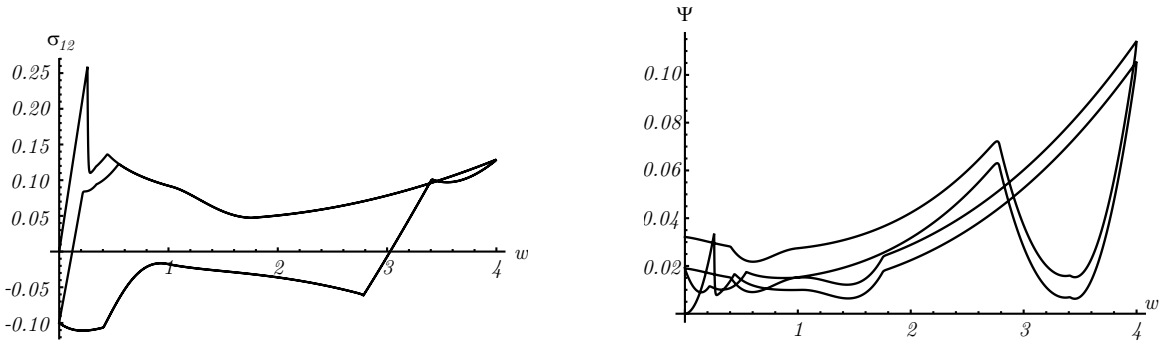

Figure 4.61.: Cauchy shear stress and energy for two shear load cycles.

The most distinct changes in the internal variables for the second cycles appear in the beginning of the second cycle. The energetically favorable microstructure remains in the material. Therefore the evolution of the stress (left hand side of Figure 4.61) in the second cycle is quite similar to the first cycle, the only differences are observed in the beginning of the second cycle. There, the plastic slip does not need to increase to a certain value in order to minimize the energy and the volume fraction starts from a value which is energetically favorable instead of zero, hence the viscous peak in the stress is smoothed. Analogously the peak in the beginning of the evolution of the energy (right hand side of Figure 4.61) is vanished for the second load cycle. At the beginning of unloading, the microstructure has to initiate again. Therefore a viscous peak occurs there again. Due to the increasing hardening parameters, the material becomes ”stiffer” in the second load cycle, therefore the evolution of the energy is shifted vertically.

Loading the material with three load cycles, like illustrated on the left side of Figure 4.62, the internal variables evolve for the third cycle similar to the second cycle.

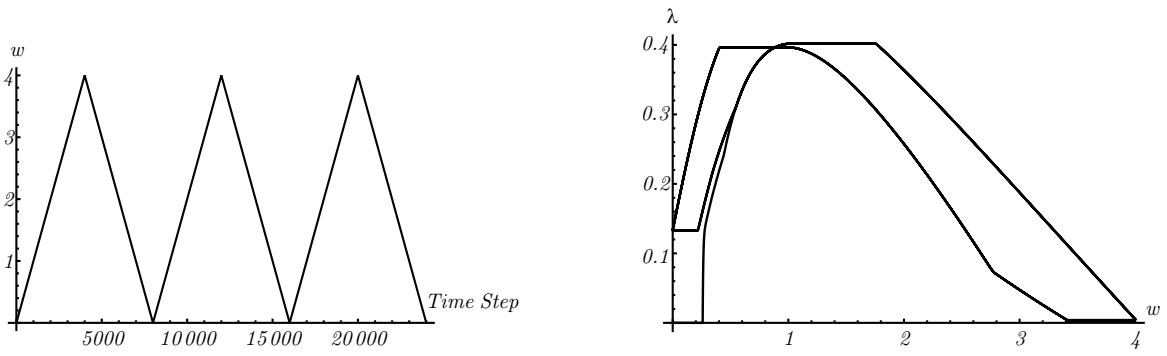

Figure 4.62.: Three load cycle of shear and corresponding evolution of volume fraction of domain two.

The evolution for volume fraction of the second domain (right hand side of Figure 4.62) in the third load cycle is completely similar to the evolution in the second load cycle.

Also the plastic slip (left hand side of Figure 4.63) evolves in the third cycle completely similar to the second cycle. The only remarkable differences in the evolution of internal variables occur in the evolution of the hardening parameters (left hand side of Figure 4.63). In the third cycle, they increase further, hence that the material becomes even stiffer.

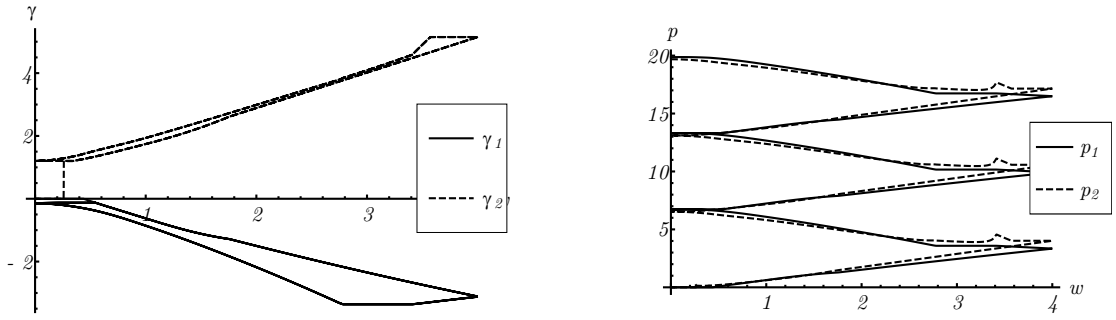

Figure 4.63.: Plastic slip and hardening in both domains for three shear load cycles.

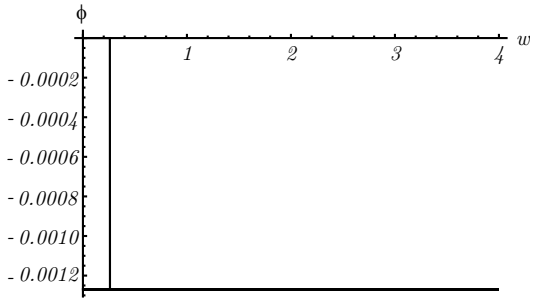

Figure 4.64.: Angle of the laminate for three shear load cycles.

As most of the internal variables do not change in the third cycle compared to the second one, also the shear stress (left hand of Figure 4.65) in the third cycle is similar to the second one. Due to the increasing hardening parameters, the material becomes stiffer and the energy increases, hence the energy curve (right hand of Figure 4.65) is again shifted vertically.

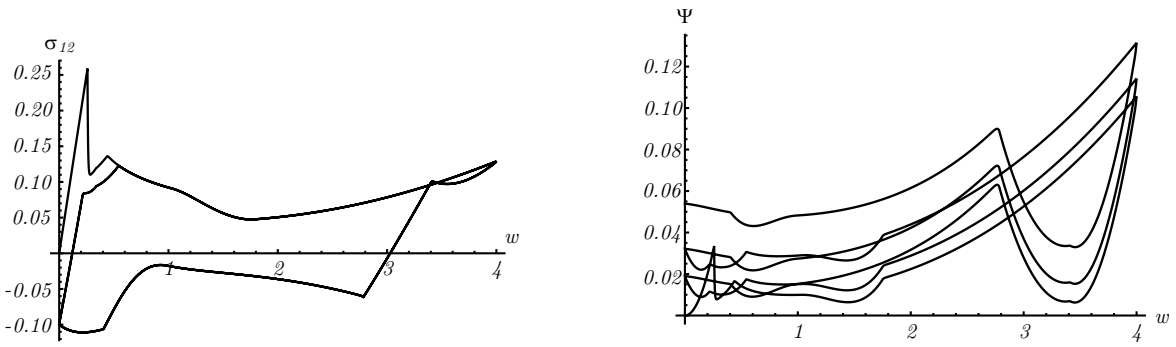

Figure 4.65.: Cauchy shear stress and energy for three shear load cycles.

Cycling of a tension-compression test

As a second example of loading and unloading, a tension-compression test is performed. Similar to the cyclic loading of the shear test, linear hardening is considered and the hardening modulus is decreased to $\kappa = 0.00001$ [GPa]. The viscous parameters are considered as $s = 0.001r$ and $\delta = 0.1r$.

For one load cycle (load cycle is shown on the left side of Figure 4.66), the evolution of the volume fraction of the second domain is presented on the right hand side of Figure 4.66.

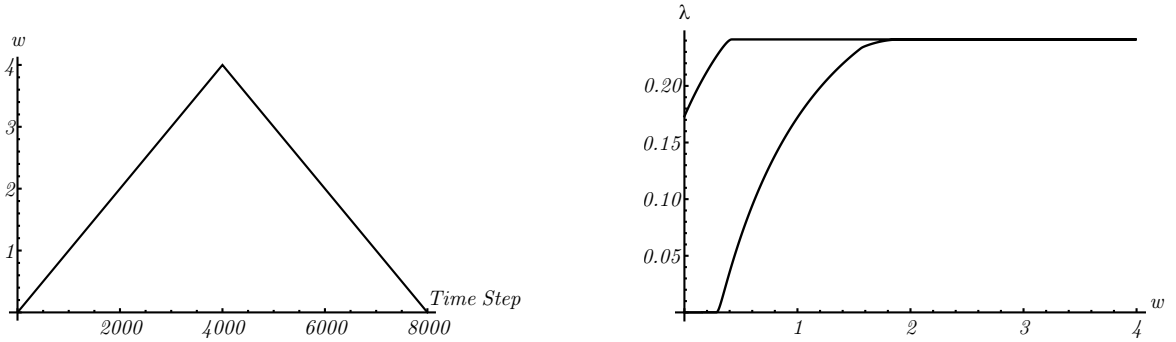

Figure 4.66.: One load cycle of tension-compression and corresponding evolution of volume fraction of domain two.

At loading, up to $w = 0.3$ the material is homogeneous. Afterwards a second domain with the volume fraction λ is established. This domain increases up to $\lambda = 0.24$ (at $w = 1.8$), hence the material consists of 24 % of domain two. Then the volume fraction remains constant for the remaining loading path. Also for unloading the volume fraction does not change until the load reaches $w = 0.3$ (where at the loading path the initiation of the microstructure takes place), then the volume fraction decreases. For zero loading the remaining volume fraction reads $\lambda = 0.17$.

The plastic slip of both domains are shown on the left hand side of Figure 4.67.

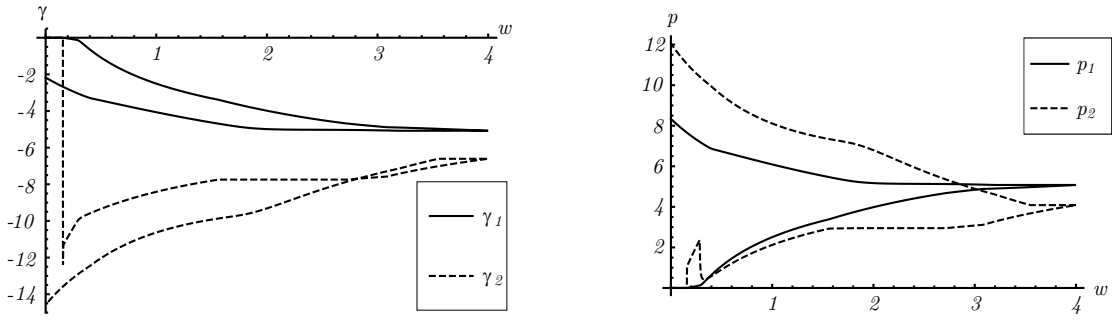

Figure 4.67.: Plastic slip and hardening in both domains for one tension-compression load cycle.

When the microstructure is initiated, the plastic slip in domain two decreases drastically to -12 in order to minimize the energy with a too small volume fraction. During further loading the plastic slip of domain two slightly increases, while at unloading it first remains constant, thus this domain is unloaded elastically. Then the plastic slip slightly decreases again. Finally at zero loading it reads $\gamma_2 = -14.1$. The plastic slip of domain one starts at zero plastic slip and decreases smoothly to -5.5 at the end of the loading path. For unloading the plastic slip also remains constant first thus the material behaves elastic before the plastic slip increases again and reaches -2 at zero loading. Since both plastic slips remain constant at the beginning of unloading the whole material is unloaded elasitically. Afterwards the plastic behavior occurs again. The hardening parameters (right hand side of Figure 4.67) both increase for loading and unloading since the absolute values of the plastic slip are their major contributions. The hardening parameter of domain two has a kink due to the jump of the plastic slip at the onset of the lamination.

The evolution of the angle of the laminate is presented in Figure 4.68.

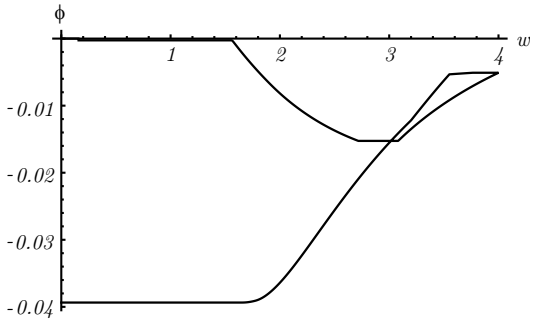

Figure 4.68.: Angle of laminate for one tension-compression load cycle.

Once the microstructure is built, the angle is found as approximately zero. From $w = 1.8$ the volume fraction of the laminate remains constant and the laminate starts to rotate. First the angle decreases and then increases. At unloading, the angle first decreases. As w reaches 1.8, the angle remains constant at -0.04 [rad].

The Cauchy normal stresses (left side of Figure 4.69) are strongly influenced by the established microstructure.

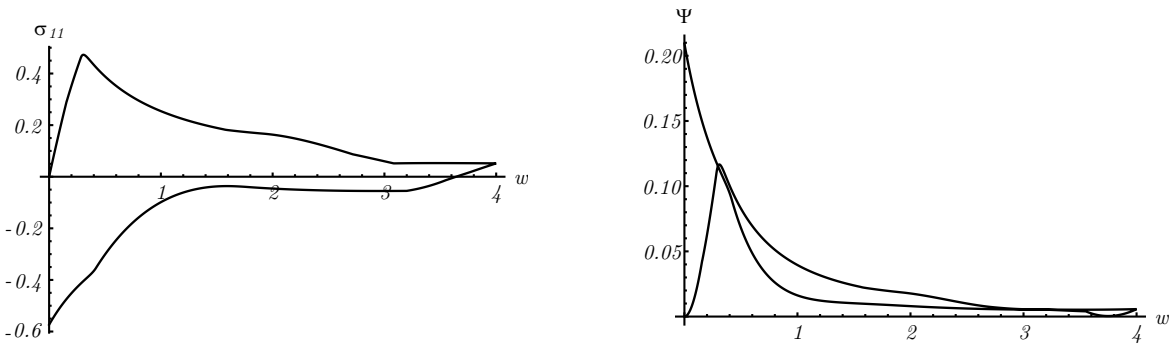

Figure 4.69.: Cauchy normal stress and energy for one tension-compression load cycle.

First the material behaves elastically, hence the stress increases linear. Due to already discussed viscous effects, the microstructure is delayed and results a peak in the stress. As the microstructure evolves, the stress decreases slowly. At unloading, as the plastic slip remains constant, the material behaves elastically first and the stress decreases linear. Afterwards the plastic slip evolves again and the stress remains constant and then decreases further. Thus, a hysteresis loop is visible. The peak due to viscous effects at the initiation of the microstructure also occurs in the energy (right hand side of Figure 4.69). Then the energy curve is convex. At unloading the energy curve increases as the hardening parameters increase, which makes the material stiffer.

For two load cycles (load cycles illustrated on the left hand side of Figure 4.70) the evolution of the volume fraction of domain two is shown on the right hand side of Figure 4.70.

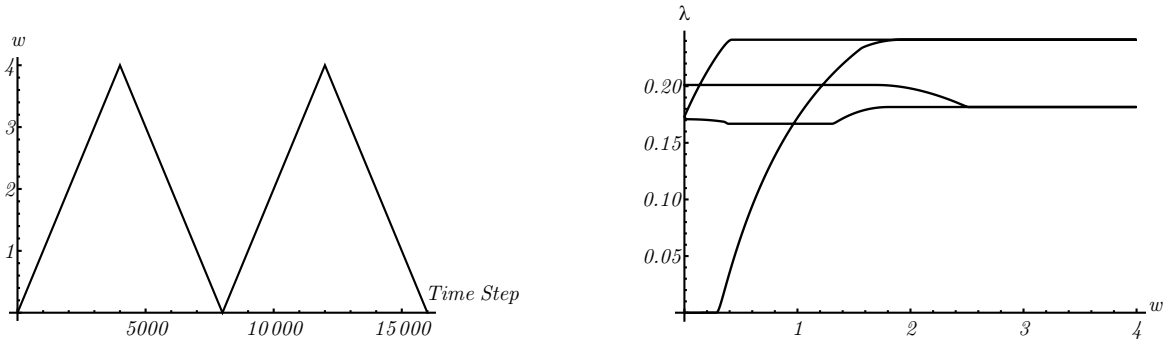

Figure 4.70.: Two load cycles of tension-compression and corresponding evolution of volume fraction of domain two.

At the beginning of the second cycle the volume fraction starts with the initial value $\lambda = 0.17$. When the starting point of the microstructure for the first cycle is reached, the volume fraction slightly drops down. At $w = 1.3$ the volume fraction increases up to $\lambda = 0.18$ and remains constant from there on. For unloading, first the volume fraction remains unchanged. The evolution starts at $w = 2.6$, the volume fraction slightly increases up to $\lambda = 0.2$ and remains again constant from there ($w = 1.8$) on. In total, the domain two is the smaller domain and even decreases further in the second cycle.

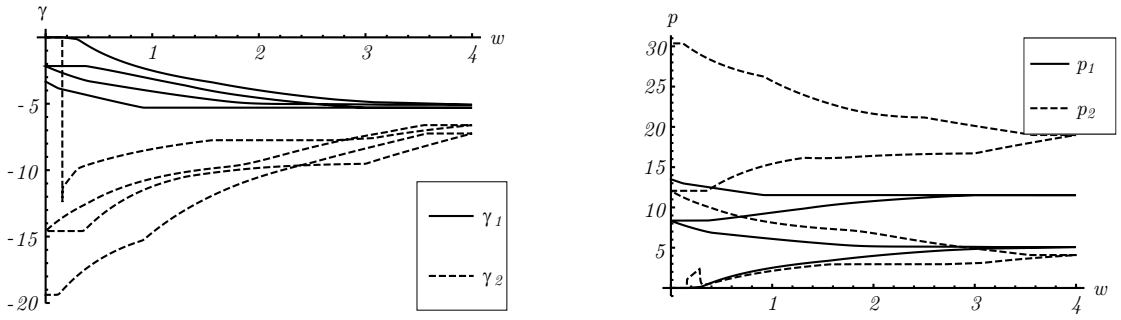

Figure 4.71.: Plastic slip and hardening of both domains for two tension-compression load cycles.

The plastic slip of both domains (left side of Figure 4.71) remains constant at the beginning of unloading but then decreases further in the second load cycle. The plastic slip in the second domain exhibits larger deviations to the first cycle compared to the first domain. This behavior is different to the results of the cycling of the shear test, where the plastic slip remains similar for all cycles. The reason for this increasing amount of plastic slip is the rotation of the laminate (Figure 4.72). When it rotates, the dislocations which cause the plastic slip cannot not vanish fully at unloading. Therefore the dislocations remain or even increase and more plastic slip is produced. Similar to the behavior of the cycling of the shear test, the hardening parameters increase monotonously.

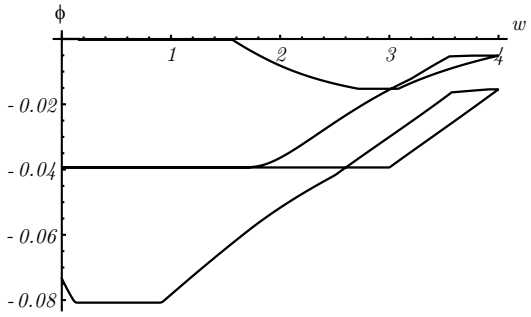

Figure 4.72.: Angle of the laminate for two tension-compression load cycles.

In the second cycle at loading, the laminate does not rotate until $w = 3$ is reached. Then the angle (Figure 4.72) increases nearly linear to $\phi = -0.02\,[\text{rad}]$. For unloading, the angle is constant for a short load period (from $w = 4$ to 3.8), but then it decreases to -0.08 at $w = 1$. Up to $w = 0.2$ the laminate does not need to rotate, afterwards the angle starts to increase. At zero loading, the angle reads $\phi = -0.075\,[\text{rad}]$.

The resulting Cauchy normal stress and the energy are presented in Figure 4.73.

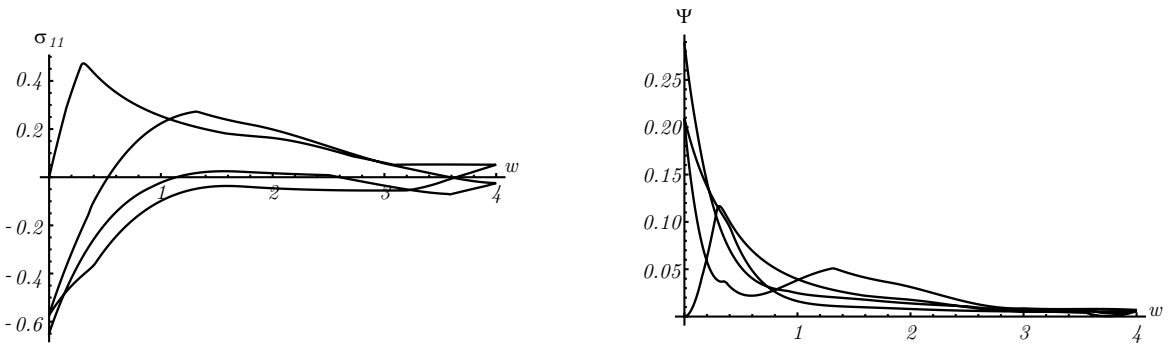

Figure 4.73.: Cauchy normal stress and energy for two tension-compression load cycles.

In the second cycle, the microstructure remains in the material. Therefore the peak in the stress due to viscous effects of the initiation does not occur in the second cycle and a hysteresis loop with a smaller width is exhibited. The evolution of the energy shows no peak in the beginning of the second load cycle as the microstructure remains in the material and does not need to be initiated. However, at the loading path, a peak occurs with a maximum at $w = 1.3$. At this point, the volume fraction of domain two starts to increase again and the peak in the energy decreases.

The loading path presented on the left hand side of Figure 4.74 illustrates three load cycles of a tension-compression test.

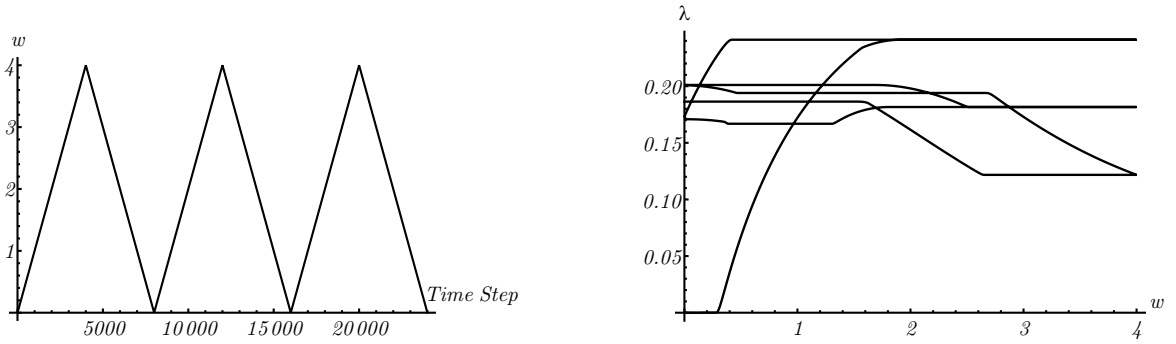

Figure 4.74.: Three load cycle of tension-compression and corresponding evolution of volume fraction of domain two.

On the right hand side of Figure 4.74 the resulting evolution of the volume fraction of domain two is shown. For the loading path of the third cycle, the volume fraction remains first unchanged. As the loading increases ($w = 2.8$ to $w = 4$) the volume fraction decreases further to 0.11. At unloading the volume fraction finally increases again and reaches 0.19 at zero loading. Obviously, the evolution of the volume fraction is different for every load cycle.

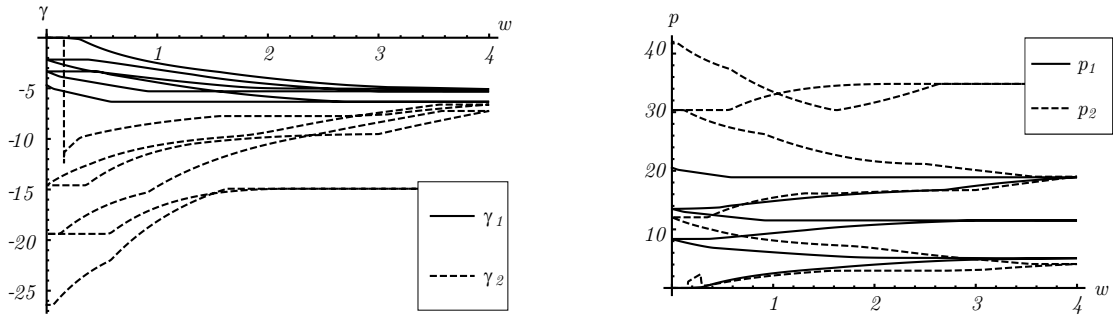

Figure 4.75.: Plastic slip and hardening in both domains for three tension-compression load cycles.

Analogously to the behavior in the second cycle the amount of plastic slip in both domains (left side of Figure 4.75) increases further since due to the rotation of the laminate, the dislocations, which cause the plastic slip, are not vanished at unloading. The hardening parameters (right side of Figure 4.75) still increase further for loading and unloading and reach already rather high values.

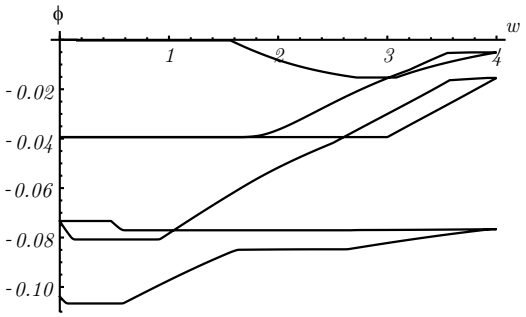

Figure 4.76.: Angle of laminate for three load cycles.

The angle of the laminate is shown in Figure 4.76. For the loading path in the third cycle, the laminate does not need to rotate, the angle is found as -0.075[rad]. At unloading the angle decreases to -0.105[rad].

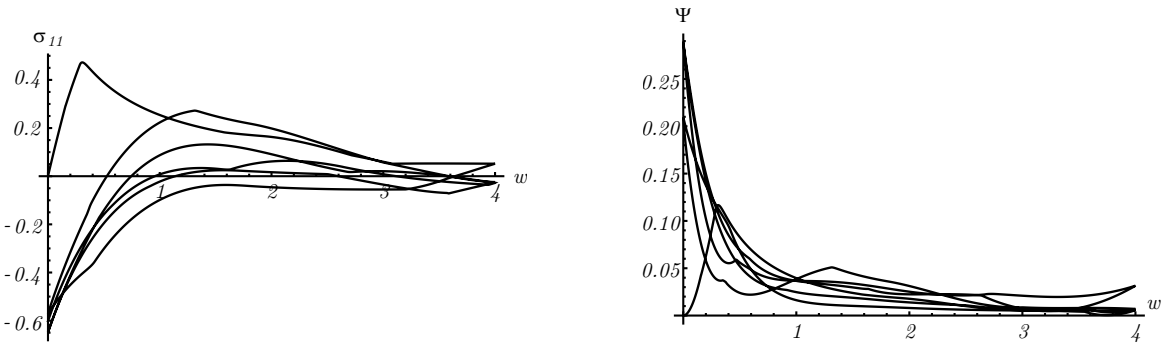

Figure 4.77.: Cauchy normal stress and energy for three tension-compression load cycles.

The energy for the load cycle three (right side of Figure 4.77) is shifted vertically due to the increased hardening parameters. The Cauchy normal stress hysteresis (left side of Figure

4.77) shrinks further. This effect is caused by the drastic enlargement of the deformed area at this tension-compression test. The Cauchy stress refers the actual force to this enlarged area, therefore the width of the hysteresis decreases. Hence the first Piola Kirchhoff stresses may be interesting because the actual force is referred to the reference area and the enlargement of the actual area is not taken into account. However they are not representing the "true" stresses. The normal Piola Kirchhoff stresses are presented in Figure 4.78.

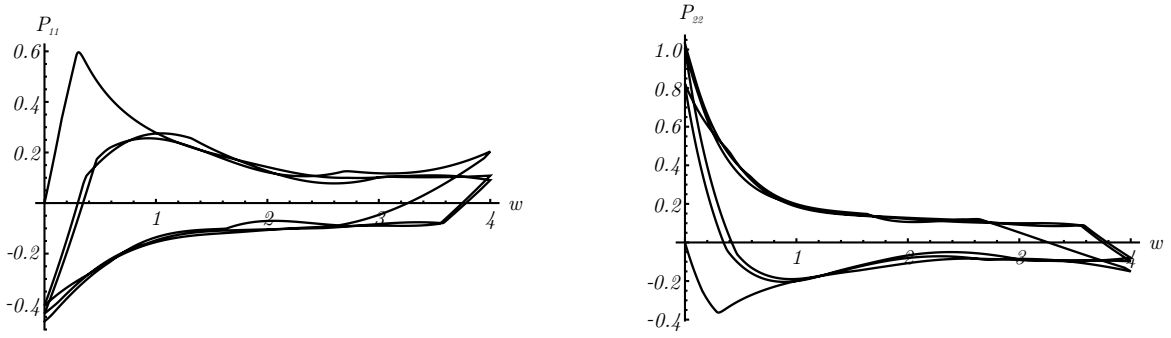

Figure 4.78.: First Piola Kirchoff stresses for three tension-compression load cycles.

Both normal stresses show a clear hysteresis loop which does not change for the second and third cycle. Therefore the changes in the Cauchy stresses are only a result of the change of area.

4.6. Discussion

In this chapter, a new approach for modeling finite plasticity is introduced by adding a vanishing viscosity to the existing model of [49]. In the first part of this chapter, the modified dissipation potential and the energy potential are presented and relaxed for an underlying microstructure. By modifying the dissipation potential explicit evolution equations for the internal variables, which characterize the current state of the microstructure, are obtained. These equations no longer consist of global minimizations, hence they can be determined with standard approaches for numerical integrations. Afterwards numerical tests are performed, here a shear and a tension-compression test are presented. Due to the chosen dissipation potential viscous effects arise and have to be reduced by introducing a relaxation time, hence reducing the loading velocity. In this chapter, the examples show that an increase of the relaxation time reduces drastically the viscous effect. As second testings, a comparison to the results of D.Kochmann and K.Hackl [48] is presented. The results show good agreements, however deviations occur, especially in the stress strain behavior. Then cycling tests are performed where clear hysteresis loops are exhibited. If the actual area enlarges, the Cauchy stress may loose its clear hysteresis character for higher numbers of load cycles. However, the first Piola Kirchoff stress still exhibits a hysteresis loop then.

In conclusion, this model has a stable character and is able to model the evolution of microbands in finite crystal plasticity. The numerical effort in comparison to the approach of [49] is reduced. However, due to the viscous contribution, a viscous material behavior is obtained which can be reduced but not vanished. The reason for the restriction to one active

slip system and a first order laminate is just the simplicity: a generalization to higher order laminates and higher order slip systems leads to a higher numerical effort.

5. Modeling finite crystal plasticity involving dislocations

In the section 3.4, the continuum theory of dislocations for small deformations is introduced. However, ECAP (equal-channel angular pressing) tests reveal that large plastic deformations may change the state of a microstructure, [38]. Crystals are pressed through a channel which is kinked by 90°. Due to that kink, large plastic deformations may appear. A comparison of the crystal before and after the test show that the grains change their size, for example from $20\mu m$ to $1\mu m$. Also the martensitic phase transformation can occur at high plastic strains. Thus, for modeling these microstructures, small deformations are not suitable and large deformations have to be considered. In order to model finite crystal plasticity, the continuum theory will be extended in the following section for large deformations. Therefore new independent kinematic quantities have to be specified which characterize the deformed state of the crystal and the change of dislocation network. Analogously to the theory with small deformations, the energy and the dissipation are described in terms of these quantities. The first who introduced this concept for large deformations were Kondo [50], Bilby et al [12] [11], Kröner [53] [54] followed by Berdichevsky and Sedov [9] and others.

In this chapter first the kinematically independent quantities which describe the deformed state of the crystal are outlined. Then the nonlinear continuum dislocation theory is employed on the examples of finite anti-plane constrained shear and plane-strain constrained shear under the assumption of uniform deformations. These results are already published in [59] and [60]. For the example of plane- strain constrained shear also a solid-solid phase transition involving dislocations which can be interpreted as a martensitic phase transition is modeled.

5.1. Kinematics

If large deformations are considered, the additive decomposition of the deformation gradient is not valid anymore. According to Equation (2.67) the deformation gradient has to be decomposed multipilcatively. Both components, hence the elastic and the plastic deformations, are orientation preserving

$$\det\mathbf{F}^{e} > 0, \quad \det\mathbf{F}^{p} > 0. \tag{5.1}$$

This implies that both deformations have inverse deformations, thus $\mathbf{F}^{p\text{-}1}$ and $\mathbf{F}^{e\text{-}1}$ exist. In the continuum dislocation theory, we assume that the plastic deformation $\mathbf{F}^{p}$ is the deformation which creates dislocations or changes the position of the dislocations, but it does not deform the crystal lattice and therefore the lattice vectors remain unchanged, see right lattice in Fig.5.1. The elastic deformation $\mathbf{F}^{e}$ instead deforms the crystal lattice with frozen dislocations. Since this deformation deforms the lattice but not the dislocations, it can be

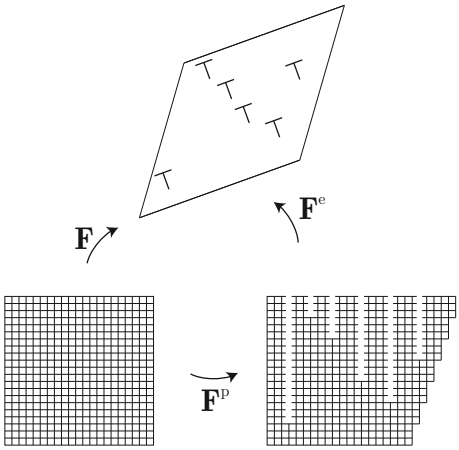

Figure 5.1.: Multiplicative decomposition of the deformation gradient, reprinted by permisson from [60]

also called lattice deformation. Under that deformation, the lattice and the shape vectors change. Both deformations together bring the crystal to its final state.

As already discussed in Section 3.4.2, the definition of the Burgers vector is still a crucial issue. When a plastic deformation takes place, this vector has to change as well, since the total closure failure changes. Ortiz and Repetto [74] already introduced the resultant Burgers vector by

$$\mathbf{b}_\mathrm{r} = \oint \mathbf{F}^\mathrm{p} \cdot \mathrm{d}\mathbf{x}. \tag{5.2}$$

The question arises, if this is a correct definition. Let us consider a non-uniform plastic deformation in the form of

$$\mathbf{F}^\mathrm{p}_1 = \mathbf{I} + c x_1 \mathbf{s}_1 \otimes \mathbf{m}_1, \tag{5.3}$$

thus a plastic slip along the x_1 axis in the reference configuration and we assume $\mathbf{s}_1^\mathrm{T} = (1\ 0\ 0)$ and $\mathbf{m}_1^\mathrm{T} = (0\ 1\ 0)$. The resulting deformation is illustrated in Fig.5.2 for a quadratic cross section with the size l. The edge dislocations are sketched as arrows of vacancies which break the lattice in the vertical columns. The subsequent elastic deformation restores these breaks in the lattice and thus brings the crystal in its final form. If the dislocations are distributed uniformly in the crystal, their density can be defined by $\rho = \frac{n}{l^2}$ with n being the number of dislocations.

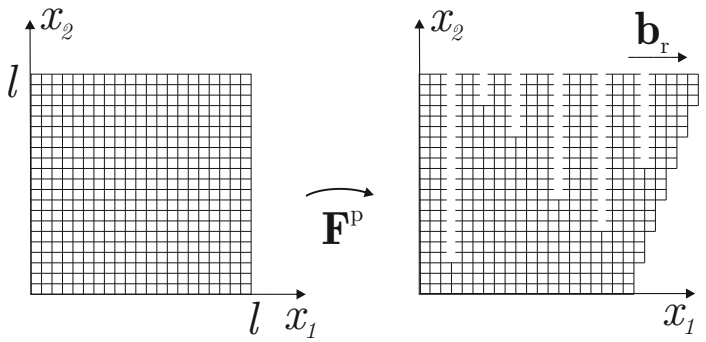

Figure 5.2.: Plastically deformed crystal including dislocations, reprinted by permisson from [59]

If the definition of (5.2) is considered, the Burgers vector of this example can be determined as

$$\mathbf{b}_\mathrm{r} = \oint \mathbf{F}^\mathrm{p} \cdot \mathrm{d}\mathbf{x} = \int_0^l c l \mathbf{s}_1 \, \mathrm{d}x_2 = c l^2 \mathbf{s}_1. \tag{5.4}$$

In order to obtain the total closure failure, c has to be equal to $c = \rho b = \frac{nb}{l^2}$, thus $\mathbf{b}_\mathrm{r} = nb\mathbf{s}_1$. Hence in the continuum limit, when the atomic distance tends to zero at fixed representative volume element and fixed dislocation density per area of the unit cell, definition (5.2) leads to the total closure failure of the single crystal with one slip system and a plastic slip introduced by $\mathbf{F}^\mathrm{p}$.

The application of Stoke's theorem (A.35) on Equation (5.2) gives

$$\mathbf{b}_\mathrm{r} = -\int_{\Omega_0} (\mathbf{F}^\mathrm{p} \times \nabla) \cdot \mathbf{n} \, \mathrm{d}a. \tag{5.5}$$

For small deformations, the relation between the dislocation density tensor and the Burgers vector is given by Equation (3.44). Analogously we define the dislocation density tensor for finite deformations by

$$\mathbf{T} = -\mathbf{F}^\mathrm{p} \times \nabla. \tag{5.6}$$

Applying this definition, the resultant Burgers vector of dislocation which cross this infinitesimal area da can be written in terms of the dislocation density,

$$\mathbf{b}_\mathrm{r} = \mathbf{T} \cdot \mathbf{n} \, \mathrm{d}a, \tag{5.7}$$

with da being an infinitesimal area having the normal vector $\mathbf{n}$. This dislocation density tensor is referred to the reference configuration. In order to compare the dislocation density with experimental results, the dislocation density of the current configuration is needed, since the experiments measure the deformed lattice, which corresponds to the current configuration (for example [56]). In order to get to the current configuration the relation (2.4) can be applied,

$$\mathbf{b}_\mathrm{r} = \oint \mathbf{F}^\mathrm{p} \mathbf{F} \cdot \mathbf{dx}. \tag{5.8}$$

Using the multiplicative decomposition of the deformation gradient (2.67), the resultant Burgers vector in the current configuration is obtained,

$$\mathbf{b}_\mathrm{r} = \oint \mathbf{F}^{\mathrm{e}\text{-}1} \cdot \mathbf{dy}. \tag{5.9}$$

Correspondingly the spatial dislocation density tensor can be introduced,

$$\mathbf{T}' = -\mathbf{F}^\mathrm{e} \times \nabla_\mathbf{y}, \tag{5.10}$$

where $\nabla_\mathbf{y}$ is the nabla operator with respect to the coordinate $\mathbf{y}$ of the current configuration.

The crucial topic of this section is the definition of the kinematically independent quantities which characterize completely the deformed state of the crystal with dislocations and the rate of changes of the dislocations network. The plastic deformation gradient $\mathbf{F}^\mathrm{p}$ depends on the cut surface and on the whole history of creating dislocations. Therefore this quantity

cannot be a state variable. Equation (5.7) shows, that the dislocation density tensor depends only on the Burgers vector and on the position of dislocation lines. Thus we choose for an isothermal process the dislocation density tensor $\mathbf{T}$ as one state variable. As a second one, the elastic deformation gradient $\mathbf{F}^{\mathrm{e}}$ could be considered, hence

$$\Psi = \Psi(\mathbf{F}^{\mathrm{e}}, \mathbf{T}). \tag{5.11}$$

However, superposing a rigid-body rotation $\mathbf{R}$ onto an actual deformation,

$$\mathbf{F}^{*} = \mathbf{R} \cdot \mathbf{F} \tag{5.12}$$

then the actual deformation gradient $\mathbf{F}$ will change to $\mathbf{F}^{*}$. Since $\mathbf{F}^{\mathrm{p}}$ is regarded as acting only in the reference configuration (it does not deform the lattice), the elastic deformation gradient has to change,

$$\mathbf{F}^{\mathrm{e}*} = \mathbf{R} \cdot \mathbf{F}^{\mathrm{e}}. \tag{5.13}$$

Since a rigid-body rotation should not change the energy, the state variable $\mathbf{F}^{\mathrm{e}}$ is replaced by the right Cauchy Green tensor for the elastic deformation (see e. g. [32]), hence

$$\Psi = \Psi(\mathbf{C}^{\mathrm{e}}, \mathbf{T}). \tag{5.14}$$

with

$$\mathbf{C}^{\mathrm{e}} = \mathbf{F}^{\mathrm{e}\,\mathrm{T}} \cdot \mathbf{F}^{\mathrm{e}} \tag{5.15}$$

analogously to the definition (2.9). Another state variable which describe the state of the crystal is the density of statistically stored dislocations. However for low temperatures they tend to be dipoles. The density of such dipoles only depends on the temperature, therefore it is a constant for an isothermal process and will be omitted.

5.2. Thermodynamic framework

For simplicity we restrict ourselves to a single crystal with one active slip system. In this case, the plastic deformation gradient can be expressed by

$$\mathbf{F}^{\mathrm{p}} = \mathbf{I} + \beta \mathbf{s} \otimes \mathbf{m}, \tag{5.16}$$

with $\mathbf{s}$ and $\mathbf{m}$ denoting the slip system as already used in the previous chapters. Kröner introduced the plastic slip in the continuum dislocation theory as β, therefore to maintain this historical tradition the plastic slip is denoted in this chapter by β instead of γ. Inserting Equation (5.16) into the definition (5.5), the dislocation density reads

$$\mathbf{T} = \mathbf{s} \otimes (\nabla \beta \times \mathbf{m}). \tag{5.17}$$

Under the assumption that all dislocation lines are straight lines parallel to the direction $\mathbf{l}$, the resultant Burgers vector of all excess dislocations whose lines cross an infinitesimal area da under 90° may be found by using Equation (5.7) as

$$\mathbf{b}_{\mathrm{r}} = \mathbf{s}\left[(\nabla \beta \times \mathbf{m}) \cdot \mathbf{l}\right] \mathrm{d}a. \tag{5.18}$$

Similar to the theory with small deformations (Equation (3.45)), the scalar dislocation density can be calculated by

$$\rho = \frac{1}{b} |(\nabla \boldsymbol{\beta} \times \mathbf{m}) \cdot \mathbf{l}|, \tag{5.19}$$

with b being the magnitude of the Burgers vector. Instead of the dislocation density tensor, this quantity can be used as a state variable, since it is also independent from the history of creating dislocations. Hence

$$\Psi = \Psi(\mathbf{C}^{\mathrm{e}}, \rho). \tag{5.20}$$

For the examined examples, a single crystal in the three dimensional euclidean space is considered which occupies in the undeformed configuration a domain Ω_0. The boundary of this crystal $\partial\Omega_0$ is divided into ∂_k, where the crystal is clamped and ∂_τ, where a dead load $\boldsymbol{\tau}$ is given. Since the boundary part ∂_k is clamped, the displacements and the plastic slip have to be zero there,

$$\mathbf{u} = 0, \;\; \boldsymbol{\beta} = 0 \;\; \text{at } \partial_k, \tag{5.21}$$

with $\mathbf{u}$ being the displacement field already defined in (2.3). In the case that no body force acts on the crystal, its energy functional is defined as

$$\mathcal{I}(\mathbf{u}, \beta) = \int_{\Omega_0} W(\mathbf{F}, \beta, \nabla\beta) \, \mathrm{d}v - \int_{\partial_\tau} \boldsymbol{\tau}\mathbf{u} \, \mathrm{d}a, \tag{5.22}$$

where $W(\mathbf{F}, \beta)$ is equal to the free energy density $\Psi(\mathbf{C}^{\mathrm{e}}, \rho)$. Assuming first that the dissipation is negligibly small the variational principle for a single crystal having one active single slip system states: The true displacement $\hat{\mathbf{u}}$ and the true plastic slip $\hat{\beta}$ minimize in the final state of the deformation the energy functional (5.22) under the boundary conditions (5.21). Applying the standard variational calculus, the first variation of the functional (5.22) is obtained,

$$\delta\mathcal{I}(\mathbf{u}, \beta) = \int_{\Omega_0} \left(W_{\mathbf{F}} : \delta\mathbf{F} + W_\beta \delta\beta + W_{\nabla\beta} \cdot \nabla\delta\beta \right) \mathrm{d}v - \int_{\partial_\tau} \boldsymbol{\tau}\delta\mathbf{u} \, \mathrm{d}a = 0. \tag{5.23}$$

The first Piola- Kirchhoff stress is defined as the derivative of the free energy with respect to the deformation gradient, hence $\mathbf{P} = \mathbf{W}_{,\mathbf{F}}$. We also may replace $\delta\mathbf{F} = \delta\mathbf{u}\nabla$ and by integrating by part, we get

$$\delta\mathcal{I} = \int_{\Omega_0} \left[(\mathbf{P} \cdot \nabla) \delta\mathbf{u} + \left(W_\beta - \nabla \cdot W_{\nabla\beta} \right) \delta\beta \right] \mathrm{d}v + \int_{\partial_\tau} \left[(\mathbf{P} \cdot \mathbf{n} - \tau) \delta\mathbf{u} + W_{\nabla\beta} \cdot \mathbf{n}\delta\beta \right] \mathrm{d}a. \tag{5.24}$$

For arbitrary variations $\delta\beta$ and $\delta\mathbf{u}$ the variation of the energy functional has to vanish, hence $\delta I = 0$. Then the result is on one hand the equilibrium of macro-forces acting on the crystal

$$\mathbf{P} \cdot \nabla = 0, \tag{5.25}$$

with $\mathbf{P}$ denoting the first Piola Kirchoff stress, illustrated in Figure 2.4. At the boundary ∂_τ the boundary condition

$$\mathbf{P} \cdot \mathbf{n} = \boldsymbol{\tau} \tag{5.26}$$

has to be fulfilled. On the other hand, the equilibrium of the micro-forces acting on the dislocations is found as

$$W_\beta - \nabla W_{\nabla\boldsymbol{\beta}} = 0, \tag{5.27}$$

where $-W_\beta$ represents the resolved shear stress and $\nabla W_{\nabla\beta}$ the back stress. The boundary condition at ∂_τ reads

$$W_{\nabla\boldsymbol{\beta}} \cdot \mathbf{n} = 0. \tag{5.28}$$

Employing the chain rule, the first Piola Kirchhoff stress, used in Equation (5.25), can be defined in terms of the strain tensor $\mathbf{C}^{\mathrm{e}}$ as

$$\mathbf{P} = W_{\mathbf{F}} = 2\mathbf{F}^{\mathrm{e}} \cdot \Psi_{\mathbf{C}^{\mathrm{e}}} \cdot \mathbf{F}^{p-T}. \tag{5.29}$$

For the resolved shear stress we obtain

$$-W_\beta = -\mathbf{s} \cdot \mathbf{F}^{\mathrm{eT}} \cdot \mathbf{P} \cdot \mathbf{m}. \tag{5.30}$$

The back stress may be calculated by inserting Equation (5.19) into Equation (5.20) and by applying the chain rule, the result reads

$$\nabla W_{\nabla\boldsymbol{\beta}} = \frac{1}{b} \operatorname{sign}((\nabla\boldsymbol{\beta} \times \boldsymbol{m}) \cdot \mathbf{l})\mathbf{l} \cdot \Psi_\rho \times \mathbf{m}. \tag{5.31}$$

The unknown variables $\mathbf{u}$ and $\boldsymbol{\beta}$ can be determined if these arguments (Equations (5.29), (5.30) and (5.31)) are inserted into the equilibrium conditions (Equation (5.25) and (5.27)).

Consider now the case that the energy dissipation cannot be neglected. In this case, following [80], the variational principle (5.23) is replaced by

$$\delta\mathcal{I} + \int_{\Omega_0} \frac{\partial D}{\partial \dot{\beta}} \delta\beta \, \mathrm{d}v = 0. \tag{5.32}$$

The last term of this equation describes the dissipation due to the dislocation motion and is assumed to be dependent only on the rate of plastic slip, hence

$$D = D\left(\dot{\beta}\right). \tag{5.33}$$

The most simple ansatz for the dissipation is

$$D\left(\dot{\beta}\right) = r\left|\dot{\beta}\right| \tag{5.34}$$

where r denotes the critical resolved shear stress. Using again the standard variational calculus, Equation (5.32) leads again to the equilibrium of macro forces, hence

$$\mathbf{P} \cdot \nabla = 0. \tag{5.35}$$

The equilibrium of micro forces changes to

$$W_{\boldsymbol{\beta}} - \nabla W_{\nabla\boldsymbol{\beta}} + \frac{\partial D}{\partial \dot{\beta}} = 0. \tag{5.36}$$

By using the relation

$$W_{\boldsymbol{\beta}} - \nabla W_{\nabla\boldsymbol{\beta}} = \frac{\delta W_{\mathbf{F}}}{\delta\beta}, \tag{5.37}$$

Equation (5.36) may be written as

$$\frac{\delta W_{\mathbf{F}}}{\delta \beta} = -\frac{\partial D}{\partial \dot{\beta}}. \tag{5.38}$$

Assuming that the sign of $\dot{\beta}$ does not change during the evolution of β, the variational equation (5.32) reduces to minimizing the relaxed energy functional,

$$\mathcal{I}(\mathbf{u},\boldsymbol{\beta},) = \int_{\Omega_0} \left[W(\mathbf{F},\boldsymbol{\beta},\nabla\boldsymbol{\beta}) + r\,\mathrm{sign}\left(\dot{\beta}\right)\beta \right] \mathrm{d}v - \int_{\partial_\tau} \boldsymbol{\tau}\mathbf{u}\,\mathrm{d}a. \tag{5.39}$$

According [16], now the true displacement $\mathbf{u}$ and the true plastic slip β minimize in the final deformed state the relaxed energy functional. If the rate of plastic slip is zero, hence $\dot{\beta} = 0$, the plastic slip is frozen and the displacements can be found by minimizing (5.22) with a constant β.

5.3. Finite anti-plane constrained shear

As a first examined example for the nonlinear dislocation theory a crystal under anti-plane constrained shear is studied. This single crystal is assumed as a beam with the length L and a rectangular cross section with the width a and height h. The crystal is plotted in Figure 5.3 with a coordinate system chosen that the coordinate x_3 corresponds to the length, x_2 to the height and x_1 to the width of the crystal. Since the crystal is considered as a beam, the width a is much smaller than the height h and the length L, $a << h$ and $a << L$.

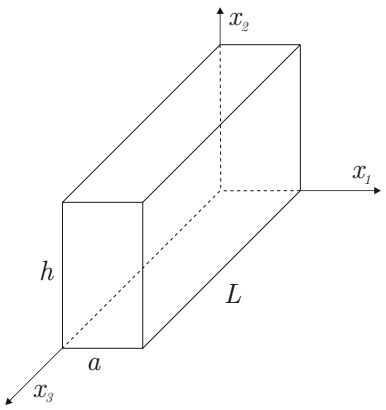

Figure 5.3.: Single crystal beam.

This crystal is put in a hard device with prescribed displacements at the surface of its cross section. At its boundaries, the displacements read

$$\mathbf{u} = \begin{pmatrix} 0 \\ 0 \\ wx_2 \end{pmatrix}. \tag{5.40}$$

This deformation is illustrated in Figure 5.4 and w corresponds to the overall strain. Since the width is assumed to be comparably small, end effects can be neglected. Hence the stresses and the strains only depend on x_1.

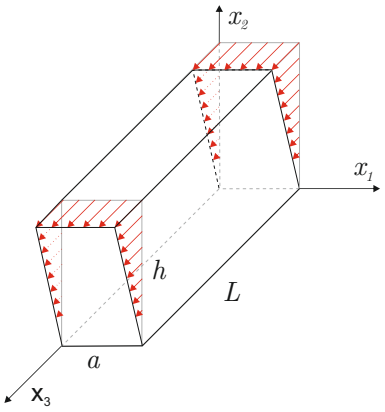

Figure 5.4.: Deformed single crystal beam under finite anti-plane constrained shear.

Applying the definition (2.6), the deformation gradient may be determined from the displacements as

$$\mathbf{F} = \begin{pmatrix} 1 & 0 & 0 \\ 0 & 1 & 0 \\ 0 & w & 1 \end{pmatrix}. \tag{5.41}$$

Assuming that all slip planes are parallel to $x_2 = 0$ and that all dislocation lines of the screw dislocations are parallel to the x_3 axis, the slip direction reads

$$\mathbf{s} = \begin{pmatrix} 0 \\ 0 \\ 1 \end{pmatrix} \tag{5.42}$$

and the normal vector to the slip plane

$$\mathbf{m} = \begin{pmatrix} 0 \\ 1 \\ 0 \end{pmatrix}. \tag{5.43}$$

We also assume that the plastic slip only depends on x_1, hence $\beta = \beta(x_1)$. The boundary is an obstacle, therefore the dislocations cannot penetrate the boundary of the crystal and the plastic slip has to be zero,

$$\beta(x_1 = 0) = \beta(x_1 = a) = 0. \tag{5.44}$$

From Equation (5.16) the plastic deformation gradient $\mathbf{F}_p$ may be determined as

$$\mathbf{F}^{\mathrm{p}} = \mathbf{I} + \beta \mathbf{s} \otimes \mathbf{m} = \begin{pmatrix} 1 & 0 & 0 \\ 0 & 1 & 0 \\ 0 & \beta & 1 \end{pmatrix}. \tag{5.45}$$

Inserting this plastic deformation into Equation (5.6), the dislocation density tensor reads

$$\mathbf{T} = \begin{pmatrix} 0 & 0 & 0 \\ 0 & 0 & 0 \\ 0 & 0 & \beta_{,x_1} \end{pmatrix}. \tag{5.46}$$

Hence, the scalar dislocation density can be obtained as

$$\rho = \frac{1}{b}\left|\beta_{,x_1}\right|. \tag{5.47}$$

Since the total deformation gradient is given and the plastic deformation gradient determined, from the multiplicative split of the deformation gradient (Equation (2.67)) the elastic deformation gradient can be evaluated as

$$\mathbf{F}^{\mathrm{e}} = \begin{pmatrix} 1 & 0 & 0 \\ 0 & 1 & 0 \\ 0 & w-\beta & 1 \end{pmatrix}. \tag{5.48}$$

The free energy density has to be considered in terms of the scalar dislocation density and the elastic strain $\mathbf{C}_e$. Berdichevsky [6] proposed the energy density in the following form

$$\Psi(\mathbf{C}^{\mathrm{e}},\rho) = \frac{1}{2}\lambda\left(\mathrm{tr}(\mathbf{E}^{\mathrm{e}})\right)^2 + \mu\mathbf{E}^{\mathrm{e}} : \mathbf{E}^{\mathrm{e}} + \mu k \ln\left(\frac{1}{1-\frac{\rho}{\rho_{\mathrm{s}}}}\right), \tag{5.49}$$

with λ and μ being the Lamé constants. The elastic strain tensor $\mathbf{E}^{\mathrm{e}}$ in the energy density is only dependent on our state variable $\mathbf{C}^{\mathrm{e}}$ and defined as

$$\mathbf{E}^{\mathrm{e}} = \frac{1}{2}\left(\mathbf{C}^{\mathrm{e}} - \mathbf{I}\right). \tag{5.50}$$

In the case of finite anti-plane constrained shear, this elastic strain tensor reads

$$\mathbf{E}^{\mathrm{e}} = \begin{pmatrix} 0 & 0 & 0 \\ 0 & \frac{1}{2}(w-\beta)^2 & \frac{1}{2}(w-\beta) \\ 0 & \frac{1}{2}(w-\beta) & 0 \end{pmatrix}. \tag{5.51}$$

The first two terms of the energy density (5.49) describe the contribution to the energy by the macroscopic elastic deformation of the crystal, while the last term corresponds to the energy of the dislocation network. According to Berdichevsky [6], the energy density of the dislocation network depends on a logarithmic term because of two facts: for small dislocation densities the energy density is the sum of the energy from non-interacting dislocations. Secondly a saturated dislocation density ρ_{s} is obtained when the closest packing of dislocations admissible in the discrete crystal lattice is reached. Therefore the energy density slope is linear for a small dislocation density ρ. If the dislocation density reaches the saturated dislocation density, the energy tends to infinity. For small up to moderate dislocation densities, the energy density due to the dislocation network can be approximated by

$$\mu k \ln\left(\frac{1}{1-\frac{\rho}{\rho_{\mathrm{s}}}}\right) \approx \mu k \frac{\rho}{\rho_{\mathrm{s}}} + \frac{1}{2}\frac{\rho^2}{\rho_{\mathrm{s}}^2}. \tag{5.52}$$

This approximation is used in the following calculations. Inserting the elastic strain tensor and the scalar dislocation density into the energy density, it is written as

$$\Psi = \frac{1}{8}(\lambda+2\mu)(w-\beta)^4 + \frac{1}{2}\mu(w-\beta)^2 + \mu k\left(\frac{\left|\beta_{,x_1}\right|}{b\rho_{\mathrm{s}}} + \frac{1}{2}\frac{\beta_{,x_1}^2}{b^2\rho_{\mathrm{s}}^2}\right). \tag{5.53}$$

5.3.1. Finite anti-plane constrained shear with zero dissipation

For simplicity and for a first analysis of the given system, zero dissipation is assumed. Then following the variational principle (5.23), the true plastic slip minimizes the energy functional

$$\mathcal{I}[\beta(x_1)] = hL\int_0^a \left[\frac{1}{8}(\lambda+2\mu)(w-\beta)^4 + \frac{1}{2}\mu(w-\beta)^2 + \mu k\left(\frac{|\beta_{,x_1}|}{b\rho_s} + \frac{1}{2}\frac{\beta_{,x_1}^2}{b^2\rho_s^2}\right)\right] \mathrm{d}x_1 \quad (5.54)$$

among all admissible functions β satisfying the boundary conditions (5.44). The total strain w is considered as the control parameter, so that the evolution of the plastic slip along a change of total strain may be determined. For convenience, dimensionless quantities replace the material constants, hence

$$c = ab\rho_s \text{ and } \eta = \frac{\lambda+2\mu}{2\mu}. \quad (5.55)$$

Analogously the variable x_1 is replaced through ξ,

$$\xi = x_1 b\rho_s \quad (5.56)$$

and the energy functional through $\mathscr{E}$,

$$\mathscr{E} = \frac{b\rho_s}{\mu hL}I. \quad (5.57)$$

The dimensionless variable ξ changes in the interval from zero to c. Finally the dimensionless energy functional reads

$$\mathscr{E}[\beta(\xi)] = \int_0^c \left[\frac{1}{2}(w-\beta)^2 + \frac{1}{4}\eta(w-\beta)^4 + k|\beta_{,\xi}| + \frac{1}{2}k\beta_{,\xi}^2\right] \mathrm{d}\xi. \quad (5.58)$$

The boundary conditions (5.44) are replaced by

$$\beta(\xi=0) = \beta(\xi=c) = 0. \quad (5.59)$$

Now the plastic slip $\beta(\xi)$ has to be determined which minimizes the dimensionless energy functional (5.58). When the shear stress is applied, positive dislocations move along the x_1 axis to the left, while negative dislocations move to the right. Based on this observation we propose to seek β in the form (see also [8])

$$\beta(\xi) = \begin{cases} \beta_1(\xi) & \text{for } \xi \in (0,l) \\ \beta_m & \text{for } \xi \in (l, c-l) \\ \beta_1(c-\xi) & \text{for } \xi \in (c-l) \end{cases} \quad (5.60)$$

with β_m being a still unknown parameter and l an unknown width of a layer of the cross section. For l $0 \le l \le \frac{c}{2}$ has to be fulfilled. We demand that the plastic slip is continuous, therefore $\beta_1(\xi = l) = \beta_m$ holds true. The physical idea of choosing this kind of plastic slip is, that under a certain deformation, dislocations start to move. The boundary of the cross section is an obstacle which cannot be penetrated. Therefore the dislocations pile up there. This pile up takes place in a small boundary layer with the width of l. Considering this type of minimizer $\beta_1(\xi)$, β_m and l still have to be determined. Replacing β by the chosen

minimizer (5.60) and assuming that the derivative of the plastic slip is positive at the small layer on the left boundary ($\beta_{1,\xi} > 0$ for $0 \le \xi \le l$), the energy functional becomes

$$\begin{aligned}\mathscr{E} = 2\int_0^l \left[\frac{1}{2}(w-\beta_1)^2 + \frac{1}{4}\eta(w-\beta_1)^4 + k\left(\beta_{1,\xi} + \beta_{1,\xi}^2\right)\right] \mathrm{d}\xi \\ + \left[\frac{1}{2}(w-\beta_\mathrm{m})^2 + \frac{1}{4}\eta(w-\beta_\mathrm{m})^4\right](c-2l)\,.\end{aligned} \tag{5.61}$$

In order to satisfy the boundary conditions (5.59) and the continuity condition,

$$\beta_1(\xi = 0) = 0 \;\text{ and }\; \beta_1(\xi = l) = \beta_\mathrm{m} \tag{5.62}$$

have to be fulfilled. The variation of energy functional (5.61), hence $\delta\mathscr{E} = 0$, leads to

$$\begin{aligned}\delta\mathscr{E} = 2\int_0^l \left[-(w-\beta_1) - \eta(w-\beta_1)^3\right]\delta\beta_1 d\xi + 2\int_0^l k\left(1+\beta_{1,\xi}\right)\delta\beta_{1,\xi}\,\mathrm{d}\xi \\ +2\left[\frac{1}{2}(w-\beta_\mathrm{m})^2 + \frac{1}{4}\eta(w-\beta_\mathrm{m})^4 + k\left(\beta_{1,\xi}(l) + \beta_{1,\xi}^2(l)\right)\right]\delta l \\ -2\left[\frac{1}{2}(w-\beta_\mathrm{m})^2 + \frac{1}{4}\eta(w-\beta_\mathrm{m})^4\right]\delta l \\ +\left[-(w-\beta_\mathrm{m}) - \eta(w-\beta_\mathrm{m})^3\right](c-2l)\,\delta\beta_\mathrm{m} = 0.\end{aligned} \tag{5.63}$$

By employing partial integration the variation with respect to $\delta\beta_{1,\xi}$ is obtained in terms of

$$2\int_0^l k\left(1+\beta_{1,\xi}\right)\delta\beta_{1,\xi}\,\mathrm{d}\xi = 2\left[k\left(1+2\beta_{1,\xi}(l)\right)\right]\delta\beta_\mathrm{m} - 2\int_0^l k\beta_{1,\xi\xi}\delta\beta_1\,\mathrm{d}\xi \tag{5.64}$$

which can be inserted into the energy variation (5.63). Thus the variation with respect to any arbitrary length δl gives

$$k\beta_{1,\xi}(l) = 0. \tag{5.65}$$

Obviously, the obtained boundary condition may be written as

$$\beta_{1,\xi}(l) = 0. \tag{5.66}$$

The variation with respect to any arbitrary $\delta\beta_\mathrm{m}$ leads to the boundary condition

$$\left[-(w-\beta_\mathrm{m}) - \eta(w-\beta_\mathrm{m})^3\right](c-2l) + 2k = 0. \tag{5.67}$$

Varying the energy functional with respect to the unknown function β_1, we obtain an Euler equation

$$-(w-\beta_1) - \eta(w-\beta_1)^3 - k\beta_{1,\xi\xi} = 0 \tag{5.68}$$

on the interval $0 \le \xi \le l$. Still unknown in this equation is β_1, which is a function dependent on ξ and describes the plastic distorsion in the small region near the boundary of the crystal. By denoting $w - \beta_1(\xi) = q(\xi)$, the Euler equation takes the form

$$-q - \eta q^3 + kq'' = 0 \tag{5.69}$$

with $q'' = \frac{d^2q}{d\xi^2}$. In order to get a solution for β_1, the first integral of the Euler equation (5.69) may be calculated as

$$-\frac{1}{4}\eta q^4 - \frac{1}{2}q^2 + \frac{1}{2}kq'^2 = \theta, \tag{5.70}$$

with θ being an unknown constant. The phase portrait of this differential equation is illustrated in Fig 5.5.

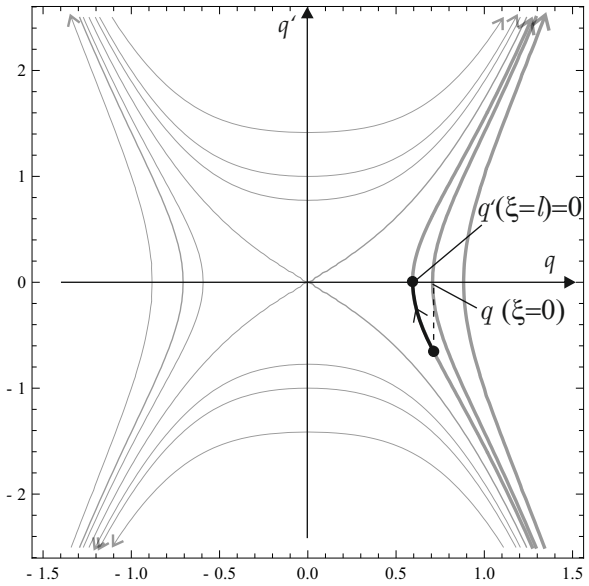

Figure 5.5.: Phase portrait.

Since we have the condition $q^{'}(\xi = l) = 0$, the phase curves lying above and below the separatrices cannot represent our solution, as they never reach the states with $q^{'} = 0$. We know that $q = w - \beta_1$, therefore we consider only positive values for q. At the left boundary layer of the crystal the plastic slip increases, consequently $q(\xi)$ must be a decreasing function of ξ. Since $q(0) = w$ and $q^{'}(l) = 0$ only the right curves (plotted bold) represent our solutions.

We already concluded that $\beta_1(l) = \beta_\mathrm{m}$, along with the boundary condition (5.66), the unknown constant θ can be determined as

$$\theta = -\frac{1}{2}(w-\beta_\mathrm{m})^2 - \frac{1}{4}\eta(w-\beta_\mathrm{m})^4. \tag{5.71}$$

Applying the separation of variables on Equation (5.69) and using the relation $q^{'} = \frac{\mathrm{d}q}{\mathrm{d}\xi}$, the differential equation reads

$$\mathrm{d}\xi = \pm\frac{\sqrt{k}\mathrm{d}q}{\sqrt{q^2 + \frac{1}{2}\eta q^4 + 2\theta}}. \tag{5.72}$$

Using $q(0) = w$, ξ may be found as

$$\xi = -\int_w^q \frac{\sqrt{k}\,\mathrm{d}\bar{q}}{\sqrt{\bar{q}^2 + \frac{1}{2}\eta\bar{q}^4 + 2\theta}}. \tag{5.73}$$

This equation gives implicitly the dependence of $q(\xi)$ on ξ. The minus in front of the integral is chosen in accordance to the phase portrait (5.5). Since the plastic slip is increasing, q has to decrease with increasing ξ, thus $\mathrm{d}q$ has to be negative. Equation (5.73) is an elliptic integral, therefore ξ can also be expressed in terms of an elliptic function. In order to find the elliptic function, the linear factor dissection is applied on the denominator, hence

$$\bar{q}^2 + \frac{1}{2}\eta\bar{q}^4 + 2\theta = \frac{1}{2}\eta\left(\bar{q}^2 + \alpha_1^2\right)\left(\bar{q}^2 - \alpha_2^2\right), \tag{5.74}$$

where $\pm\alpha_1$ and $\pm\alpha_2$ are the roots of the polynomial. They are determined by employing the Cardano' s method (for details take a look at [13]) as

$$\alpha_1 = \pm\sqrt{\frac{1}{\eta} + \sqrt{\frac{1}{\eta^2} - \frac{4\theta}{\eta}}} \qquad \alpha_2 = \pm\sqrt{-\frac{1}{\eta} + \sqrt{\frac{1}{\eta^2} + \frac{4\theta}{\eta}}}. \tag{5.75}$$

According to [27], the elliptic function is found as

$$\xi(q) = -\frac{\sqrt{\frac{2k}{\eta}}}{\sqrt{\alpha_1^2+\alpha_2^2}}\left[F\left(\arcsin\left(\sqrt{\frac{\sqrt{\alpha_1^2+\alpha_2^2}}{\sqrt{\alpha_1^2+w^2}}}\right),m\right) - F\left(\arcsin\left(\sqrt{\frac{\sqrt{\alpha_1^2+\alpha_2^2}}{\sqrt{\alpha_1^2+q^2}}}\right),m\right)\right] \tag{5.76}$$

with F denoting the inverse Jacobian elliptic function and $m = \frac{\alpha_1}{\sqrt{\alpha_1^2+\alpha_2^2}}$. Using Equation (5.76), the function q can be determined implicitly in terms of ξ. Since $q = w-\beta$ holds true, the plastic slip β is then also found for fixed overall strain w. Figure 5.6 shows the plastic slip over the cross section dependent on the dimensionless width ξ for different overall strains: $w = 0.005$, $w = 0.01$ and $w = 0.015$. For this example, the material parameters are chosen as $k = 1.138 * 10^{-3}$, $b = 2.5 * 10^{-10}$ [m] and $\rho_s = 8.8 * 10^{15}\left[\mathrm{m}^{-2}\right]$. The geometry of the crystal is considered as $a = 10^{-6}$ [m], hence $c = ab\rho_s = 2.2$ and $\eta = 1$.

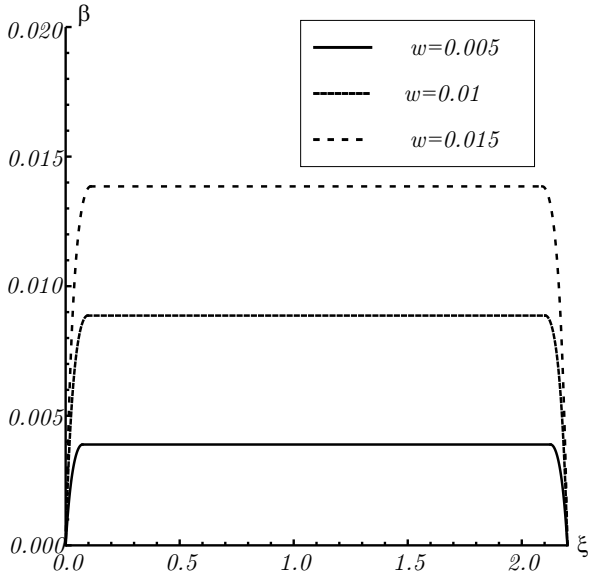

Figure 5.6.: Plastic slip β as a function of ξ for different overall strain w, reprinted by permission from [59].

At the boundary of the crystal, the plastic slip is zero. This is already required by a boundary condition as the dislocations cannot penetrate through this obstacle. In a small layer near the boundary, the plastic slip increases (at the left side) or decreases (at the right side). These small layers near the boundaries, where the plastic slip increases (or decreases) have the width l. Since $q(l) = w-\beta_m$ holds true at $\xi = l$, this width may be determined by

$$l = \xi(w-\beta_m), \tag{5.77}$$

where ξ is obtained by using the elliptic function (5.76). Along the rest of the width of the cross section, the plastic slip stays constant, $\beta = \beta_m$. As expected, with an increasing overall

strain w, the total amount of plastic slip increases as well. When $w = 0.005$, the plastic slip reaches $\beta_m = 0.004$, for $w = 0.01$ the plastic slip reaches $\beta_m = 0.009$.

An important variable which describes the crystal including a dislocation network is the dislocation density. In the case of finite anti-plane constrained shear, the dimensionless dislocation density may be calculated by $\rho = \beta_{,\xi}$. Taking the first integral (5.70), $q_{,\xi}$ may be obtained by

$$q_{,\xi} = \sqrt{\frac{1}{k}\left[2\theta + q^2 + \frac{1}{2}\eta q^4\right]} \tag{5.78}$$

where q is determined implicitly by the elliptic function (5.76). Since $q = w - \beta$ holds true, the dimensionless dislocation density is equal to $-q_{,\xi}$. In Figure 5.7 the dimensionless dislocation density as a function of ξ at different w is presented. For this example, the same constants are taken as before.

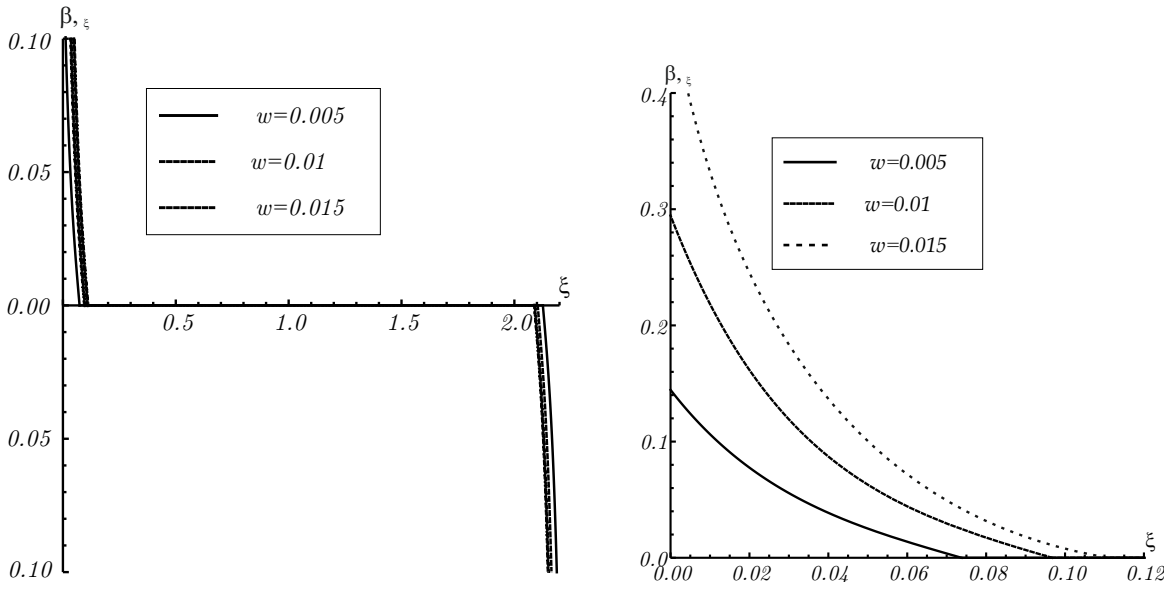

Figure 5.7.: Dimensionless dislocation density as a function of ξ for different overall strain w, partly reprinted by permission from [59].

The dislocation density for all amounts of overall strains is only non-zero at small layers with the width of l near the boundary. At the left side, the dislocation density increases and on the right boundary, the dislocation density decreases. On the right hand side of Figure 5.7, a zoom of this small layer at the left boundary is shown. For the overall shear $w = 0.005$, width of this layer is $l = 0.075$. When the overall strain is increased to $w = 0.015$ the zone enlarges to $l = 0.11$. At the boundary $\xi = 0$, the dislocation density at $w = 0.005$ is $\beta_{,\xi} = 0.15$, for $w = 0.015$ the value is bigger, $\beta_{,\xi} = 0.41$. Outside of these small layers near the boundary, the dislocation density is zero. This behavior may be explained physically: due to the shear, dislocations are nucleated and positive dislocations are pulled to the left side and negative dislocations to the right side. No dislocations remain in the middle of the crystal. When the dislocations reach the boundary, they cannot move further since the penetration of the boundary is not possible. Then they pile up at the boundary. A higher overall shear produces more dislocations, therefore zone has to be larger and hence l increases.

The boundary layer l in which the pile up of dislocations takes place is dependent on the plastic slip, thus also on our control parameter, the shear strain. In Fig. 5.8 this dependence is shown.

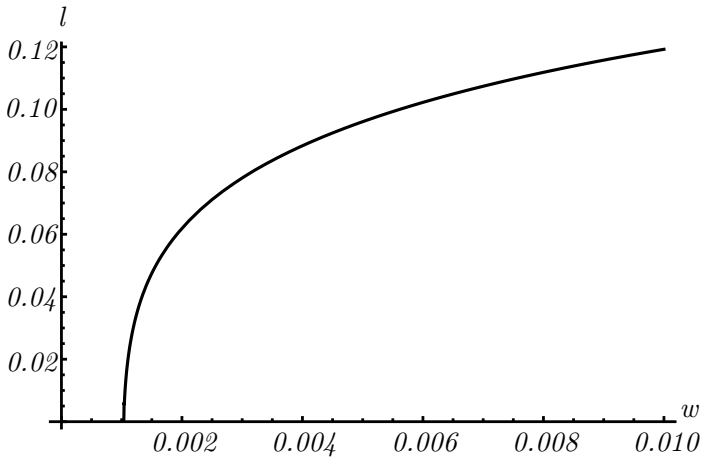

Figure 5.8.: Width l of boundary layer versus deformation.

The width of the boundary layer is zero while the crystal behaves elastic, since no dislocations pile up. When the threshold value $w = w_{\text{en}}$ is reached, the width of the layer, thus the number of the dislocation which pile up, increases strongly. With further increasing strain, the width of the boundary layer still increases, but more slowly.

A very interesting result is the stress in this plastically deformed crystal. In order to calculate this stress the threshold value w_{en} has to be determined, the strain at which the crystal starts to behave plastic and dislocations start to nucleate. At this threshold value, β_{m} is still zero since no dislocations are introduced and therefore the length of the layer l also tends to zero. Taking this into account, the boundary condition (5.67) reads

$$2k = \left(w + \eta w^3\right) c. \tag{5.79}$$

The threshold value w_{en} is the real root of this equation. For $w < w_{\text{en}}$, no dislocations are nucleated and hence the plastic slip is zero. Equation (5.79) depends on the dimensionless width of the crystal c, hence the threshold value w_{en} also depends on the geometry, exhibiting clearly the size effect. This size effect is also illustrated in Figure 5.9.

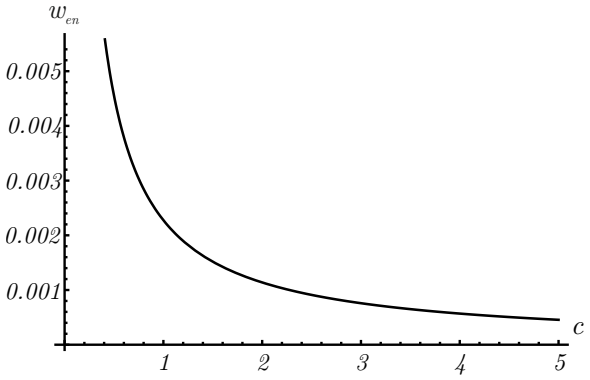

Figure 5.9.: Threshold value w_{en} dependent on dimensionless width c.

With a width tending to zero, the threshold value w_{en} tends to infinity, thus the model is not working correctly there. However, the model is a continuum model, therefore the width of the crystal c needs to be much larger than the Burgers vector, so that enough atoms and dislocations are in the crystal. Afterwards the threshold value depends reciprocally on the width c, with an increasing width, the threshold value decreases. Therefore with a larger width c, the crystal starts to behave plastic at a smaller strain w_{en} compared to one with a smaller width. For large width c, the threshold value tends to zero, which is not physically consistent as the crystal behaves elastic first. Therefore dissipation needs to be considered as well, in order to obtain a realistic behavior for a large width c.

For the case of anti plane constrained shear, the average shear component P_{32} of the first Piola Kirchhoff stress tensor is most significant. Employing the definition (5.29), the average of the first Piola Kirchoff shear stress may be obtained by

$$\bar{P}_{32} = \frac{P_{32}}{\mu} = \frac{1}{c}\int_0^c \left[\eta(w-\beta)^3 + (w-\beta)\right] \mathrm{d}\xi. \tag{5.80}$$

Figure 5.10 shows the dimensionless average shear component of the first Piola Kirchhoff stress as a function of the overall strain w.

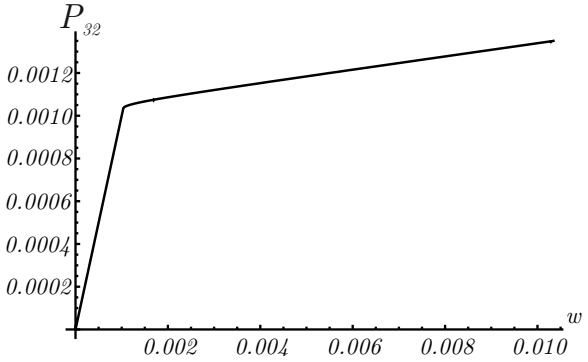

Figure 5.10.: Shear stress versus overall strain, reprinted by permission from [59].

Until the threshold value w_{en} is reached, the crystal behaves purely elastic and the plastic slip β is zero. From $w > w_{\text{en}}$, the stress increases with a smaller slope. This effect can be also called work hardening, due to the pile up of dislocations at the boundaries. There is no residual strain, this means for unloading, the stress follows the same path back. Therefore the plastic deformation is completely reversible and no energy is dissipated. This behavior is physically not consistent, the nucleation and the movement of dislocations cause dissipation, which has to be considered as well in order to obtain realistic results.

5.3.2. Finite anti-plane constrained shear with non-zero dissipation

As already mentioned in the previous section, the movement of dislocations costs energy and therefore the dissipation has to be considered as well. If the simplest type of dissipation (Equation (5.33)) is considered and under the assumption that the sign of $\dot{\beta}$ does not change, the solutions are obtained by minimizing the relaxed energy functional (5.39). For the case

of anti- plane constrained shear, this functional reads

$$\begin{aligned}\mathcal{I}[\beta(x_1)] = hL\int_0^a \Bigg[&\frac{1}{8}(\lambda+2\mu)(w-\beta)^4+\frac{1}{2}\mu(w-\beta)^2\\ &+\mu k\left(\frac{\left|\beta_{,x_1}\right|}{b\rho_{\mathrm{s}}}+\frac{1}{2}\frac{\beta_{,x_1}^2}{b^2\rho_{\mathrm{s}}^2}\right)+r\,\mathrm{sign}\left(\dot{\beta}\right)\beta\Bigg]\,\mathrm{d}x_1\end{aligned} \tag{5.81}$$

For convinience, dimensionless quantities ξ, c, E and η are introduced, taking the definitions from the previous section ((5.55), (5.56) and (5.57)). Similar to these dimensionless quantities, w_{c} is introduced to replace the critical resolved shear stress r by

$$w_{\mathrm{c}} = \frac{r}{\mu}. \tag{5.82}$$

Using these quantities, the energy functional becomes

$$\mathscr{E}[\beta(\xi)] = \int_0^c \left[\frac{1}{2}(w-\beta)^2+\frac{1}{4}\eta(w-\beta)^4+k\left|\beta_{,\xi}\right|+\frac{1}{2}k\beta_{,\xi}^2+w_{\mathrm{c}}\,\mathrm{sign}\left(\dot{\beta}\right)\beta\right]\mathrm{d}\xi. \tag{5.83}$$

The unknown minimizer $\beta(\xi)$ is considered again in the form of Equation (5.60). The minimizer is constant (β_{m}) along the width of the cross section except at small boundary layers with the width l, where the plastic slip de- or increases. The width of this layer is an unknown constant. This chosen minimizer has to fulfill the boundary conditions

$$0 \le l \le \frac{c}{2} \qquad \text{and} \qquad \beta_1(l) = \beta_{\mathrm{m}}. \tag{5.84}$$

Similar to the previous case without dissipation, the derivative $\beta_{,\xi}$ is assumed to be positive at the left boundary layer, hence

$$\beta_{,\xi} > 0 \qquad \text{for} \qquad 0 \le \xi \le l. \tag{5.85}$$

Furthermore the rate of the plastic slip is assumed to be positive ($\mathrm{sign}\left(\dot{\beta}\right) > 0$) for loading, while for loading in the opposite direction the rate considered to be negative. Considering first loading, the energy functional becomes

$$\begin{aligned}\mathscr{E} = 2\int_0^l \Bigg[&\frac{1}{2}(w-\beta_1)^2+\frac{1}{4}\eta(w-\beta_1)^4+k\left(\beta_{1,\xi}+\beta_{1,\xi}^2\right)+w_{\mathrm{c}}\beta\Bigg]\,\mathrm{d}\xi\\ &+\left[\frac{1}{2}(w-\beta_{\mathrm{m}})^2+\frac{1}{4}\eta(w-\beta_{\mathrm{m}})^4+w_{\mathrm{c}}\beta\right](c-2l).\end{aligned} \tag{5.86}$$

The function β_1 is subjected to the boundary conditions (5.62). The variation of this relaxed energy functional with respect to the unknown constants β_{m} and l leads to two boundary conditions at $\xi = l$, hence

$$\beta_{1,\xi}(l) = 0 \qquad \text{and} \qquad 2k = \left[(w-\beta_{\mathrm{m}})+\eta(w-\beta_1)^3-w_{\mathrm{c}}\right](c-2l). \tag{5.87}$$

The variation of the relaxed energy functional under loading with respect to the unknown function β_1 gives the Euler equation in the form

$$(w-\beta_1)+\eta(w-\beta_1)^3-w_{\mathrm{c}}+k\beta_{1,\xi,\xi} = 0. \tag{5.88}$$

Analogously to the case without dissipation, the function β_1 is still unknown in this Euler equation. We may replace $w-\beta_1$ by introducing q, then the first integral from the differential equation (5.88) can be determined as

$$\frac{1}{2}kq'^2-\frac{1}{2}q^2-\frac{1}{4}\eta q^4+w_{\mathrm{c}}q = \theta, \tag{5.89}$$

where θ is a still unknown constant. Since $q'(l) = 0$ and $q(l) = w - \beta_\mathrm{m}$ hold true, θ is identified as

$$\theta = -\frac{1}{2}(w-\beta_\mathrm{m})^2 - \frac{1}{4}(w-\beta_\mathrm{m})^4 + w_\mathrm{c}(w-\beta_\mathrm{m}). \tag{5.90}$$

From the first integral (5.89), $d\xi$ by using $q' = \frac{\mathrm{d}q}{\mathrm{d}\xi}$ is obtained as

$$\mathrm{d}\xi = \pm\frac{\sqrt{k}\mathrm{d}q}{\sqrt{q^2 + \frac{1}{2}\eta q^4 - 2w_\mathrm{c}q + 2\theta}}, \tag{5.91}$$

with the minus sign chosen again due to a phase portrait analogously to the case without dissipation. Taking $q(0) = w$ into account, we get the elliptic integral

$$\xi = -\int_w^q \frac{\sqrt{k}\,\mathrm{d}\bar{q}}{\sqrt{\bar{q}^2 + \frac{1}{2}\eta\bar{q}^4 - 2w_\mathrm{c}\bar{q} + 2\theta}}. \tag{5.92}$$

In order to express this elliptic integral by an elliptic function, the polynomial in the integrand has to be factorized. For small w_c, this factorization reads

$$\bar{q}^2 + \frac{1}{2}\eta\bar{q}^4 - 2w_\mathrm{c}\bar{q} + 2\theta = \frac{1}{2}\eta(\bar{q}-\alpha_1)(\bar{q}-\alpha_2)\left[(\bar{q}-\chi_1)^2 + \chi_2^2\right], \tag{5.93}$$

with α_1 and α_2 being the real roots of the polynomial and $\chi_1 \pm i\chi_2$ being the complex-conjugate roots. These roots are determined with the Cardano's method [13]. Ordering the real roots such that $\alpha_1 < \alpha_2$ and taking into account that w and q are larger than α_2, the elliptic function for ξ dependent on q [27] reads

$$\xi = \frac{\sqrt{\frac{2k}{\eta}}}{\sqrt{f_1 f_2}}\left[F\left(2\arctan\left(\sqrt{\frac{f_2(w-\alpha_2)}{f_1(w-\alpha_1)}}\right), m\right) - F\left(2\arctan\left(\sqrt{\frac{f_2(q-\alpha_2)}{f_1(q-\alpha_1)}}\right), m\right)\right], \tag{5.94}$$

with $f_1 = \sqrt{(\chi_1-\alpha_2)^2 + \chi_2^2}$, $f_2 = \sqrt{(\chi_1-\alpha_1)^2 + \chi_2^2}$ and $m = \frac{1}{2}\sqrt{\frac{(f_1+f_2)^2 - (\alpha_1+\alpha_2)^2}{f_1 f_2}}$. Using the elliptic function (5.94), the plastic slip β may be determined implicitly since $q = w - \beta$. In Figure 5.11, the plastic slip along the width of the cross section for different total strains is presented. The material and geometry constants are taken from the case of no dissipation and the dimensionless critical resolved shear stress is set to $w_\mathrm{c} = 2 \cdot 10^{-3}$.

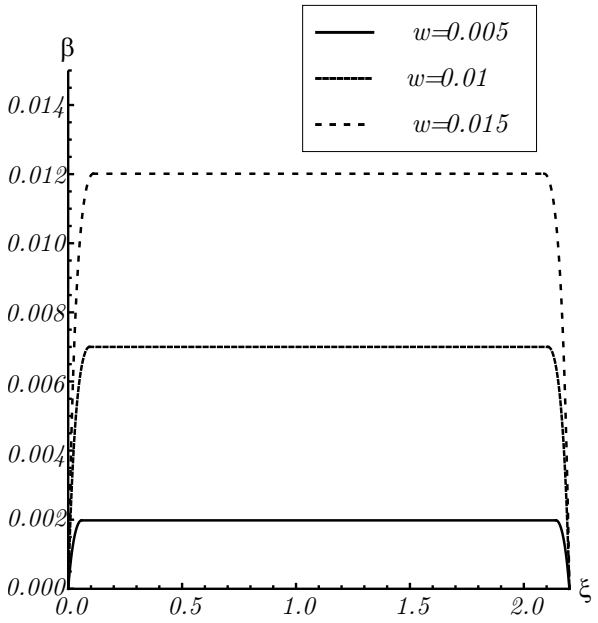

Figure 5.11.: Plastic slip β as a function of ξ for different w, reprinted by permission from [59].

At the boundary $\xi = 0$ the plastic slip is zero, then it increases up to $\beta = \beta_{\mathrm{m}}$. A higher total strain leads to an increased β_{m}. Near the right boundary, in a small layer, the plastic slip decreases to zero. Compared to the case without dissipation, the behavior of the plastic slip is similar, but the maximum of the plastic slip is decreased. For a total strain of $w = 0.015$, if dissipation is taken into account, the plastic slip reaches $\beta_{\mathrm{m}} = 0.002$. For the same strain but zero dissipation, the plastic slip reaches $\beta_{\mathrm{m}} = 0.004$. The physical explanation for this behavior is that the dissipation due to the movement of dislocations costs energy, therefore less dislocations can be moved and less plastic slip is produced. The basic mechanism stays the same: due to the shear, dislocations are nucleated and pulled to the boundaries where they pile up.

Analogously to the case without dissipation, the dislocation density may be determined by $\rho = q_{,\xi}$ and from formula (5.89) the result finally reads

$$q_{,\xi} = \sqrt{\frac{1}{k}\left(q^2 + \frac{1}{2}\eta q^4 - 2w_{\mathrm{c}}q + 2\theta\right)}, \tag{5.95}$$

where q dependent on ξ obtained implicitly by Equation (5.94). This dimensionless dislocation density along the cross section is shown in 5.12 for different total strain.

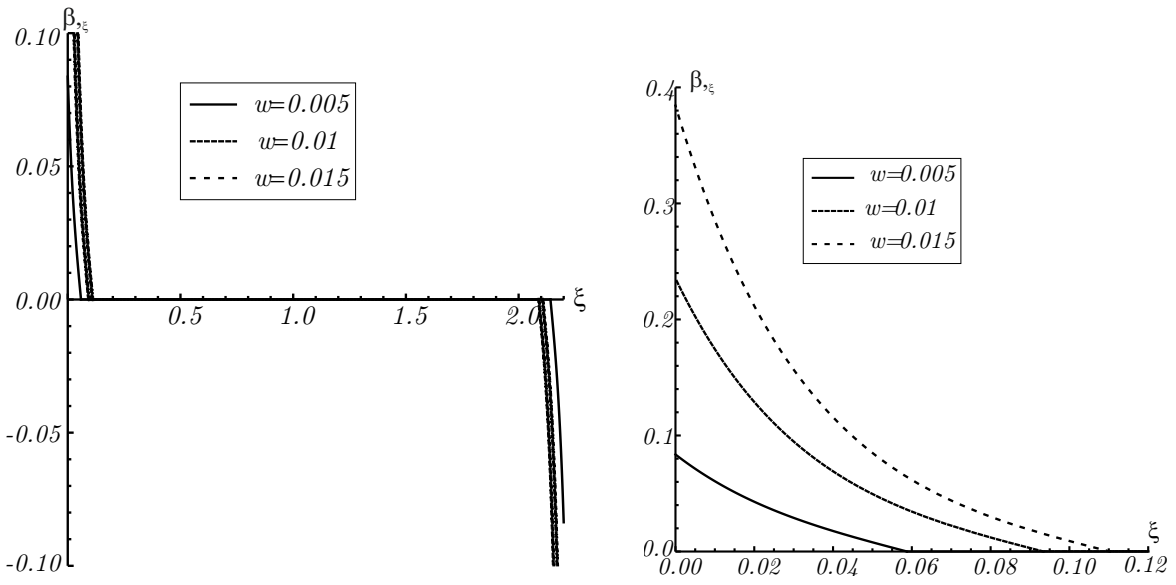

Figure 5.12.: Dimensionless dislocation density $q_{,\xi}$ as a function of ξ for different w, partly reprinted by permission from [59].

The behavior of the dimensionless dislocation density is similar to the case without dissipation. Due to the loading, dislocations are nucleated and pulled to the boundaries. The positive ones to the left boundary and the negative ones to the right. The boundary is an obstacle which cannot be penetrated, hence they pile up. A higher amount of overall strain leads to more piled up dislocations, for $w = 0.001$, the density at the boundary is $q_{,\xi} = 0.1$, while for $w = 0.015$ the density reads $q_{,\xi} = 0.38$. The dissipation reduces the amount of dislocations, from $q_{,\xi} = 0.14$ for $w = 0.001$ without dissipation to $q_{,\xi} = 0.1$ with the same strain but considering dissipation. Due to the dissipated energy, less dislocations can be moved to the boundary.

Similar to the case without dissipation, the threshold value w_y, at which the nucleation of dislocations starts, has to be determined in order to obtain the stresses. If the total strain is smaller then the threshold value, no dislocations are nucleated and therefore the plastic slip is zero. The threshold value may be determined by using the boundary condition (5.87) with β_m and l tending to zero since no plastic slip is present. Thus the threshold value is the root of

$$\eta w^3 + w = w_\mathrm{c} + \frac{2k}{c}. \tag{5.96}$$

From (5.96) we see that w_y depends on c which is the dimensionless width of the cross section, this exhibits the size effect. The dependence of the threshold value w_y with the width c is presented in Figure 5.13

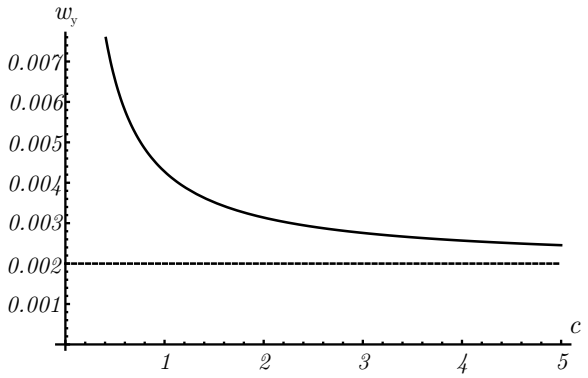

Figure 5.13.: Threshold value w_y dependent on c.

As the dimensionless width of the geometry tends to zero (which is physically not possible), the threshold value tends to infinity, similar to the case without dissipation. Again, this continuum model needs a width c larger than the Burgers vector, so that enough dislocations can be inside the crystal. With an increasing width c, the threshold value decreases. Due to the dissipation, for large width c, the threshold value tends to w_c, which is illustrated by a dashed line in Fig. 5.13.

If dissipation is taken into account, the direction of the load is important in the minimizing problem. Loading in the opposite direction as before, the rate of the plastic slip is negative, hence $\mathrm{Sign}\left(\dot{\beta}\right) = -1$. The minimizer β has to be considered again in the form of formula (5.60) and inserted into the relaxed energy functional. Then this relaxed energy functional reads

$$\begin{aligned}\mathscr{E} = 2\int_0^l \left[\frac{1}{2}(w-\beta_1)^2 + \frac{1}{4}\eta(w-\beta_1)^4 + k\left(\beta_{1,\xi} + \beta_{1,\xi}^2\right) + w_c\beta\right] \mathrm{d}\xi \\ + \left[\frac{1}{2}(w-\beta_m)^2 + \frac{1}{4}\eta(w-\beta_m)^4 - w_c\beta\right](c-2l)\,.\end{aligned} \tag{5.97}$$

Analogously to the loading case, the variation of this functional with respect to β_m and l leads to two boundary conditions,

$$\beta_{1,\xi}(l) = 0 \qquad \text{and} \qquad 2k = \left[(w-\beta_m) + \eta(w-\beta_1)^3 + w_c\right](c-2l)\,. \tag{5.98}$$

The variation with respect to the unknown function β_1 gives the differential equation

$$(w-\beta_1) + \eta(w-\beta_1)^3 + w_c + k\beta_{1,\xi,\xi} = 0. \tag{5.99}$$

The procedure of solving this problem remains the same. We set $w-\beta_1$ and determine the first integral, hence

$$\frac{1}{2}kq'^2 - \frac{1}{2}q^2 - \frac{1}{4}\eta q^4 - w_c q = \theta. \tag{5.100}$$

The phase portrait of this differential equation shows similar characteristics to the previous ones. The constant θ is determined by the conditions $q'(l) =$ and $q(l) = w-\beta_m$ as

$$\theta = -\frac{1}{2}(w-\beta_m)^2 - \frac{1}{4}(w-\beta_m)^4 - w_c(w-\beta_m)\,. \tag{5.101}$$

From the first integral (5.100) and $q(0) = w$, the implicit dependence of q on ξ in terms of the elliptic integral is obtained,

$$\xi = -\int_w^q \frac{\sqrt{k}\,\mathrm{d}\bar{q}}{\sqrt{\bar{q}^2 + \frac{1}{2}\eta\bar{q}^4 + 2w_c\bar{q} + 2\theta}}, \tag{5.102}$$

with $-\mathrm{d}q$ chosen in accordance to the phase portrait. The polynomial can be again factorized like in the previous case as

$$\bar{q}^2 + \frac{1}{2}\eta\bar{q}^4 - 2w_c\bar{q} + 2\theta = \frac{1}{2}\eta(\bar{q} - \alpha_1)(\bar{q} - \alpha_2)\left[(\bar{q} - \chi_1)^2 + \chi_2^2\right]. \tag{5.103}$$

Then the elliptic function that calculates q implicitly is given by Equation (5.94). The only difference is the values of roots from the polynomial and in this loading case α_2 and w may have negative values in some range of $0 \leq l \leq \frac{c}{2}$.

Between loading and loading in the opposite direction, the material is unloaded and $\dot{\beta} = 0$. In this process, the dislocations remain frozen hence the plastic slip remains constant.

After the determination of the plastic slip, the energy can be calculated and the stresses as well. In Figure 5.15 the average shear component of the first Piola-Kirchhoff stress tensor for one load cycle (illustrated in Figure 5.14) is shown. The stress component is calculated by Equation (5.80).

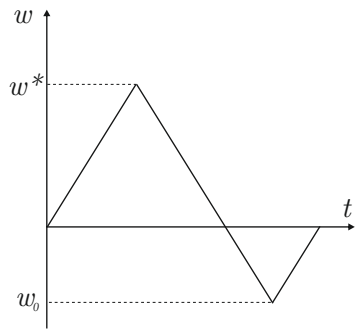

Figure 5.14.: Loading path of finite anti-plane constrained shear, reprinted by permission from [59].

First the crystal is loaded up to the strain w^*, then unloaded and loaded in the opposite direction up to w_0. We choose $w_0$that all dislocation which were created at loading are vanished by loading in the opposite direction. Therefore w_0 is found by $\beta = 0$. Afterwards, the crystal is unloaded until the total strain is zero.

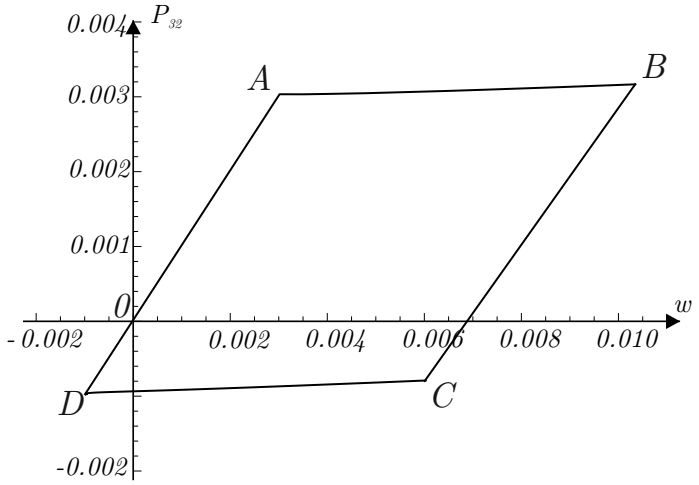

Figure 5.15.: Dimensionless shear stress for one load cycle, reprinted by permission from [59].

For a strain smaller than w_y, no dislocations are nucleated, therefore the plastic slip is zero and the crystal behaves elastic. This behavior implies that the stress strain cure is linear. From A to B, the crystal is loaded further ($w > w_y$) with $\dot{\beta} > 0$. Dislocations are nucleated and pulled to the boundaries where they pile up. This pile up leads to a work hardening in the stress strain curve. After the loading process, the crystal is unloaded (line BC) and the strain decreases from w^* to some value between w^* and w_0. The plastic slip remains constant at β^* as the dislocations are frozen. Hence the crystal behaves elastically and the stress strain curve decreases linearly. As the strain is further decreased, the crystal is loaded in the opposite direction and plastic behavior occurs (with $\dot{\beta} > 0$). At this loading path, all dislocations which has been nucleated are pulled to the opposite direction. Therefore the stress strain curve exhibits work hardening again. The dislocations annihilate and at loading point D (which corresponds to our chosen w_0) all dislocations are vanished. Finally, since all dislocations are vanished, the crystal behaves elastic again (line D0). Dissipation only occurs when the plastic slip changes, hence at line AB and CD. The stress strain curve exhibits the Bauschinger effect: due to the plastic deformations, the yield stress is decreased (shifted vertically). This behavior is achieved without any assumptions, it occurs due to the dislocation movements.

5.4. Finite plane-strain constrained shear

In this section, the nonlinear continuum dislocation theory is applied to a crystal under plane-strain constrained shear. For this example the single crystal is considered as a strip with the undeformed length L and a rectangular cross section with the width a and the height h (presented in Figure 5.16). The length L of this strip is considered to be large enough in comparison to the width and height to guarantee the plane strain state.

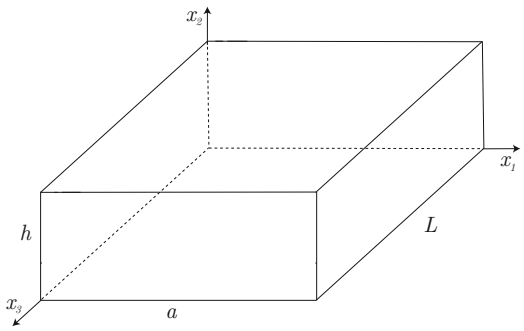

Figure 5.16.: A strip of a single crystal.

This crystal is assumed to be dislocation free at the beginning. It is placed in a hard device with prescribed displacements at its boundary, illustrated in Figure 5.17. The displacements at the upper and lower sides of the boundaries read

$$\begin{aligned} u_1(x_2 = 0) = u_2(x_2 = 0) = u_3(x_2 = 0) = 0 \\ \text{and } u_1(x_2 = h) = wh, u_2(x_2 = h) = u_3(x_2 = h) = 0, \end{aligned} \tag{5.104}$$

with w being the overall strain.

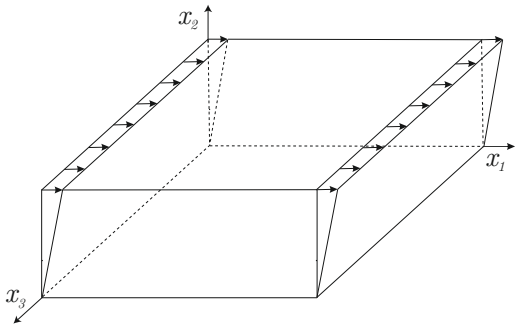

Figure 5.17.: Deformed strip under plane-strain constrained shear, reprinted by [60].

Using these boundary conditions, the displacements are found as

$$u_1 = wx_2 \qquad \text{and} \qquad u_2 = u_3 = 0. \tag{5.105}$$

By employing definition (2.6) on the displacements, the total deformation gradient is obtained as

$$\mathbf{F} = \begin{pmatrix} 1 & w & 0 \\ 0 & 1 & 0 \\ 0 & 0 & 1 \end{pmatrix}. \tag{5.106}$$

If the total shear strain is sufficiently small, the crystal behaves purely elastic. Therefore the plastic deformation gradient and the plastic slip are zero. When a critical shear strain is archived, edge dislocations appear and plastic slip occurs. The slip direction of this slip is assumed to be parallel to the x_1 axis and the slip planes parallel to the plane $x_2 = \text{const}$, hence

$$\mathbf{s} = \begin{pmatrix} 1 \\ 0 \\ 0 \end{pmatrix} \qquad \text{and} \qquad \mathbf{m} = \begin{pmatrix} 0 \\ 1 \\ 0 \end{pmatrix}. \tag{5.107}$$

Then the dislocation lines are parallel to the x_3 axis. Considering these assumptions, the plastic slip is dependent on x_1 and x_2,

$$\beta = \beta(x_1, x_2). \tag{5.108}$$

Analogously to the previous example, the plastic deformation gradient may be determined by Equation (5.45) as

$$\mathbf{F}^{\mathrm{p}} = \begin{pmatrix} 1 & \beta(x_1,x_2) & 0 \\ 0 & 1 & 0 \\ 0 & 0 & 1 \end{pmatrix}. \tag{5.109}$$

Using the multiplicative split of the deformation gradient (Eq (2.67)), the elastic deformation gradient is calculated as

$$\mathbf{F}^{\mathrm{e}} = \begin{pmatrix} 1 & w-\beta(x_1,x_2) & 0 \\ 0 & 1 & 0 \\ 0 & 0 & 1 \end{pmatrix}. \tag{5.110}$$

Taking the infinitesimal area da perpendicular to the x_3 axis, the resultant Burgers vector of all excess dislocations whose dislocation lines cross da reads

$$\mathbf{b}_{\mathrm{r}} = \begin{pmatrix} \beta_{,x_1} \\ 0 \\ 0 \end{pmatrix} da \tag{5.111}$$

using the definitions (5.6) and (5.7). This vector is parallel to the slip direction, since only edge dislocations appear in this example. The number of excess dislocations per unit area represents the scalar dislocation density and takes the form

$$\rho = \frac{1}{b}\left|\beta_{,x_1}\right|. \tag{5.112}$$

5.4.1. Prototype free energy density

Our main interest is the modeling of the martensitic phase transformation, which arise due to a non-convexity of our chosen energy density. In order to employ the nonlinear continuum dislocation theory, the energy of the crystal should be dependent on the elastic deformation gradient and the scalar dislocation density. For a first examination of the problem, a prototype free energy density per unit volume of the undeformed crystal under plain strain constrained shear with the form

$$\Psi(\mathbf{F}^{\mathrm{e}}, \rho) = \frac{1}{2}\mu(w-\beta)^2(w-\beta-1)^2 + \mu c b^2 \rho \tag{5.113}$$

is analyzed. The first part of Equation (5.113) describes the elastic energy of the crystal due to macroscopic elastic deformations. For a small shear strain, this term is quadratic and the material behavior elastic, for a larger range, it becomes non convex with respect to the elastic shear strain $(w-\beta)$. Thus, a martensitic phase transformation will occur in the range of large deformations. The last subtrahend "1" in the second factor may be interpreted as the transformation strain, from $w = 1$ no phase mixing is possible anymore. The second term of the energy density (5.113) represents the energy of the dislocation network for small dislocation densities (taken from [74]). The material constant c is considered later as 0.3. For

larger dislocation densities, this energy assumption is not appropriate anymore and should be replaced by a logarithmic form including the saturated dislocation density proposed from Berdichevsky [5] [6].

As already mentioned in the previous example, the dissipation caused by the dislocation movement cannot be neglected. Considering the simplest kind of dissipation, the relaxed energy functional may be determined as

$$\mathcal{I}[\beta] = L\int_0^h \int_0^a \left[\frac{1}{2}\mu(w-\beta)^2(w-\beta-1)^2 + \mu cb\left|\beta_{,x_1}\right| + r\,\mathrm{Sign}\left(\dot{\beta}\right)\beta\right] \mathrm{d}x_1\,\mathrm{d}x_2 \tag{5.114}$$

if no forces act on the crystal. Then the true plastic slip minimizes this energy functional (Eq (5.114)) among all admissible functions $\beta(x_1, x_2)$ which fulfill the boundary conditions

$$\beta(x_1, x_2 = 0) = \beta(x_1, x_2 = h) = 0. \tag{5.115}$$

Additionally, the plastic slip has to be a continuous function of the total strain. If the total strain is zero, no plastic slip and no dislocations are nucleated.

Finite plane-strain constrained shear with uniform deformations

If a shear is applied to the crystal, which is higher then a threshold value, dislocations are created and move to the boundary. If the boundary is free, they form there legs as their traces. Then the dislocation density inside the crystal is vanished and the plastic deformations can be considered to be uniform, hence $\beta = \text{const.}$. In this case, the energy of the dislocation network is zero and the relaxed energy functional reads

$$\mathcal{I}_\mathrm{u}[\beta] = Lah\left[\frac{1}{2}\mu(w-\beta)^2(w-\beta-1)^2 + r\,\mathrm{Sign}\left(\dot{\beta}\right)\beta\right]. \tag{5.116}$$

Similar to the previous example of anti-plane constrained shear for convenience dimensionless quantities are introduced. The dimensionless energy per unit volume at uniform deformations can be expressed as

$$\mathscr{E}_\mathrm{u}[\beta] = \frac{\mathcal{I}_\mathrm{u}[\beta]}{Lah} = \left[\frac{1}{2}\mu(w-\beta)^2(w-\beta-1)^2 + w_\mathrm{c}\,\mathrm{Sign}\left(\dot{\beta}\right)\beta\right]. \tag{5.117}$$

with $w_\mathrm{c} = \frac{r}{\mu}$. The crystal is slowly loaded from zero up to a large value of w and we assume for this loading process that $\dot{\beta} > 0$, hence $\mathrm{Sign}\left(\dot{\beta}\right) = 1$. Then the uniform plastic slip minimizes the relaxed energy functional and the sufficient condition reads

$$\frac{\mathrm{d}\mathscr{E}_\mathrm{u}}{\mathrm{d}\beta} = 0, \tag{5.118}$$

or

$$2(w-\beta)^3 - 3(w-\beta)^2 + (w-\beta) - w_\mathrm{c} = 0. \tag{5.119}$$

Applying a substitution $(w-\beta) = \theta$, this equation is cubic for θ and therefore three roots exist. If w_c is sufficiently small, these three roots are real and may be denoted with θ_1, θ_2 and θ_3 such that $\theta_1 < \theta_3 < \theta_2$. In Figure 5.18 the roots are illustrated with $w_\mathrm{c} = 10^{-3}$.

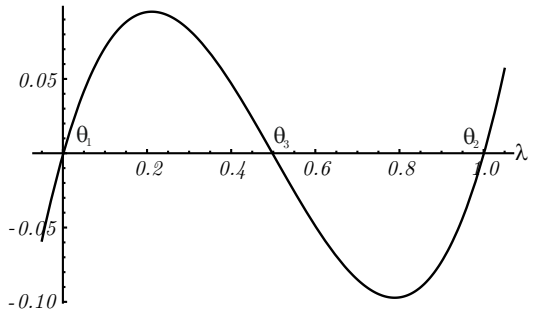

Figure 5.18.: Roots of cubic Equation, reprinted by permission from [60].

For the determination of the minimum of the relaxed energy, in addition to the sufficient condition, the necessary condition $\frac{\mathrm{d}^2 E_\mathrm{u}}{\mathrm{d}\beta^2} > 0$ has to be fulfilled. Therefore only the roots θ_1 and θ_2 minimize the relaxed energy. From these two roots θ_i the plastic slip is obtained by

$$\beta_i = w - \theta_i \qquad \text{for } i = 1,2. \tag{5.120}$$

Initially, the crystal is dislocation free hence the plastic slip is zero, $\beta = 0$. Then it is loaded with an increasing w, at $w = \theta_1$, dislocations occur and the plastic slip starts to increase. Therefore root $\theta_1 \approx w_\mathrm{c}$ can be interpreted as the threshold value. As long as the total strain is smaller than θ_1, the plastic slip is zero, no dislocations are nucleated and the crystal behaves completely elastic. Since no plastic slip is present for $w < \theta_1$, the minimum relaxed energy in this region reads

$$\mathscr{E}_\mathrm{u} = \frac{1}{2} w^2 (w-1)^2 . \tag{5.121}$$

When the total strain reaches the threshold value and increases further ($w > \theta_1$), dislocations are nucleated and move to the boundaries where they form legs. The plastic slip is obtained as $\beta = w - \theta_1$ and the minimum of the relaxed energy is determined as

$$\mathscr{E}_\mathrm{u} = \frac{1}{2} \theta_1^2 (\theta_1 - 1)^2 + w_\mathrm{c} (w - \theta_1) . \tag{5.122}$$

When the total strain becomes much larger than the threshold value, the dissipation due to dislocation gliding dominates the relaxed energy. The second minimum of the energy is obtained when $w > \theta_2 \approx 1 + w_\mathrm{c}$ holds true and then the plastic slip reads $\beta = w - \theta_2$. The energy is found as

$$\mathscr{E}_\mathrm{u} = \frac{1}{2} \theta_2^2 (\theta_2 - 1)^2 + w_\mathrm{c} (w - \theta_2) . \tag{5.123}$$

The determined uniform deformations (5.120) do not fulfill the boundary condition (5.115), since the plastic slip is a nonzero constant. Therefore the plastic slip has to be modified slightly to

$$\beta = \begin{cases} \frac{w-\theta_i}{\epsilon} x_2 & \text{if } 0 \le x_2 \le \epsilon \\ w - \theta_i & \text{if } \epsilon \le x_2 \le h - \epsilon \\ \frac{w-\theta_i}{\epsilon} (h - x_2) & \text{if } h - \epsilon \le x_2 \le h \end{cases} \tag{5.124}$$

with $i = 1,2$. This modified plastic slip is constant along the height except near to the boundaries: there it in- or decreases to zero. This correction is also illustrated in Figure 5.19.

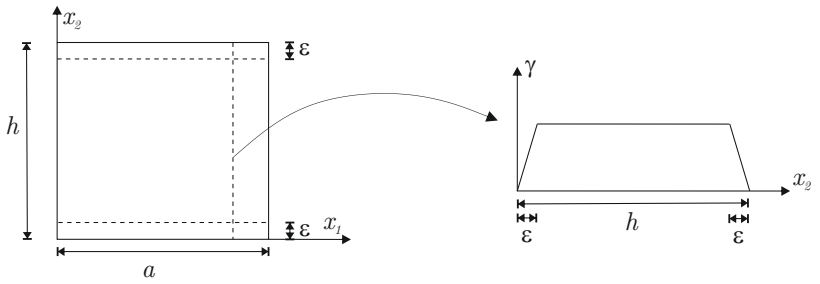

Figure 5.19.: Modified plastic slip.

The constant ϵ describes the small width of the layer in which the plastic slip tends to zero. This modified plastic slip satisfies the boundary conditions (5.115) and the contribution of this correction tends to zero as the width ϵ tends to zero.

The shear stress is calculated by $P_{12} = \frac{\mathrm{d}\mathscr{E}}{\mathrm{d}w}$ as

$$P_{12} = \mu(w-\beta)(w-\beta-1)^2 + \mu(w-\beta)^2(w-\beta-1) \tag{5.125}$$

with β being piecewise constant dependent on w. The stress strain curve is presented in Figure 5.20.

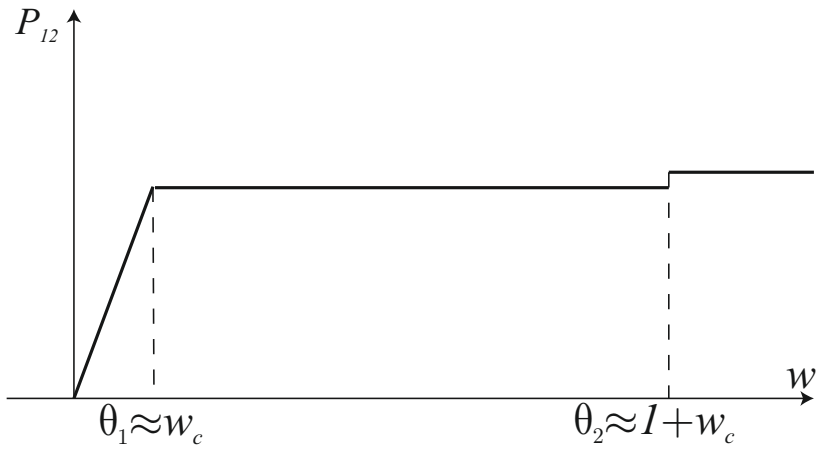

Figure 5.20.: Stress strain curve for uniform plastic deformations.

Up to $w = \theta_1 \approx w_c$, no dislocations are nucleated and the plastic slip is zero, hence the stress strain relation is purely elastic. When the threshold value is reached, the dislocations appear and move to the boundaries where they form the legs, the plastic slip is $\beta = w - \theta_1$ and the stress is constant with an increasing strain. At $w = 1 + w_c$ the stress has a jump since the plastic slip jumps from $\beta = w - \theta_1$ to the other state $\beta = w - \theta_2$.

Finite plane-strain constrained shear with laminate structure as energy minimizer

In Figure 5.21 the energy density versus the elastic deformation is presented. In this figure, the contribution to the energy density due to the dislocation network is neglected since it is independent of the elastic deformation.

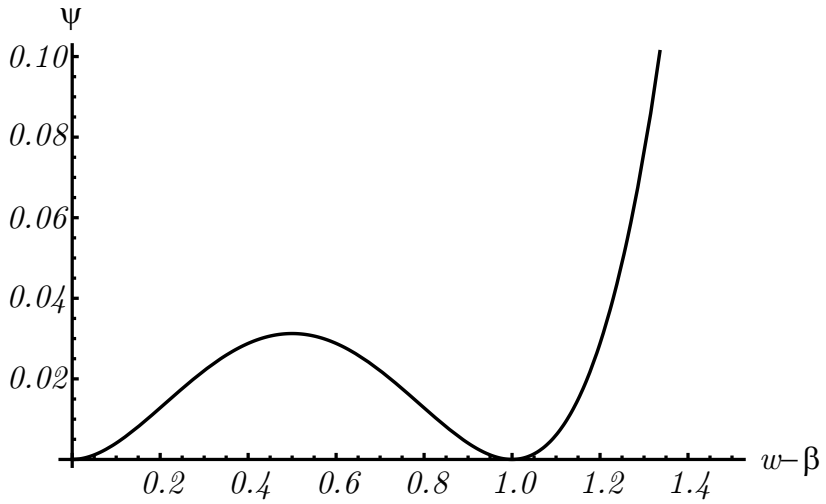

Figure 5.21.: Energy density versus $w-\beta$.

In this figure the non-convexity of the energy density in the range of $0 < w-\beta < 1$ is visible. Therefore the uniform deformations which are found in the previous section cannot minimize the relaxed energy functional in that region ($0 < w < 1$). As explained in 2.6.2, a formation of a microstructure is energetically favorable for the homogeneous crystal. We consider a laminate structure depending on x_1 such that the first phase occupies the volume fraction λ. In this phase the plastic slip is $\beta = w$. The second phase has the volume fraction $1-\lambda$ and the plastic slip in this phase reads $\beta = w-1$. The plastic slip is now piecewise constant along x_1. This constructed minimizer is schematically sketched in Figure 5.22.

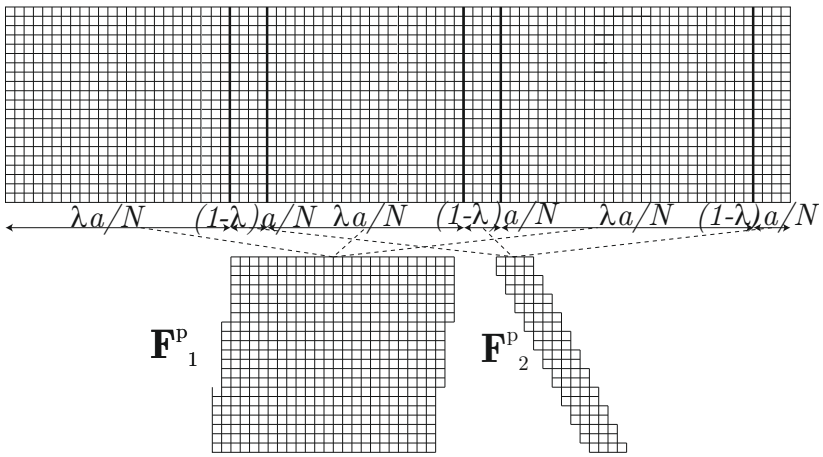

Figure 5.22.: Minimizer: Piecewise constant plastic deformation, reprinted by permission from [60].

In order to get a minimal dissipation, the parameter λ is determined by the condition

$$\int_A \beta \, \mathrm{d}x_1 \, \mathrm{d}x_2 = 0 \tag{5.126}$$

which leads for these patterns to

$$\int_0^{a\lambda} w \, \mathrm{d}x_1 + \int_0^{(1-\lambda)a} (w-1) \, \mathrm{d}x_1 = 0 \qquad \Rightarrow \qquad \lambda w + (1-\lambda)(w-1) = 0. \tag{5.127}$$

Hence, the volume fraction reads $\lambda = 1 - w$.

Since the elastic deformations (Equation (5.110)) are dependent on the plastic slip, they have to be piecewise constant as well. The elastic shearing $(w - \beta)$ is zero in the first phase (there $\beta = w$) and in the second phase $(w - \beta) = 1$. Figure 5.23 shows schematically the plastic and elastic deformations in both phases.

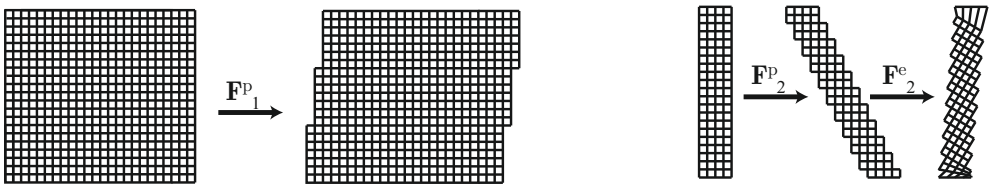

Figure 5.23.: The sequences of deformations in both phases, reprinted by permission from [60].

As already mentioned before, the elastic deformation gradient deforms the crystal lattice with frozen dislocations, therefore the lattice of the first phase is not changed, as the elastic deformation gradient is zero there, while the lattice of phase two is strongly changed.

The elastic and the plastic shearing of both phases bring the crystal to its final shape, shown in Figure 5.24.

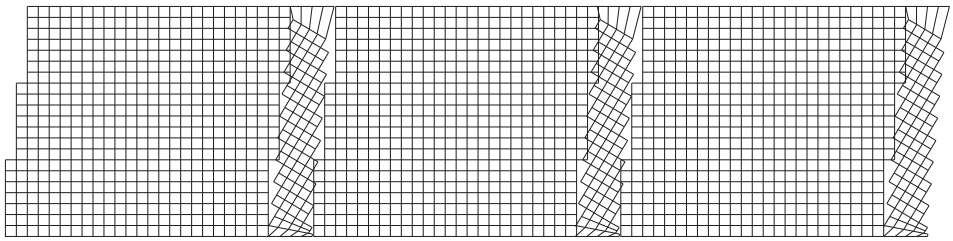

Figure 5.24.: Final shape of the crystal, reprinted by permission from [60].

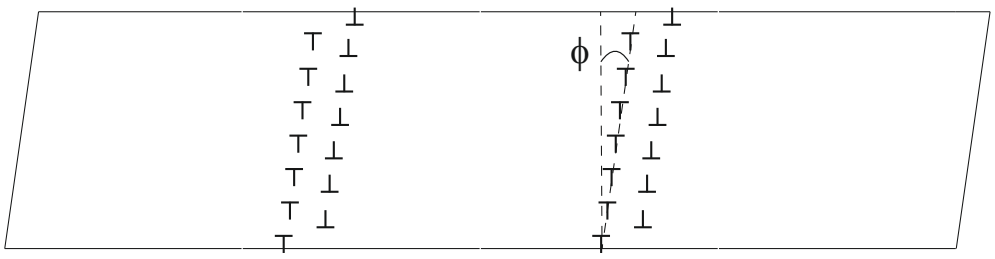

Figure 5.25.: Dislocation arrays in deformed crystal, reprinted by permission from [60].

Since both deformations are nonuniform and discontinuous, two dislocation array occur. For small s, the two close disloaction arrays act like a double array. As the plastic slip in both phases is the same, the surface energy density with zero resultant Burgers vector reads

$$\rho = \pm b. \tag{5.128}$$

Due to the rotation of the lattice in phase two, resulting from the elastic deformation gradient, the dislocation arrays are inclined by an angle ϕ such that $\tan\phi = w$, as presented in Figure 5.25. The total deformation is compatible.

Now we have to show that the relaxed energy caused by the laminar structure is less then the resulting relaxed energy under uniform plastic deformations. Therefore the resulting energies have to be compared. First the relaxed energy caused by the laminar structure is examined. The contribution of the relaxed energy functional (5.114) caused by the macroscopic elastic deformation (first term) vanishes for both phases (Remark: $\beta = w$ for the first phase, $\beta = w - 1$ in the second). The integration over the dissipation term for both phases leads to

$$\mathscr{E} = \int_0^{\lambda a} w_c w \, \mathrm{d}x_1 + \int_0^{(1-\lambda)a} w_c (1-w) w \, \mathrm{d}x_1 = a\left[w_c (w\lambda + (1-\lambda)(w-1))\right]. \tag{5.129}$$

Due to the choice of λ (Equation (5.127)), this equation is equal to zero. The energy contributed by the dislocation network is also zero in the phases since the plastic slip is constant in each phase. The only contribution to the energy is introduced by the jumps of the plastic slip at the surfaces of theses phases. These jumps can be calculated by

$$\mathscr{E}_i = \mu L h N c b \tag{5.130}$$

where N is the number of jump surfaces. This energy term is consistent to the term of the dislocation network of the relaxed energy (5.114) and is the only term in the relaxed energy for the material with a laminate structure. The non-convexity in the energy occurs at $0 < w - \beta < 1$, in that region, the relaxed energy with uniform plastic deformations is found by Equation (5.122). Thus as long as the relaxed energy resulting from the microstructure is smaller than the energy caused by homogenous deformations, or as long as

$$N c b < a\left[\frac{1}{2}\lambda_1^2 (1-\theta_1)^2 + w_c (w - \theta_1)\right] \tag{5.131}$$

is fulfilled, the laminar structure is preferable because the relaxed energy is smaller. From Equation (5.130), we see that a phase mixing with one jump surface (one dislocation array) gives the smallest relaxed energy of the crystal. A larger number of phases is also possible as local minimizer but the relaxed energy is higher. These metastable solutions may occur if there is an obstacle (for example impurities) which prevents the expansion of one phase. If the energy barrier due to this obstacle is higher than the energy of the interface, it is favorable building a finer microstructure.

Similar to the uniform plastic deformations, the piecewise constant plastic deformations do not satisfy the boundary condition (5.115). Therefore, the plastic slip in the first phase has to be corrected to

$$\beta = \begin{cases} \frac{w}{\epsilon} x_2 & \text{if } 0 \le x_2 \le \epsilon \\ w & \text{if } \epsilon \le x_2 \le h - \epsilon \\ \frac{w}{\epsilon}(h - x_2) & \text{if } h - \epsilon \le x_2 \le h \end{cases} \tag{5.132}$$

and in the second phase to

$$\beta = \begin{cases} \frac{w-1}{\epsilon} x_2 & \text{if } 0 \le x_2 \le \epsilon \\ w - 1 & \text{if } \epsilon \le x_2 \le h - \epsilon \\ \frac{w-1}{\epsilon}(h - x_2) & \text{if } h - \epsilon \le x_2 \le h \end{cases}. \tag{5.133}$$

In Figure 5.26 the corrected plastic slip is presented.

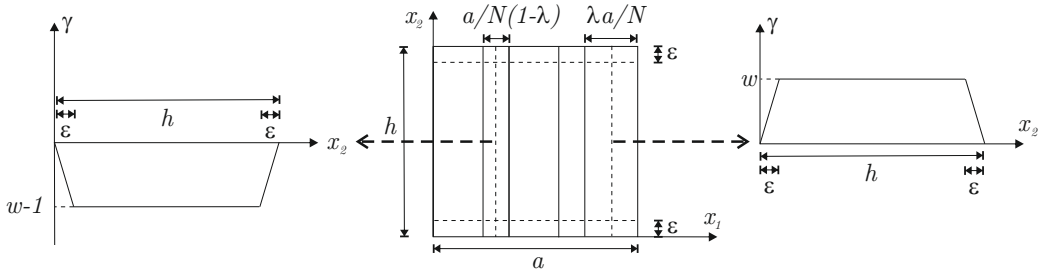

Figure 5.26.: Modified plastic slip.

The correction of the plastic slip is negligible small and tends to zero as the width of the zone ϵ goes to zero. Due to the large resolved shear stress in the small zone at the boundaries, a second slip system for the plastic slip might be activated. In this case the relaxed energy (5.114) has to be extended by the term $\mu cb\left|\beta_{,2}\right|$ in the integrand. However, this correction does not affect the energy essentially since b is much smaller than a.

The laminate structure of the material leads to a stress strain curve for loading schematically shown in Figure 5.27. The shear stress is evaluated by $P_{12} = \frac{\mathrm{d}E}{\mathrm{d}w}$.

Figure 5.27.: Stress- strain curve, reprinted by permission from [60].

For small strains, the stress strain curve behaves completely elastic. When the shear strain overcomes the threshold value θ_1 dislocations start to nucleate and plastic slip occurs. The condition (5.131) has to be checked, whether it is energetically favorable building phases. Then with phase mixing, the shear stress drops to zero and remains vanished up to $w = 1$. At first sight, the zero stress at phase mixing seems to be surprising since the incoherent phase interfaces in form of dislocation arrays cause stress. However, both phases are stress free due to our choice so that they can coexist without violating the equilibrium condition. According to Read and Shockley [77] or Berdichevsky [7], the stress field resulting from the dislocation arrays has a very short range character localized only near the interface. This stress strain behavior can also describe the martenisitic phase transition. Both phases, the martensitic and the austenitic phase are stress free, except at the incoherent interface boundary where dislocation arrays occur. From $w = 1$, the energy density is convex again and no phase

mixing is possible anymore. At $w = 1$ the plastic slip is zero, since the condition $\dot{\beta} > 0$ has to be fulfilled, the plastic slip is zero up to $w = \theta_2$. Therefore the stress strain curve is again a linear line and describes the elastic material behavior of the second phase. For $w > \theta_2$, the plastic slip is uniform and the stress is constant.

From this example, we see that a phase transition involving dislocations is possible. The phase boundaries are incoherent in form of dislocation arrays. Like the model presented in chapter 4 the phase transition is energy driven and the microstructure is energetically favorable. This underlying mechanism can be for example interpreted as a martensitic phase transition. However, the assumed energy density is highly hypothetical in order to understand the basic mechanism.

5.4.2. Realistic double-well free energy density

The basic mechanism of the phase transformation involving dislocations is studied in the previous section on a very simple idealized energy density. Using this prototype free energy density a microstructure is obtained which is energetically favorable and minimizes the energy. The analysis with a more realistic energy density may lead to further results. Therefore a double-well free energy density is considered in the general form

$$\Psi(\mathbf{F}^{\mathrm{e}}, \rho) = \varphi(\theta) + \mu c b^2 \rho, \tag{5.134}$$

where the elastic strain is equal to $\theta = w - \beta$. The shear modulus is denoted by μ and the energy density φ due to macroscopic elastic deformations reads

$$\varphi(\theta) = \min_{\theta} \left\{ \frac{1}{2}\mu\theta^2, \frac{1}{2}\mu(\theta - w_{\mathrm{t}})^2 + \tau_{\mathrm{m}} w_{\mathrm{t}} \right\}. \tag{5.135}$$

In this energy density w_{t} can be interpreted as the transformation strain and correspondingly τ_{m} as the transition stress. The normalized free energy density due to macroscopic elastic deformations is shown schematically in Figure 5.28 with the material constants $w_{\mathrm{t}} = 0.01$ and $w_{\mathrm{m}} = \frac{\tau_{\mathrm{m}}}{\mu} = 0.001$.

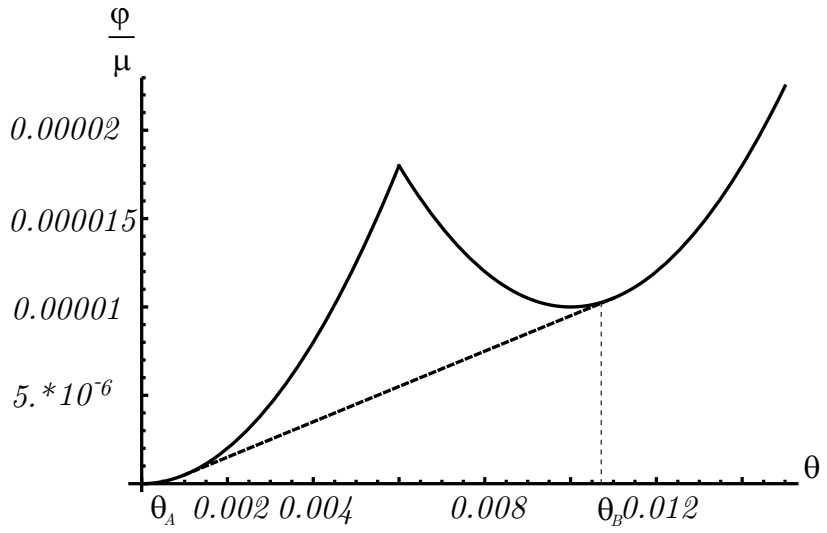

Figure 5.28.: Non-convexity and the convex envelope, reprinted by permission from [60].

Due to our choice of φ, the function is non-smooth at the intersection between both quadratic functions of the energy density. In the neighborhood of this point the function can be smoothed to remove that behavior. The graph in Figure 5.28 illustrates that the chosen energy density is non-convex. In the region of the non-convexity (between θ_A and θ_B), a tangent can be found as a convex hull which replaces the non-convex function. This tangent (denoted by φ^{c}) touches the curve φ with the slope τ_0, hence the function reads

$$\varphi^{\mathrm{c}} = \tau_0 \theta. \tag{5.136}$$

In order to construct the convex hull, θ_A, θ_B and the slope τ_0 have to be determined. At the touching point from the tangent with the function, the slopes have to be the same,

$$\frac{\mathrm{d}\phi}{\mathrm{d}\theta}(\theta_A) = \tau_0 = \frac{\mathrm{d}\phi}{\mathrm{d}\theta}(\theta_B). \tag{5.137}$$

At the touching points, the values of the functions have to be equal to the values of the tangent,

$$\varphi(\theta_A) = \tau_0 \theta_A, \qquad \text{and} \qquad \varphi(\theta_B) = \tau_0 \theta_B. \tag{5.138}$$

From Equations (5.137) and (5.138) the unknowns are identified as

$$\tau_0 = \frac{w_{\mathrm{m}}}{\mu} = \tau_{\mathrm{m}}, \qquad \theta_A = w_{\mathrm{m}} \qquad \text{and} \qquad \theta_B = w_{\mathrm{m}} + w_{\mathrm{t}}. \tag{5.139}$$

Using this free energy density, the relaxed energy functional reads

$$\mathcal{I}[\beta(\mathbf{x})] = L \int_0^h \int_0^a \left[\varphi(w-\beta) + \mu c b \left|\beta_{,x_1}\right| + r\mathrm{Sign}\left(\dot{\beta}\right)\beta\right] \mathrm{d}x_1 \, \mathrm{d}x_2. \tag{5.140}$$

In this example, r is chosen as $r = \tau_{\mathrm{y}} = \tau_{\mathrm{m}} + \tau_* = \mu(w_{\mathrm{t}} + w_*)$, where w_* is much smaller than w_{t}. In that case, r is a little bit higher than τ_{m}. The true plastic slip, which should be determined, minimizes among all admissible plastic slips $\beta(x_1, x_2)$ the relaxed energy functional (5.140) fulfilling also the boundary conditions (5.115). At the beginning of the section, the crystal is considered as dislocation free for zero loading, therefore the plastic slip is zero at zero strain ($\beta(w = 0) = 0$). With an increasing strain, the plastic slip has to be a continuous function of the control parameter w.

Finite plane-strain constrained shear with uniform deformations

First the relaxed energy at uniform plastic deformations is examined. When a critical load is reached, dislocations occur and move to the free boundaries where they can form steps. Since the plastic slip is constant, the relaxed energy functional becomes

$$\mathcal{I}_{\mathrm{u}}(\beta) = ahL\left[\varphi(w-\beta) + \tau_{\mathrm{y}}\mathrm{Sign}\left(\dot{\beta}\right)\beta\right]. \tag{5.141}$$

The minimum of this relaxed minimum is found by $\frac{\mathrm{d}E_{\mathrm{u}}}{\mathrm{d}\beta} = 0$ and by assuming $\dot{\beta} > 0$, this equation reads

$$\frac{\mathrm{d}\varphi}{\mathrm{d}\beta} - \tau_{\mathrm{y}} = 0. \tag{5.142}$$

Due to the choice of τ_y, the roots of this equation (substituting again $\theta = w - \beta$) are larger than the corresponding roots of Equation (5.138). If these roots are denoted by θ_1 and θ_2, we may write $\theta_1 > w_m$ and $\theta_2 > w_m + w_t$. Then the homogeneous plastic slip is determined by

$$\beta_i = w - \theta_i \qquad \text{for } i = 1, 2. \tag{5.143}$$

Analogously to the solution with the prototype free energy, initially the plastic slip is zero and no dislocations occur. The material behaves purely elastic and the relaxed energy per unit volume for $w < \theta_1$ reads

$$\mathscr{E}_u = \frac{1}{2}\mu w^2. \tag{5.144}$$

If the total strain w reaches θ_1, the dislocations are nucleated. So θ_1 can be interpreted as the threshold value. When the strain is higher than the threshold value, the nucleated dislocations move to the boundaries and the plastic slip is calculated as

$$\beta = w - \theta_1. \tag{5.145}$$

In this region the uniform plastic deformations lead to the relaxed energy per unit volume in the form of

$$\mathscr{E}_u = \frac{1}{2}\mu\theta_1^2 + \tau_y (w - \theta_1). \tag{5.146}$$

With an increasing shear strain, the second minimum θ_2 is archived and the plastic slip is determined by

$$\beta = w - \theta_2. \tag{5.147}$$

The relaxed energy per unit volume then reads

$$\mathscr{E}_u = \frac{1}{2}\mu(\theta_2 - w_t)^2 + \tau_y (w - \theta_2). \tag{5.148}$$

The resulting shear stress is determined again by $P_{12} = \frac{dE_u}{dw}$ and the stress-strain relation for homogeneous deformations is shown in Fig.5.29.

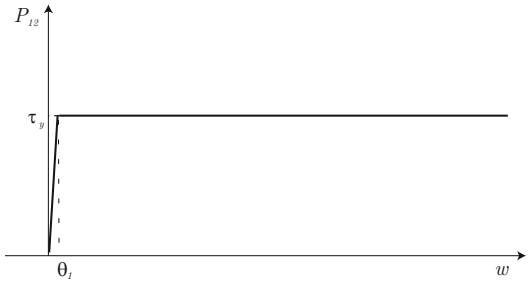

Figure 5.29.: Stress strain curve for uniform deformations.

Finite plane- strain constrained shear with laminate structure as energy minimizer

Similar to the case with a prototype free energy density, the solution with the uniform plastic slip does not give the minimum to the relaxed energy functional in the region where the energy density is non-convex ($\theta_A < w < \theta_B$). There (up to $w = \theta_B$), a microstructure has to be found as a minimizer. We consider a laminate structure with one layer occupying the volume fraction λ where the plastic slip is $\beta = w - \theta_A$ and the other layer with the volume fraction $1 - \lambda$ and the plastic slip $\beta = w - \theta_B$. In this case the plastic deformation is nonuniform but piecewise constant. The volume fraction λ can be determined in such way that

$$\int_A \beta \mathrm{d}a = 0 \tag{5.149}$$

is fulfilled. This condition leads to

$$\int_0^{a\lambda} w - \theta_A \, \mathrm{d}x_1 + \int_0^{(1-\lambda)a} w - \theta_B \, \mathrm{d}x_1 = 0 \qquad \Rightarrow \qquad \lambda(w - \theta_A) + (1-\lambda)(w - \theta_B) = 0. \tag{5.150}$$

Hence, $\lambda = 1 - \frac{(w - w_\mathrm{m})}{w_\mathrm{t}}$.

Due to the multiplicative decomposition of the deformation gradient, a piecewise plastic deformation gradient leads to a piecewise constant elastic deformation gradient. In this loading example, only an elastic shearing exists (see Equation (5.48)). In the first phase the elastic shearing is θ_A and in the second θ_B. The combination of the elastic and the plastic shearing, both discontinuous and nonuniform, brings the crystal in its final shape with parallel dislocation arrays inclined at an angle ϕ to the x_2 axis. The final shape is similar to the result of the case with the prototype free energy density and is illustrated in Figure 5.25. The surface dislocation density of each array is the difference of the plastic slips of both phases, hence

$$\rho = \pm \frac{1}{b}(\theta_B - \theta_A) = \frac{w_\mathrm{t}}{b}. \tag{5.151}$$

In order to show that the plastic slip is a true minimizer, the average relaxed energy per unit volume caused by the laminate structure has to be less than the relaxed energy minimized by uniform plastic deformations. For the constructed laminate structure, the first term of the relaxed energy functional (5.140) becomes after averaging φ^c since the convex hull minimizes the energy density where it is non-convex. Due to our choice of a piecewise constant plastic slip, the second term has to vanish. Analogously to the case with the prototype free energy density, the third term is zero due to our choice of λ. However, the piecewise constant plastic slips in the laminate cause jumps in the plastic slip at the surfaces. These jumps contribute energy to the relaxed average energy functional, which can be determined by $\mu N c b \frac{w_\mathrm{t}}{a}$ where N is again the number of jump surfaces. Taking all contributions into account, the average relaxed energy density reads

$$\bar{\mathscr{E}}_i = \varphi^\mathrm{c}(w) + \mu N c b \frac{w_\mathrm{t}}{a}. \tag{5.152}$$

As long as the average relaxed energy caused by the laminate structure is less than the one caused by the uniform plastic slip, thus as long as

$$\varphi^\mathrm{c}(w) + \mu N c b \frac{w_\mathrm{t}}{a} < \frac{1}{2}\mu\theta_1^2 + \tau_\mathrm{y}(w - \theta_1), \tag{5.153}$$

the phase mixing is energetically favorable.

Once again, the piecewise constant plastic slip does not satisfy the boundary condition (5.115). Therefore the plastic slip has to be modified near the boundaries in the standard way. In the first phase the plastic slip reads

$$\beta = \begin{cases} \frac{w-\theta_A}{\epsilon} x_2 & \text{if } 0 \le x_2 \le \epsilon \\ w - \theta_A & \text{if } \epsilon \le x_2 \le h - \epsilon \\ \frac{w-\theta_A}{\epsilon} (h - x_2) & \text{if } h - \epsilon \le x_2 \le h \end{cases} \tag{5.154}$$

and in the second phase

$$\beta = \begin{cases} \frac{w-\theta_B}{\epsilon} x_2 & \text{if } 0 \le x_2 \le \epsilon \\ w - \theta_B & \text{if } \epsilon \le x_2 \le h - \epsilon \\ \frac{w-\theta_B}{\epsilon} (h - x_2) & \text{if } h - \epsilon \le x_2 \le h \end{cases} . \tag{5.155}$$

When ϵ tends to zero, the contribution of this correction to the relaxed energy goes to zero.

Also for the phase mixing, the stress can be determined by $P_{12} = \frac{\mathrm{d}E}{\mathrm{d}w}$. The stress-strain curve is presented in Fig.5.30.

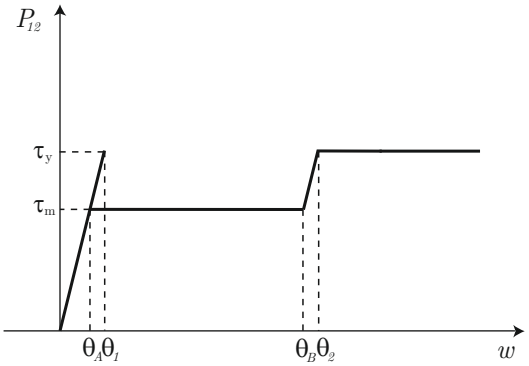

Figure 5.30.: Stress strain curve, reprinted by permission from [60].

The stress strain behavior is linear up to θ_1, thus the material behaves elastic. Before the microstructure minimizes the energy, dislocation arrays occur, therefore the stress still follows the elastic path before it drops down to τ_m and the microstructure minimizes the energy. From θ_B, the energy is convex thus the material homogenous again. As $\beta = 0$ at $w = \theta_B$, the plastic slip is zero up to $w = \theta_2$ and the material behaves elastic. Afterwards, the stress remains constant at $P_{12} = \tau_\mathrm{y}$ with the constant plastic slip $\beta = w - \theta_2$.

5.5. Discussion

In the first part of this chapter the kinematically independent variables which characterize the energy of the crystal including the dislocation network and the changes of the network are defined. Here, these quantities are the dislocation density and the right Cauchy Green tensor for elastic deformations. Afterwards the energy and the dissipation are expressed

through these quantities and the variational calculus is applied in order to obtain the unknown plastic slip. Then this method is applied to a single crystal under finite anti-plane constrained shear and finite plane-strain constrained shear. In the case of finite plane-strain constrained shear a non-convex energy functional is considered, therefore a laminate structure is energetically preferable than the homogeneous state. For both loading examples the stress strain curve is presented. In the first example a load cycle is performed and the stress response is a hysteresis loop exhibiting work hardening due to the dislocation pile-ups. In the second example the stress strain curve exhibits a sharp load drop at the onset of the laminar structure, followed by a stress plateau.

6. Conclusions and outlook

The main focus on this work is the modeling of microstructures in finite crystal plasticity. In this thesis, two approaches are presented. Both applied approaches are based on variational concepts.

The first ansatz models microbands and is based on a modification of the existing model of [49] by adding a vanishing viscosity in order to regularize the model in time. The resulting evolution equations which describe the current state of the microstructure are given in an explicit form. These equations are not based on a global minimization hence they can be calculated directly. First numerical examples are illustrated here, a shear test and a tension-compression test. In both tests, a microstructure arises and evolves in order to minimize the energy. The introduced vanishing viscosity leads to a delay in the energy minimization and to peaks in the stresses and the energy. However, if the relaxation time is increased by reducing the pseudo-velocity, the viscous effect decreases. Therefore the effect of the pseudo-velocity on the evolution of the microstructure is examined. With a decreasing pseudo-velocity, the evolution converges to a viscosity limit. This approach is also compared to the results of the existing model, presented in [48]. Both results show a good agreement, however differences appear. Also cycling tests are performed, where the stress strain curve exhibits a hysteresis loop. Since the hardening increases with every loading cycle, the material gets stiffer and the energy increases. In total, the algorithm of the evolution of the microstructure is stable and further treatments, as the implementation in a finite element code or the comparison to experiments can be performed. Still missing is the verification by experimental results. Also the solution of full boundary-value problems and the extension of the model to higher order slip systems are still open tasks.

The second ansatz is able to model the martensitic phase transformation. For this approach, first the kinematically independent quantities which describe the energy and the change of the dislocation network in the framework of finite deformations and the nonlinear continuum dislocation theory are defined. Then the energy and the dissipation can be determined and the variational calculus applied. In order to apply the nonlinear continuum dislocation theory on a first example, a single crystal is loaded under finite anti-plane constrained shear. For simplicity the dissipation is neglected in the first step, then the basic mechanism of the dislocation pile-up already occurs. Afterward the dissipation is also taken into account. This first example is determined by assuming a convex energy density, hence only homogeneous deformations occur as minimizers. This test shows whether it is possible to solve problems in the framework of nonlinear continuum dislocation theory. For one load cycle a hysteresis loop is exhibited as a stress strain curve. Due to the dislocation pile up at the loading paths, the stress strain curve exhibits work hardening. After the verification that the nonlinear continuum dislocation theory is applicable, in order to model a martensitic phase transition, a crystal with a non-convex energy is loaded by finite plane-strain constrained shear. At first a very simple prototype free energy density is assumed. Already in this case a formation of pattern is energetically favorable. The plastic slip in these patterns is analyzed. In order to solve the variational principle and to fulfill the boundary conditions, the plastic slip has to

be corrected. Finally the resulting stress strain curve is determined. When the patterns are energetically favorable, the stress has a sharp drop and is zero. After studying the simple energy density, a more realistic energy density is considered as well. Also then in this case patterns are energetically preferred. Further testings could verify the results and the applicability of this material model. However, in other examples, the analytical solution may be very evolved and the application of the finite element method could be necessary. Also for this approach, the comparison to experimental data is a very interesting topic.

A. Mathematics

In this chapter, the used mathematical definitions and properties are shortly given. These basics and more details are provided in [33], [24], [13] and [39].

A.1. Euclidean vector space

In order to define the length of a vector or its angle, we need to introduce the euclidean vector space. This physical space has three dimensions, hence three orthonormal vectors may be used to define vectors. We denote this basis by

$$B = \begin{bmatrix} \mathbf{e}_1 & \mathbf{e}_2 & \mathbf{e}_3. \end{bmatrix} \tag{A.1}$$

with

$$\mathbf{e}_1 = \begin{pmatrix} 1 \\ 0 \\ 0 \end{pmatrix}, \qquad \mathbf{e}_2 = \begin{pmatrix} 0 \\ 1 \\ 0 \end{pmatrix}, \qquad \mathbf{e}_3 = \begin{pmatrix} 0 \\ 0 \\ 1 \end{pmatrix}. \tag{A.2}$$

These three basis vectors (A.2) define the space of all three-dimensional vectors. In Figure A.1 this space and an arbitrary vector are sketched. This vector $\mathbf{v}$ can be determined by

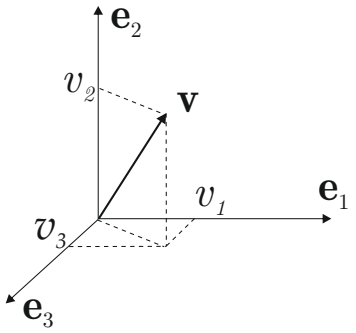

Figure A.1.: Basic vectors denote the space

$$\mathbf{v} = \sum_{i=1}^{3} v_i \mathbf{e}_i \tag{A.3}$$

where v_i is the cartesian entry of the vector $\mathbf{v}$. In this space, the scalar product, the angle between two vectors and the length of a vector are defined and described in the following.

A.2. Some Matrix and vector operations

A.2.1. Products

There are different kinds of products for scalars, vectors and matrices which are used in this thesis. The multiplication of a scalar by an array (including vectors and matrices) is defined as the multiplication of the scalar by every entry of the array, hence

$$a\mathbf{s} = \begin{pmatrix} as_1 \\ as_2 \\ as_3 \end{pmatrix}. \tag{A.4}$$

Using this definition, a vector in the euclidean space can be expressed through

$$\mathbf{s} = \sum_{i=1}^{3} s_i \mathbf{e}_i = s_i \mathbf{e}_i. \tag{A.5}$$

The second definition uses the Einstein summation convention. Everytime an index is repeated, we have to sum up over this index from 1 to 3.

One product between two vectors is the dot-product. Each entry of one vector is multiplied with the same entry of the other vector and then summed up. The result of the dot-product is a scalar, therefore the dot- product is also called scalar product. It is defined by

$$\mathbf{s} \cdot \mathbf{m} = \sum_{i} s_i m_i = s_i m_i = sm\cos(\varphi), \tag{A.6}$$

with φ being the angle between the two vectors, here between $\mathbf{s}$ and $\mathbf{m}$. The angle can be determined by

$$\cos(\varphi) = \frac{\mathbf{s} \cdot \mathbf{m}}{|\mathbf{s}| \cdot |\mathbf{m}|}. \tag{A.7}$$

We can easily see that the scalar product of two orthogonal vectors ($\varphi = 90°$) vanishes,

$$\mathbf{e}_1 \cdot \mathbf{e}_2 = 0. \tag{A.8}$$

Another multiplication of two vectors is the dyadic product. The definition of this product is the following

$$\mathbf{s} \otimes \mathbf{m} = s_i m_j \mathbf{e}_i \mathbf{e}_j = s_i m_j = \begin{pmatrix} s_1 m_1 & s_1 m_2 & s_1 m_3 \\ s_2 m_1 & s_2 m_2 & s_2 m_3 \\ s_3 m_1 & s_3 m_2 & s_3 m_3 \end{pmatrix}. \tag{A.9}$$

The third multiplication between two vectors is the cross product or also referred as screw product,

$$\mathbf{s} \times \mathbf{m} = s_i m_j \varepsilon_{ijk} \mathbf{e}_k. \tag{A.10}$$

ε denotes the permutation tensor and is defined by

$$\varepsilon_{ijk} = \begin{cases} 1 & \text{if } i,j,k \text{ is an even permutation} \\ 0 & \text{if two indices are the same} \\ -1 & \text{if } i,j,k \text{ is an uneven permutation.} \end{cases} \tag{A.11}$$

A.2.2. Further useful operations

Beside the products of vectors, another important operation is the length of a vector. In the Euclidean space its definition reads

$$|\mathbf{s}| = \sqrt{\mathbf{s}\cdot\mathbf{s}} = \sqrt{s_i s_i}. \tag{A.12}$$

A unit vector like $\mathbf{e}_i$ has the unit length 1. Analogously to the definition of the length of vector, there exists the norm of tensor, denoted by

$$\|\mathbf{F}\| = \sqrt{T_{ij}T_{ij}}. \tag{A.13}$$

This norm is called Hilbert-Schmidt norm.

A special tensor is the identity tensor, which is defined by

$$\mathbf{I} = \delta_{ij}\mathbf{e}_i \otimes \mathbf{e}_j, \tag{A.14}$$

where δ denotes the Kronecker delta

$$\delta_{ij} = \mathbf{e}_i \cdot \mathbf{e}_j = \begin{cases} 1, & \text{if } i = j, \\ 0, & \text{if otherwise.} \end{cases} \tag{A.15}$$

The partial derivative of a function is denoted by

$$\mathbf{u}_{,i} = \partial_i \mathbf{u}. \tag{A.16}$$

The comma in the index indicates the partial derivative, the following entry shows to which variable the function is differentiated.

If a function depends on several variables, which can be assembled in a vector, this function is called field function. The gradient of a scalar field function leads to

$$\nabla a(\mathbf{x}) = \frac{\partial a(\mathbf{x})}{\partial x_i}\mathbf{e}_i = \begin{pmatrix} \frac{\partial a}{\partial x_1} \\ \frac{\partial a}{\partial x_2} \\ \frac{\partial a}{\partial x_3} \end{pmatrix}. \tag{A.17}$$

Obviously the gradient for a scalar is a vector-valued function. Analogously the gradient of a vector may be obtained, for example for a vector $\mathbf{u} = (u_1,\ u_2,\ u_3)^T$ the result reads

$$\nabla \mathbf{u}(\mathbf{x}) = \frac{\partial u_i}{\partial x_j}\mathbf{e}_i \cdot \mathbf{e}_j = \begin{pmatrix} \frac{\partial u_1}{\partial x_1} & \frac{\partial u_1}{\partial x_2} & \frac{\partial u_1}{\partial x_3} \\ \frac{\partial u_2}{\partial x_1} & \frac{\partial u_2}{\partial x_2} & \frac{\partial u_2}{\partial x_3} \\ \frac{\partial u_3}{\partial x_1} & \frac{\partial u_3}{\partial x_2} & \frac{\partial u_3}{\partial x_3} \end{pmatrix}. \tag{A.18}$$

A.2.3. Principal directions and invariants

If the coordinate system is rotated, the components of a tensor change. However, there are scalar quantities of a tensor which do not change, therefore they are called invariants.

Consider a tensor $\boldsymbol{\sigma}$ of second rank

$$\boldsymbol{\sigma} = \begin{pmatrix} \sigma_{xx} & \sigma_{xy} & \sigma_{xz} \\ \sigma_{yx} & \sigma_{yy} & \sigma_{yz} \\ \sigma_{zx} & \sigma_{zy} & \sigma_{zz} \end{pmatrix}. \tag{A.19}$$

The components of this stress tensor undergo a transformation, if the coordinate system is rotated. The maximum normal stresses are achieved if the shear stresses vanish, hence

$$\boldsymbol{\sigma} = \begin{pmatrix} \sigma_1 & 0 & 0 \\ 0 & \sigma_2 & 0 \\ 0 & 0 & \sigma_3 \end{pmatrix}. \tag{A.20}$$

The entries of the diagonal correspond to the principal normal stresses. From the condition that the shear stresses vanish at principal stresses, three equations are obtained. To admit a nonzero solution of this system, the coefficient determinant has to be zero,

$$\det \begin{pmatrix} \sigma_{xx} - \sigma & \sigma_{xy} & \sigma_{xz} \\ \sigma_{yx} & \sigma_{yy} - \sigma & \sigma_{yz} \\ \sigma_{zx} & \sigma_{zy} & \sigma_{zz} - \sigma \end{pmatrix} = 0. \tag{A.21}$$

Equation (A.21) is cubic, and therefore we obtain three real roots for σ, the principal stresses σ_1, σ_2 and σ_3. Since the principal stresses for one point are fixed for every rotation, the coefficients of Equation (A.21) also remain constant and invariant for every rotation. Equation (A.21) is also referred as the eigenvalue problem and may be written in the form

$$\sigma^3 - I_1\sigma^2 + I_2\sigma - I_3 = 0, \tag{A.22}$$

where I_1, I_2 and I_3 are called the invariants of the tensor. The first invariant is the trace of the tensor,

$$I_1 = \sigma_{xx} + \sigma_{yy} + \sigma_{zz} = \sigma_{ii} = \mathrm{tr}\boldsymbol{\sigma}. \tag{A.23}$$

The second invariant is referred as the sum of principal minors,

$$I_2 = \frac{1}{2}\left(\sigma_{ii}\sigma_{jj} - \sigma_{ij}\sigma_{ji}\right). \tag{A.24}$$

The determinant of the tensor is the third invariant

$$I_3 = \det\boldsymbol{\sigma}. \tag{A.25}$$

A.3. Legendre transform

Considering a single, smooth convex function F with one single variable x, the Legendre transform of $F(x)$ reads

$$G(s) = sx(s) - F(x(s)) \tag{A.26}$$

with s being the slope of F, $s = \frac{\mathrm{d}F(x)}{x}$. This transform is presented graphically in Figure A.2. In this figure, the convex function F is plotted versus its variable x. A point on this curve may be chosen, then the horizontal distance to the origin to this point can be denoted with

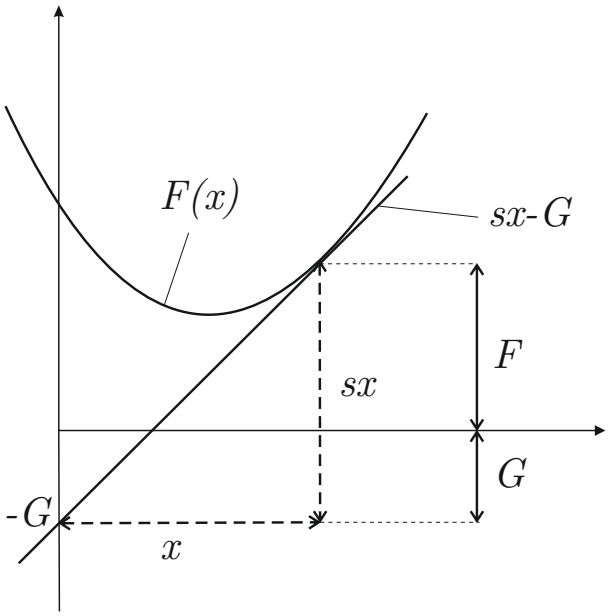

Figure A.2.: Graphic presentation of a Legendre transform

x. From this point a tangent is constructed with the slope s and its intercept is $-G$. Then it is obvious that $sx = F + G$ holds true. The Legendre transform leads to a function which has the same information as the former function, but it is dependent on the derivative, not on the variable anymore.

If the function F is non-convex, the Legendre transform is not unique but multi-valued. Then the Legendre transform may develop discontinuous first derivatives. By performing another transformation, the convex hull of the original would be obtained. These information and further details are presented in [89].

A.4. Variational Calculus

Functionals play an important role in solving mechanical problems. Since the variational calculus of a functional is used in this thesis, a basic introduction is presented here. The basics are taken from [26], where further information are revealed.

A functional is a function, where the variable is a function itself. Even the first problems in this area are already solved by Euler (1707-1783), the calculus of functionals still does not have general solving methods. Finding minima and maxima of a functional is referred as the calculus of variation. One necessary condition for an extremum (here at $y = \hat{y}$) is, that the variation of the functional (here denoted by $\mathscr{J}$) vanishes for $y = \hat{y}$, hence

$$\delta \mathscr{J} = 0. \tag{A.27}$$

The functions y which satisfy this condition are called admissible functions. The concept of variation of a functional is similar to the concept of a differential of a function. As a simple example we may consider a differentiable functional $\mathscr{J}$ dependent on the function $y[x]$,

hence

$$\mathscr{J}[y] = \int_a^b F[x, y, y'] \, \mathrm{d}x \tag{A.28}$$

with the boundary condition $y[a] = A$ and $y[b] = B$. Then the necessary condition (A.27) leads to

$$F_{,y} - \frac{\mathrm{d}}{\mathrm{d}x} F_{y'} = 0. \tag{A.29}$$

This second-order differential equation is also called the Euler's equation. Its solutions are determined from the boundary conditions $y[a] = A$ and $y[b] = B$.

A.5. Elliptic integrals and functions

In Chapter 5, elliptic integrals and functions are used. Therefore, a short introduction is revealed, for more details and information, we refer to [52]. In general, elliptic integrals are given in the form

$$E(x) = \int_a^x R\left(\mathrm{t}, \sqrt{p(\mathrm{t})}\right) \mathrm{dt}, \tag{A.30}$$

where R is a rational function and p a polynomial of third or fourth order with no repeated roots. One of the first historical elliptic integrals reads

$$E(x) = \int_a^x \frac{1}{\sqrt{p(\mathrm{t})}} \mathrm{dt}. \tag{A.31}$$

From this example it can be easily seen, that the roots of the polynomial cause a division by zero. Hence an elementary integral cannot be found. However, all elliptic integrals can be reduced to one of the three Legendre forms or a Weierstrass form.

The inverse functions of these elliptic integrals are called elliptic functions. These elliptic functions help to find explicit solutions of differential equations and to determine integrals. [27] provides tables of elliptic integrals and their elliptic functions.

A.6. Divergence theorem

In this thesis, a surface integral over the surface $\partial\Omega$ is denoted by

$$\int_{\partial\Omega} \mathrm{d}S \tag{A.32}$$

and a volume integral over a body Ω by

$$\int_{\Omega} \mathrm{d}V. \tag{A.33}$$

Ω is assumed as a bounded region with the boundary $\partial\Omega$. Furthermore, Ω is considered as the domain of a scalar field m, a vector field $\mathbf{x}$ and a tensor field $\mathbf{F}$. If the outward unit normal vector $\mathbf{n}$ of the boundary $\partial\Omega$ is known, the divergence theorem reads

$$\int_{\partial\Omega} m\mathbf{n}\,\mathrm{d}S = \int_{\Omega} \mathrm{grad}m\,\mathrm{d}V, \tag{A.34}$$

$$\int_{\partial\Omega} \mathbf{x}\cdot\mathbf{n}\,\mathrm{d}S = \int_{\Omega} \mathrm{div}\mathbf{x}\,\mathrm{d}V \tag{A.35}$$

and

$$\int_{\partial\Omega} \mathbf{F}\cdot\mathbf{n}\,\mathrm{d}S = \int_{\Omega} \mathrm{div}\mathbf{F}\,\mathrm{d}V. \tag{A.36}$$

This divergence theorem is important for the derivation of basic laws in mechanics, like the balance of linear moment.

A.7. Convexity

In the following chapters, which are dealing with microstructures, the notations of quasi-convexity and rank-one convexity of the energy appear. Therefore, a short definition of convexity is revealed, more detailed information are presented in [19], [79] or [47].

The energy potential may be defined as a functional in the form

$$\mathcal{I}[\mathbf{u}] = \int_{\Omega} \Psi(\nabla\mathbf{u})\,\mathrm{d}V - l(\mathbf{u}), \tag{A.37}$$

where $\mathbf{u}$ is the displacement field, Ψ an energy density and l a linear functional resulting from loading e.g. body forces. Microstructures commonly arise whenever a non uniform deformation field leads to a lower energy than the homogeneous deformation state. Then the energy is replaced by a hull with the microstucture as its minimizer. The homogeneous deformations are obtained from the minimum of total energy (see section 2.6.1). This minimum principle leads to a minimum if three conditions are fulfilled: the energy potential has to be bounded, coercive and weakly lower semi-continuous. The mathematical notations can be found in [19]. According to Ball [2], these conditions can be replaced by conditions for the energy density: the energy density has to be coercive, bounded and quasiconvex.

The energy density is called quasiconvex if for every domain ω and every perturbation field α of the deformation gradient $\mathbf{F}$

$$\Psi(\mathbf{F}) \leq \frac{1}{\omega}\int_{\omega} \Psi(\mathbf{F}+\nabla\boldsymbol{\alpha})\,\mathrm{d}V \quad \text{with } \boldsymbol{\alpha} = 0 \text{ on } \partial\omega \tag{A.38}$$

holds true, [69]. This condition is poorly applicable, since it is non-local.

In order to get applicable conditions, the quasi convexity is replaced by approximate local conditions, like the convexity. A potential is convex [79] if

$$\Psi(\lambda\mathbf{F}_1 + (1-\lambda)\mathbf{F}_2) \leq \lambda\Psi(\mathbf{F}_1) + (1-\lambda)\Psi(\mathbf{F}_2) \tag{A.39}$$

with $\mathbf{F}_1$ and $\mathbf{F}_2$ being arbitrary and λ varying from 0 to 1 is fulfilled.

According to [2], a potential which is polyconvex can always be expressed through a convex function f, such that

$$\Psi(\mathbf{F}) = f(\mathbf{F}, \mathrm{cof}\mathbf{F}, \det\mathbf{F}) \tag{A.40}$$

is satisfied.
A potential is called rank-one-convex if condition (A.39) is fulfilled with

$$\mathrm{rank}(\mathbf{F}_1 - \mathbf{F}_2) \leq 1 \tag{A.41}$$

holds true [19]. These definitions imply that a convex potential is also polyconvex and rank-one-convex. A polyconvex potential is always rank-one-convex.

Bibliography

[1] H. Altenbach. *Kontinuumsmechanik*. Springer, 2012.

[2] J. M. Ball. Convexity conditions and existence theorems in nonlinear elasticity. *Arch. Rat. Mech. Anal.*, 63:337–403, 1977.

[3] J. M. Ball and R. D. James. Fine phase mixtures as minimizers of energy. *Arch. Rat. Mech. Anal.*, 100:13–52, 1987.

[4] Y. Basar and D. Weichert. *Nonlinear continuum mechanics of solids*. Springer, 2000.

[5] V. L. Berdichevsky. Continuum theory of dislocations revisited. *Contin. Mech. Thermodyn.*, 18:195–222, 2006.

[6] V. L. Berdichevsky. On the thermodynamics of crystal plasticity. *Scr. Mater.*, 54:711–716, 2006.

[7] V. L. Berdichevsky. On dislocation models of grain boundaries. *Contin. Mech. Thermodyn.*, 23:185–209, 2011.

[8] V. L. Berdichevsky and K. Le. Dislocation nucleation and work hardening in anti-plane constrained shear. *Contin. Mech. Thermodyn.*, 18:455–467, 2007.

[9] V. L. Berdichevsky and L. I. Sedov. Dynamic theory of continuously distributed dislocations. its relation to plastic theory. *Appl. Math. Mech. (PMM)*, 31:989–1006, 1967.

[10] H. Berns and W. Theisen. *Eisenwerkstoffe - Stahl und Gusseisen*. Springer-Verlag Berlin Heidelberg, 2006.

[11] B. A. Bilby, R. Bullough, and R. Smith. Continuous distributions of dislocations: a new application of the method of non-riemannian geometry. *Proc. R.Soc*, A231:263–273, 1955.

[12] B. A. Bilby, L.R.T Gardner, and A.N. Stroh. Continuous distributions of dislocations and the theory of plasticity. *Extrait des acte du IX^e congres international de mechanique appliquee*, pages 35–44, 1957.

[13] I. N. Bronstein, K. A. Semendjajew, G. Musiol, and H. Mühlig. *Taschenbuch der Mathematik*. Verlag Harri Deutsch, 2008.

[14] J. M. Burgers. Some considerations on the fields of stress connected with dislocations connected in a regular crystal lattice. *Kon. Nederl. Akad. v. Wet.*, 42:293–325, 1939.

[15] C. Carstensen, S. Conti, and A. Orlando. Mixed analytical-numerical relaxation in finite single-slip crystal plasticity. *Contin. Mech. Thermodyn.*, 20:275–301, 2008.

[16] C. Carstensen, K. Hackl, and A. Mielke. Non-convex potentials and microstructures in finite-strain plasticity. *Proc. R.Soc. London*, A458:299–317, 2002.

[17] P. Cermelli and M. E. Gurtin. On the characterization of geomentrically necessary dislocations in finite plasticity. *J. Mech. Phy. Solids*, 50:5–32, 2001.

[18] T. J. Chung. *Continuum mechanics*. Prentice-Hall International, Inc, 1988.

[19] B. Dacorogna. *Direct methods in the calculus of Variations*. Springer, 2000.

[20] O. Dmitrieva, P. W. Dondl, S. Müller, and D. Raabe. Lamination microstructure in shear deformed copper single crystals. *Acter Mater.*, 57:3439–3449, 2009.

[21] G. Eggeler. Martensitic Transformations and Shape Memory Alloys–GE II. Presentation in the 3rd Spring School on Simulation-Based Microstructure Design.

[22] J. A. Ewing and W. Rosenhain. Experiments in micro-metallography: Effects of strain, preliminary notice. *Proc. R.Soc. London*, 65:85–90, 1899.

[23] J. A. Ewing and W. Rosenhain. The crystalline structure of metals. *Philos. Trans. R. Soc.*, 193:353–375, 1900.

[24] W. Flügge, editor. *Handbook of engeneering mechanics*. McGraw- Hill Book Company, 1962.

[25] F. C. Frank and W. T. Read. Multiplication processes for slow moving dislocations. *Phys. Rev.*, 79:722–724, 1950.

[26] I. M. Gelfand and S. V. Fomin. *Calculus of variations*. Dover Publications, INC New York, 2000.

[27] I. S. Gradshteyn and I. M. Ryzhik. *Table of integrals, series and products*. Academic Press, 1980.

[28] C. Günther, P. Junker, and K. Hackl. Modeling the evolution of microstructures in finite plasticity. PAMM: to appear.

[29] C. Günther, P. Junker, and K. Hackl. A variational viscosity-limit approach to the evolution of microstructures in finite crystal plasticity. *Proc. R. Soc. A*, 471:2015011, 2015.

[30] C. Günther, D. M. Kochmann, and K. Hackl. Rate-independent versus viscous evolution of laminate microstructures in finite crystal plasticity. In S. Conti and K.Hackl, editors, *Analysis and Computation of Microstructure in Finite Plasticity*, chapter Rate-Independent versus Viscous Evolution of Laminate Microstructures in Finite Crystal Plasticity, pages 63–88. Springer, 2015.

[31] M. E. Gurtin. *Encyclopedia of Physics VIa/2*, chapter The linear theory of elasticity. Springer Verlag Berlin, 1972.

[32] M. E. Gurtin. *An Introduction to Continuum Mechanics.* Academic Press, 1981.

[33] M. E. Gurtin, E. Fried, and L. Anand. *The Mechanics and Thermodynamics of Continua*. Cambridge University Press, 2010.

[34] P. Haasen. *Physical metallurgy*. Cambridge University Press, 1978.

[35] K. Hackl and F. D. Fischer. On the relation between the principle of maximum dissipation and inelastic evolution given by dissipation potenials. *Proc. R.Soc*, 464:117–132, 2007.

[36] K. Hackl and D. Kochmann. *Multiscale Methods in Computational Mechanics*, chapter An incremental strategy for modeling laminate microstructures in finite plasticity–energy reduction, laminate orientation and cyclic behavior, pages 117–134. Springer, 2011.

[37] K. Hackl and D. M. Kochmann. *Theoretical, Computational and Modelling Aspects of inelastic media*, chapter Relaxed potentials and evolution equations for inelastic microstructures. Springer, Berlin, 2008.

[38] H. Weizhong Han, L. Shouxin, W. Shiding, and Z. Zhefeng. Deformation mechanisms of single crystals and bicrystals subjected to equal-channel angular pressing—-review. *Materials Science Forum*, 633-634:511–525, 2010.

[39] G. A. Holzapfel. *Nonlinear Solid Mechanics A Continuum Approach for Engineering*. John Wiley & Sons, LTD, 2005.

[40] S. Horiuchi, K. Asakura, G. Wassermann, and J. Grewen. Microbands in 80 % drawn copper single crystals with <111 >and <100>starting orientations. *Texture*, 2:17–34, 1975.

[41] E. Hornbogen and H. Warlimont. *Metallkunde*. Springer, 2001.

[42] R. Houwink. *Elastizität/Plastizität und Strucktur der Materie*. Dresden und Leipzig Verlag von Theodor Steinkopff, 1958.

[43] P. Junker and K. Hackl. A condensed variational model for thermo-mechanically coupled phase transformations in polycrystalline shape memory alloys. *Journal of the Mechanical Behavior of Materials*, 22:111–118, 2013.

[44] P. Junker, J. Makowski, and K. Hackl. The principle of the minimum of dissipation potential for non-isothermal processes. *Continuum Mech. Thermodyn.*, 2013.

[45] A. A. Khan and S. Huang. *Continuum Theory of Plasticity*. John Wiley & Sons, Inc., 1995.

[46] C. Kittel. *Introduction to Solid State Physics*. Wiley, 2004.

[47] D. M. Kochmann. *Mechanical Modeling of Microstructures in Elasto- Plastically Deformed Crystaline Solids*. PhD thesis, Ruhr-Universität Bochum, 2009.

[48] D. M. Kochmann and K. Hackl. The evolution of laminates in finite crystal plasticity: a variational approach. *Continuum Mechanics and Thermodynamics*, 23:63–85, 2011.

[49] D.M. Kochmann and K. Hackl. Influence of hardening on the cyclic behavior of laminate microstructures in finite crystal plasticity. *Technische Mechanik*, 30:387–400, 2010.

[50] K. Kondo. On the geometrical and physical foundations of the theory of yielding. *Proceedings of the 2nd Japan Congress in Applied Mechanics*, pages 41–47, 1952.

[51] I. Kovacs and L. Zsolodos. *Dislocations and Plastic Deformation*. Pergamon Press, 1973.

[52] M. Kroecher and A. Krieg. *Elliptische Funktionen und Modulformen*. Springer, 2007.

[53] E. D. Kröner. *Kontinuumstheorie der Versetzungen un Eigenspannungen*. Springer Verlag, 1958.

[54] E. D. Kröner. Allgemeine Kontinuumstheorie der Versetzungen und Eigenspannungen. *Arch. Rat. Mech. Anal.*, 4:273–334, 1960.

[55] E. D. Kröner. Mikrostrukturmechanik. *GAMM- Mitteilungen*, 15:104–119, 1992.

[56] J. W. Kysar, Y. Saito, M. S. Oztop, D. Lee, and W. T. Huh. Experimental lower bounds on geomentrically necessary dislocation density. *Int. J. Plasticity*, 26:1097–1123, 2010.

[57] M. Lambrecht, C. Miehe, and J. Dettmar. Energy relaxation of non-convex incremental stress potentials in a strain-softening elastic-plastic bar. *Int. J. Solids Struct.*, 40:1369–1391, 2003.

[58] K. C. Le. *Introduction to Micromechanics*. Nova Science publisher, 2012.

[59] K. C. Le and C. Günther. Nonlinear continuum dislocation theory revisited. *Int. J. Plasticity*, 53:164–178, 2014.

[60] K.C. Le and C. Günther. Martensitic phase transition involving dislocations. *JMPS*, 79:67–79, 2015.

[61] E. H. Lee and D. T. Liu. Finite-strain elastic-plastic theory particulary for plane wave analysis. *J. Appl. Phys.*, 38:19–27, 1967.

[62] G. Maier. Some theorems for plastic strain rates and plastic strains. *J. Mech.*, 8:5–19, 1969.

[63] J. B. Martin and A. R. S. Ponter. A note on a work inequality in linear viscoelasticity. *Q. Appl. Math.*, 24:161–165, 1966.

[64] G. A. Maugin. *The thermodynamics of plasticity and fracture.* Cambridge University Press, 1992.

[65] C. Miehe and M. Lambrecht. Analysis of microstructure development in shearbands by energy relaxation of incremental stress potentials: Large-strain theory for standard dissipative solids. *International Journal for Numerical Methods in Engineering*, 58:1–41, 2003.

[66] C. Miehe, M. Lambrecht, and E. Gürses. Analysis of material instabilities in inelastic solids by incremental energy minimization and relaxation: Evolving deformation microstructures in finite plasticity. *J. Mech. Phy. Solids*, 52:2725–2769, 2004.

[67] A. Mielke. *Finite elastoplasticity, Lie groups and geodesics on SL(d)*. Springer, Berlin, 2002.

[68] A. Mielke. Deriving new evolution equations for microstructures via relaxation of variational incremental problems. *Comp. Meth. Appl. Mech. Eng.*, 193:5095–5127, 2004.

[69] C. B. Morrey. Quasi-convexity and the lower semicontinuity of multiple integrals. *Pacific J. Math.*, 2:25–53, 1952.

[70] N. F. Mott and F. R. N. Nabarro. *Report on strength of solids*. Physical Society, London, 1948.

[71] S. Müller. *Calculus of Variations and Geometric Evolution Problems*, chapter Variational models for microstructure and phase transitions, pages 85–210. Springer, 1999.

[72] J. F. Nye. Some geometrical relations in dislocated crystals. *Acta Metall*, 1:153–162, 1953.

[73] W. Orowan. Zur Kristallplastiziät III Über den Mechanismus des Gleitvorganges. *Z. Phys.*, 89:634–659, 1934.

[74] M. Ortiz and E. A. Repetto. Nonconvex energy minimization and dislocation structures in ductile single crystals. *J. Mech. Phy. Solids*, 47:397–462, 1999.

[75] M. Ortiz, E. A. Repetto, and L. Stainier. A theory of subgrain dislocation structures. *J. Mech. Phys. of Solids*, 48:2077–2114, 2000.

[76] M. Polanyi. Über eine Art Gitterstörung, die einen Kristall plastisch machen könnte. *Z. Phys.*, 89:660–664, 1934.

[77] W. T. Read and W. Schockley. Dislocation models of crystal grain boundaries. *Phys. Rev.*, 78:275–289, 1950.

[78] J. N. Reddy. *Energy principles and variational methods in applied mechanics*. John Wiley & Sons, Inc., 2002.

[79] R. T. Rockafella. *Convex Analysis*. Princeton University Press, 1970.

[80] L. I. Sedov. Mathematical methods of constructing models of continuum media. *Usp. Matem. Nauk.*, 20:123–182, 1965.

[81] L. I. Sedov. *Irreversible aspects of continuum mechanics*, chapter Variational methods of constructing models of continuous media. Springer, 1968.

[82] P. G. Sembiring. *Analytical and numerical solutions to plane strain problems in continuum dislocation theory*. PhD thesis, Ruhr Universität Bochum, 2014.

[83] J. C. Simo and T. J. R. Hughes. *Computational inelasticity*. Springer, 1998.

[84] T. Suzuki, S. Takeuchi, and H. Yoshinaga. *Dislocation Dynamics and Plasticity*. Springer Verlag, 1989.

[85] G. I. Taylor. The mechanism of plastic deformation of crystals. part i: Theoretical. *Proc. R.Soc. London Soc*, 145:362–387, 1934.

[86] C. Truesdell and W. Noll. *Encyclopedia of Physics III/3*, chapter The nonlinear field theories of mechanics. Springer Berlin, 1965.

[87] T. Waitz, V. Kazykhanov, and H. P. Karnthaler. Martensitic phase transformations in nanocrystalline niti studied by tem. *Acta Materialia*, 52:3439– 3449, 2004.

[88] J. Weertmann and J. R. Weertmann. *Elementary dislocation theory*. MacMillan, New York, 1966.

[89] R. K. P. Zia, E.F. Redish, and S. R. McKay. Making sense of the legendre transform. *American Journal of Physics*, 77:614–622, 2009.

Curriculum Vitae

Christina Günther

Date of Birth	17 November 1986
Place of Birth	Bochum
Marital Status	Single
Nationality	German

School Education

1993 – 1997	Grundschule in der Vöde, Bochum
1997 – 2006	Hildegardis-Schule, Bochum

University Education

2006 – 2011	Civil Engineering, Ruhr-Universität Bochum, Bochum

Professional Occupation

2007 – 2011	Student Assistant, Lehrstuhl für Allgemeine Mechanik, Ruhr-Universität Bochum, Bochum
2011 – present	Research Associate, Lehrstuhl für Mechanik- Materialtheorie, Ruhr-Universität Bochum, Bochum

November 27, 2015

Mitteilungen aus dem Institut für Mechanik

Nr. 1 Theodor Lehmann: 1976
Große elasto-plastische Formänderungen

Nr. 2 Bogdan Raniecki/Klaus Thermann: 1978
Infinitesimal Thermoplasticity and Kinematics of Finite Elastic-Plastic Deformations. Basic Concepts

Nr. 3 Wolfgang Krings: 1976
Beitrag zur Finiten Element Methode bei linearem, viskoelastischem Stoffverhalten Stoffverhalten

Nr. 4 Burkhard Lücke: 1976
Theoretische und experimentelle Untersuchen der zyklischen elastoplastischen Blechbiegung bei endlichen Verzerrungen

Nr. 5 Knut Schwarze: 1976
Einfluß von Querschnittsverformungen bei dünnwandigen Stäben mit stetig gekrümmter Profilmittellinie

Nr. 6 Hubert Sommer: 1977
Ein Beitrag zur Theorie des ebenen elastischen Verzerrungszustandes bei endlichen Formänderungen

Nr. 7 H. Stumpf/F. J. Biehl: 1977
Die Methode der orthogonalen Projektionen und ihre Anwendungen zur Berechnung orthotroper Platten

Nr. 8 Albert Meyers: 1977
Ein Beitrag zum optimalen Entwurf von schnellaufenden Zentrifugenschalen

Nr. 9 Berend Fischer: 1977
Zur zyklischen, elastoplastischen Beanspruchen eines dickwandigen Zylinders bei endlichen Verzerrungen

Nr. 10 Wojciech Pietraszkiewicz: 1977
Introduction to the Non-Linear Theory of Shells

Nr. 11 Wilfried Ullenboom: 1977
Optimierung von Stäben unter nichtperiodischer dynamischer Belastung

Nr. 12 Jürgen Güldenpfennig: 1977
Anwendung eines Modells der Vielkristallplastizität auf ein Problem

gekoppelter elastoplastischer Wellen

Nr. 13 Pawel Rafalski: 1978
Minimum Principles in Plasticity

Nr. 14 Peter Hilgers: 1978
Der Einsatz eines Mikrorechners zur hybriden Optimierung und Schwingungsanalyse

Nr. 15 Hans-Albert Lauert: 1979
Optimierung von Stäben unter dynamischer periodischer Beanspruchung bei Beachtung von Spannungsrestriktionen

Nr. 16 Martin Fritz: 1979
Berechnund der Auflagerkräfte und der Muskelkräfte des Menschen bei ebenen Bewegungen aufgrund von kinematographischen Aufnahmen

Nr. 17 H. Stumpf/F. J. Biehl: 1979
Approximations and Error Estimates in Eigenvalue Problems of Elastic Systems with Application to Eigenvibrations of Orthotropic Plates

Nr. 18 Uwe Kohlberg: 1979
Variational Principles and theirNumerical Application to Geometrically Nonlinear v. Karman Plates

Nr. 19 Heinz Antes: 1980
Über Fehler und Möglichkeiten ihrer Abschätzung bei numerischen Berechnungen von Schalentragwerken

Nr. 20 Czeslaw Wozniak: 1980
Large Deformations of Elastic and Non-Elastic Plates, Shells and Rods

Nr. 21 Maria K. Duszek: 1980
Problems of Geometrically Non-Linear Theory of Plasticity

Nr. 22 Burkhard von Bredow: 1980
Optimierung von Stäben unter stochastischer Erregung

Nr. 23 Jürgen Preuss: 1981
Optimaler Entwurf von Tragwerken mit Hilfe der Mehrzielmethode

Nr. 24 Ekkehard Großmann: 1981
Kovarianzanalyse mechanischer Zufallsschwingungen bei Darstellung der mehrfachkorrelierten Erregungen durch stochastische Differentialgleichungen

Nr. 25 Dieter Weichert: 1981
Variational Formulation and Solution of Boundary-Value Problems in the Theory of Plasticity and Application to Plate Problems

Nr. 26 Wojciech Pietraszkiewicz: 1981

On Consistent Approximations in the Geometrically Non-Linear Theory of Shells

Nr. 27 Georg Zander: 1981
Zur Bestimmung von Verzweigungslasten dünnwandiger Kreiszylinder unter kombinierter Längs- und Torsionslast

Nr. 28 Pawel Rafalski: 1981
An Alternative Approach to the Elastic-Viscoplastic Initial-Boundary Value Problem

Nr. 29 Heinrich Oeynhausen: 1981
Verzweigungslasten elastoplastisch deformierter, dickwandiger Kreiszylinder unter Innendruck und Axialkraft

Nr. 30 F.-J. Biehl: 1981
Zweiseitige Eingrenzung von Feldgrößen beim einseitigen Kontaktproblem

Nr. 31 Maria K. Duszek: 1982
Foundations of the Non-Linear Plastic Shell Theory

Nr. 32 Reinhard Piltner: 1982
Spezielle finite Elemente mit Löchern, Ecken und Rissen unter Verwendung von analytischen Teillösungen

Nr. 33 Petrisor Mazilu: 1982
Variationsprinzipe der Thermoplastizität I. Wärmeausbreitung und Plastizität

Nr. 34 Helmut Stumpf: 1982
Unified Operator Description, Nonlinear Buckling and Post-Buckling Analysis of Thin Elastic Shells

Nr. 35 Bernd Kaempf: 1983
Ein Exremal-Variationsprinzip für die instationäre Wärmeleitung mit einer Anwendung auf thermoelastische Probleme unter Verwendung der finiten Elemente

Nr. 36 Alfred Kraft: 1983
Zum methodischen Entwurf mechanischer Systeme im Hinblick auf optimales Schwingungsverhalten

Nr. 37 Petrisor Mazilu: 1983
Variationsprinzipe der Thermoplastizität II. Gekoppelte thermmomechanische Prozesse

Nr. 38 Klaus-Detlef Mickley: 1983
Punktweise Eingrenzung von Feldgrößen in der Elastomechanik und ihre numerische Realisierung mit Fundamental-Splinefuntionen

Nr. 39 Lutz-Peter Nolte: 1983

Beitrag zur Herleitung und vergleichende Untersuchung geometrisch nichtlinearer Schalentheorien unter Berücksichtigung großer Rotationen

Nr. 40 Ulrich Blix: 1983
Zur Berechnung der Einschnürung von Zugstäben unter Berücksichtigung thermischer Einflüsse mit Hilfe der Finite-Element-Methode

Nr. 41 Peter Becker: 1984
Zur Berechnung von Schallfeldern mit Elemtmethoden

Nr. 42 Diemar Bouchard: 1984
Entwicklung und Anwendung eines an die Diskrete-Fourier-Transformation angepaßten direkten Algorithmus zur Bestimmung der modalen Parameter linearer Schwingungssysteme

Nr. 43 Uwe Zdebel: 1984
Theoretische und experimentelle Untersuchungen zu einem thero-plastischen Stoffgesetz

Nr. 44 Jan Kubik: 1985
Thermodiffusion Flows in a Solid with a Dominant Constituent

Nr. 45 Horst J. Klepp: 1985
Über die Gleichgewichtslagen und Gleichgewichtsbereiche nichtlinearer autonomer Systeme

Nr. 46 J. Makowski/L.-P. Nolte/H. Stumpf: 1985
Finite In-Plane Deformations of Flexible Rods - Insight into Nonlinar Shell Problems

Nr. 47 Franz Karl Labisch: 1985
Grundlagen einer Analyse mehrdeutiger Lösungen nichtlinearer Randwertprobleme der Elastostatik mit Hilfe von Variationsverfahren

Nr. 48 J. Chroscielewski/L.-P. Nolte: 1985
Strategien zur Lösung nichtlinearer Probleme der Strukturmechanik und ihre modulare Aufbereitung im Konzept MESY

Nr. 49 Karl-Heinz Bürger: 1985
Gewichtsoptimierung rotationssymmetrischer Platten unter instationärer Erregung

Nr. 50 Ulrich Schmid: 1987
Zur Berechnung des plastischen Setzens von Schraubenfedern

Nr. 51 Jörg Frischbier: 1987
Theorie der Stoßbelastung ortotroper Platten und ihr experimentelle Überprüfung am Beispiel einer unidirektional verstärkten CFK-Verbundplatte

Nr. 52 W. Tampczynski: 1987

Strain history effect in cyclic plasticity

Nr. 53 Dieter Weichert: 1987
Zum Problem geometrischer Nichtlinearitäten in der Plastizitätstheorie

Nr. 54 Heinz Antes/Thomas Meise/Thomas Wiebe: 1988
Wellenausbreitung in akustischen Medien Randelement-Prozeduren im 2-D Frequenzraum und im 3-D Zeitbereich

Nr. 55 Wojciech Pietraszkiewicz: 1988
Geometrically non-linear theories of thin elastic shells

Nr. 56 Jerzy Makowski/Helmut Stumpf: 1988
Finite strain theory of rods

Nr. 57 Andreas Pape: 1988
Zur Beschreibung des transienten und stationären Verfestigungsverhaltens von Stahl mit Hilfe eines nichtlinearen Grenzflächenmodells

Nr. 58 Johannes Groß-Weege: 1988
Zum Einspielverhalten von Flächentragwerken

Nr. 59 Peihua LIU: 1988
Optimierung von Kreisplatten unter dynamischer nicht rotationssymmetrischer Last

Nr. 60 Reinhard Schmidt: 1988
Die Anwendung von Zustandsbeobachtern zur Schwingungsüberwachung und Schadensfrüherkennung auf mechanische Konstruktionen

Nr. 61 Martin Pitzer: 1988
Vergleich einiger FE-Formulierungen auf der Basis eines inelastischen Stoffgesetzes

Nr. 62 Jerzy Makowski/Helmut Stumpf: 1988
Geometric structure of fully nonlinear and linearized Cosserat type shell theory

Nr. 63 O. T. Bruhns: 1989
Große plastische Formänderungen - Bad Honnef 1988

Nr. 64 Khanh Chau Le/Helmut Stumpf/Dieter Weichert: 1989
Variational principles of fracture mechanics

Nr. 65 Guido Obermüller: 1989
Ein Beitrag zur Strukturoptimierung unter stochastischen Lasten

Nr. 66 Herbert Diehl: 1989
Ein Materialmodell zur Berechnung von Hochgeschwindigkeitsdeformationen

metallischer Werkstoffe unter besonderer Berücksichtigung der Schädigung durch Scherbänder

Nr. 67 Michael Geis: 1989
Zur Berechnund ebener, elastodynamischer Rißprobleme mit der Randelementmethode

Nr. 68 Günter Renker: 1989
Zur Identifikation nichtlinearer strukturmechanischer Systeme

Nr. 69 Berthold Schieck: 1989
Große elastische Dehnungen in Schalen aus hyperelastischen inkompressiblen Materialien

Nr. 70 Frank Szepan: 1989
Ein elastisch-viskoplastisches Stoffgesetz zur Beschreibung großer Formänderungen unter Berücksichtigung der thermomechanischen Kopplung

Nr. 71 Christian Scholz: 1989
Ein Beitrag zur Gestaltsoptimierung druckbelasteter Rotationsschalen

Nr. 72 J. Badur/H. Stumpf: 1989
On the influence of E. and F. Cosserat on modern continuum mechanics and field theory

Nr. 73 Werner Fornefeld: 1990
Zur Parameteridentifikation und Berechnung von Hochgeschwindigkeitsdeformationen metallischer Werkstoffe anhand eines Kontinuums-Damage-Modells

Nr. 74 J. Saczuk/H. Stumpf: 1990
On statical shakedown theorems for non-linear problems

Nr. 75 Andreas Feldmüller: 1991
Ein thermoplastisches Stoffgesetz isotrop geschädigter Kontinua

Nr. 76 Ulfert Rott: 1991
Ein neues Konzept zur Berechnung viskoplastischer Strukturen

Nr. 77 Thomas Heinrich Pingel: 1991
Beitrag zur Herleitung und numerischen Realisierung eines mathematischen Modells der menschlichen Wirbelsäule

Nr. 78 O. T. Bruhns: 1991
Große plastische Formänderungen - Bad Honnef 1991

Nr. 79 J. Makowski/J. Chroscielewski/H. Stumpf:
Computational Analysis of Shells Undergoing Large Elastic Deformation Part I:Theoretical Foundations

Nr. 80 J. Chroscielewski/J. Makowski/H. Stumpf:
Computational Analysis of Shells Undergoing Large Elastic Deformation Part II: Finite Element Implementation

Nr. 81 R. H. Frania/H. Waller: 1992
Entwicklung und Anwendung spezieller finiter Elemente für Kerbspannungsprobleme im Maschienebau

Nr. 82 B. Bischoff-Beiermann: 1992
Zur selbstkonsistenten Berechnung von Eigenspannungen in polykristallinem Eis unter Berücksichtigung der Monokristallanisotropie

Nr. 83 J. Pohé: 1993
Ein Beitrag zur Stoffgesetzentwicklung für polykristallines Eis

Nr. 84 U. Kikillus: 1993
Ein Beitrag zum zyklischen Kiechverhalten von Ck 15

Nr. 85 T. Guo: 1993
Untersuchung des singulären Rißspitzenfeldes bei stationärem Rißwachstum in verfestigendem Material

Nr. 86 Achim Menne: 1994
Identifikation der dynamischen Eigenschaften von hydrodynamischen Wandlern

Nr. 87 Uwe Folchert: 1994
Identifikation der dynamischen Eigenschaften Hydrodynamischer Kopplungen

Nr. 88 Jörg Körber: 1994
Ein verallgemeinertes Finite-Element-Verfahren mit asymptotischer Stabilisierung angewendet auf viskoplastische Materialmodelle

Nr. 89 Peer Schieße: 1994
Ein Beitag zur Berechnung des Deformationsverhaltens anisotrop geschädigter Kontinua unter Berücksichtigung der thermoplastischen Kopplung

Nr. 90 Egbert Schopphoff: 1994
Dreidimensionale mechanische Analyse der menschlichen Wirbelsäule

Nr. 91 Christoph Beerens: 1994
Zur Modellierung nichtlinearer Dämpfungsphänomene in der Strukturmechanik

Nr. 92 K. C. Le/H. Stumpf: 1994
Finte elastoplasticity with microstructure

Nr. 93 O. T. Bruhns: 1994
Große plastische Formänderungen - Bad Honnef 1994

Nr. 94 Armin Lenzen: 1994
Untersuchung von dynamischen Systemen mit der Singulärwertzerlegung - Erfassung von Strukturveränderungen

Nr. 95 J. Makowski/H. Stumpf: 1994
Mechanics of Irregular Shell Structures

Nr. 96 J. Chroscielewski/J. Makowski/H. Stumpf: 1994
Finte Elements for Irregular Nonlinear Shells

Nr. 97 W. Krings/A. Lenzen/u. a.: 1995
Festschrift zum 60. Geburtstag von Heinz Waller

Nr. 98 Ralf Podleschny: 1995
Untersuchung zum Instabilitätsverhalten scherbeanspruchter Risse

Nr. 99 Bernd Westerhoff: 1995
Eine Untersuchung zum geschwindigkeitsabhängigen Verhalten von Stahl

Nr. 100 Marc Mittelbach: 1995
Simulation des Deformations- und Schädigungsverhaltens beim Stoßversuch mit einem Kontinuums-Damage-Modell

Nr. 101 Ulrich Hoppe: 1996
Über grundlegende Konzepte der nichtlinearen Kontinuumsmechanik und Schalentheorie

Nr. 102 Marcus Otto: 1996
Erweiterung des Kaustikenverfahrens zur Analyse räumlicher Spannungskonzentrationen

Nr. 103 Horst Lanzerath: 1996
Zur Modalanalyse unter Verwendung der Randelementemethode

Nr. 104 Andreas Wichtmann: 1996
Entwicklung eines thermodynamisch konsistenten Stoffgesetzes zur Beschreibung der Reckalterung

Nr. 105 Bjarne Fossa: 1996
Ein Beitrag zur Fließflächenmessung bei vorgedehnten Stoffen

Nr. 106 Khanh Chau Le: 1996
Kontinuumsmechanisches Modellieren von Medien mit veränderlicher Mikrostruktur

Nr. 107 Holger Behrens: 1997
Nichtlineare Modellierung und Identifikation hydrodynamischer Kupplungen mit allge- meinen diskreten Modellansätzen

Nr. 108 Johannes Moosheimer: 1997

Gesteuerte Schwingungsdämpfung mit Elektrorheologischen Fluiden

Nr. 109 Dirk Klaus Anding: 1997
Zur simultanen Bestimmung materialabhängiger Koeffizienten inelastischer Stoffgesetze

Nr. 110 Stephan Weng: 1997
Ein Evolutionsmodell zur mechanischen Analyse biologischer Strukturen

Nr. 111 Michael Straßberger: 1997
Aktive Schallreduktion durch digitale Zustandsregelung der Strukturschwingungen mit Hilfe piezo-keramischer Aktoren

Nr. 112 Hans-Jörg Becker: 1997
Simultation des Deformationsverhaltens polykristallinen Eises auf der Basis eines monokristallinen Stoffgesetzes

Nr. 113 Thomas Nerzak: 1997
Modellierung und Simulation der Ausbreitung adiabatischer Scherbänder in metallischen Werkstoffen bei Hochgeschwindigkeitsdeformationen

Nr. 114 O. T. Bruhns: 1998
Große plastische Formänderungen

Nr. 115 Jan Steinhausen: 1998
Die Beschreibung der Dynamik von Antriebssträngen durch Black-Box-Modelle hydrodynamischer Kupplungen

Nr. 116 Thomas Pandorf: 1998
Experimentelle und numerische Untersuchungen zur Kerbspitzenbeanspruchung bei schlagbelasteten Biegeproben

Nr. 117 Claus Oberste-Brandenburg: 1999
Ein Materialmodell zur Beschreibung der Austenit-Martensit Phasentransformation unter Berücksichtigung der transformationsinduzierten Plastizität

Nr. 118 Michael Märtens: 1999
Regelung mechanischer Strukturen mit Hilfe piezokeramischer Stapelaktoren

Nr. 119 Dirk Kamarys: 1999
Detektion von Systemveränderungen durch neue Identifikationsverfahren in der experimentellen Modalanalyse

Nr. 120 Wolfgang Hiese: 2000
Gültigkeitskriterien zur Bestimmung von Scherbruchzähigkeiten

Nr. 121 Peter Jaschke: 2000
Mathematische Modellierung des Betriebsverhaltens hydrodynamischer Kupplungen mit hybriden Modellansätzen

Nr. 122 Stefan Müller: 2000
Zum Einsatz von semi-aktiven Aktoren zur optimalen Schwingungsreduktion in Tragwerken

Nr. 123 Dirk Eichel: 2000
Zur Kondensation strukturdynamischer Aufgaben mit Hilfe von Polynommatrizen

Nr. 124 Andreas Bürgel: 2000
Bruchmechanische Kennwerte beim Wechsel im Versagensverhalten dynamisch scherbeanspruchter Risse

Nr. 125 Daniela Lürding: 2001
Modellierung großer Deformationen in orthotropen, hyperelastischen Schalenstrukturen

Nr. 126 Thorsten Quent: 2001
Ein mikromechanisch begründetes Modell zur Beschreibung des duktilen Verhaltens metallischer Werkstoffe bei endlichen Deformationen unter Berücksichtigung von Porenschädigung

Nr. 127 Ndzi C. Bongmba: 2001
Ein finites anisotropes Materialmodell auf der Basis der Hencky-Dehnung und der logarithmischen Rate zur Beschreibung duktiler Schädigung

Nr. 128 Henning Schütte: 2001
Ein finites Modell für spröde Schädigung basierend auf der Ausbreitung von Mikrorissen

Nr. 129 Henner Vogelsang: 2001
Parameteridentifikation für ein selbstkonsistentes Stoffmodell unter Berücksichtigung von Phasentransformationen

Nr. 130 Jörn Mosler: 2002
Finite Elemente mit sprungstetigen Abbildungen des Verschiebungsfeldes für numerische Analysen lokalisierter Versagenszustände

Nr. 131 Karin Preusch: 2003
Hierarchische Schalenmodelle für nichtlineare Kontinua mit der p-Version der Finite-Element Methode

Nr. 132 Christoph Müller: 2003
Thermodynamic modeling of polycrystalline shape memory alloys at finite strains

Nr. 133 Martin Heiderich: 2004
Ein Beitrag zur zerstörungsfreien Schädigungsanalyse

Nr. 134 Raoul Costamagna: 2004
Globale Materialbeziehungen für das geklüftete Gebirge

Nr. 135 Markus Böl: 2005
Numerische Simulation von Polymernetzwerken mit Hilfe der Finite-Elemente-Methode

Nr. 136 Gregor Kotucha: 2005
Regularisierung von Problemen der Topologieoptimierung unter Einbeziehung von Dichtegradienten

Nr. 137 Michael Steiner: 2006
Deformations- und Versagensverhalten innendruckbeanspruchter Stahlrohre durch Stoßbelastung

Nr. 138 Dirk Bergmannshoff: 2006
Das Instabilitätsverhalten zug-/scherbeanspruchter Risse bei Variation des Belastungspfades

Nr. 139 Olaf Schilling: 2007
Über eine implizite Partikelmethode zur Simulation von Umformprozessen

Nr. 140 Jörn Mosler: 2007
On the numerical modeling of localized material failure at finite strains by means of variational mesh adaption and cohesive elements

Nr. 141 Rainer Fechte-Heinen: 2007
Mikromechanische Modellierung von Formgedächtnismaterialien

Nr. 142 Christian Grabe: 2007
Experimental testing and parameter identification on the multidimensional material behavior of shape memory alloys

Nr. 143 Markus Peters: 2007
Modellierung von Rissausbreitung unter Verwendung der p-Version der XFEM mit einer adaptiven Integrationsmethode

Nr. 144 Claus Oberste-Brandenburg: 2007
Thermomechanical modeling of shape memory alloys at different length scales

Nr. 145 Stefan Reichling: 2007
Das inverse Problem der quantitativen Ultraschallelastografie unter Berücksichtigung großer Deformationen

Nr. 146 Kianoush Molla-Abbasi: 2008
A Consistent Anisotropic Brittle Damage Model Based on the Concept of Growing Elliptical Cracks

Nr. 147 Sandra Ilic: 2008
Application of the multiscale FEM to the modeling of composite materials

Nr. 148 Patrick Luig: 2008
A consistent Eulerian rate model for shape memory alloys

Nr. 149 Lidija Stanković: 2009
Describing multiple surface localised failure by means of strong discontinuities at finite strains

Nr. 150 Thorsten Bartel: 2009
Multiskalenmodellierung martensitischer Phasentransformationen in Formgedächtnislegierungen unter Verwendung relaxierter Energiepotenziale

Nr. 151 Zoran Stanković: 2009
Detection of fatigue crack growth using nondestructive testing methods

Nr. 152 Dennis M. Kochmann: 2009
Mechanical Modeling of Microstructures in Elasto-Plastically Deformed Crystalline Solids

Nr. 153 Trinh Bach Tuyet: 2009
Constitutive Modelling and Numerical Simulation of Localization Phenomena in Solid Materials with Application to Soils and Geomaterials

Nr. 154 Bojan Dimitrijevic: 2010
On a regularization framework for inelastic material models via gradient enhancement of the free energy function

Nr. 155 Philipp Junker: 2011
Simulation of Shape Memory Alloys - Material Modeling Using the Principle of Maximum Dissipation

Nr. 156 Muhammad Sabeel Khan: 2013
An Investigation of Material Microstructures via Relaxation of Non-convex Potentials

Nr. 157 K. Hackl, H. Steeb, U. Hoppe, R. Jänicke, P. Junker: 2013
Übungen zu Mechanik A

Nr. 158 K. Hackl, H. Steeb, U. Hoppe, R. Jänicke, P. Junker: 2013
Übungen zu Mechanik B

Nr. 159 Patrick S. Kurzeja: 2013
Waves in partially saturated porous media: An investigation on multiple scales

Nr. 160 Christoph Moos: 2013
An FFT Based Algorithmfor Damage Mechanics

Nr. 161 Carlo Vinci: 2014
Hydro-mechanical coupling in fractured rocks: modeling and numerical simulations

Nr. 162 Pramio G. Sembiring: 2014
Analytical and Numerical Solutions to Plane Strain Problems in Continuum Dislocation Theory

Nr. 163 Timo Reisner: 2015
Fluid compressibility in a solid-fluid mixture flow: Experiments, modeling and numerical application to batch sedimentation

Nr. 164 Alexander Schaufler: 2015
Multi-physical simulations: transport and infiltration of suspensions in granular porous media

Nr. 165 Christina Günther: 2015
Continuum modeling of ductile crystals with evolving microstructures

Mitteilungen aus dem Institut für Mechanik
RUHR-UNIVERSITÄT BOCHUM
Nr. 165, Oktober 2015

ISBN 978-3-935892-43-8